Avalanche Studies and model Validation in Europe, SATSIE

1st Annual Report

20021048-3 28 November 2003

Client: **European Commission**

Contact person: Maria Yeroyanni
Contract reference: Contract of 18.10.02

For the Norwegian Geotechnical Institute

Project Manager: Karstein Lied

Report prepared by: Dieter Issler

Reviewed by: Karstein Lied

Work also carried out by: WP-leaders

Postal address: P.O. Box 3930 Ullevaal Stadion, N-0806 OSLO, NORWAY
Street address: Sognsveien 72, OSLO
Internet: http://www.ngi.no
Telephone: (+47) 22 02 30 00
Telefax: (+47) 22 23 04 48
e-mail: ngi@ngi.no
Postal account: 0814 51 60643
Bank account: 5096 05 01281
Business No. 958 254 318 MVA

European Commission

Fifth Framework Programme

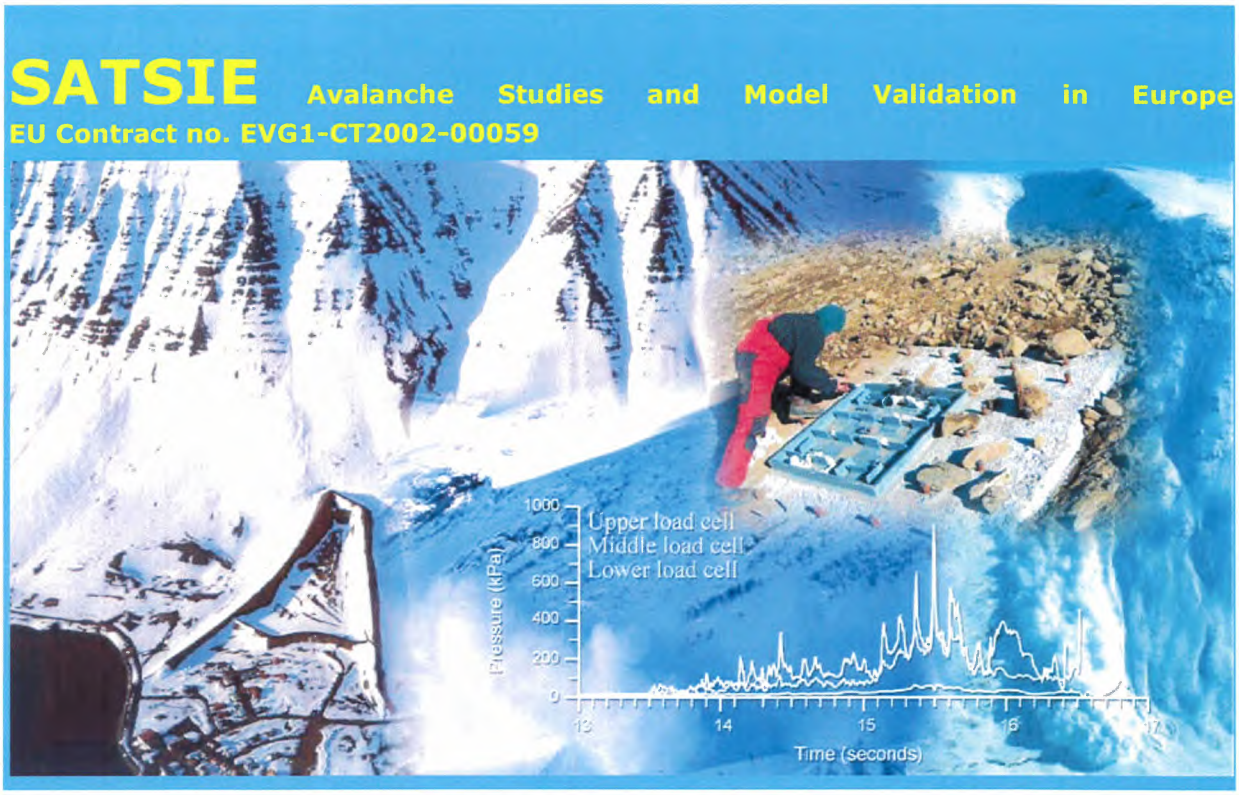

1st Annual Report

Deliverable D3

30 November 2003

Reporting period: 1 October 2002 – 30 September 2003

Coordinator: Norwegian Geotechnical Institute

CONTENTS

Summary

During the first year of the SATSIE project, emphasis was on preparatory activities, i.e., development of sensors and data analysis methods, installation of new equipment in the experimental facilities, exploration of different options for developing new models, and establishing a web-site for communication within the project and to the interested public. Two measurement campaigns could be conducted at the full-scale site Ryggfonn (Norway), albeit with limited instrumentation only, as had been anticipated. At all the chutes, however, intensive experimentation has begun and has already produced intriguing preliminary results that will be tested and extended in the second project year. In view of the planned model development, candidate rheological approaches and entrainment mechanisms have been investigated for their relevance and applicability.

In the following, we summarise the main activities and results in the six work packages of the project and the expenditures of each partner during the reporting period. In six separate chapters, a more detailed account of the activities and results of all the work packages is given. The Appendix collects several scientific papers and reports written in the first year of SATSIE are collected for reference.

WP 1 – Sensor development

Investigation of avalanche processes in situ or in a laboratory requires specially adapted instrumentation. Suitable sensors that are commercially available were purchased by the SATSIE consortium. However, required sensors that are not available on the market have to be developed by us. This work package, devoted to adapting and developing instrumentation, is therefore one of the basic work packages of this project. It is organised in six tasks. Each of them concerns the development of a specific sensor type.

The development of two types of radar has advanced very far during the first year of SATSIE:
Pulsed Doppler radar for measuring avalanche velocities;
Frequency-modulated continuous-wave (FMCW) radar for investigating the internal structure and velocity profile of avalanches.
Both radars will be installed in the Ryggfonn test site towards the end of 2003.
Video methods for analysis of avalanche dynamics are under development with the main focus on colour or black-and-white systems, high-speed or high-resolution machine vision systems or digital camcorders, more than 8-bit field camera for better grey-level depth, multi-shuttering capabilities and digitisation systems.

Vertical arrays of horizontally oriented pairs of Luminous Electric Diodes (LED) can be combined with the cross-correlation method as an alternative method for determining the velocity profiles inside dense snow flows. A new system was designed, developed, tested and installed at Col du Lac Blanc (CLB). During the winter 2002–2003, 20 experiments were performed.

Two tri-axial load plates, each with an area of 1 m^2, were installed in the upstream face of the catching dam in Ryggfonn in September 2002. The load plates measure shear stress along the two perpendicular axes in the plane of the dam front, and normal stress perpendicular to the dam front.

A snow rheometer for studying the constitutive law of snow is under development. A seismic sensor system was planned and installed in Ryggfonn in the summer of 2003.

WP 2 – Development of data analysis techniques

One task comprises the development of algorithms and data-analysis techniques for the two different types of radar sensors: Pulsed Doppler radar and FMCW radar. Work on the design of algorithms (porting from existing radars), DSP-software development and PC-software development (data-analysis and data-representation) has begun. The software has been mostly completed so the radar can be installed in Ryggfonn this fall (2003) and record data during the coming winters.

The software for processing video film clips has been finished and applied to snow avalanches and laboratory experiments. Control points, which are necessary for camera calibration, have only been obtained for one avalanche and used to obtain a velocity profile down the track. For the remainder of the project the software will be applied to any avalanches that are observed.

Work has been done on analysing the frequency response of an ultra-low differential pressure sensor system. This sensor has been used in laboratory experiments of powder snow avalanches. The data has been presented at two conferences and a paper will shortly be completed. A brief paper has been written on filming avalanches.

Discussions on impact pressure analysis have been carried out with SLF, Davos, on the current state-of-the-art, and preliminary work started on the design of new algorithms.

Existing options for acquiring and consequent processing of avalanche seismic data are reviewed. In general, relatively little has been published in terms of the seismic detection and analysis techniques of avalanches.

In terms of choosing specific seismic data analysis software, it was decided to use the programs SAC and CORAL. As of the beginning of the year, the above mentioned software has been installed on a dedicated PC running under the Linux OS. Seismic data from Ryggfonn has been analysed using these tools.

On correlation methods, two papers have been written on the analysis and design of opto-electronic sensors. Software for calculating the correlations has been completed. Work is currently underway applying ideas of matched filtering to improve the signal-to-noise ratio, and thus reduce the errors. A paper using the techniques will be completed in the next six months.

WP 3 – Instrumentation of selected facilities

At the full-scale test site Ryggfonn in Norway, two load plates were installed on the front side of the dam and two trenches constructed for housing the ground radars and the University of Barcelona's geophones. A Doppler radar for the deflecting dam at Flateyri (Iceland) was installed at Ryggfonn temporarily for testing. Electronics damaged by severe lightning had to be replaced. Pressure sensors were also installed at the Taconnaz retarding and deflecting dam system in France.

Further instrumentation work in France concentrated on the snow chute at Col du Lac Blanc where the data acquisition system and sensors measuring the flow depth, bed stresses and the velocity profile were installed, tested and used. The measurement equipment for the indoor chute at the University of Pavia was enhanced by acquiring two frame-grabber devices and PCs so that high-speed video capturing is now possible at three locations.

Additional chutes that are used in SATSIE are located in Grenoble and Bristol. No changes were made to their instrumentation, but they will also be briefly described below to complete the overview of the experimental facilities used in SATSIE.

WP 4 – Measurement campaigns and data analysis

This chapter reports on the results obtained in experiments on two real snow avalanches at the Norwegian test site Ryggfonn, one small-scale experiments with snow in the chute at the Col du Lac Blanc (France), and one small-scale experiments with dry granular materials or water at laboratory chutes in Pavia (Italy) and Bristol (England). All experimental facilities are described in the chapter on WP 3, while the new non-standard sensors are discussed in the one on WP 1. Furthermore, the experiments carried out in Pavia and Bristol are covered in detail in two reports (Barbolini and Pagliardi, 2003; Hákonardóttir *et al.*, 2003) that are reproduced in full in the annex to the present report. Those experiments will therefore only be summarised in this chapter.

Despite the unusually mild conditions in western Norway with few significant precipitation periods throughout the winter 2003–2003, measurements were obtained of two avalanches at Ryggfonn, one spontaneous of medium size and one small, artificially released. Only pressure measurements at one obstacle in the path and one at the dam could be obtained from the spontaneous event, as the FMCW radars developed by SATSIE are scheduled to be installed by the end of 2003. Velocity measurements with AIATR's pulsed Doppler radar were made of the artificially released avalanche. Load data were obtained at the measurement points in the path, but due to the short run-out there were no data from the dam. In Flateyri and Taconnaz there was no avalanche activity this winter. None of these two sites were instrumented at the time.

During the first year of SATSIE, the experiments at the chutes in Pavia and at Col du Lac Blanc focussed on the flow regimes exhibited by flows over smooth and rough surfaces, and with snow and dry granular materials. Experiments in Pavia on a smooth bed clearly showed the characteristics of the collisional flow regime in the body and the grain-inertia regime in the more dilute head, with significant slip at the bed. Moreover, the non-dimensionalised velocity profiles collapse intriguingly well with those measured in snow flows over a wide range of scales. Over a rough bed, steady-state flow was not achieved, and high particle concentrations indicative of the frictional (quasi-static) flow regime were found in the body of the flow; in agreement with this, the velocity profiles were linear without slip at the bed. In contrast, the measurements at the snow chute achieved steady-state flow over an even rougher bed than in Pavia, but the linear velocity profiles showed little shear and very pronounced slip. At first sight, the results appear to be somewhat contradictory between the snow flows and the granular ones, but it is conjectured that the observed differences are due to different boundary conditions, slope inclination and particle properties. Further measurements will be made during the second year to clarify these points.

Chute experiments in Bristol confirm that dry granular flows impacting on deflecting or catching dams are quite well described by shocks in shallow-water theory—even better than water flows themselves. Further work will focus on understanding the observed deviations from theory, investigating the effect cohesion has on the impact behaviour, up-scaling to real avalanches and extracting the consequences for the design of protection dams. For this last step, observations of real snow avalanches impacting on the dams in Ryggfonn, Flateyri and Taconnaz would be highly desirable.

Task 4.3 (cross-comparison of experimental results at different sites and scales) could not yet be tackled in full because the FMCW radar devices under development (WP 1) are needed to obtain information on the processes in the interior of the avalanches at Ryggfonn. Task 4.4 is scheduled only for the third year of SATSIE.

WP 5 – Model development and validation

During an intensive workshop, held at the University of Leeds in Jnauary 2003, current knowledge on flow regimes, entrainment and avalanche interaction with obstacles was reviewed, with a view towards both to the experimental programme at the chutes and the choice of modelling approach. There are presently two main approaches promising to lead beyond the ad-hoc rheological assumptions on which most two-parameter avalanche flow models in use today are based: (i) The dependence of the effective friction coefficient on the Froude number of the flow is determined empirically in chute experiments. Both snow and dry granular materials covering a wide range of material (grain) properties and flow conditions are used. The obtained relationship is then directly implemented in a dynamical model. (ii) The Criminale–Ericksen–Filbey rheology is a quite general constitutive equation combining properties of visco-elasto-plastic materials with granular behaviour in the frictional and collisional regimes. It appears to encompass the spectrum of flow behaviour observed in snow-avalanches. Further experiments should be made and old measurements reanalysed in order to select the most promising approach.

Possible snow entrainment mechanisms were studied theoretically in order to estimate expected entrainment rates and compare them to the rates inferred from observations and measurements. Another study investigated the dependence of the run-out distance on the entrainment rate and the mode of entrainment (at the front of the avalanche or along all its body). It found entrainment indeed to be an important factor, but under realistic conditions the effect depended only weakly on the exact properties of the entrainment model. This supports the expectation that a useful entrainment model can be developped even without a perfect theory of entrainment.

Shallow-flow models with frictional behaviour, implemented in a higher-order shock-capturing numerical scheme, give astonishingly good results in the simulations of flow over various obstacles, even though they do not account for compressive dissipation in the impact. We thus intend to use such a numerical basis for the new model with flow-regime trnasitions and entrainment/deposition. This will improve the model's suitability in the design process of protection dams.

Theoretical analysis of the implications of laboratory experiments on the formation of a suspension layer from a dense gravity mass flow has emphasised the role of the Richardson number in determining the air entrainment rate at the surface of a powder-snow avalanche. This work will be continued in the second year of SATSIE..

WP 6 – Data sharing and dissemination of results

This work package comprises two tasks that focus on internal communication and data exchange, one task ascertaining the safety of valuable data, and three tasks concerned with communication with the outside and dissemination of our results to avalanche professionals in Europe. Accordingly, the first group had to be started very early in the project. While the project web-site was soon operational, database design has been delayed due to external reasons.

The tasks oriented towards disseminating the results of the project can only be started in the late phase of SATSIE when sufficiently well tested results from experiments and modelling have been obtained.

Summary of expenditures

The project expenditures of each partner institution during the first year are summarised in the table below. The over-all sum is slightly larger than budgeted, mostly due to higher costs of installing experimental equipment. Generally, institutions with experimental infra-structure have used a relatively larger fraction of their total allocation for the entire three-year period than the partners active mostly in data analysis and modelling, who will make their largest contributions later in the project.

By and large, budgeting thus has proved to be realistic. It should be noted, however, that many budgets are extremely tight due to the cuts imposed on the project during the negotiation period. As the cost of necessary equipment could not be reduced in most cases, personnel expenditures had to be cut dramatically. This implies that much analysis and modelling work cannot be done that would be required to reach the maximum benefit from the experiments.

SATSIE: Costs per partner

For period from 2002-10-01 to 2003-09-30

Contractor	Costs								
	Person-nel	Durable equipment	Travel	Consum-ables	Other specific costs	Coordina-tion	Over-heads	**Total costs**	Budget 1st year
NGI	100 235	66 533	1 618	23 930	0	31 294	78 758	**302 369**	302 386
IMO	26 835	21 384	13 911	788	0	0	21 468	**84 385**	71 619
SGUL	1 804	139	656	124	0	0	545	**3 267**	17 389
DAMTP	25 027	0	2 415	3 608	0	0	6 210	**37 260**	47 663
AIATR	14 499	0	7 624	3 700	0	0	11 599	**37 421**	38 838
INW	50 676	11 100	2 205	10 259	0	0	14 848	**89 088**	98 579
ETNA	155 802	36 464	9 360	3 346	0	0	42 354	**247 325**	188 975
DIIA	21 769	4 425	4 167	0	0	0	0	**30 361**	40 006
DGG	16 157	8 317	11 002	1 541	897	0	7 583	**45 499**	48 748
TOTAL	**412 804**	**148 362**	**52 958**	**47 297**	**897**	**31 294**	**183 364**	**876 975**	**854 203**

WP 1 – Sensor development (ETNA)

(Work package leader: Mohamed Naaim)

Introduction and summary

Understanding snow avalanche requires good qualitative and quantitative measurements of the physical processes involved in avalanche dynamics, both in situ and in the laboratory. The only way to obtain such measurements is the use of a variety of accurate instruments. Snow is a complex material and avalanches are a very violent phenomenon, thus classical sensors cannot always be used. In the framework of this work package, we adapt three existing sensor types to the specific needs of avalanche research, namely image analysis, force measurements and seismic sensors. Light-emitting diode/photocell arrays and radar have been used in avalanche research already for two decades; here, our work aims at a leap in the performance of these systems and also at reducing the cost of the radar systems to the point where they can be widely used in avalanche alarm systems.

The data from all these sensors need to be analysed with sophisticated techniques in order to extract the full information contained in it. The development of these techniques is the topic of Work Package 2.

Task 1.1. Radar techniques (INW/NGI)

(Task leader: Helmut Schreiber)

This task includes the development of two different radar sensors:

- Pulsed Doppler radar allows remote measurement of the velocity distribution simultaneously in several segments of an avalanche and so provides fundamental information for understanding the structure of avalanche flows and validating dynamical models. The Institute of Communication and Wave Propagation (INW) of the Technical University of Graz develops a state-of-the-art system at a significantly lower cost than older, less performant designs.
- Frequency-modulated continuous-wave (FMCW) radar measures profiles of reflection intensity through the snow cover and an avalanche flowing over it; the rate of snow entrainment or deposition can be deduced from these data. Cross-correlating the signals from two devices a short distance apart in the flow direction, velocity profiles may be obtained. A system with much better collimation, spatial and time resolution is being developed jointly by NGI and INW.

FMCW radar

INW and NGI have during 2003 been developing an FMCW radar (Frequency Modulated Continuous Wave Radar Profiler) optimised for measuring the velocity and the density inside snow avalanches. The radars (4 in total) will be placed in pairs at two locations upstream of the Ryggfonn dam. The first pair, 100 m upslope from the dam, will measure the undisturbed flow of avalanches approaching the dam, whereas the second pair close to the base of the dam gives information on the piling up of snow at the dam. The radars will be installed in caverns with lids flush with the ground, the antennas being directed upwards.

The operation frequency (2.6-4.6 GHz), the huge bandwidth (2 GHz), the measurement frequency (> 80 measurements/s) and the narrow fan-shaped antenna pattern are the main characteristics that make this radar system uniquely suited for the task at hand.

The original SATSIE project plan stipulates that the radars shall be installed in Ryggfonn this fall (2003) and record data during the coming winters. There have been unfortunate delays in the development. The main reasons for this delay are very long lead time for some of the electronic components and reduced work capacity of a key developer due to a severe illness in his closest family. Despite this delay, it is our intention to install the radars in the late fall of 2003.

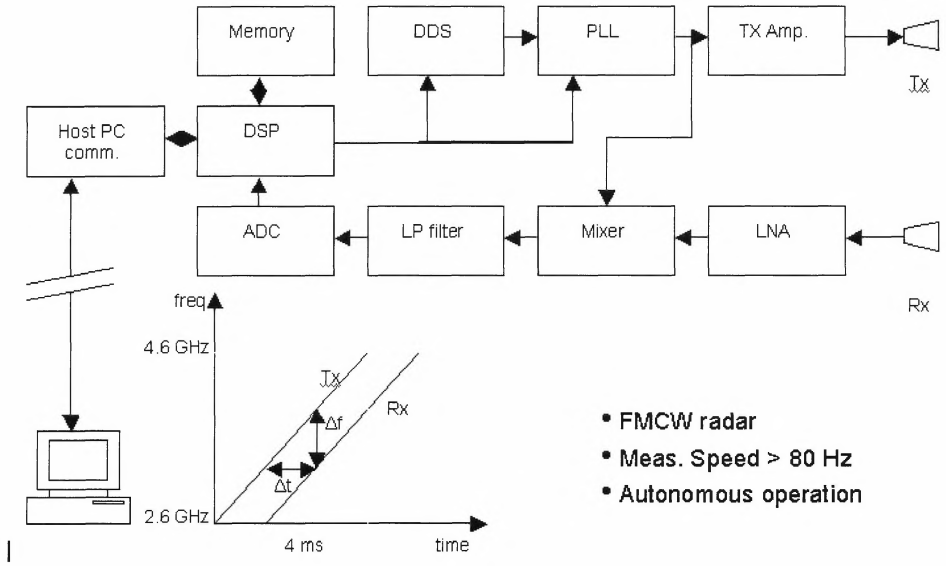

Fig. 1.1.1. Working principle of the FMCW radar [DSP : Digital Signal Processor, PLL : Phase Locked Loop, Tx Amp: Transmitter Amplifier, LNA: Low Noise Amplifier, LP filter: Low-Pass filter, ADC: Analogue-to-Digital Converter]

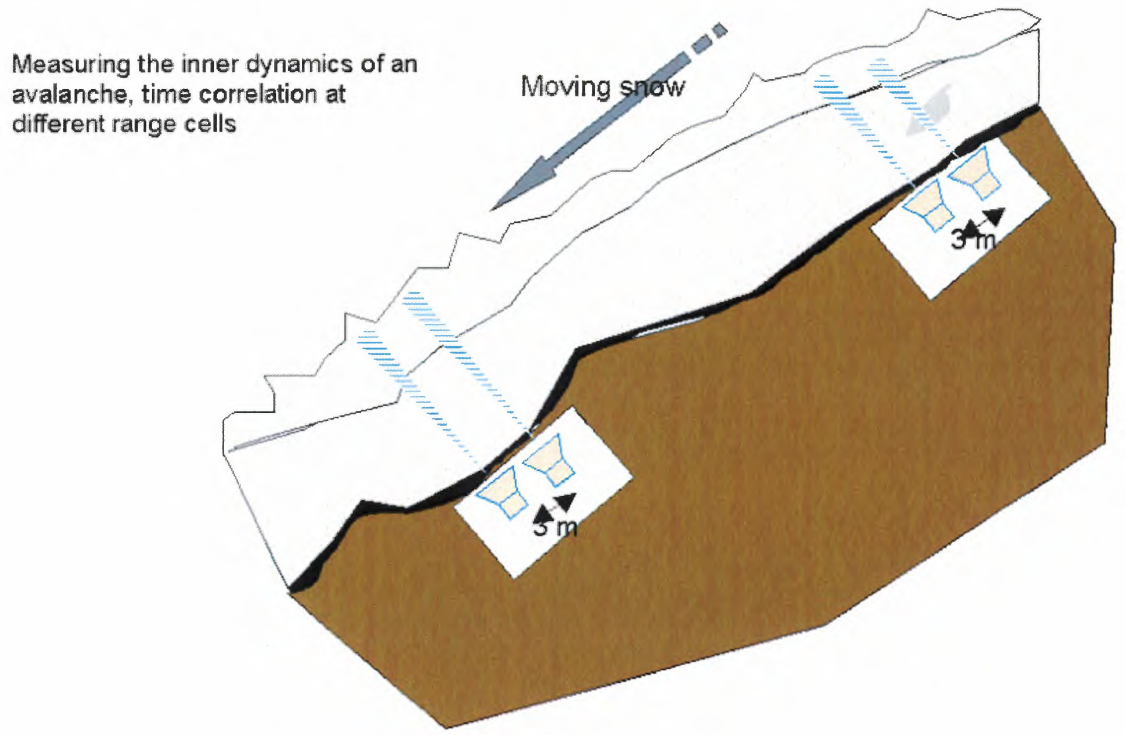

Fig. 1.1.2. Schematic view of FMCW radar location in the ground.

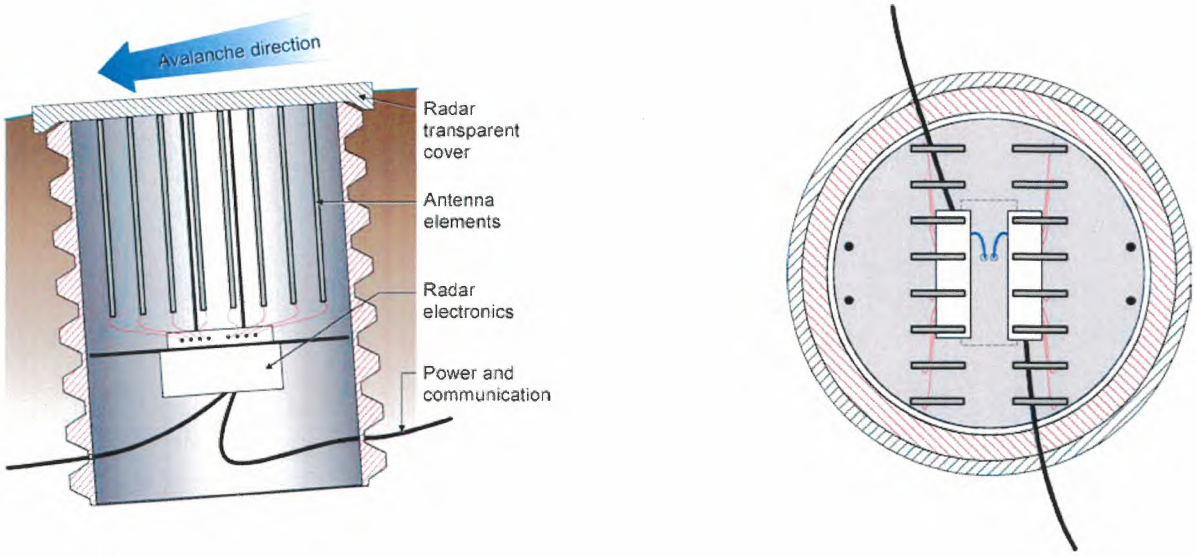

Fig. 1.1.3. Schematic view of FMCW radar in its container inside a concrete tube in the ground.

*(**a**) Side view. (**b**) Top view, with the avalanche flow direction from top to bottom.*

Pulsed Doppler radar

INW has developed a new pulsed Doppler radar system during 2003. This radar allows separate measurement of the internal velocity spectra of snow avalanches in up to 80 range gates, which may be as short as 25 m (see Fig. 1.1.4). After a short pulse has been emitted by the antenna; echoes reflected by objects in the direction of the beam return with a time lag proportional to the distance between the reflecting object and the antenna. For each pulse, the echoes are sampled in up to 80 time windows, which may be as short as 0.1667 μs (corresponding to a range-gate length of 25 m). Combining measurements in corresponding time windows of a sequence of pulses, velocity spectra are obtained for each range gate.

Compared to already existing avalanche radars, the design has been completely revised using microwave circuits developed in-house and a new DSP board (DSP: Digital Signal Processing).

The main characteristics of the radar is the possibility to obtain up to 10 sets of velocity spectra per second where one set of spectra consists of up to 80 spatial resolution cells (so called range gates). The operation frequency is 5.8 GHz and the minimum pulse width, which determines the resolution, is 0.1667 μs.

According to the SATSIE project plan, the radar will be installed in Ryggfonn in the fall of 2003 and record data during the coming winters. It will be placed at the foot of the slope opposite to the Ryggfonn path, slightly to the east of the main flow direction, in a compromise between safety and best measurement conditions. The same location has been used in measurements with AIATR's older system in 1997 and 2003 (see WP 3 for results from the latter campaign). Using a 1.2 m diameter antenna, its beam will cover the whole slope from the release area down to the run-out zone (dam).

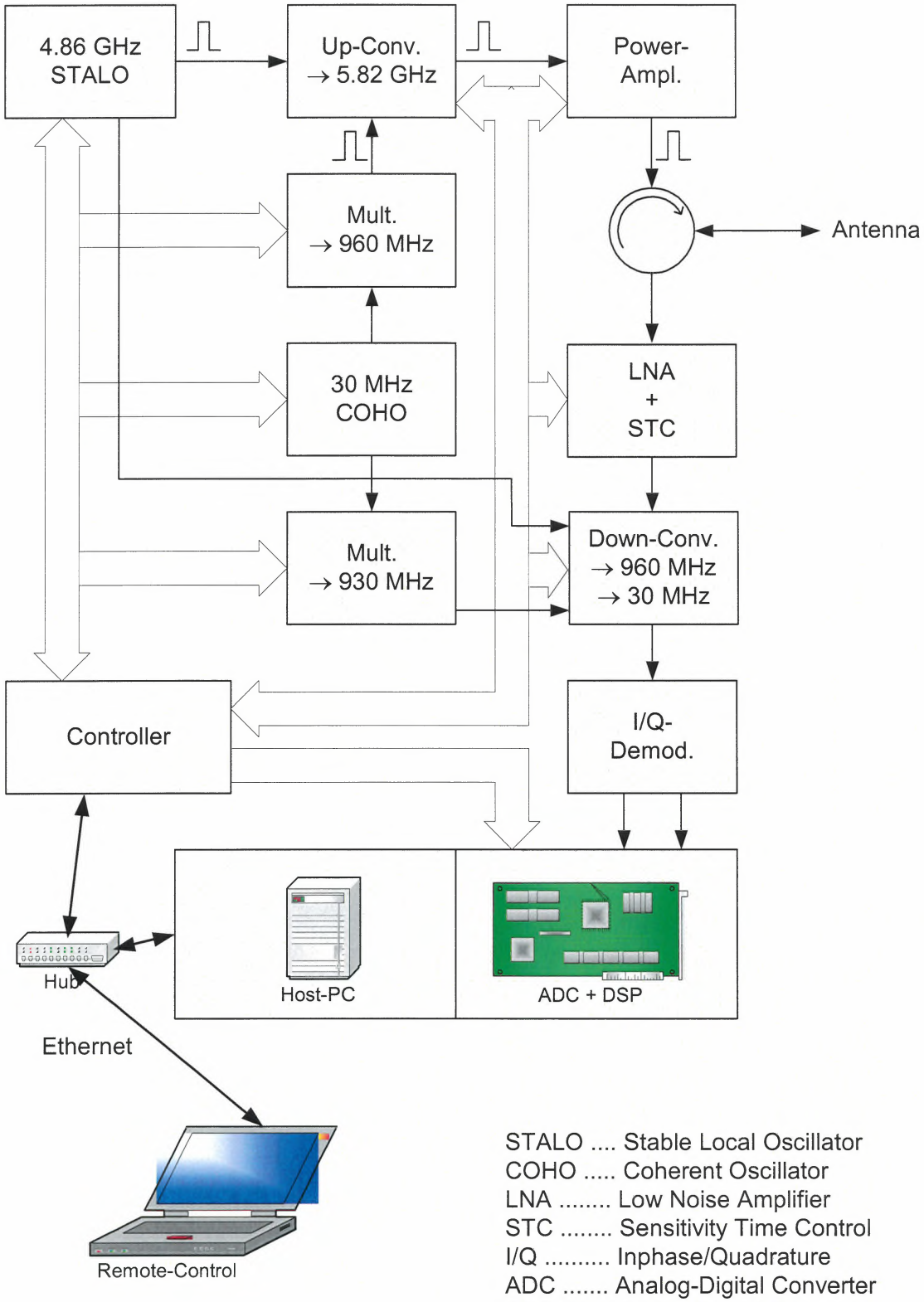

Fig 1.1.4. Block diagram of the pulsed-Doppler radar.

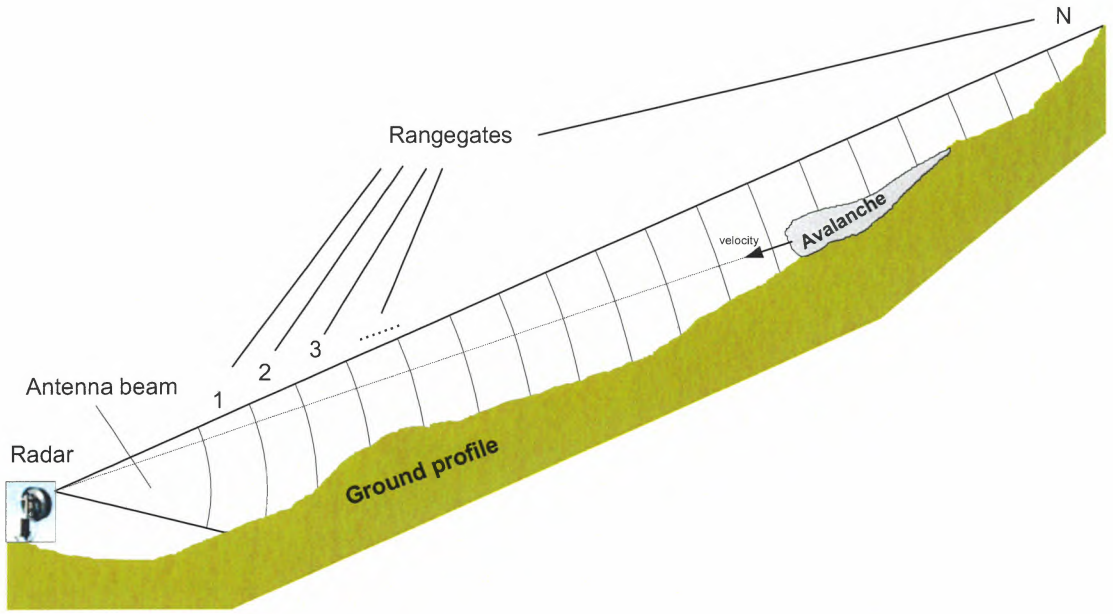

Figure 1.1.5. Range gating principle. Up to 10 spectra/s can be measured in each range gate with the new pulsed Doppler radar.

Technical data of INW Avalanche radar	
Transmission frequency	5820 MHz
Transmission power	40 dBm at amplifier output
Pulse width, sampling interval	n * 0.1667 µs (n = 1,2,3,... configurable)
Range resolution	$n \cdot 25$ m
Pulse repetition frequency (prf)	configurable (typically 20–60 kHz)
Unambiguous range	7500 – 2500 m
Max. measurement range	~ 4000 m
Antenna beam width	~ 10° (must be adapted to the situation)
Number of range gates	up to 80 (depends on configuration: prf, range resolution,..)
Max. sampling rate	2 · 6 MSamples/s (I- & Q-channel)
Over-sampling (coherent averaging)	configurable, typically eightfold
FFT	256 point ,complex
Averaging (incoherent, of amplitude spectra)	configurable
Measurement duration (prf = 50 kHz, eightfold oversampling, twofold averaging)	81 ms
Max. velocity (prf = 50 kHz, eightfold oversampling)	80,5 m/s
Velocity resolution	0,63 m/s

Table 1.1.2. Specifications of pulsed Doppler radar built by INW.

Task 1.2. Video methods

(Task leader: Philippe Frey)

The main work in making video analysis a routine technique in avalanche research obviously is in the development of effective and efficient analysis methods and programmes and is reported on in the chapter on Work Package 2. Nevertheless, there are also some questions concerning the proper choice of hardware, of locations and of filming techniques that are the subject of this task within Work Package 1.

Existing avalanches films

In order to focus the development of new analysis techniques and the choice of the optimum hardware equipment on the specific problems of snow avalanche recordings, we have begun to process four film clips of avalanches in motion from Ryggfonn (Norway), Col du Lautaret (France) and two sites in Spain. A protocol to optimise the digitisation of existing films (especially on Hi8 format) was fixed. The digitisation process will be completed during the next six months.

Future films

For future filming a protocol is required. The protocol must give a balance between constraints imposed on field observations and the requirements of accurate analysis. One of the main problems is the low contrast of typical images because snow avalanches are obviously white objects on a white field. To a lesser extent, climatic conditions (low temperature, wind, etc.) also require careful consideration.

Image processing algorithms are also important to consider. As an example, if particle image velocimetry (PIV) has to be used, cameras with multi-shuttering capabilities might be necessary. Indeed, in the laboratory, pairs of images are usually obtained by adjusting the lighting (stroboscopic lighting or pulsed laser) which is not possible with the continuous solar light where it is up to the camera to deliver pairs of images or multi-shuttered images. Other issues to be addressed are synchronisation of multi-camera systems and the placement of cameras.

The different options under examination are:

- Colour or black-and-white systems
- High-speed or high-resolution machine vision systems or digital camcorders more than 8-bit field camera for better grey level depth
- Multi-shuttering capabilities
- Digitisation system / frame grabber
- Rugged design suitable for field operation in adverse conditions

The choice of the cameras and frame grabber will be coupled with the writing of recording procedures which will be adapted to each field site.
Apart from the choice of camera and frame grabber, special attention is given to the choice of reference points, which must be matched to the digital terrain model.

Task 1.4. Optimisation of arrays of paired LED sensors

(Task leader: Hervé Bellot)

Summary of the activities completed

During the first six months, the (Luminous Electric Diode) LED technology was used to determine the velocity profiles inside dense snow flows. A new system was designed, developed, tested and installed at the snow chute at Col du Lac Blanc (CLB). This system was first severely tested and calibrated. During the first winter (2002–2003), 20 experiments were performed using 10 pairs of LEDs. These allowed the determination of the velocity profile inside the chute flow for different flow rate and chute slope.

Major problem we faced during this period

As pointed out in the first six months report, the developed system worked well for shallow flows. For deep flows, the sensor situated at the bottom of the flow saturated. The signal attained and stayed at its maximum value during a part of the flow duration. It was then impossible to detect and calculate the correlations.

During the second period (summer 2003), we modified the electronic components of the sensors and reduced the distance between the sensors and the flow. The tests we realised with granular material showed very good results. For the second year we will test the new version of sensors during the 2003–2004 winter measurements campaign.

Task 1.5. Shear / normal stress sensors

(Task leader: Lambert Rammer)

Summary of the sensors installed in Ryggfonn

Two tri-axial load plates, each with an area of 1 m², were installed at the front of the catching dam in Ryggfonn in the fall of 2002. The load plates measure shear stresses in two perpendicular axes in the plane of the dam front, and normal stress perpendicular to the dam front. The design and the installation of these load plates have been described and illustrated in the first Management Progress Report (pp. 9–11).

Activities completed in Cemagref chute

For measuring stresses (both shear stresses in the flow direction and normal stresses), we used a bi-component piezo-electric sensor (Kistler 9601A21-2-20) sandwiched between two metal plates whose dimensions are 20 ×50 cm^2. To avoid tilting of the upper plate, it has been necessary to use two sensors. The lower plate is fixed to the beam so that it does not move. The upper plate is connected to the lower one only through the sensors. The stresses applied by the flow on the upper plate are therefore transmitted to the piezo-electric transducers, which then produce positive and negative charges proportional to the applied stress. These charges are transformed into a voltage by the charge amplifiers. This kind of sensor was chosen because it was the only one that offered the required sensitivity at stresses of a few Newton and could also be conveniently installed in our channel.
For a description of the snow chute and images of it, see the chapter on Work Package 3.

Activities completed at the Taconnaz avalanche site

We have designed a shear and normal stresses measurement system dedicated to measure local forces during the interaction of the Taconnaz avalanche with existing defence structures (see the chapter on Work Package 3 for a description of the site and the complex system of defence structures). Two "blades" (large walls 1.5 m wide, 10 m long and 7 m high), situated at the end of the avalanche gully and at the transition from the track to the run-out zone of this path, were used as sensor support. The installed load plates have a surface area of 0.04 m^2 and the load cells are designed to measure up to 100 kN. We purchased two three-component sensors from FGP (France). The required force measurement ranges from 0 to 100 kN, the measurement frequency is 50 Hertz.

Task 1.6. Adaptation of concentric-cylinder shear cell for snow

(Task leader: Mohamed Naaim)

The main objective of this task is the adaptation and test of a concentric-cylinder shear cell to study the constitutive laws of dense snow. The internal stresses are determined by the local shear flow and the measurable material parameters of the snow (density, granulometry, cohesion, etc.). Once formulated, the new knowledge will be used to identify different flow regimes. The envisaged experiments need to probe the internal dynamics of snow by simultaneously measuring stresses, velocity profiles and fluctuating internal motions in the annular rheometer under controlled conditions, systematically varying the key flow parameters.

The chosen device is a large concentric cylinder (see Fig. 1.6.1), which can attain 60 rpm and consists of a drum with a fixed outer wall and a rotating internal cylinder. After the analysis of a series of unsuccessful tests, we proposed the following adaptations to suppress the formation of shear bands as much as possible:

- A lateral load must be applied
- A vertical load is also necessary
- It was also decided to have a Plexiglas lid to enable visual observation of the experiment
- These modifications will be realised in the next reporting period

Fig. 1.6.1. Photo of the large rheometer.

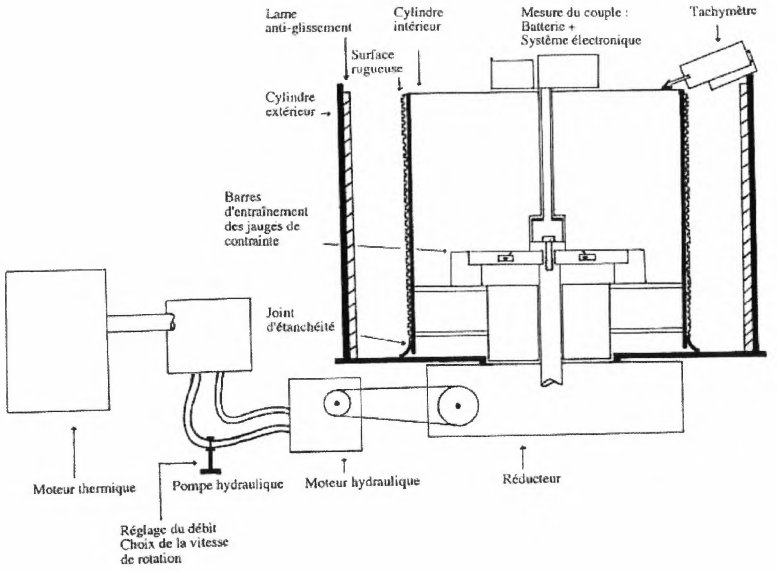

Figure 1.6.2: Schematic of rheometer.

Task 1.7. Seismic sensors (UB)

(Task leader: Emma Suriñach Cornet)

Our initial goal of purchasing and subsequently installing an Orion seismic signal acquisition system by Nanometrics Inc. at the test site at Ryggfonn had to be changed. This is due to the fact that the above-mentioned company no longer produces and sells Orion systems. We were hopeful that at least we would be able to acquire a newer-generation system manufactured by Nanometrics Inc., called Trident, but it turns out that this product is still under development and currently cannot be purchased by end-users.

For the above-mentioned reasons, we launched an extensive search for an equivalent data acquisition system. Specifically, we were looking for a system that would satisfy the following requirements, among others:

Ability to record data from 6 input channels (i.e., 2 three-component seismometers).
Presence of a 24 bit Digital to Analogue Converter (DAC) to ensure a sufficient dynamic range. (Signals of a starting avalanche are rather weak, but they become very strong as the avalanche passes over the sensor.)
Ability to operate in low temperatures and humid conditions (i.e., the enclosure should be waterproof).
Ability to access the system via Internet and/or telephone modem connection for uploading data and changing the setup.
Ability to record data with a sampling rate of 100 samples per second or higher.

Initially, we focussed our search on three specific companies, with one specific manufacturer from the U.K. being the preferred candidate, owing to the high quality of their product and a lower price tag. Nevertheless, due to the unsatisfactory post-sales customer service, after several months of evaluating the existing options we had to abandon the idea of purchasing the data acquisition system from this particular enterprise. As a result of further investigations

and consultations with colleagues from various countries, our choice finally fell on a "third-generation broad-band seismic recorder" manufactured by Refraction Technology Inc. (REFTEK) (*http://www.reftek.com*). From among the geophones belonging to the Geophysics and Geodynamics Department of the University of Barcelona, we decided to install sensors of 0.2 Hz eigenfrequency at this site, instead of others of 1 or 0.5 Hz. This choice allows us to obtain a large range of frequencies. This decision was based on our spectral analysis of previously recorded signals from avalanches in the Alps and the Pyrenees.

At the beginning of 2003, we purchased the REFTEK model 130-01-6 Data Acquisition System (DAS, Fig 1.7.1), which meets all five criteria listed above. Due to the ability of the system to record signals from six input channels, we have reconsidered the initial deployment design of the seismic instruments at the Ryggfonn experimental site and instead of placing just one three-component seismometer in the avalanche path, we placed an additional geophone of identical characteristics near the instrumentation shelter, approximately 400 meters away from the other geophone. The proximity of the seismic sensor in the path to other instruments (particularly, the FMCW radar system) will enable us to compare the seismic signals with more directly measured avalanche parameters.

Regarding the sampling rate, we plan to initially record data from both sensors with 100 samples per second (sps); however, at a later stage, depending on the characteristics of the obtained data, we envisage changing the sampling frequency. This will be possible because the parameters of the recording can be changed via modem from Barcelona.

One of the main challenges that we have faced during the installation of the seismic equipment at Ryggfonn was the excessive length of the cable (close to 500 m) between the DAS inside the shelter and the seismic sensor installed in the avalanche path. Although equipment manufacturer asserted that this configuration is feasible, we had to ensure that the transmitted signal was still strong enough to avoid the loss of the signal in the electronic and background seismic noises. The conducted tests were satisfactory (Fig. 1.7.2), and we are confident that the seismic energy generated by the avalanches and recorded by the sensor in the path will be successfully recorded by the DAS inside the shelter.

In addition to the installation procedures described above, we had to solve the problem of setting a common time base for various instruments deployed at Ryggfonn. Among all the instruments at the test site, the seismic DAS is the only one with a precise absolute time, derived from GPS satellites. If the other instruments also possessed a time base of similar quality, the common time reference problem would have been solved. However, since this was not the case, a special triggering signal will be fed into various instrument data streams, which will serve as a common reference base for all the instruments. In our case, we are mainly interested in the comparison of the seismic signals recorded by our instruments with data from the FMCW radars and with the high-frequency one-component geophones deployed by NGI in the lower part of the avalanche path. Specifically, a geophone placed in a mast in the middle of the track will produce the trigger signal, according to a criterion to be selected, and feed it into one of the auxiliary channels of the seismic DAS recorder.

Figure 1.7.1: 6-channel Reftek seismic recorder acquired for installation in Ryggfonn.

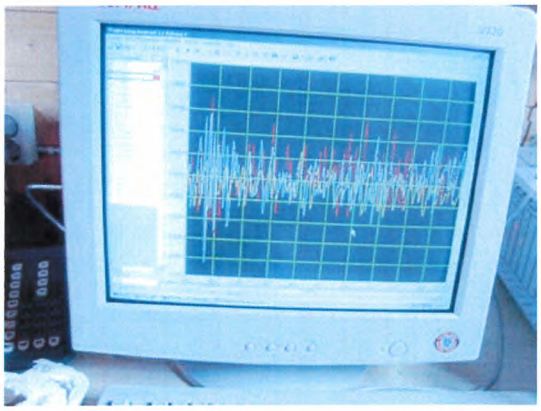

Figure 1.7.2: Seismic signals produced by the sensor installed in the Ryggfonn avalanche path and recorded in the hut at a distance of 500 m.

Main scientific results obtained in Work Package 1

Two types of radars have been developed and were approaching pre-operational status at the end of the reporting period:

Pulsed Doppler Radar for measurement of dense-flow avalanche velocities,
FMCW radar for investigation of the internal structure and velocities of avalanches.
Both radars will be installed in Ryggfonn at the end of 2003 and will be used for the next winter season.

The hardware aspects of video methods for avalanche dynamics analysis are under development, with the main focus on colour or black-and-white systems, high-speed or high-resolution machine vision systems or digital camcorders, field cameras with more than 8-bit sampling precision for better grey-level depth, multi-shuttering capabilities and digitisation systems.

The Luminous Electric Diode-technology (LED) combined with cross-correlation methods was developed further and used to determine the velocity profiles inside dense snow flows. During the winter 2002–2003, 20 experiments were performed.

Two tri-axial load plates, each with an area of 1 m^2, were installed at the front of the catching dam in Ryggfonn in the fall of 2002. The load plates measure shear stresses in two perpendicular axes in the plane of the dam front and normal stress perpendicular to the dam front. Two small tri-axial load plates (0.2×0.2 m^2) were set up at the end of the flowing zone of the Taconnaz site. These plates were installed on existing walls that are part of the defence structure.

The adaptation of a large annular rheometer for the study of the constitutive laws of snow is continuing. The first tests will be undertaken during the next season.

A third-generation seismic sensor and recording system was developed and installed in Ryggfonn in the summer of 2003.

WP 2 - Data analysis techniques

(Work package leader: Jim N. McElwaine)

Overview and summary

One task comprises the development of algorithms and data-analysis techniques for the two different types of radar sensors: Pulsed Doppler radar and FMCW radar. Work on the design of algorithms (porting from existing radars), DSP-software development and PC-software development (data-analysis and data-representation) has begun. The software has been mostly completed so the radar can be installed in Ryggfonn this fall (2003) and record data during the coming winters.

The software for processing video film clips has been finished and applied to snow avalanches and laboratory experiments. Control points, which are necessary for camera calibration, have only been obtained for one avalanche and used to obtain a velocity profile down the track. For the remainder of the project the software will be applied to any avalanches that are observed

Work has been done on analysing the frequency response of an ultra-low differential pressure sensor system. This sensor has been used in laboratory experiments of powder snow avalanches. The data has been presented at two conferences and a paper will shortly be completed. A brief paper has been written on filming avalanches.

Discussions on impact pressure analysis have been carried out with SLF, Davos, on the current state-of-the-art, and preliminary work started on the design of new algorithms.

Existing options for acquiring and consequent processing of avalanche seismic data are reviewed. In general, relatively little has been published in terms of the seismic detection and analysis techniques of avalanches.

In terms of choosing specific seismic data analysis software, it was decided to use the programs SAC and CORAL. As of the beginning of the year, the above mentioned software has been installed on an especially dedicated PC running under the Linux OS. Seismic data from Ryggfonn has been analysed using these tools.

On correlation methods, two papers have been written on the analysis and design of opto-electronic sensors. Software for calculating the correlations has been completed. Work is currently underway applying ideas of matched filtering to improve the signal-to-noise ratio, and thus reduce the errors. A paper using the techniques will be completed in the next six months.

Task 2.1 Radar analysis (INW)

(Task leader: Helmut Schreiber)

Task 2.1 comprises the development of data analysis techniques for two different radar sensors:
Pulsed Doppler radar (development by INW/TU Graz only)
FMCW radar (common development by NGI and INW/TU Graz, data analysis by NGI only)

Pulsed Doppler radar

INW has been developing a new pulsed Doppler radar system together with the necessary data analysis techniques during 2003 (see report on Work Package 1). The software is mainly based on existing data analysis algorithms developed for the precursor system owned by AIATR, which run under the operating system OS/2 and therefore had to be converted to Microsoft Windows and Linux for the new system.

Furthermore, a new and more powerful DSP (Digital Signal Processing) board has been purchased for data acquisition and calculation of the velocity spectra in this system. For this reason, the DSP algorithms had to be ported to the new hardware.

The software has been largely completed so the radar can be installed in Ryggfonn this fall (2003) and record data during the coming winters. In the following years the software will be revised: Bugs detected during the initial tests will be fixed and new data analysis features will be added.

FMCW radar

During the first year of SATSIE, the focus in FMCW radar development was on hardware. The data analysis software will be built up in successive steps as soon as test data from artificial sources and then from snow avalanches becomes available in the second year of SATSIE. Basic treatment of the raw data will in the beginning be based on software that has been used at NGI for the treatment of data from ground-penetrating radar.

Task 2.2 Video analysis (DAMTP)

(Task leader: Jim N. McElwaine)

The software for video analysis is now complete. Video sequences from large-scale avalanches and small-scale experiments can be automatically processed to produce front position, size and velocity. Four film clips of avalanches have been partly processed (one from NGI, one from Cemagref and two from DGG). The change-point method with shadow detection has been shown to work with them. A paper describing the approach has been written (McElwaine, 2003). The software has been revised to deal with black-and-white images and an arbitrary number of change points. The software has also been applied to powder snow avalanche experiments with polystyrene balls and snow—the preliminary results from this are included in the appendix. For one avalanche from Roies (Catalan Pyrenees), camera control points have been obtained and the camera calibration calculated. For the Ryggfonn and Col du Lautaret avalanches, control points have not yet been obtained.

A document detailing advice for filming avalanches has been prepared and is contained in the appendix.

The DAMTP contribution to this task is essentially completed, and the remaining work will be applying the software to any avalanches that are observed during the project.

During the first year of the project, the avalanche team at DGG (University of Barcelona) has participated in this task providing basic information and data for the video processing carried out by DAMPT. Two video clips recorded by the Unitat d'Audiovisuals (UB) in collaboration with DGG (UB), SGC (ICC) and Estació de Muntanya i d'Esquí Boí-Taüll, on 11–12 January 1996, were provided. They correspond to the artificially triggered avalanches of Raspes Roies and Cervi (Boí-Taüll ski resort, Central Pyrenees, Spain). The digital topographic map of the avalanche paths area (ICC, 1988-90) and the digital orthophoto (ICC, 1997), at original scale 1:5000, were also provided.

As field experts with knowledge of the area, we identified a set of control or calibration points for the Raspes Roies avalanche. These points are used to transform the 2D screen coordinates of the image to 3D physical coordinates. This work was carried out by comparing the screen images extracted from the video, the overlap of the topographic map and the orthophoto and conventional vertical aerial photographs (classical observation with a stereoscope). Previous work related to this avalanche was published in (Sabot *et al.*, 1998).
Data about snow and meteorological conditions during the experiments are being compiled.

Task 2.3 Air pressure sensor analysis (DAMTP)

(Task leader: Jim N. McElwaine)

Work has been done on analysing the frequency response of an ultra-low differential pressure sensor system. This can measure pressures corresponding to air flow velocities of only 0.3 m/s with a frequency response, for the complete system, of order 100 Hz. This system has been used for measuring the air flow in small-scale powder snow avalanche experiments with polystyrene balls and powder snow. The results from this have been presented at two conferences and a paper is currently being written.

Task 2.4 Avalanche-dam interaction (IMOR)

This task has been integrated in Task 5.4.

Task 2.5 Impact pressure analysis (DAMTP)

(Task leader: Jim N. McElwaine)

Discussions have been carried out with Mark Schaer (Swiss Federal Institute for Snow and Avalanche Research, Davos, Switzerland) on the current state-of-the-art, and preliminary work started on the design of new algorithms.

Task 2.6 Seismic signal analysis

(Task leader: Emma Suriñach Cornet)

The objectives of the task are:

a) Development of techniques and software for inferring properties of avalanches from seismic signals in the time and frequency domain

b) Review of current techniques and proposals for improving measurements
c) Review of data analysis with proposals for improving measurements
d) Development of data analysis techniques

During the first year of the project, we have reviewed various options for acquiring and subsequent processing of avalanche seismic data. In general, relatively little has been published specifically in terms of the seismic detection and analysis techniques of avalanches.
In terms of choosing specific seismic data analysis software, we decided to use the following two programs:

1. SAC (Seismic Analysis Code) developed at Lawrence Livermore National Labs (http://www.llnl.gov/sac/).
2. PITSA, developed by Frank Scherbaum and colleagues (Scherbaum and Johnson, 1992). Version 4.5 of PITSA that we currently use at DGG has been developed by the Synapse Science Centre in Moscow, Russia (http://www.synapse.ru/).

In addition to this standard software, we developed different algorithms in MATLAB, a commercial development software package, for specific data analysis tasks, such as the analysis of the avalanche seismic data in the time and frequency domains. This was done using our previously recorded avalanche data from the Pyrenees and the Alps. The bulk of the data is from the avalanche test site at Vallée de la Sionne, Switzerland. As part of the given work, a PhD thesis was defended at the University of Barcelona in July 2003 (Biescas, 2003). Some results of the given dissertation were published in a paper (Biescas *et al.*, 2003).

Recently NGI has provided us with a set of seismic data recorded by their 6 geophone array at the test site in Ryggfonn (Figure 2.6.1). Specifically, we have analysed the data from the avalanche that occurred on 17 February 2000. The sensors deployed by NGI at the Ryggfonn site are 1D vertical-component 4.5 Hz geophones of the model SM-6 manufactured by Input/Output Inc. These geophones were not installed with the aim of studying the characteristics of avalanche seismic signals but for the purpose of supplementing other observational techniques by providing the trigger signal (Lied *et al.*, 2003).

The distribution of these geophones in the centre line of the avalanche path, from about 60 m in front of the dam to the top of the dam, allows us to obtain some information that will be useful for further studies. We have used these signals to analyse differences between the signals in terms of the sampling frequency, the amplification and the frequency distribution. This study has facilitated the choice of set-up parameters for the present installation of seismic equipment (see Task 3.1). As an example, in Figure 2.6.3 we present different parts of NGI geophone signals with their corresponding total spectra.

During the first year of the project we have also reviewed options for determining the avalanche velocity using seismic sensors. Although some studies had been conducted in this direction previously, e.g. (Schaerer and Salway, 1980), no conclusive results have been obtained. We attempted to determine the avalanche propagation velocity from NGI's geophone data described above by using a cross-correlation method between the signals recorded at different sensors along the track of the avalanche. We selected distinct time windows within the entire signal on the basis of an inspection of the spectrograms. Figure 2.6.4 shows the cross-correlation between the signals recorded at geophones #2 and 3; the maximum correlation occurs at a time lag of 16 samples (i.e. 128 ms). Taking into account that the distance between the sensors is 47 m, we get a propagation velocity of more than 1000 km/h. Obviously, this is not the avalanche speed but the propagation velocity of the acoustic wave. This work is still

underway and we are hopeful that by increasing the distance between the analysed geophones as well as selecting different windows of the signal, we will be able to get an order-of-magnitude estimate of the avalanche velocities.

In addition, we are working on applying techniques developed in other fields of seismology to our particular problem. Considerable work has been done on other types of moving sources, such as volcanic debris flow, rock falls, etc. (Almendros *et al.*, 2002; Ibanez *et al.*, 2000; Jolly *et al.*, 2002; Arattano and Moia, 1999). We studied the applicability of these methods to our particular problems and concluded that a simple adaptation is not possible. Nevertheless, methods used in volcanic or mud debris flow studies could be useful, and we plan to collaborate with our colleagues in this field of research.

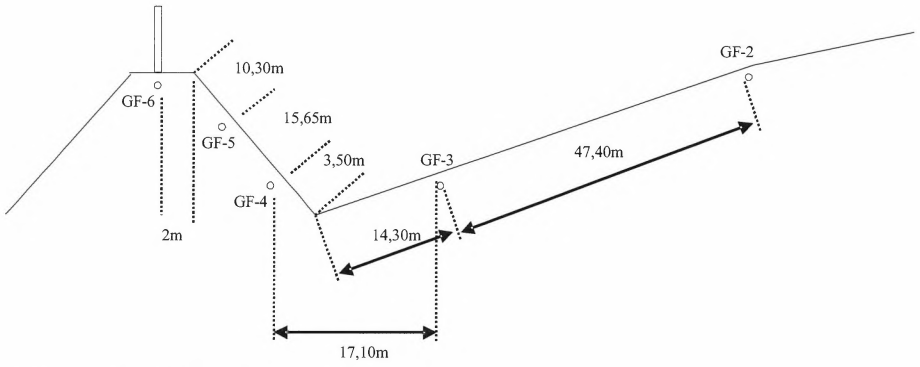

Figure 2.6.1: Location of the 1D 4.5 Hz geophones at the Ryggfonn test site.

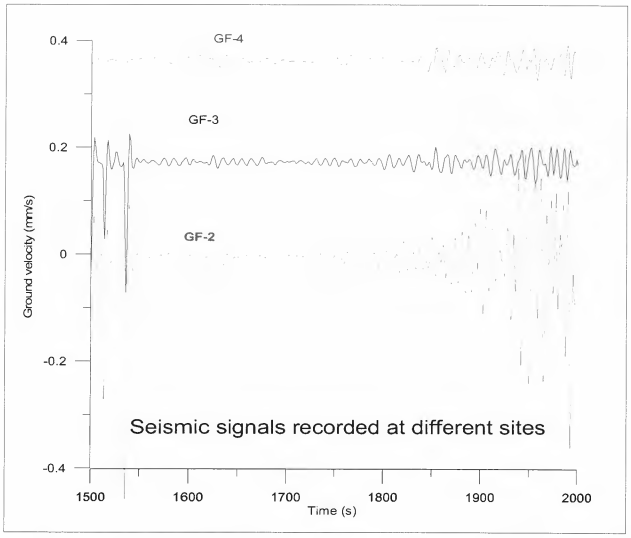

Figure 2.6.2: Seismic records of the 17/02/2000 avalanche recorded at the Ryggfonn test site by various geophones of the NGI.

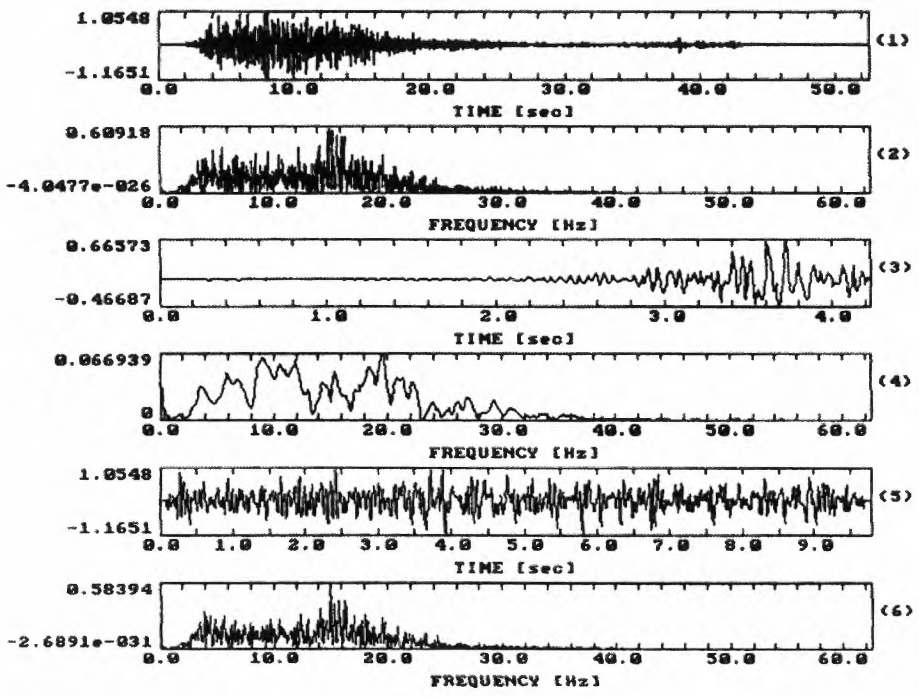

Figure 2.6.3: Seismic signal and their corresponding spectrum for different parts of the record of GF2.

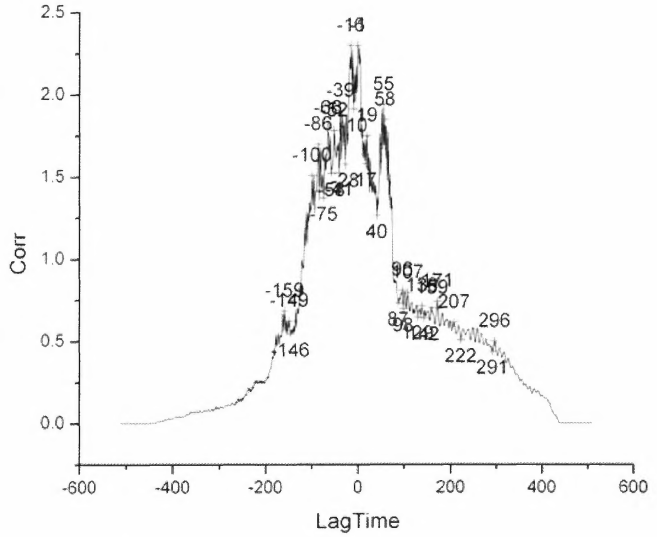

Figure 2.6.4: Cross-correlation analysis between the first seconds of signals recorded in geophones GF2 and GF3.

Task 2.7 Correlation Methods (DAMTP)

(Task leader: Jim N. McElwaine)

Two papers (McElwaine and Tiefenbacher, 2003; McElwaine, 2004) have been written on the analysis and design of opto-electronic correlation sensors. McElwaine and Tiefenbacher (2003) analyse the traditional cross-correlation approach in one dimension and introduce a continuous method. (McElwaine, 2004) discusses the calculation of two-dimensional velocities and gives a more complete description of the continuous approach. The papers contain design criteria for the sensors. Software for calculating the correlations has been written and tested. A third paper is under preparation comparing different analysis techniques and the applications of matched filtering.

Main scientific results obtained in the Work Package

The basic data analysis software for the pulsed Doppler radar has been ported to the new operating system environment and is operational. For the FMCW radar, the development of the software will be initiated as soon as the devices have been completed and data from first tests are available.

The video analysis software has been used to show the importance of air entrainment during the motion of powder snow avalanches. The results showed a very large increase in avalanche volume with slope angle leading to an increased drag that almost exactly matches the increased down-slope component of gravity, with the result that avalanche speed is almost independent of the slope.

Air pressure data from experiments has been used to explain previously misunderstood data from avalanches. The air pressure inside the head of an avalanche is negative showing that there is a large two-dimensional vortex and that the head is far from hydrostatic equilibrium.

Discussions on impact pressure analysis have been carried out with SLF, Davos, on the current state-of-the-art, and preliminary work started on the design of new algorithms.

Besides the choice and adaptation of seismic data analysis software for the newly acquired stations, possible approaches to the problem of measuring avalanche speeds with geophones have been investigated. The results are inconclusive at present, and the applicability of methods used with other geophysical mass flows will be studied in the upcoming project period.

Work on the correlation sensors has shown that previous results using these sensors maybe have serious errors and a careful re-evaluation is necessary. The theory suggests that with careful design and analysis these sensors can give high-accuracy velocity measurements and work is underway to construct such sensors.

WP3 - Instrumentation of selected facilities

(WP leader: Massimiliano Barbolini)

Summary of work package activity

At the full-scale test site Ryggfonn in Norway, two load plates were installed on the front side of the dam and two trenches constructed for housing the ground radars and the University of Barcelona's geophones. A Doppler radar for the deflecting dam at Flateyri (Iceland) was installed at Ryggfonn temporarily for testing. Electronics damaged by severe lightning had to be replaced. Pressure sensors were also installed at the Taconnaz retarding and deflecting dam system in France.

Further instrumentation work in France concentrated on the snow chute at Col du Lac Blanc where the data acquisition system and sensors measuring the flow depth, bed stresses and the velocity profile were installed, tested and used. The measurement equipment for the indoor chute at the University of Pavia was enhanced by acquiring two frame-grabber devices and PCs so that high-speed video capturing is now possible at three locations.

Additional chutes that are used in SATSIE are located in Grenoble and Bristol. No changes were made to their instrumentation, but they will also be briefly described below to complete the overview of the experimental facilities used in SATSIE.

Task 3.1 – Ryggfonn instrumentation

(Task leaders: Karstein Lied and Erik Lied)

Introduction

The Ryggfonn full-scale avalanche test site has been in operation since 1980. During a period of 22 years, an average of 2–3 avalanches per year has been released in the path. The Ryggfonn avalanche has a vertical drop of about 900 m and a horizontal length of 2100 m. The avalanches range in magnitude from 10,000 m^3 to 500,000 m^3, with maximum velocities up to 60 m/s (see Fig. 3.1.1).

Fixed installations in the avalanche path

In the lowest part of the avalanche path, there is a 16 m high and 75 m wide retaining dam, see Fig. 3.1.2. In the dam front, two tri-axial load plates, each with an area of 1 m^2, measure the shear stress in two perpendicular axes in the plane of the dam front and the normal stress perpendicular to the dam front.

The design load of the plates is 200 kN for shear stress and 400 kN for normal stress. (For details see the description of the load plates in WP 1). The load plates were designed during the summer of 2002 and installed in September 2002 as a part of the SATSIE project. All the other instrumentation in Ryggfonn except for these load plates, the FMCW radar, the tri-axial geophones mentioned below and the data acquisition system were implemented prior to the SATSIE project.

On top of the dam there is a 6.5 m high steel mast, see Fig. 3.1.2, instrumented with a horizontal geophone and the IMO Doppler radar antenna. This continuous-wave Doppler radar was purchased for the SATSIE project and has been installed at Ryggfonn in order to compare its results with the Pulsed Doppler Radar velocity measurements performed by AIATR, before the radar will be installed in Iceland.

In the ground, 60 m up-slope from the top of the dam, there are 5 vertical geophones measuring ground vibrations (see Fig. 3.1.3).

Figure 3.1.1. The Ryggfonn avalanche

Two tri-axial geophones (Lennartz LE3D-5s) were installed with the University of Barcelona in September 2003. One is located 100 m upslope from the catching dam and one close to the instrument shelter 400m to the side of the avalanche path. These geophones will have a data recording system separate from all the other instruments; installation is planned for December 2003.

230 m up-slope from the dam is a 4.5 m high concrete structure fitted with three single-axis load plates, each with an area of 0.72 m^2 and a weight of 150 kg. The design load of these plates is 600 kN, see Fig. 3.1.4.

320 m up-slope from the dam, a 6 m high tubular steel tower is fitted with a horizontal geophone and two single-axis load plates of the same type as on the concrete structure. The tower consists of three sections, each having a diameter of 1335 mm and a plate thickness of 15 mm, see Fig. 3.1.5. Both load-plate types are based on load pins with strain gages as the sensing element. All NGI geophones are low-cost SM-6 or HS-1 sensors from Geo Space LP.

Seismic sensors

In the beginning of October, the University of Barcelona team—with active participation and help of NGI—installed 2 three-component seismic sensors manufactured by Lennartz Electronic GmbH (*http://www.lennartz-electronic.de*) of the type LE-3D/5s and owned by the University of Barcelona.

Figure 3.1.2. The catching dam with the steel mast on top

Each of the sensors was placed inside a hole in the ground to ensure better coupling with the ground and protection from the snow and avalanches, see Fig. 3.1.7. The sensor in the track at location A in Fig. 3.1.6 was placed at the bottom of an 80 cm diameter and 1 meter deep hole located 100 m above the dam along the avalanche path (Fig. 3.1.7). Within several metres from this hole two other holes have been prepared to house the FMCW radars. The proximity of the seismic sensor to the latter instruments will enable us to compare the two types of data.

The second seismic sensor is installed 40 m away from the instrument shelter on the bottom of a hole that measures 40 cm in diameter and 60 cm in depth (location B in Fig. 3.1.7, right panel). The REFTEK data acquisition system (DAS, Fig. 3.1.7) is placed inside the instrument shelter, where it will be connected to the GPS receiver for keeping accurate time. The shelter already possesses a phone line and internet connection, which will be utilized for downloading the acquired data and remote setup of the DAS.

As a result of discussions with the colleagues from NGI, we decided that at the initial stage the downloading procedure will take place from Barcelona via the telephone modem. In the future, we hope to overcome the internet security issues and utilize the possibility of the installed DAS to be directly connected to the network. Data will be stored and processed in special cartridges (SCSI).

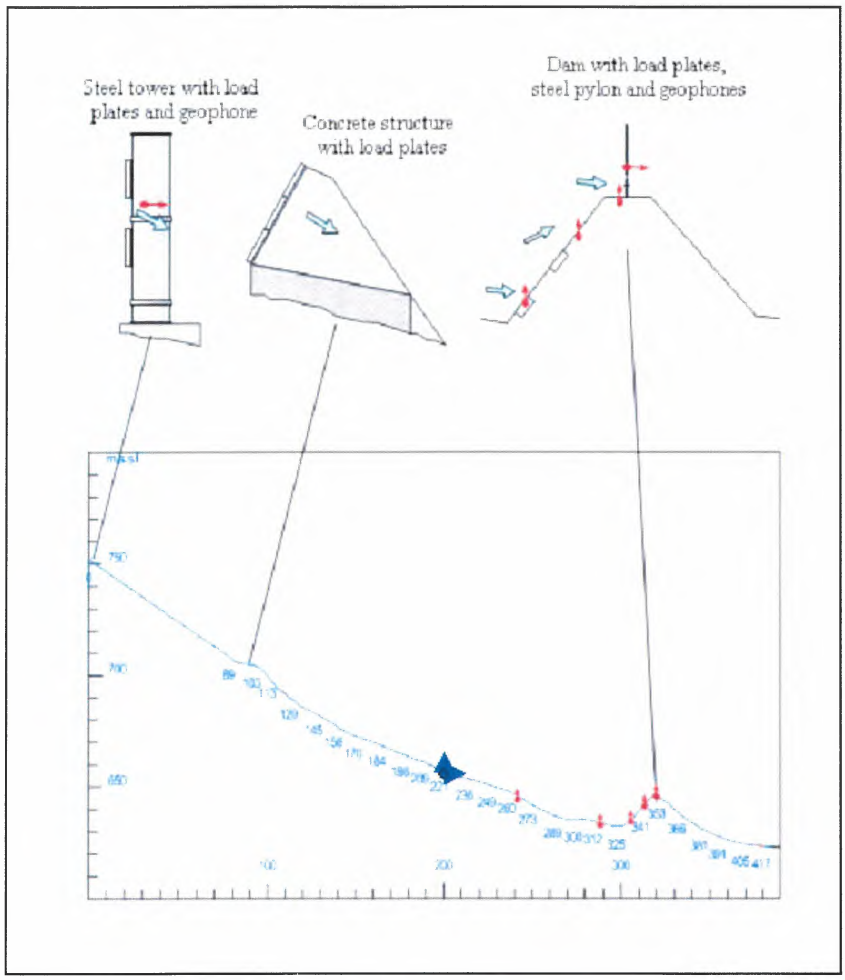

Figure 3.1.3 Cross section of the Ryggfonn run-out area. Red arrows mark the positions of NGI's geophones. Blue arrows mark geophones from the University of Barcelona.

Figure 3.1.4. The concrete structure with 3 load plates

Figure 3.1.5 The steel mast with 2 load plates

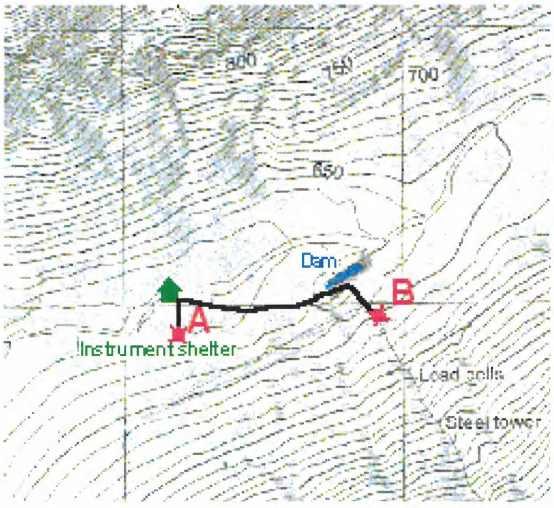

Figure 3.1.6 Sketch of the installation scheme of the geophones. Red arrows show were the geophones (A and B) are placed.

To avoid lightning damage to the DAS, we have purchased and installed special COMTRAB modular CTM surge voltage protection plugs (manufactured by Phoenix Contact GmbH) for every conductor between the DAS and the two sensors.

Figure 3.1.7 Detail of the installation of the 3-component LE-3D/5s Lennartz Geophones belonging to the University of Barcelona.

Radar installation

Continuous-wave Doppler radar of IMO

On the 6.5 m high steel mast on top of the dam (Fig. 3.1.2), the antenna of the IMO Doppler radar is mounted; the radar was installed on 3 February 2003. The device has been installed at Ryggfonn temporarily so that its measurements can be compared with the Pulsed Doppler Radar velocity measurements performed by AIATR before the radar will be installed at its definitive location in Flateyri, Iceland.

Pulsed Doppler radar of AIATR

The antenna of the AIATR pulsed Doppler Radar was positioned at a distance of 150 m from the dam, on the opposite slope, during the experiment of 6 April (Fig. 3.1.8).

A pulsed radar system as used by AIATR transmits short pulses of microwave energy and analyses the received echoes reflected from the target objects hit by the antenna beam. In the case of the avalanche radar, the reflecting object is the ground covered with steady or moving snow. The echo is sampled separately during a number of adjacent time "windows" and analysed for its frequency content within each time window. The delay of an echo segment with respect to the emitted pulse is proportional to the distance of the reflector from the antenna (Fig. 3.1.9). The frequency shift of the echo is proportional to the velocity of the reflector in the antenna direction; the frequency spectrum thus represents the velocity distribution in a collection of reflecting particles. This process is called range gating and allows determining not only the time evolution, but also the spatial structure along the avalanche path, so that by comparison of subsequent measurements a clear identification of snow movements on the ground becomes possible (e.g. snow moving through one range element must appear, with a certain delay, in the adjacent lower range element also).

The use of two frequencies (5.8 GHz and 35.8 GHz) is necessary since electromagnetic waves of different wavelengths interfere differently with the dense-flow and the powder-snow parts of avalanches. One needs a short wavelength (corresponding to high frequency) to get reflections from the small snow and ice particles of the powder-snow cloud.

Figure 3.1.8 Antenna of the AIATR radar facing the avalanche path

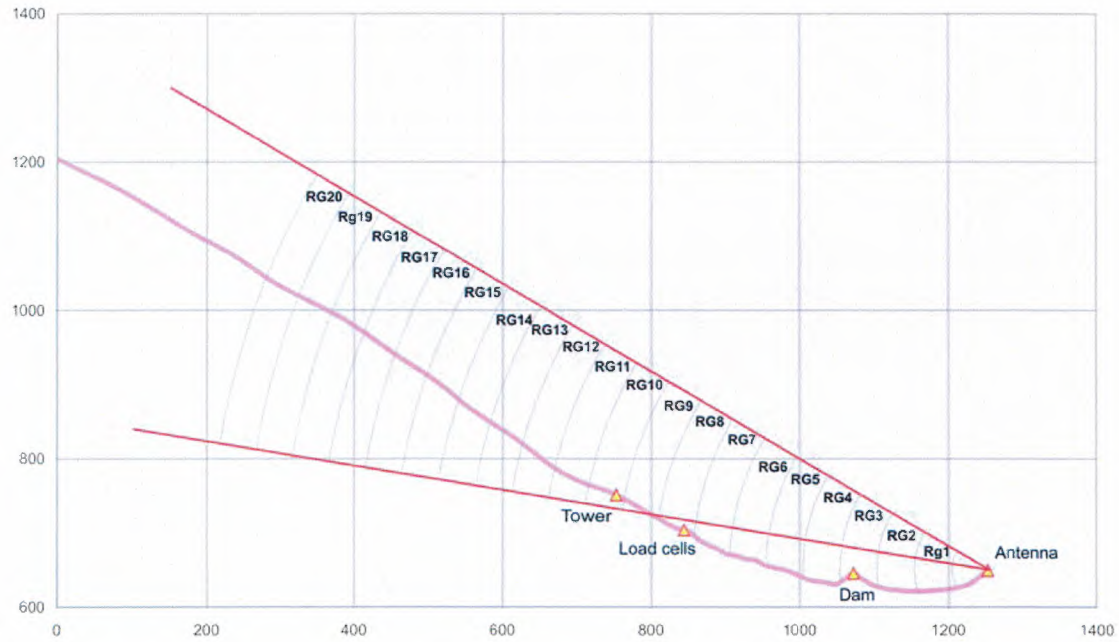

Figure 3.1.9 Range-gating for radar velocity measurement of Ryggfonn avalanche. The vertical axis gives the altitude above sea level, the release area extends some 500 m further to the left, to an altitudeof almost 1600 m a.s.l.

Data recording equipment

Cables connect the instruments in the avalanche path to an instrument shelter containing data recording equipment, a computer and the Doppler radar cabinet. The distance from the dam to the instrument shelter is about 450 m (see Fig. 3.1.10).

Data from the IMO Doppler radar are stored internally, and automatically transferred to the computer after a trigger event.

Signals from all other sensors are recorded by a data logger (Hottinger Baldwin MGCPlus) and stored internally after trigger events. Transfer of data from the logger to the computer is done manually. All sensors are sampled at a rate of 150Hz and low-pass filtered with a filter cut-off frequency of 40 Hz.

The computer that controls both the radar and the data logger can be controlled from NGI's office in Oslo, and data may be transferred there after avalanche events.

Data of the AIATR pulsed Doppler radar are recorded on a hard disk of the radar control computer, which is situated in a weather-proof enclosure close to the instrument in the field.

Figure 3.1.10 Instrument shelter (red circle) seen from the dam crest

Activities over the last 6 months

Two 3-axial geophones (Lennartz LE3D-5s) were installed for the University of Barcelona in September 2003.
Repair of signal cable from the uppermost steel mast.
Repair of sensors at the uppermost steel mast that were incapacitated by lightning in the autumn 2002.

Planned activities for the next 6 month period

Installation of 4 FMCW radars in the ground above the dam, see Task 1.1

Commissioning of new pulsed Doppler radar, see Task 1.1
Installation of data acquisition system for the new geophones

Task 3.2 – Instrumentation of dams

(Task leaders: Thierry Faug and Tómas Jóhannesson)

Flateyri dam

General description of the facility

Two 15–20 m high deflecting dams have been constructed above the village Flateyri, in north-western Iceland, after the catastrophic avalanche accident on 26 October 1995 when 20 people were killed (Figs. 3.2.1–3).

Figure 3.2.1. Rescue workers at work at Flateyri after the avalanche on 26 October 1995.

Both deflectors have since been hit by moderately large avalanches, in each case with a volume over 100,000 m^3 and an estimated return period of 10–30 years. These avalanches hit the deflectors with deflecting angles between 20° and 25° and reached a maximum run-up of 12–13 m.

In both cases, the impact with the dam canalised the avalanche in part or over the whole width into a 20–80 m wide flow, the run-out of which is estimated to have been increased by over 100 m by the deflection of the avalanche by the dam. The dams at Flateyri provide a unique location for direct observations of avalanches that hit deflecting dams. Although the avalanches that have so far hit the deflecting dams are much smaller than the design avalanches of the dams, they have provided avalanche professionals and the public in Iceland with much welcomed direct evidence of the effectiveness of the defence structures at Flateyri against moderately sized avalanches.

Instrumentation and some examples of typical measurements

Currently there is no permanently installed instrumentation to monitor avalanche flow at Flateyri. After avalanches have fallen, IMO staff measure the outlines of the avalanches, and the snow thickness in the tongue and the run-up on the sides of the dams for avalanches that reach the dams.

As examples of the measurements that have been carried out at Flateyri, Fig. 3.2.4 shows the run-up on the eastern and western dams for the avalanches that hit them on 21 February 1999 and 28 February 2000.

Figure 3.2.2 Flateyri (photo: Oddur Sigurðsson).

Figure 3.2.3 Flateyri (photo: © Mats Wibe Lund)

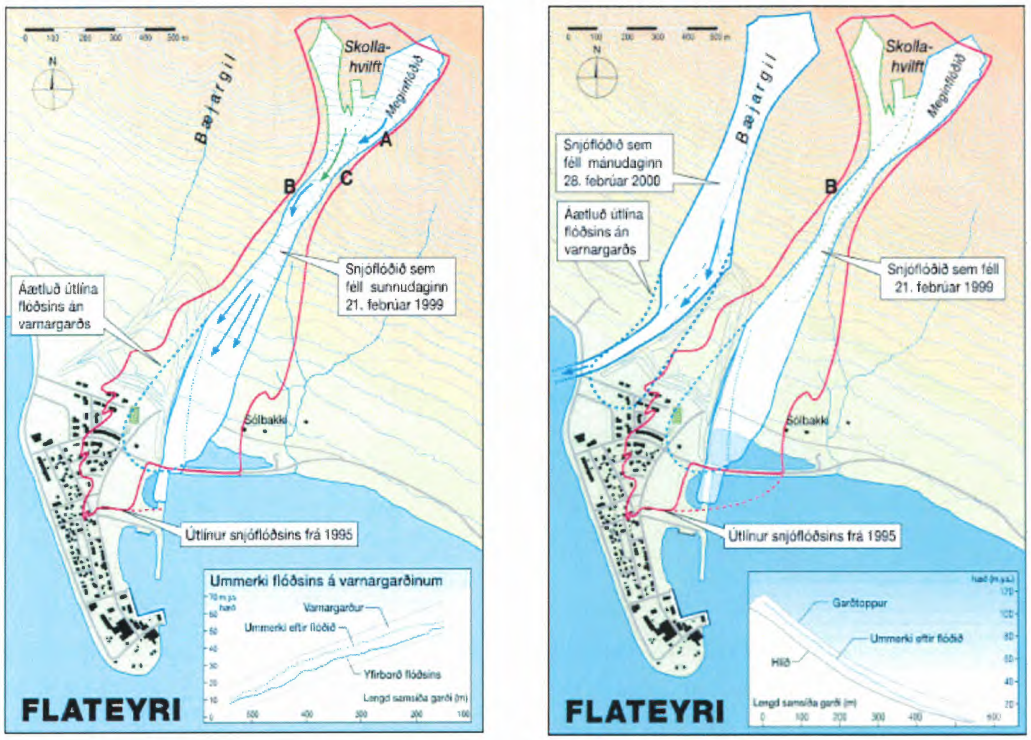

Figure 3.2.4 Deflection and run-up(inset) on the eastern and western dams at Flateyri for the avalanches on 21 February 1999 (left panel) and 28 February 2000 (right panel). The red line circumscribes the deposits of the catastrophic 1995 avalanche before the dams were constructed. The dotted blue lines indicates the estimated run-out areas of the 1999 and 2000 avalanches if there had been no dams.

Future improvement (new installation) planned during the SATSIE project

A continuous-wave Doppler radar for measuring the speed of the avalanches will be installed on the easternmost Flateyri dam as a part of the SATSIE project. The radar will make it possible to obtain direct estimates of the speed of avalanches as they approach the dam instead of having to rely on speeds estimated by unverified model computations. The radar has been temporarily installed at Ryggfonn in order to compare its performance with that of AIATR's pulsed Doppler Radar, before the radar will be installed in Iceland in 2004. The necessary foundations and communication cables at Flateyri are under construction and will be completed in 2003.

Taconnaz dam

A very large defence system against avalanches from the northern slope of Mt. Blanc was constructed above the hamlet Taconnaz a few kilometres west of Chamonix, France in 1991. Eleven walls (1.5 m wide, 10 m long and 7 m high) were built in the beginning of the avalanche stopping area. One wall in the upstream row is situated right in the centre of the path. Two sensors for measuring avalanche forces were designed and installed on this latter at two different heights. Each sensor measures the three components of the force exerted by the avalanche flow. The data are recorded on a data logger from Campbell Scientific, Inc. The maximum sampling frequency is 50 Hz for each force component.

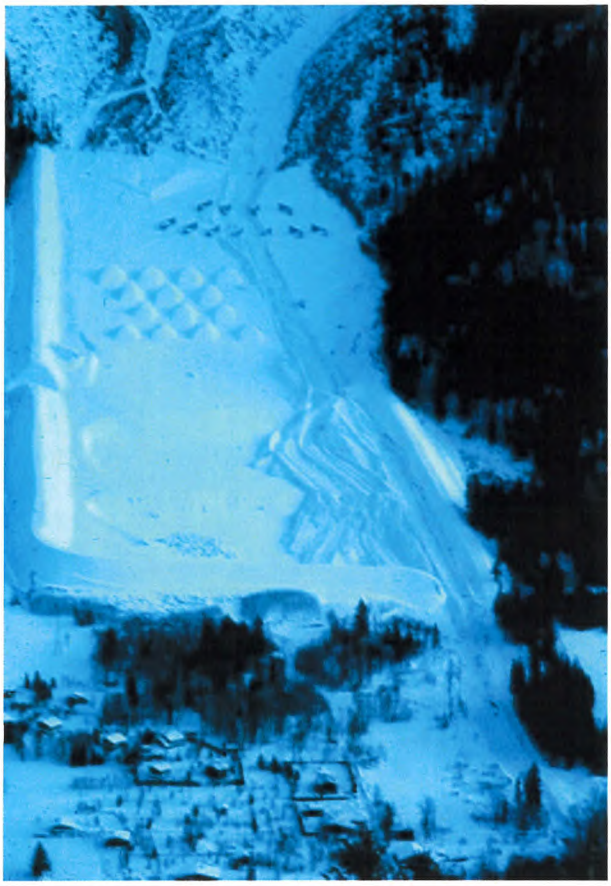

Figure 3.2.5 The Taconnaz dam system. At the left edge of the picture and just above the little patch of forest in the foreground, a huge deflecting/catching dam can be seen. On the left side of the upper half of the defence area, 14 braking mounds slow down parts of the avalanche en route towards the inhabited area. Finally, just below the end of the gully, two rows of deflecting walls attempt to diffuse the avalanche flow sideways. Pressure sensors have been installed on one of the middle walls of the upper row.

Task 3.3 – Snow chute instrumentation

(Task leader: Mohamed Naaim)

The goal was to build a "laboratory" type of experiment in which the flow can easily be controlled and reproduced. At the same time, it should be located at an altitude high enough so that snow can be brought directly from the ground to the experiment after a snow fall. Such a device has been built near the Alpe d'Huez ski resort. A large number of preliminary tests were performed in the course of the winter 2002/03 in order to achieve full control of the instrumentation, and finally, the first results were obtained at the end of the season.

The cohesive nature of snow forced us to have a motorised feeding system for the flow. We were afraid that if one stocked snow in a hopper and just opened it, cohesion due to sintering would prevent the snow from flowing. Therefore, we designed a feeding system which consists of a storage hopper with an Archimedes' screw. Such feeding systems are commonly used in industry and are known to provide a constant flow rate. The screw is 4 m long and its diameter is 60 cm. It has a slightly increasing step to avoid compaction of the snow while it is carried out. The screw is driven by a diesel engine by means of a hydraulic transmission. This enables us to set any constant rate up to 220 m^3/h. Since the storage capacity of the hopper is around 5 m^3, the flow can last from one to several minutes. However, to avoid significant compaction of the snow, the hopper is filled only to

one half of its capacity, leading to flows of about 40 to 60 seconds, which is long enough for our purposes.

Flow channel

The channel is sitting on a beam whose inclination is adjustable. The slope of the channel can be set from 27° to 45° in steps of 2°. The channel length is 10 m, its width 20 cm and its height 20 cm. Since it is narrower than the screw, a funnel-shaped slide links the end of the screw to the beginning of the channel. The bottom of the channel is covered with sand paper so as to achieve a roughness similar to that of a snow cover. Underneath, the channel has a double bottom where the electronic systems required for the sensors are installed.

Experimental procedures

It took us a fair number of unsuccessful attempts before becoming able to produce flows as steady and uniform as possible. The main obstacle to this is the sintering cohesion of snow in the hopper that, in the best case, transforms the flow into a succession of blocks sliding into the channel an, in the worst case, is so strong that it prevents the rotation of the screw. Therefore, a sieve was installed on top of the hopper, through which the snow has to pass before being stored in the hopper. This operation has to be done only a few seconds before the beginning of the experiment so as to reduce the sintering.

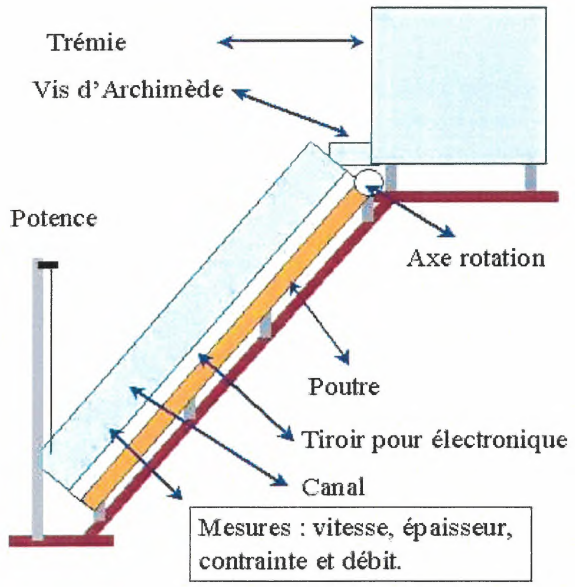

Figure 3.3.1 Schematic of the Col du Lac Blanc chute.

The other difficulty we had to resolve was the transformation of the snow grains through heating or through solar radiation. This led us to perform our experiments by night, which is the best guarantee to have cold weather and no sun.

Instrumentation of the CLB chute

The sensors installed in the channel measure (i) the flow height, (ii) the normal and shear stresses at the bottom of the flow, and (iii) the velocities inside the flow, from which velocity profiles are derived. At the same time, these measurements enable us to also obtain the effective friction coefficient, defined as the ratio of the shear and normal stresses, and the mean density of the flow.

A common criterion for the choice of all sensors was their performance under the temperature and humidity conditions of the high-mountain environment.

For measuring the flow height, we use three optic distance sensors mounted above the flow, perpendicular to the chute plane. The sensors are LEUZE ODS M/V-5010-600-421, recalibrated to measure distances from 100 mm to 350 mm. Mounting them 30 cm above the bottom of the channel allowed us to measure flow heights from 0 to 20 cm to a precision of 1 mm, which is only slightly larger than the typical grain size.

To measure stresses (both the normal and shear stresses) we used a two-component piezo-electric sensor (Kistler 9601A21-2-20) sandwiched between two metal plates, whose dimensions are 20×50 cm^2. To avoid tilting of the upper plate, it was necessary to use two sensors. The lower plate is fixed to the beam so that it does not move. The upper plate is connected to the lower one only through the sensors. The stresses applied by the flow on the upper plate are therefore transmitted to the piezo-electric sensors, which charge a capacitor in proportion to the stress. These charges are then transformed into a voltage by the charge amplifiers. This kind of sensor was chosen for it was the only one that combined the required sensitivity to stresses of only a few Newton with convenient installation in our channel.

However, the charge amplifiers contain complex electronics that are very sensitive to temperature and humidity conditions. In particular, it is crucial that their temperature remain above 0°C. Therefore, they have to be warmed up before and during the experiments. Moreover, their calibration fluctuates because of changing humidity. To perform correct measurements, one has to calibrate the system in conditions as close as possible to those of the experiments. We finally resorted to calibrating them just a few seconds before the snow flow.

Figure 3.3.2 A view of the hopper used to store the snow for experiments at Col du Lac Blanc.

To measure velocities we used the cross-correlation method applied previously by J. D. Dent and by K. Nishimura and co-workers. based on the correlation of two signals obtained by two identical

sensors located downstream one from the other. Basically, each velocity sensor is made of two identical optical devices. These devices are very sensitive to the amount of light collected by the phototransistor. Since this amount of light depends on the granularity state of the reflecting surface, the signal obtained is characteristic of the snow pack that reflected the light from the LED to the phototransistor.

Resources employed

a) 4 persons were used for 4 months to set up and test the chute.
b) Purchase of the sensors and data acquisition system.

Task 3.4 – Instrumentation of chutes for granular flow studies

(Task Leader: Massimiliano Barbolini)

Pavia chutes

Two distinct chutes for experimental studies with granular materials are presently available at the Pavia laboratory.

Chute A

The channel (see Figure 3.4.1) has rectangular shape and is 35 cm wide and 6 m long, with a constant slope which can be adjusted from 0° up to about 45°. The bed of the channel is metallic and the lateral walls (50 cm high) are made of Plexiglas. A pneumatic gate is installed at the beginning of the channel. The reservoir is 0.8 m long, has a volume of about 0.15 m^3, and must be loaded manually.

Section shape	Rectangular
Length	6 m
Width	35 cm
Height of the lateral walls	50 cm
Roughness (with water)	$N = 1$ (*Manning*)

Table 3.4.1. Main features of Chute A

Figure 3.4.1 View of the experimental chute

In the experiments the inclination of the chute was set to 30°, and was held fixed. The video-recordings were made in a window located about 4.5 meters downstream from the release gate (see figure 3.4.2).

In order to vary the frictional properties of the sliding surface, we constructed two rough surfaces that can be used as chute bed in addition to the metallic bed: one was made rough by gluing a layer of particles onto a board and the other by using no. 60 sand paper.

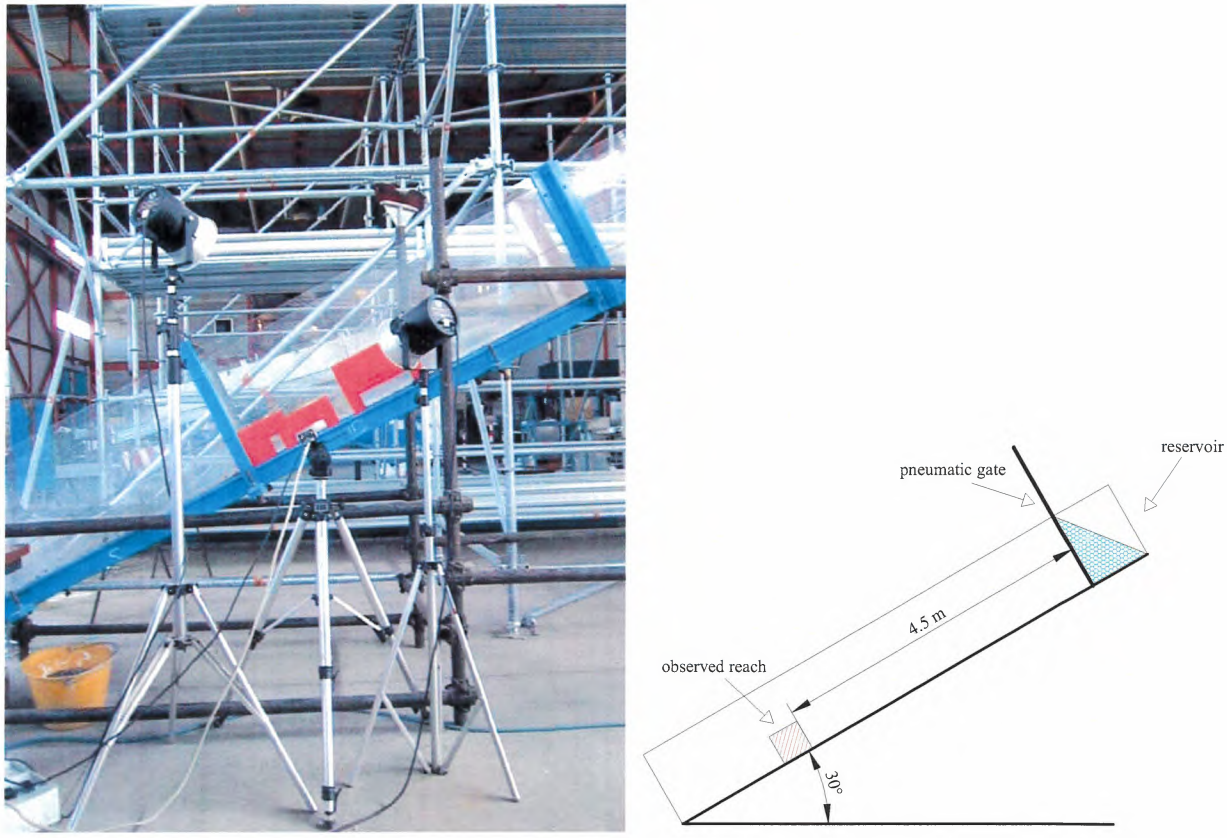

Figure 3.4.2 Side view of the chute, with indication of the recording area

Chute B

The construction of a new experimental chute (chute B) has been recently completed (Figure 3.4.3). It is 10.38 m long and 30 cm wide, the lateral walls are 30 cm high. It is made of two Plexiglas segments: the first is 5 m long and the second is 5.38 m long. The two segments can be inclined at very different angles.

This channel will be mainly employed to study bed erosion and deposition phenomena, and flow regime transition related to slope changes. Table 3.4.2 summarises the features of Chute B.

Figure 3.4.3 Side view of the Chute B and the supporting structure

Cross-section	Rectangular
Length of first segment	5 m
Length of second segment	5.38 m
Width	30 cm
Height of the lateral walls	30 cm
Roughness (with water)	N = 1 (Manning)

Table 3.4.2 Main features of the Chute B

High-speed camera

Even though high-speed capturing systems have existed for many years, the hardware and software components are still very expensive. Our main aim was to build a system with a frame rate that was higher than in usual analogue cameras, but at a comparable cost. In order to achieve this goal, we used off-the-shelf components and avoided, when possible, special purpose parts that raise the cost of the system significantly. Moreover all the software had to be open-source so it was easily adaptable to our needs and it carried no direct additional costs.

The heart of the system is an advanced camera with digital interface made by Pulnix. It is capable of a sustained rate of 30 million pixels per second that may be arranged into different frame-rates as shown in table 3.4.3.

	Width	Height	Frequency
Full height	640	480	120 Hz
Half height	640	198	240 Hz
Quarter height	640	100	350 Hz

Table 34.3. Image sizes and frame frequencies available in the high-speed camera system.

The camera has an electronic shutter able to manage exposure times from 1/60 s up to 1/32'000 s. In order to illuminate the stage, two photographic lights, with a power of 1250 W each, are used.

Activities started

In the first year of the project, purchase of new equipment to be used during the SATSIE project has been planned. In particular, two additional digital frame grabbers have been acquired (only one was available so far) so that we can use three cameras simultaneously during experiments. Also, two PCs for data logging have been bought, as well as different kinds of granular material for experiments.

Activities during the last 6 months

a) Chute experiments for analysing flow regimes (started in the summer 2003)

Experiments with granular materials were carried out at the Pavia chutes to investigate several aspects of flow regimes. Granular materials exhibiting some cohesion and locking properties were used. High-speed video recordings at different locations and with different chute beds were used to compare the velocity profile. The use of coloured particles helps in identifying them and in understanding the velocity fluctuations in the flow.

b) Erosion/Deposition experiments (started in the summer 2003)

Some experiment with granular materials were carried out at Pavia chutes, and more experiments will follow, to investigate aspects of erosion/deposition processes, such as the location of primary erosion and deposition zones (at the front, at the bottom, in the tail), the erosion rate, and how the eroded material is merged with the moving one. Similar experiments should also be carried out with snow at the Col du Lac Blanc chute.

Planned activities for the next 6 month period

a) Deflecting dam experiments (starting in spring 2004)

A series of experiments will be performed at Pavia chutes to analyse the dynamics of granular flows that hit deflecting dams, with special emphasis on the conditions that determine overflow of the dams. The results will be compared with traditional criteria for the design of deflecting dams and formulas recently derived from shock dynamics, and also with results of similar experiments performed in a smaller chute in Bristol in the spring of 2003.

b) Catching dam experiments (starting in spring 2004)

A series of experiments will be performed to analyse the dynamics of granular flows that hit catching dams, with special emphasis on the conditions that determine overflow over the dam and dissipation of kinetic energy in the impact with the dam. The results will be compared with traditional formulas for the design of catching dams and recent results from experiments at other scales in Bristol, Reykjavík and Davos.

Chutes at Cemagref Grenoble: granular flows and interaction with obstacles

Chute for continuous granular flows

The experimental set-up consists of a 2 m long and 5 cm wide Plexiglas channel, two hoppers and a pumping system (as is illustrated in Fig. 3.4.4). Glass plates (2 mm thickness) on vertical walls allow to limit electrostatic effects and to preserve the good transparency of the sidewalls. The inner width of the channel is thereby reduced to 46 mm. A rough channel bottom is obtained by gluing beads (with the same diameter as the beads used in the flow) on a thin PVC band (thickness 1 mm, length 2 m). The technique involved depositing beads on a double-sided adhesive film. The pumping system allows us to let the material circulate without interruption. We use a rough bed in order

to make steady uniform flow possible in a whole range of channel inclinations. Indeed, studies on granular flows down rough inclined channels (Savage, 1984; Ancey et al., 1996) showed the existence of steady uniform flows in a whole range of inclination angles (spanning 5-10°) starting from a value close to the internal friction angle of the material obtained from the traditional tri-axial measurements of soil-mechanics.

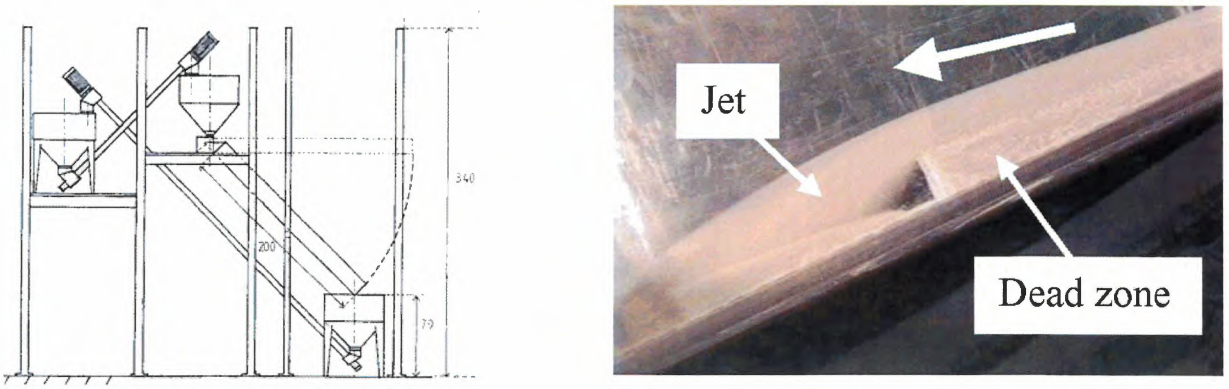

Figure 3.4.4 Schematic view of the chute for continuous granular flows (left side) and photo showing the interaction of a continuous granular flow with a dam (right side).

For controlling the mass flow rate, the supply hopper at the upper channel entrance is equipped with a cone-shaped valve which more or less obstructs the hopper exit. The material flows down the channel and falls into a collection hopper. Screws powered by two Siemens gears return the material to the supply hopper. The cone-shaped valve is calibrated by weighing the mass of fallen material for a given interval time. As is well known for hoppers, the mass flow rate is independent of the height of material stocked inside it; it usually depends only on the size of the particles and the exit geometry. The uncertainty of the mass flow rate is estimated around 5%. The channel inclination can be varied between 0° and 45°. Flow depths are measured with a video camera or with optical sensors. Uncertainty of the flow depth is estimated around 0.5 mm. The discharge Q is deduced from the mass flow rate Q_m by assuming that the density is nearly uniform for a steady flow: $Q_m = \phi \rho_P Q$, with the solid concentration ϕ assumed constant. The mean velocity is computed as: $u = q/h$, where $q = Q/\ell$ is the discharge per unit width, h the flow depth and ℓ the channel width. This experimental set-up is used to compare flows hitting obstacles with reference flows without obstacles. It allows quantifying the zones of influence upstream and downstream of the obstacle.

Chute for transient granular flows

As is illustrated in Fig. 3.4.5, the experimental set-up consists of two inclined planes (1 m wide), a channel with two side-walls that are 0.93 m long and 0.2 m apart, and a box to store the granular material before releasing it. The released mechanism allows to simulate dam-break release or to control the starting height of the flow. The first plane is 2 m long and the second is 1 m long. The bed consists of PVC covered with sandpaper or of particles glued to the bottom (the same material is used as in the flow). The two planes can be inclined independently.

Several variables are measured in the reference granular avalanches (i.e., without obstacles): (i) the front velocity in the channel (flow zone of the granular avalanche) with a video camera, (ii) surface velocities in the channel with a video camera (using coloured beads), (iii) flow depth with a video camera positioned sideways or with optical sensors, and (iv) the front velocity downstream of the channel (in the run-out zone of the granular avalanche) with a video camera. The maximum run-out distance and the deposit shape are also measured.

This experimental set-up is used to study the effects of obstacles on transient granular flows. Different configurations of obstacles (depending on obstacle shape and location at the channel exit or in the run-out zone) are being tested. These measurements allow quantifying the influence of obstacles on the run-out deposit of granular avalanches.

The two side-walls and the box are connected and can easily be moved to another inclined plane with a more accurate inclination measurement system. This technique has been used to study the retaining capacity of a dam located at the channel exit.

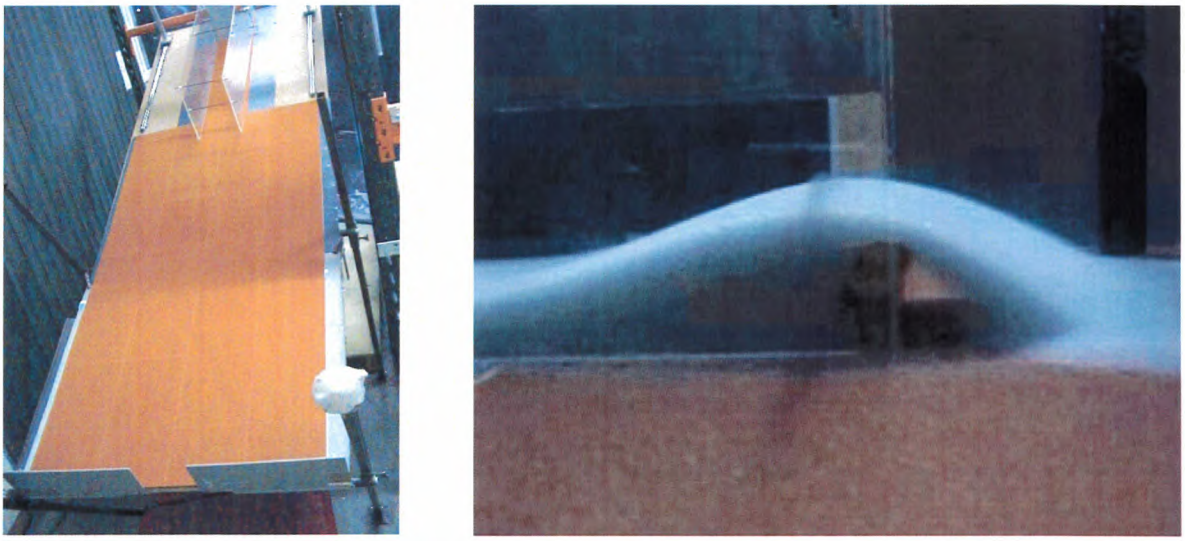

Figure 3.4.5 The transient granular flow chute (left side) and interaction of a transient granular flow with a dam (right side).

The Cemagref water tank

The experimental set-up consists of a 4×2×4.5 m^3 water tank with glass walls (Figure 3.4.6). Buoyant clouds flow along an inclined plane from a small immersed tank (length 20 cm, width 15 cm, capacity 4 l) with a release gate. Powder-snow avalanches are simulated by a heavy fluid (salt water plus kaolin) dispersing into a lighter one. The density of the heavy fluid relative to water is 1.2. By adding kaolin, the gravity current in the water tank becomes visible. Kaolin is also necessary because ultrasonic velocity measurement methods depend on particles within the suspension. Contrary to what occurs in nature, the avalanches in the laboratory simulation start already as suspension flows. Furthermore, the entrainment of particles is not simulated.

Both 3D and 2D simulations can be performed. In the 2D configuration, the avalanche is confined to a channel along the entire path (length 285 cm, width 15 cm, height 50 cm). In the 3D configuration, the avalanche is first confined to a short channel representing a gully (length 47 cm, width 15 cm, height 30 cm) before flowing down on an open slope (length 300 cm, width 190 cm). The experiments can also be carried out with obstacles representing defence structures. We determined experimentally that the highly turbulent nature of the avalanches requires ensemble averaging over five identical experiments (see Fig. 3.4.8).

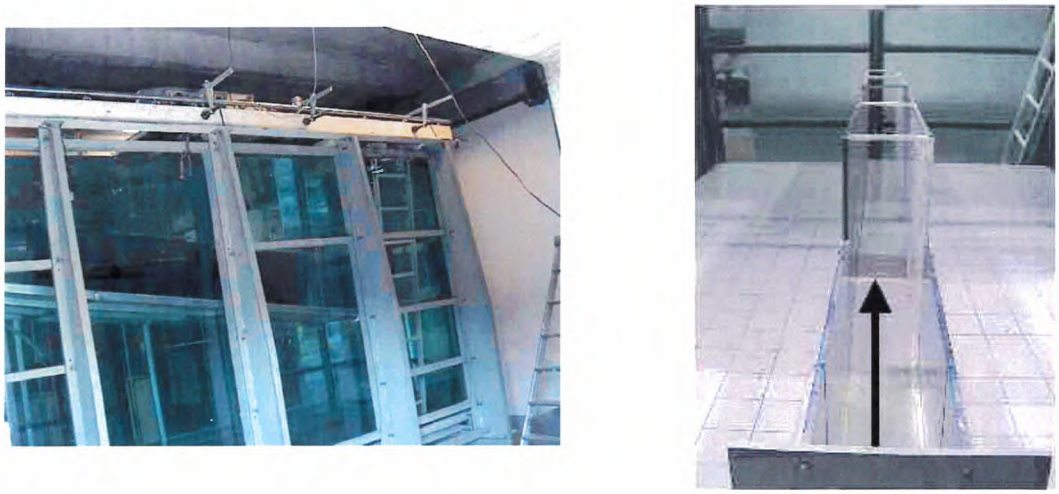

Figure 3.4.6 A general view of the water tank with the submerged channel and the 2D channel.

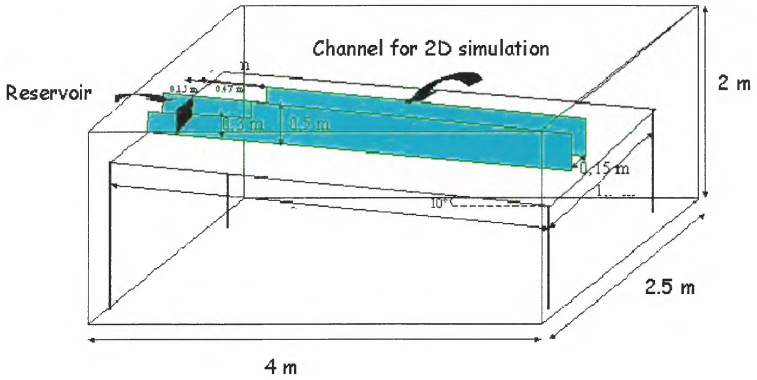

Figure 3.4.7 Schematic drawing of the water tank with the submerged channel

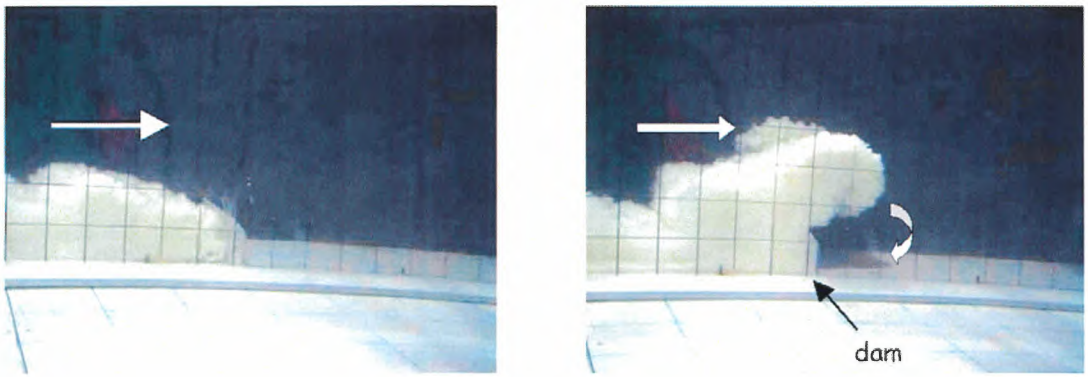

Figure 3.4.8 A typical flow: the obstacle caused an acceleration of the flow above it. This acceleration caused a vortex to appear downstream of the dam.

Measurement techniques

Two cameras are used (top and side views) to obtain the height, length, width, shape and front velocity of the flow. The Doppler ultrasonic velocimeter measures the component of the particle ve-

locity vector in the direction of the transducer. This sensor exploits the frequency change of an acoustic wave as it is scattered back from moving particles present in the heavy fluid.

In the near-field zone between the head of the transducer and a distance of 16.7 mm, the acoustic field is basically cylindrical, with a diameter of 5 mm. In the far-field zone, the intensity of the acoustic field varies as the inverse of the square of the distance from the transducer and oscillates in the plane perpendicular to the axis of propagation (see Fig. 3.4.9).

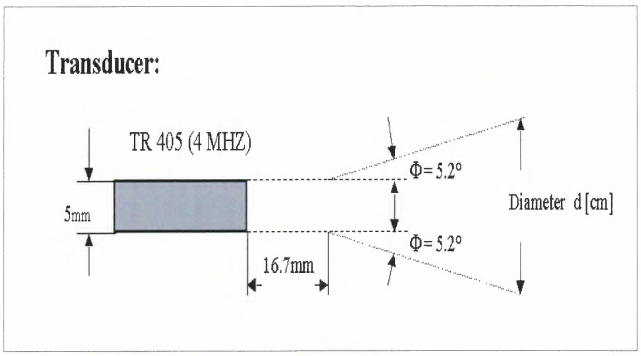

Figure 3.4.9 Transducer with apex angle of the acoustic field.

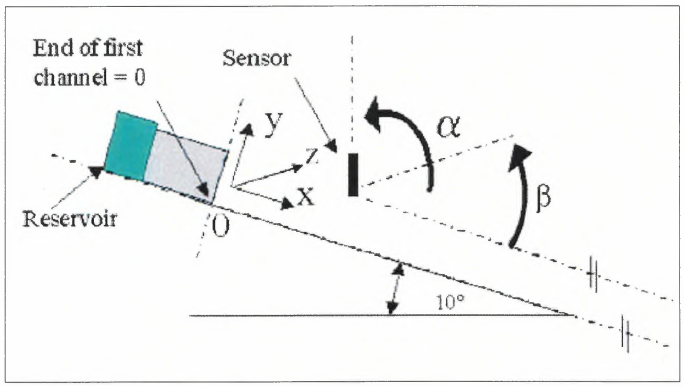

Figure 3.4.10 Side view of the chute.

In the experiments, the following dimensionless numbers are used (see Table 3.4.5):

	Nature	Laboratory
Relative density difference $\frac{\Delta\rho}{\rho}$	4	0.2
Reynolds number Re	10^8	10^4
Densimetric Froude number $\frac{U}{\sqrt{gH\Delta\rho/\rho}}$	2.2	2.2

Table 3.4.5 Dimensionless numbers in nature and in laboratory experiments

Chute and flume in Bristol

The experimental chute and flume in Bristol are situated in the Department of Applied Mathematics of the University of Bristol. The laboratory is a fluid dynamics laboratory that has recently been established. It is equipped with various chutes and tanks for fluid experiments along with analogue and digital video cameras and other instruments.

The wooden chute for granular flows

The experiments in this chute were designed to study high Froude number granular flows deflected by a dam and identify the flow behaviour in the interaction with the dam.

The experimental chute is a 6m long plywood chute consisting of two straight sections, one inclined at 38° and the other one horizontal, see Fig. 3.4.11 and 3.4.12. The sections are connected by a thin plywood sheet, positioned 232 cm down-slope from the gate, to obtain a smooth transition between the sections. The chute has 20 cm high side walls made out of Perspex to allow for video recording from the sides.

Figure 3.4.11 A photograph of the experimental set-up of the wooden chute at Bristol University.

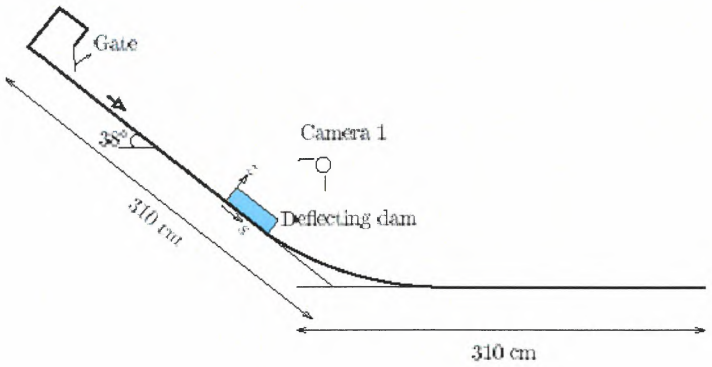

Figure 3.4.12 Schematic of experimental set-up.

The deflecting dams are constructed out of plywood and positioned at the upper section of the chute, 169 cm down-slope from the gate, at five different deflecting angles to the flow (8°; 15°; 24°; 32° and 44°), see Fig. 3.4.13. The ratio of the dam height to the flow depth was varied from 1 to the dam height needed to fully deflect the flow for each deflecting angle, or up to a maximum of 20.

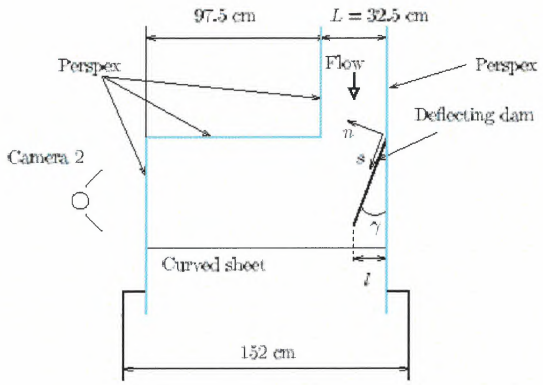

Figure 3.4.13 Plan view of the chute section next to the deflecting dam. Camera 1 is located above the deflecting dam.

Glass ballotini particles of mean size 90 μm, density 2500 kg m^{-3} (bulk density of 1600 kg m^{-3}) and approximately spherical shape were used. The flow speed on the chute was measured by tracking tracer particles that were thrown into the flow, and the flow depth was measured using an optical depth sensor (Leuze ODS96M/D-5020-600-222) that uses infrared light to measure the distance to a surface. Time series of the depth and the flow speed were obtained in this way. The interaction between the flow and the deflecting dams were recorded from above and from one side by video and subsequently analysed. The run-out length and distribution of the deposited particles were measured.

The Perspex flume for water flows

Experiments in the water flume were conducted to test how well shallow-water shock theory agrees with shallow water flow against a deflecting dam. The experiments involved a steady stream of water flowing down a 20 cm wide channel, hitting a deflecting dam and forming a steady hydraulic jump. The depth profile and deflecting angles were photographed with a digital camera, through the side of the dam and from above.

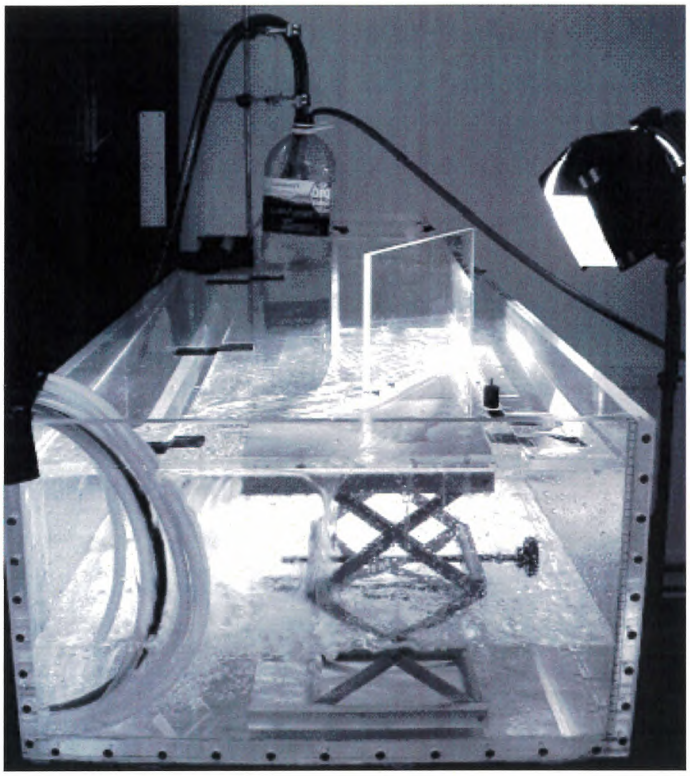

Figure 3.4.14 Set-up for deflection experiments with water. A steady stream of water is supplied through three hoses and stored in a reservoir. The water flows over a weir and under a gate to minimise turbulence and wave action. It then continues down the 20 cm wide Perspex channel before finally hitting a deflecting dam. The super-critical flow is 5 mm deep on average, with a speed of just over 1 m s^{-1}.

WP 4 – Measurement campaigns (AIATR)

(Work package leader: Lambert Rammer)

Summary of experiments during the winter 2003 (Tasks 4.1 to 4.4)

This chapter reports on the results obtained in experiments on two real snow avalanches at the Norwegian test site Ryggfonn, one small-scale experiments with snow in the chute at the Col du Lac Blanc (France), and one small-scale experiments with dry granular materials or water at laboratory chutes in Pavia (Italy) and Bristol (England). All experimental facilities are described in the chapter on WP 3, while the new non-standard sensors are discussed in the one on WP 1. Furthermore, the experiments carried out in Pavia and Bristol are covered in detail in two reports (Barbolini and Pagliardi, 2003; Hákonardóttir *et al.*, 2003) that are reproduced in full in the annex to the present report. Those experiments will therefore only be summarised in this chapter.

Despite the unusually mild conditions in western Norway with few significant precipitation periods throughout the winter 2003–2003, measurements were obtained of two avalanches at Ryggfonn, one spontaneous of medium size and one small, artificially released. Only pressure measurements at one obstacle in the path and one at the dam could be obtained from the spontaneous event, as the FMCW radars developed by SATSIE are scheduled to be installed by the end of 2003. Velocity measurements with AIATR's pulsed Doppler radar were made of the artificially released avalanche. Load data were obtained at the measurement points in the path, but due to the short run-out there were no data from the dam. In Flateyri and Taconnaz there was no avalanche activity this winter. None of these two sites were instrumented at the time.

During the first year of SATSIE, the experiments at the chutes in Pavia and at Col du Lac Blanc focussed on the flow regimes exhibited by flows over smooth and rough surfaces, and with snow and dry granular materials. Experiments in Pavia on a smooth bed clearly showed the characteristics of the collisional flow regime in the body and the grain-inertia regime in the more dilute head, with significant slip at the bed. Moreover, the non-dimensionalised velocity profiles collapse intriguingly well with those measured in snow flows over a wide range of scales. Over a rough bed, steady-state flow was not achieved, and high particle concentrations indicative of the frictional (quasi-static) flow regime were found in the body of the flow; in agreement with this, the velocity profiles were linear without slip at the bed. In contrast, the measurements at the snow chute achieved steady-state flow over an even rougher bed than in Pavia, but the linear velocity profiles showed little shear and very pronounced slip. At first sight, the results appear to be somewhat contradictory between the snow flows and the granular ones, but it is conjectured that the observed differences are due to different boundary conditions, slope inclination and particle properties. Further measurements will be made during the second year to clarify these points.

Chute experiments in Bristol confirm that dry granular flows impacting on deflecting or catching dams are quite well described by shocks in shallow-water theory—even better than water flows themselves. Further work will focus on understanding the observed deviations from theory, investigating the effect cohesion has on the impact behaviour, up-scaling to real avalanches and extracting the consequences for the design of protection dams. For this last step, observations of real snow avalanches impacting on the dams in Ryggfonn, Flateyri and Taconnaz would be highly desirable.

Task 4.3 (cross-comparison of experimental results at different sites and scales) could not yet be tackled in full because the FMCW radar devices under development (WP 1) are needed to obtain information on the processes in the interior of the avalanches at Ryggfonn. Task 4.4 is scheduled only for the third year of SATSIE.

Task 4.1 Ryggfonn full-scale experiments (NGI)

(Task leader: Karstein Lied; participation of K. Kristensen, L. Rammer, H. Schreiber)

The avalanches studied at the Ryggfonn site are both natural and artificially released. In the case of natural avalanches, the recording system starts when the signal from a geophone on the uppermost construction (the steel tower) exceeds a pre-set triggering level.

Artificial avalanches are released by detonating up to five pre-placed charges in the starting zone by means of a radio-controlled detonating system. Typically, each charge consists of 75 to 100 kg of dynamite. Artificial avalanches are usually videotaped and photographed with a time-lapse camera. In some cases, filming is done from the opposite mountain ridge. Avalanche debris boundaries are mapped and the surfaces surveyed for volume calculations.

In the winter 2002–2003 two avalanches were recorded. A natural avalanche occurred in mid-January and another avalanche was artificially released on April 6th, 2003 (Fig. 4.1.1).

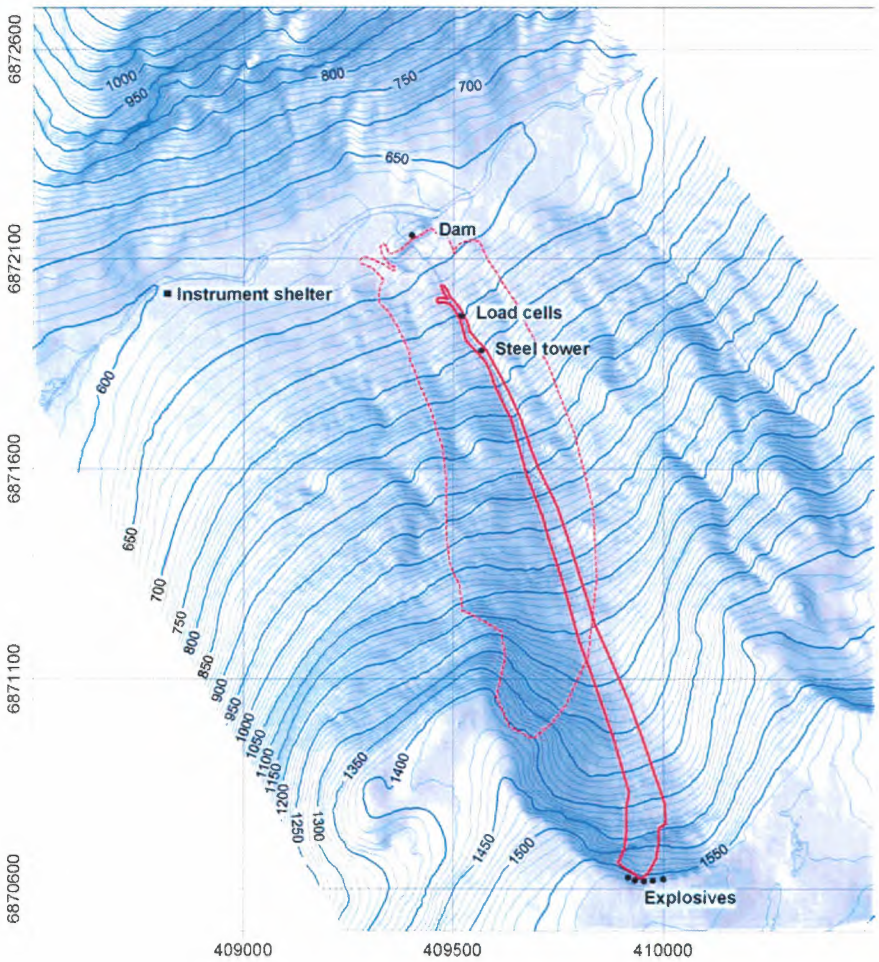

Fig. 4.1.1. Map of the test site with the avalanches recorded in 2003. The dotted line indicates the natural avalanche recorded on January 15th, while the solid line represents an artificially released avalanche on April 6th

Brief description of avalanche events

Natural avalanche on January 15th

The winter 2002–2003 had unusually stable weather and comparatively small amounts of snow. Despite of this, data from one cycle of natural avalanches and one artificially released avalanche were obtained.

During a period of strong winds and snow from January 11th to 18th, several natural avalanches ran in the Ryggfonn path and the adjacent area. The largest avalanche in this period occurred on January 15th at 13.27 h. Because the 0°C isotherm was at around 1000 m a.s.l. at the time of release, the avalanche consisted of partly wet snow.

As can be seen from Fig. 4.1.2, the avalanche originated from the west side of the cirque and lower on the west ridge. Bad visibility and irregular terrain made it difficult to estimate the depth and extent of the initial fracture. A rough estimate of the mean fracture height would be around 1.5 m. The areal extent of the initial slab would be around 50,000 m^2 (horizontal projection). However, it is evident that some entrainment of the loose, wet snow in the lower path has taken place. The volume of the deposit in the run-out zone below the load cells on the concrete structure is estimated to around 120,000 m^3.

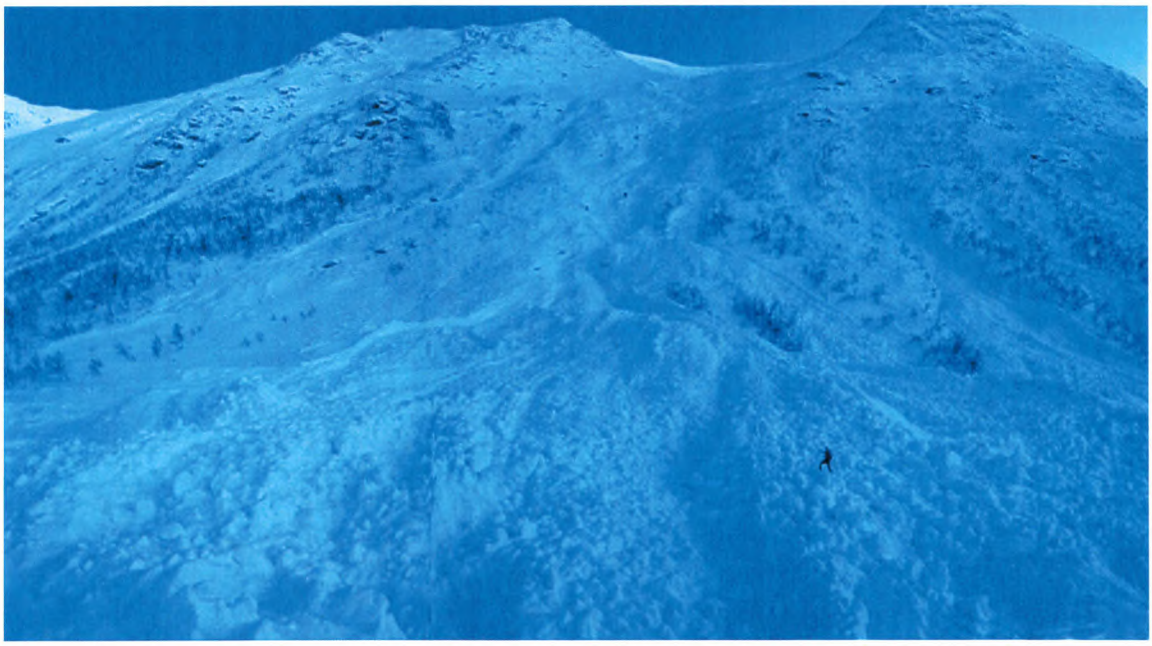

Figure 4.1.2. Deposit of the January 15th avalanche. Photo taken from the dam.crest.

Artificially released avalanche on April 6th

Following the mid-January storm period, there was unusually little precipitation in Western Norway: Despite the fact that the snow cover was rather unstable because of depth hoar formation in the early winter, no further natural avalanches were released. After a brief period of snowy weather in the beginning of April, it was decided to try to release an artificial avalanche on April 6th. The automatic measurements were extended with manually operated Doppler radar velocity measurements by the AIATR team. Video recordings were taken from the opposite mountain ridge. The release was triggered by detonating 150 kg of pre-placed explosives buried under the massive cornice at the top of the starting zone. The resulting ava-

lanche was comparatively small, but it did reach the load cells in the lower path. However, it stopped about 150 m short of the dam.

The avalanche was released during dry snow conditions with fresh wind slab formation in the starting zone. In the lower half of the path, most of the snow pack consisted of melt-freeze metamorphosed snow, covered by about 10 cm of dry new snow at the top. The initial slab had an area of about 18,000 m^2 (horizontal projection) and the crown height was about 1 m. Because of the more stable snow in the lower part of the path, entrainment gradually decreased and there was a loss of mass before the avalanche reached the measurement devices. Only a small fraction of the mass was able to pass the concrete structure.

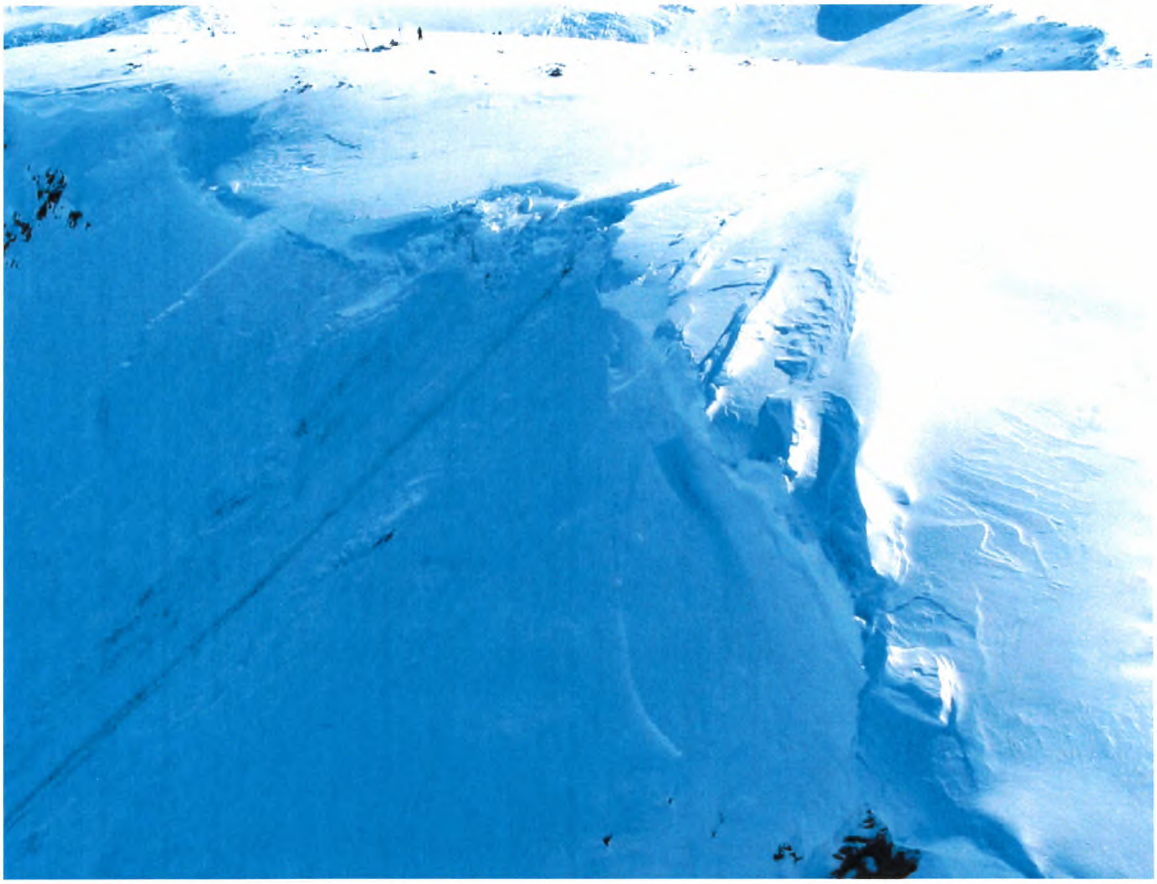

Figure 4.1.3. Starting zone of the avalanche that was released artificially on April 6th. The initial slab fracture can be seen below the blasted cornice.

Results

Natural avalanche on January 15th

Load data were obtained from the load cells at the steel tower (Fig. 4.1.4), the concrete structure (Fig. 4.1.5) and the load plates on the dam (Fig. 4.1.6). Because of the unusual starting zone, the avalanche appears to have entered the normal path from an angle, thus hitting the steel tower and the concrete structure further down-slope nearly at the same time. This would explain the simultaneous impact times observed (Fig. 4.1.7), but this also makes any speed estimate difficult.

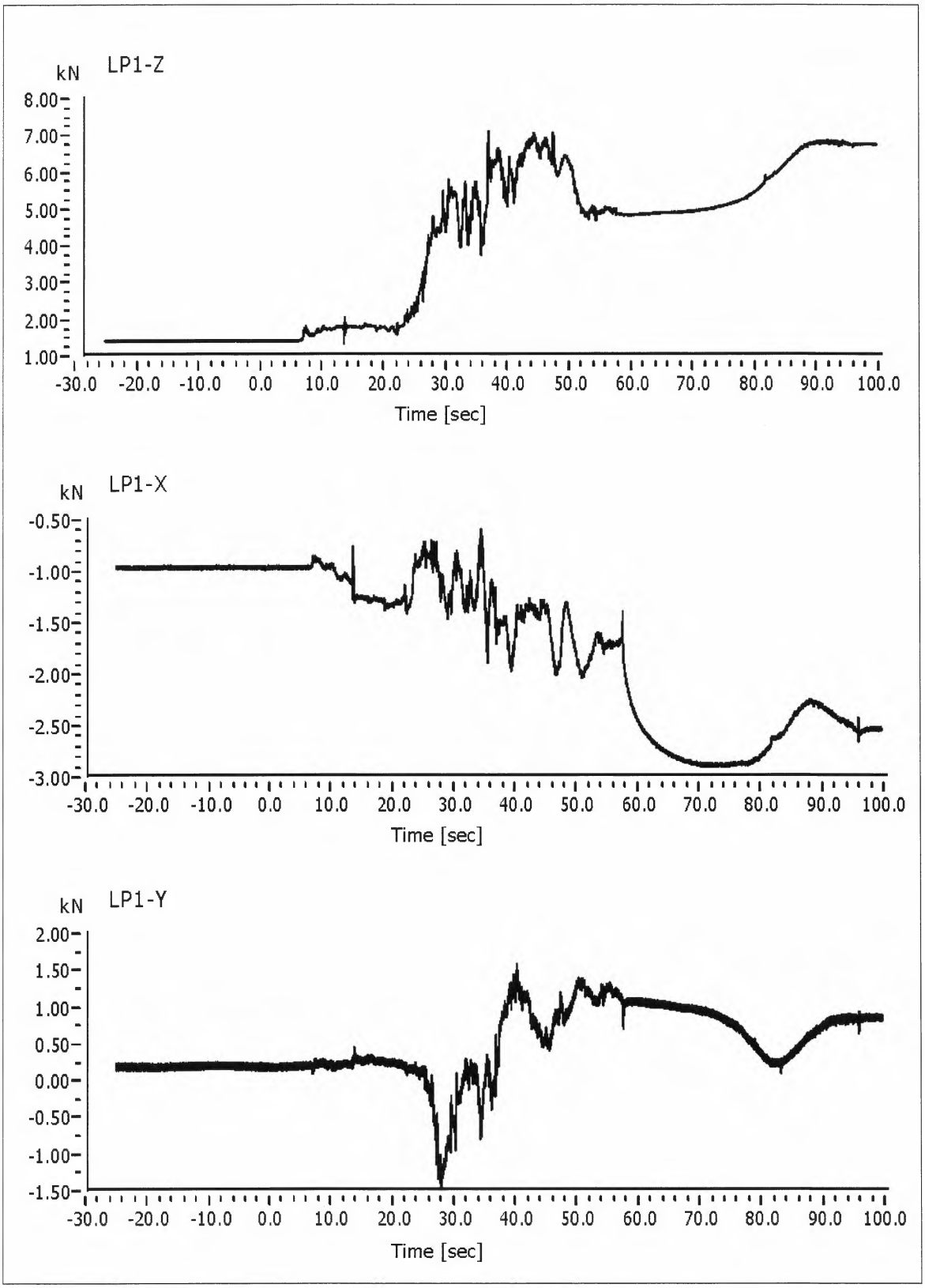

Figure 4.1.4. Load plate measurements at the steel tower during the January 15th avalanche .

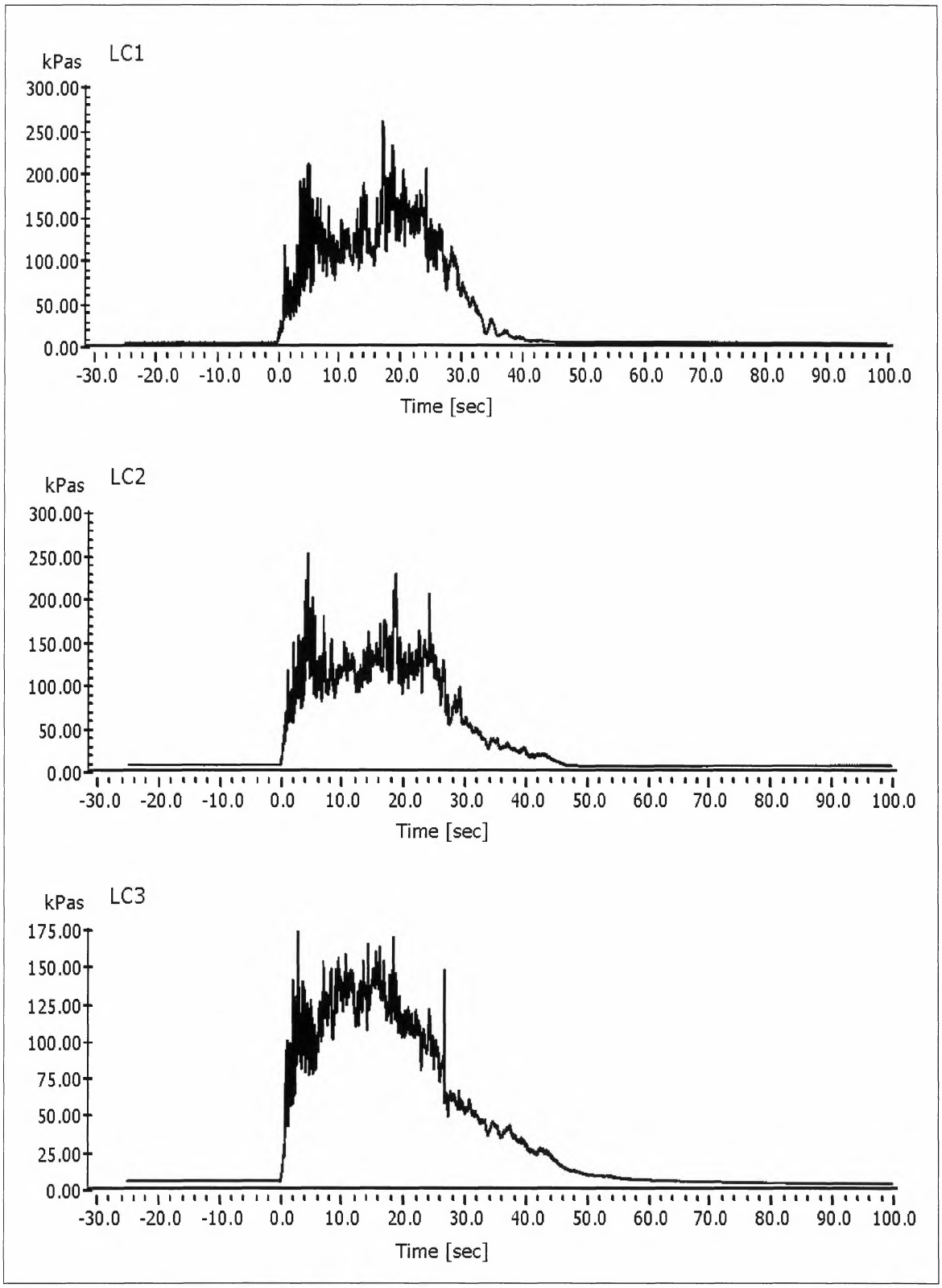

Figure 4.1.5. Load cell measurements at the concrete structure during the January 15th avalanche .

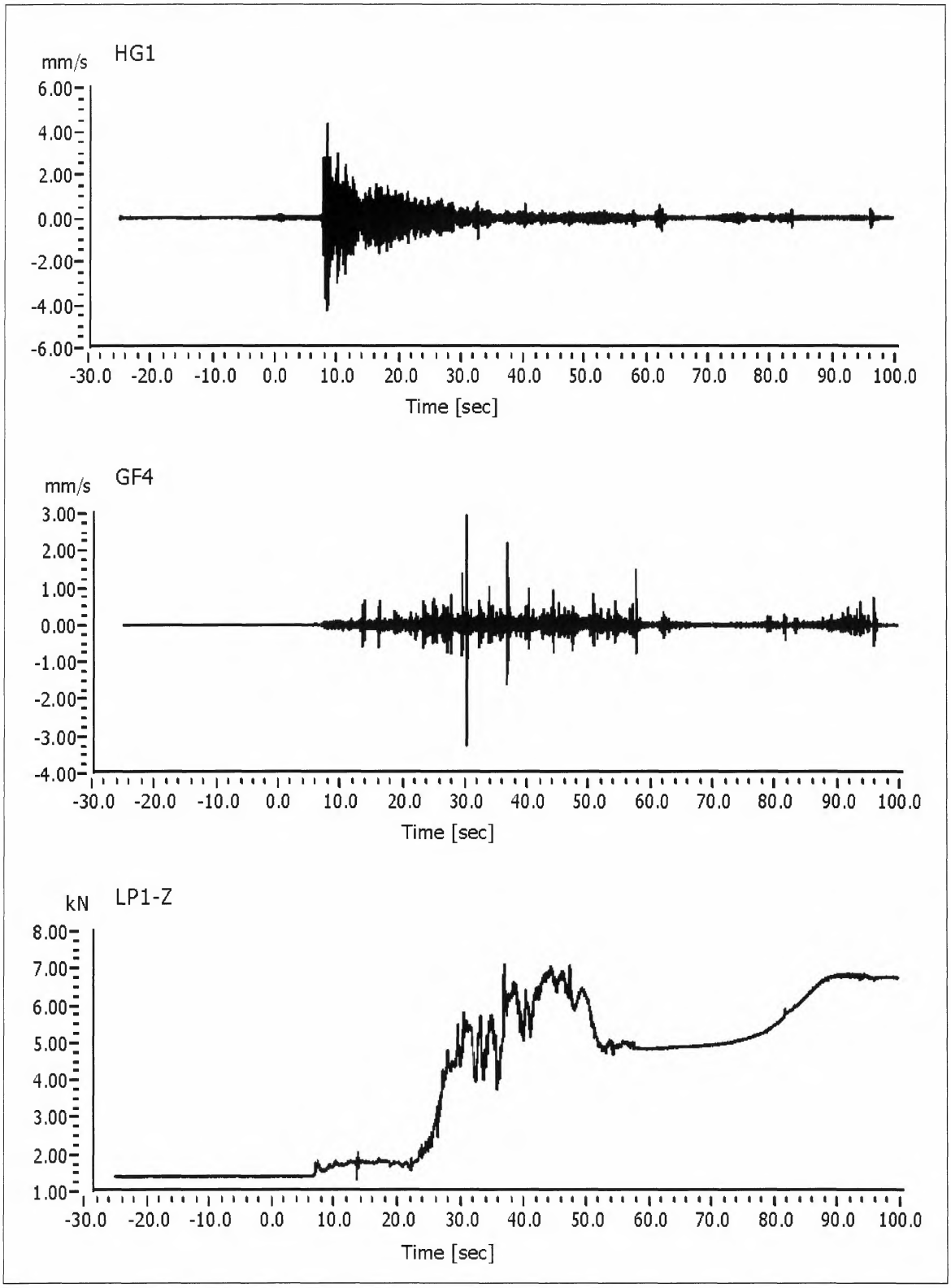

Figure 4.1.6. Geophone and load cell measurements at the impact on the dam during the January 15th avalanche.

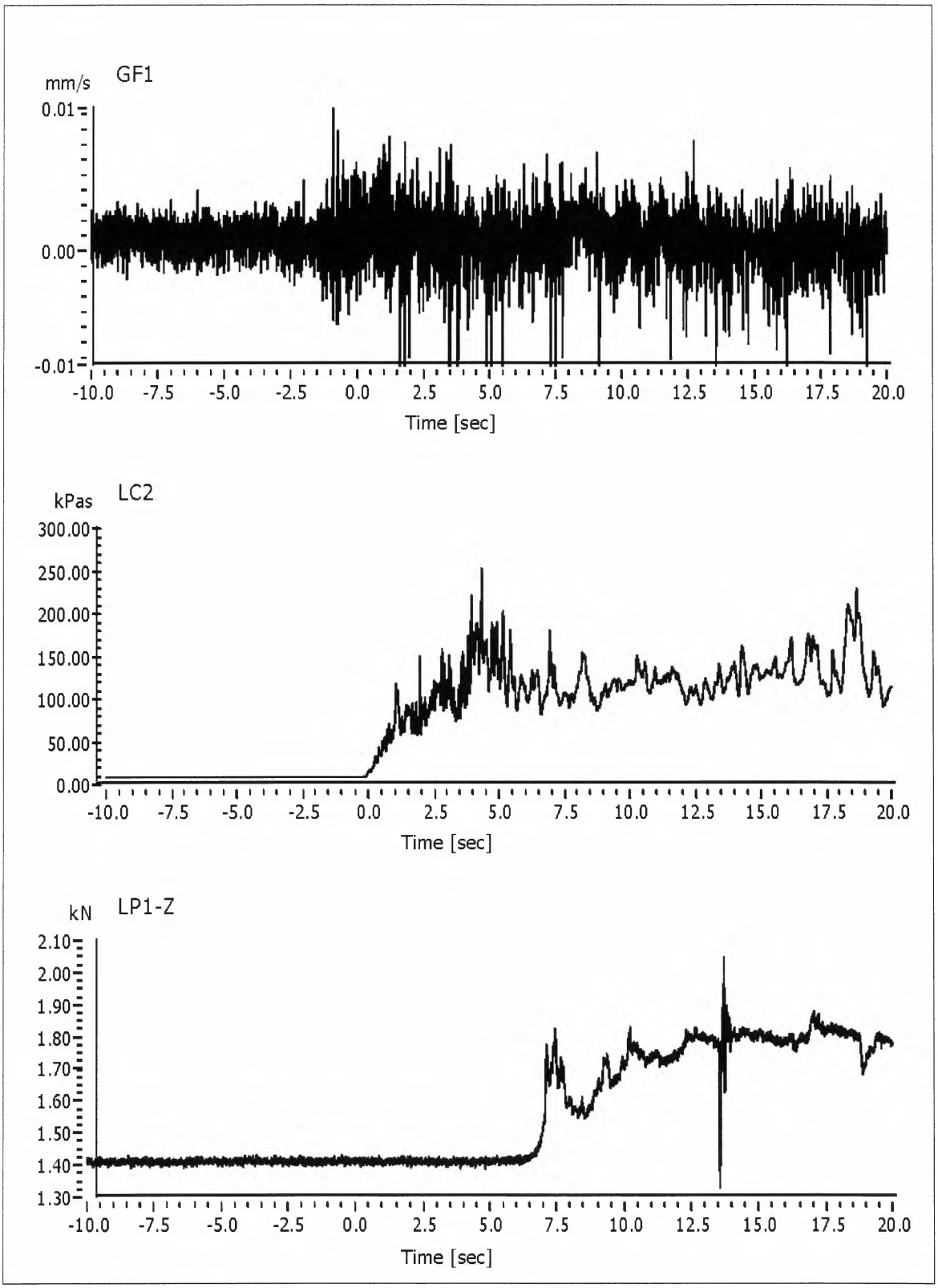

Figure 4.1.7. Avalanche arrival times at the steel mast, concrete structure and catching dam of the January 15th avalanche.

Artificially released avalanche on April 6th

At the time of release the load cells furthest up in the path, on the steel tower were malfunctioning, thus no data were obtained from this point. The load cells further down at the concrete structure were functioning, but show fairly low load values (Fig. 4.1.9). Since the avalanche came to a halt shortly below the concrete structure, no data were obtained from the sensors at the dam.

The antenna of the pulsed Doppler radar of AIATR was set up on the slope opposite the avalanche track at an elevation of about 25 m above the bottom of the valley and at a distance of 150 m from the crest of the dam. The radar control system was situated about 50 m further up in the slope for higher safety. The centre line of the radar beam pointed to an area in the avalanche track approximately 250 m above the steel tower. The angle at which the efficiency of the microwaves is half of the efficiency at the centre line is 9.5° on both sides of the centre line in the vertical, and 5.5° in the horizontal direction. In the upper part of the track, at a distance of about 1200 m from the antenna, the avalanche cannot be detected by the radar beam because it is hidden by a convexity in the terrain profile.

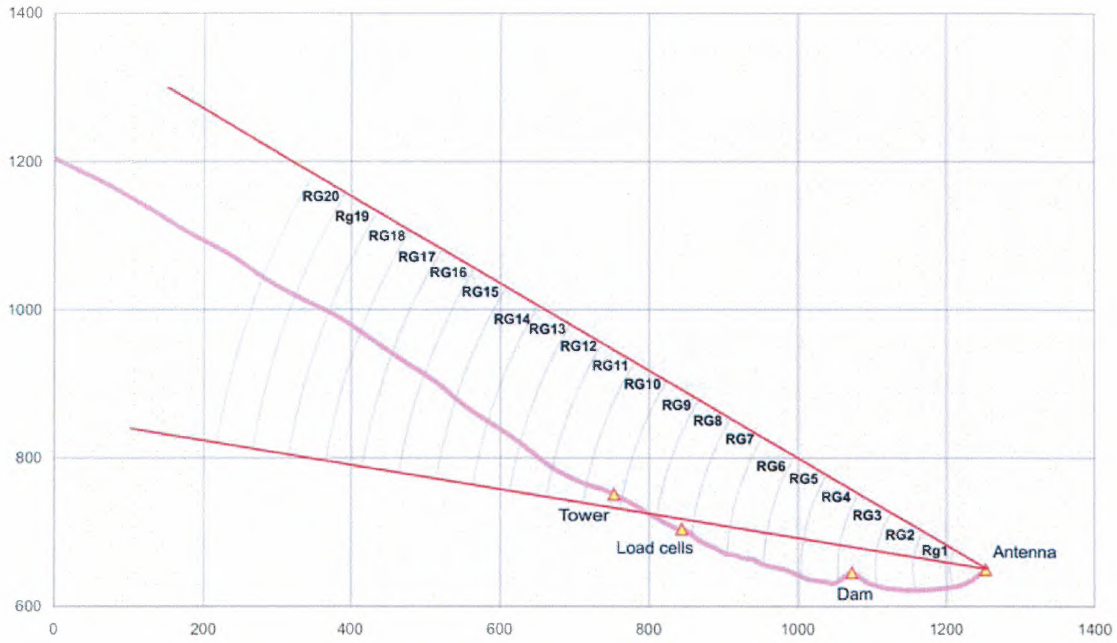

Figure 4.1.8. Range gate settings for the radar measurements on April 6th at Ryggfonn.

The radar data acquisition software was set up with 40 range gates (RG) with a length of 50 m each, beginning at a distance of 50 m from the antenna. Trigger values were defined as three times the noise level for the intensity of the signal and as 2.5 km/h for the velocity. The end of the run-out occurred in RG 7 at 400–350 m from the antenna or about 230 m before the dam. The steel tower is located at the beginning of RG 10; the concrete structure is located at the beginning of RG 8 (Fig. 4.1.8).

Because the released avalanche was very small, no reflection signal could be recorded at large distances. The measurements could be analysed only for a distance of 900 m or less from the antenna position. The time diagrams (Fig. 4.1.9) could be plotted beginning at range gate 18 (950–900 m from the antenna) and ending at RG 7 (400–350 m). Each diagram of the velocity at maximum signal intensity shows 40 s of avalanche running time.

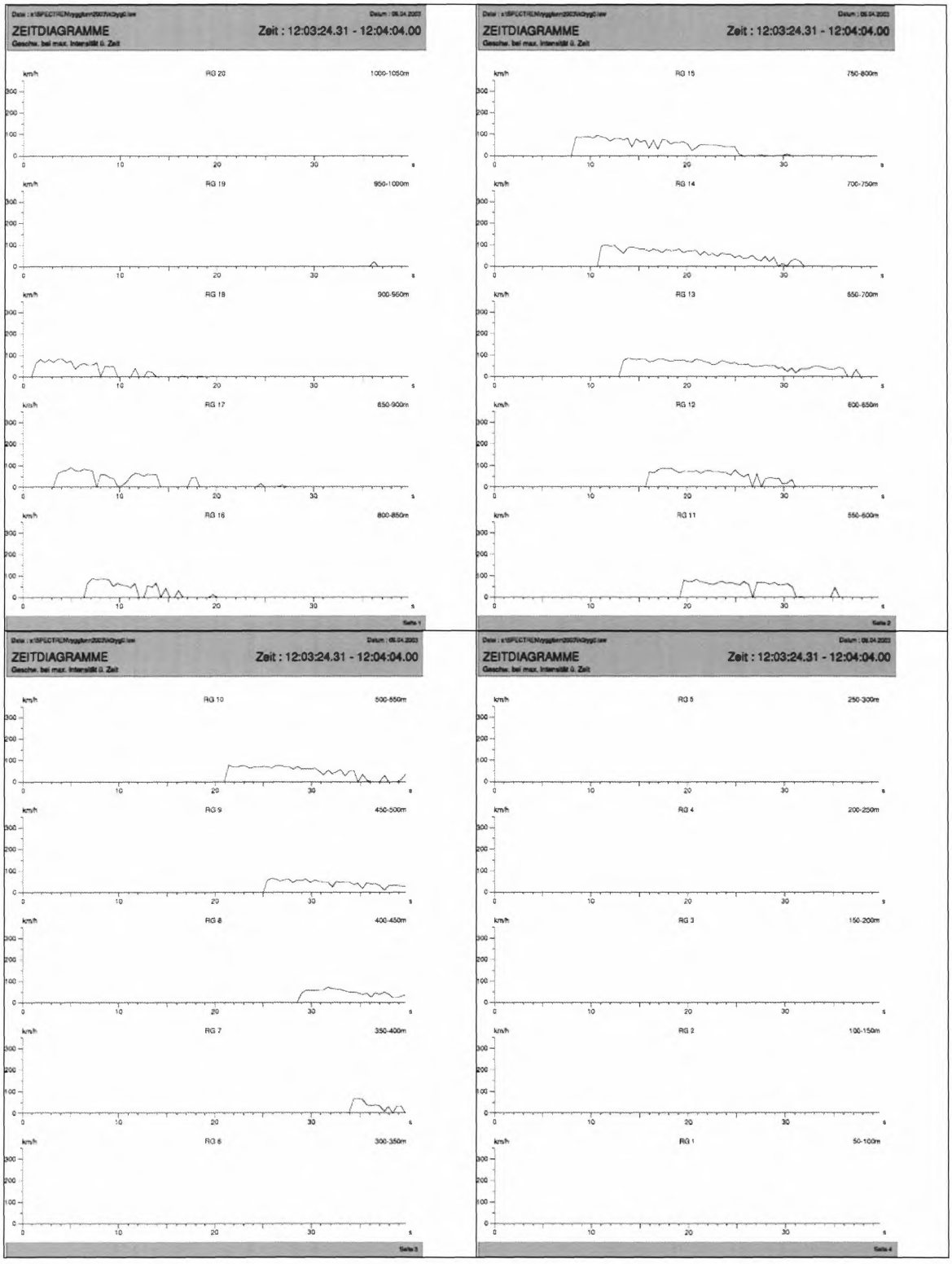

Figure 4.1.9. Time-velocity diagrams at maximum intensity from range gate 20 to range gate 1.

For each RG (except RG 8), the peak velocity occurs when the avalanche head enters the RG, decreasing to zero after about 12–15 s in most of the measured track, and after about 25 s in RGs 14 and 13.

Figure 4.1.10 shows the corrected front velocity along the slope profile. The plot starts in RG 18 with about 70 km/h, and then the velocity decreases to about 60 km/h at the end of RG 16. In RG 14 and RG 11, the velocity peaks twice above 90km/h. Afterwards, the avalanche begins to slow down, hitting the tower with 57 km/h and the concrete structure in RG 8 with 40km/h. In RG 7, the avalanche runs out and stops about 230m before the dam.

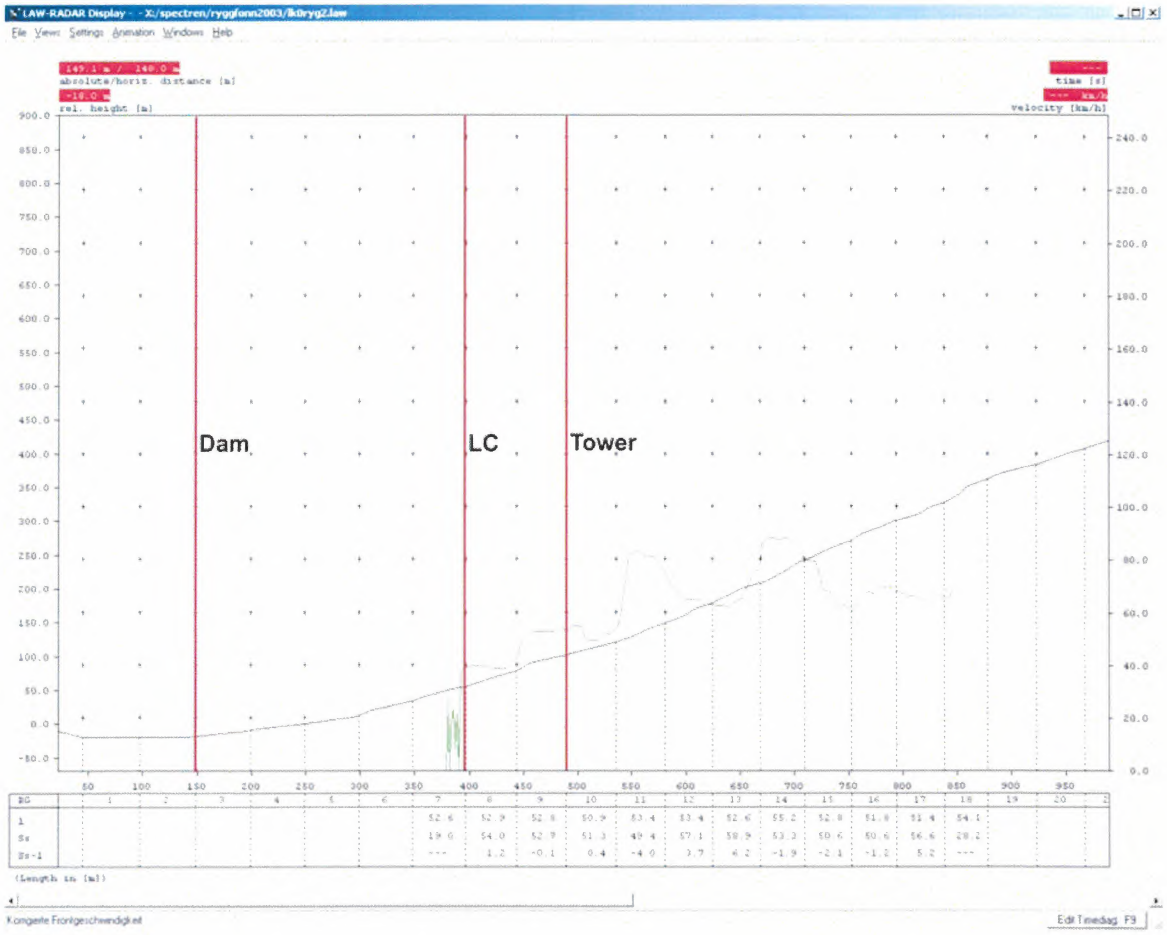

Figure 4.1.10. Corrected front-velocity diagram over avalanche path, avalanche of April 6th 2003.

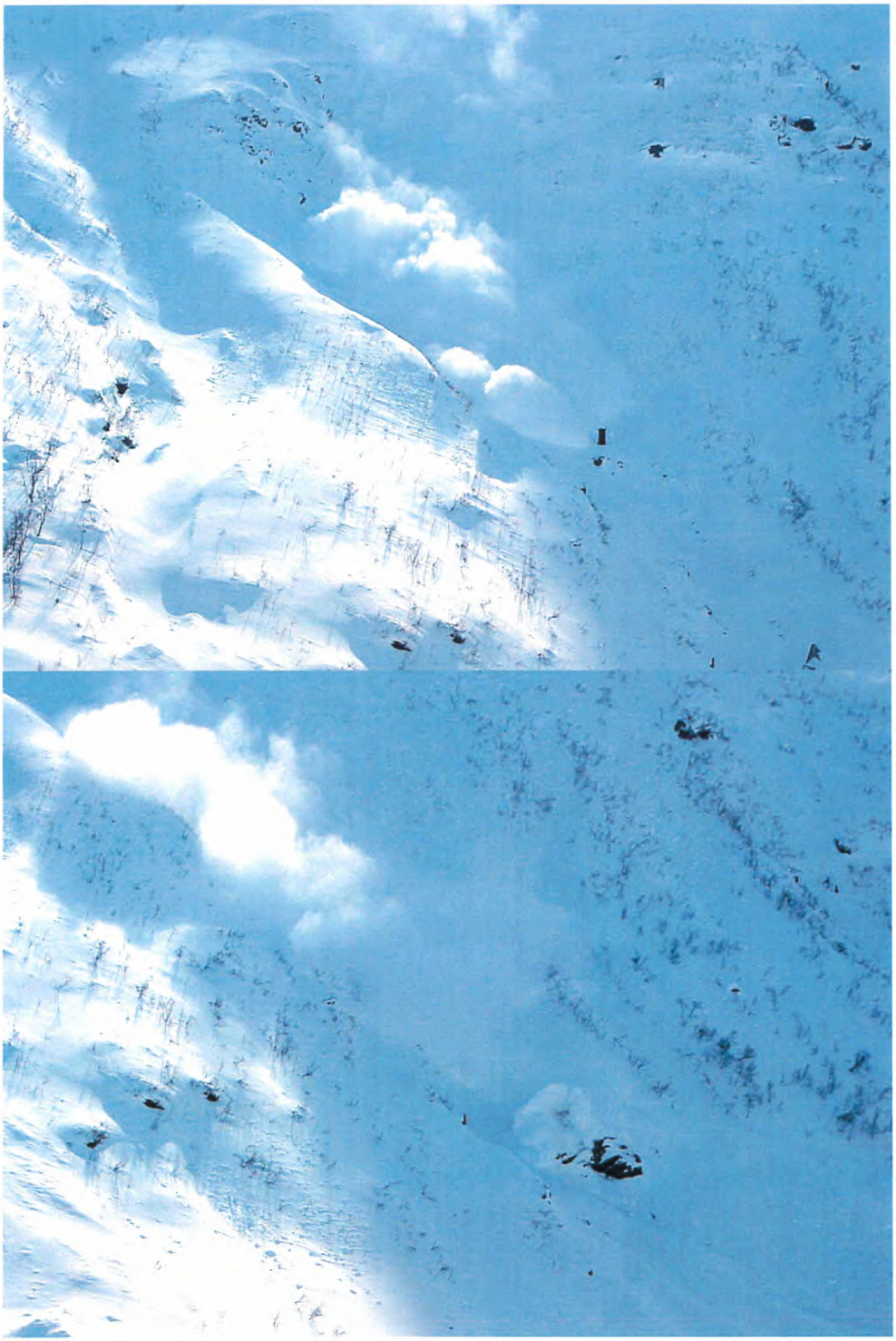

Figure 4.1.11. Impact of the April 6th avalanche on the steel tower (top) and the concrete structure (bottom).

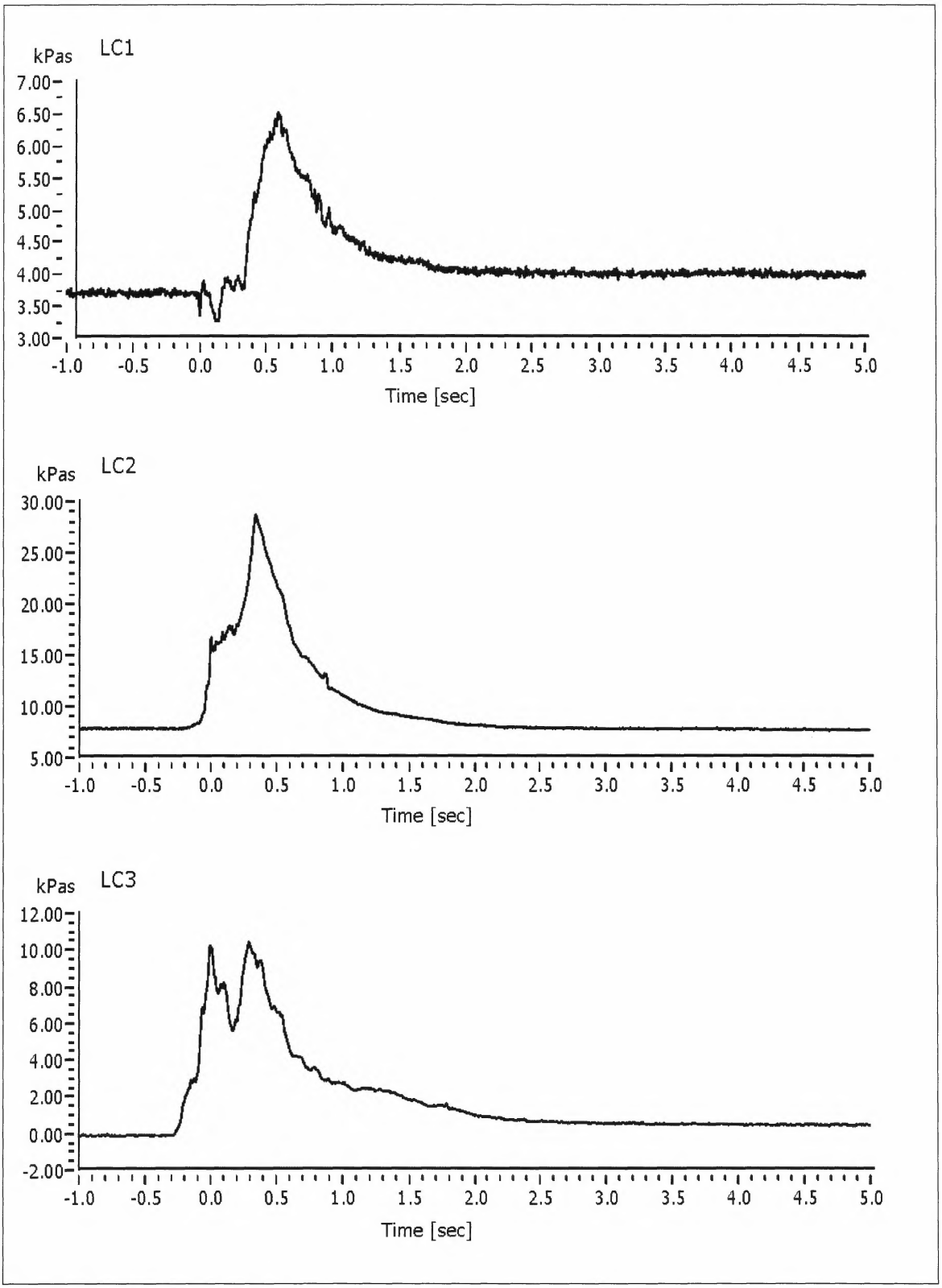

Figure 4.1.12. Load-cell measurements at the concrete structure during the April 6th avalanche.

Task 4.2: Chute experiments – Introduction to the task (SGUL)

(Task leader: Chris Keylock)

A variety of chute measurement campaigns have commenced within the first 12 months of SATSIE. These include:

- Experiments on the overtopping of deflecting dams by granular flows (IMO - University of Bristol);
- Analysis of the velocity profile in flowing snow (ETNA - Col du Lac Blanc);
- Preliminary test experiments on the flow of granular material in experimental chutes (DIIA -Pavia);
- Preliminary experiments using polystyrene particles on steep slopes to simulate the suspension observed in powder snow avalanches.

Of these, only the first three are reported upon in this section. The final set of experiments is coupled to the improvement of powder snow models and is reported in more detail in Work Package 5.

The research undertaken during these measurement campaigns maps onto a set of sub-tasks defined for Task 4.2 following the meeting in Leeds in January:

4.2.1 – Tests of Froude scaling
4.2.2 – Deflecting dam experiments in the Bristol chute
4.2.3 – Catching dam experiments in the 5+5 m Pavia chute
4.2.4 – Deflecting dam experiments in the 6 m Pavia chute
4.2.5 – Erosion/deposition experiments in the Pavia and Col du Lac Blanc chutes
4.2.6 – Chute experiments for analysing flow regimes

Subtask 4.2.1 – Froude Scaling

The Froude number (Fr) is a dimensionless quantity used to determine if a flow is sub- or super-critical. It is defined by

$$\mathrm{Fr} = U / (g\,h)^{1/2} \qquad (4.1)$$

where U is the depth-averaged velocity, g is the gravitational acceleration and h is the flow depth. The purpose of this subtask is to determine whether the flow of snow or granular material exhibits Froude scaling. In other words, does the velocity in different flows with the same Froude number scale with the square root of the flow depth? If this is the case, then it suggests that a drag term proportional to the velocity-squared or the shear rate squared should be included in the rheological model.

Experiments to determine if this scaling exists in flows of snow will be undertaken at Col du Lac Blanc this coming winter. The experiments undertaken at Col du Lac Blanc last winter indicate that a simple model for the velocity profile of a slip velocity plus a constant shear rate may explain the data, unless there is a great deal of shear in the bottom 1 cm of the flow (Fig. 4.2.1). A meta-analysis of different profiles to determine if the bottom measurement is consistently skewed to below the mean line-of-best-fit will help support this simple interpreta-

tion of the data. By performing a greater number of experiments with a variety of flow velocities and flow volumes, the Froude-scaling hypothesis will be tested in flowing snow.

In addition, some evidence for the existence of such a scaling has arisen from experiments with dry granular material undertaken by Kristín Martha Hákonardóttir of the IMO at Bristol University. Her work will also explore this issue in greater detail in the forthcoming year.

Hence, there would appear to be some experimental support for the Froude scaling hypothesis. Ongoing experiments will widen the observed parameter space and increase the robustness of this result. This work will take place this year and will be reported upon more fully next year.

Subtask 4.2.2 – Deflecting dam experiments

The purpose of this task is to improve our understanding of how an avalanche interacts with a variety of designs of defensive structures and the applicability of standard hydraulic theories to avalanche flows in these situations. Figure 4.2.2 shows an experimental test in Bristol where a flow is leaping over a defensive structure. Such experiments are vital for developing models of such flows (Task 5.4).

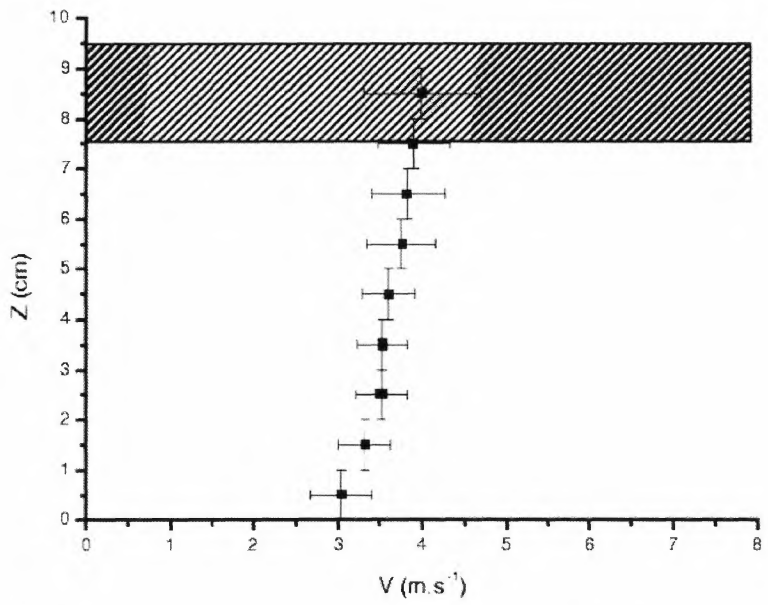

Figure 4.2.1. An example of a velocity profile from the Col du Lac Blanc snow chute obtained during the winter 2002/03.

Figure 4.2.2. An avalanche of granular material leaping over a defensive structure.

One of the main results from this task so far relates to the applicability of hydraulic flow theory to the run-up of avalanches upon deflecting structures, which aim to deflect the avalanche away from the location of interest rather than stopping it in its tracks. An example of such a structure is given by the deflecting wall at Flateyri, Iceland (Fig. 4.2.3). Figure 4.2.4 shows these results. The observed values are in good agreement with theory, suggesting that up to deflecting angles of approximately 30°, hydraulic theory gives good predictions and that these remain reasonable at angles less than 44°. However, because the angle at which an avalanche strikes such a dam may vary with changes in the release position of the avalanche, a factor of safety will be required in dam design to account for the greater observed elevation of the flow at higher angles. An alternative will be to apply more advanced, unsteady flow theories to this data to see if an improved level of agreement can be found. Greater detail on the results of this part of the project is provided in (Hákonardóttir *et al.*, 2003).

Figure 4.2.3. The deflecting wall at Flateyri, Iceland.

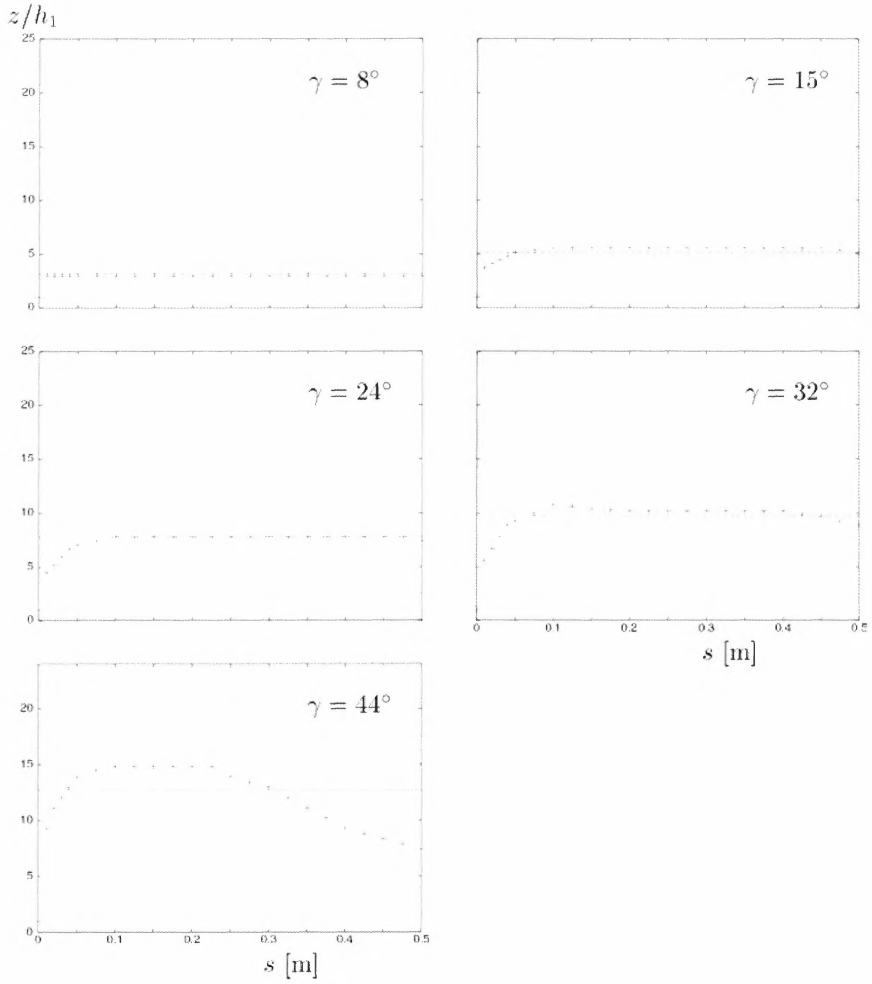

Figure 4.2.4. Run-up profile for a granular flow with an approaching internal Froude number of 12. Each graph is a plot of the observed depth profile along the deflecting dam, non-dimensionalised with the depth of the approaching stream, (z/h) at a fixed deflecting angle, γ. The theoretical non-dimensional shock height is shown as a dashed line. The shock was unsteady for γ > 44°.

Subtasks 4.2.3–4.2.6 Additional experiments in the chutes in Pavia

The first twelve months of the SATSIE project have seen the purchase of cameras and an image acquisition system in Pavia and the development of analysis procedures for the data obtained using this equipment. All subsequent experimental results are predicated upon the successful verification and validation of this data analysis system. Hence, a great deal of effort has been expended in exploring the potential of this system for flows over beds differing in roughness. A typical image is shown in Fig. 4.2.5. By analysing successive pairs of these images it is possible to derive profiles of velocity, granular temperature (velocity fluctuations) and flow concentration. However, with a flow with a velocity of the order of 3 m s^{-1} and a camera speed of 250 Hz, a typical grain will have travelled 12 mm (or three grain diameters using the material shown in Fig. 4.2.5) between images. This introduces error to the velocity and granular temperature estimates, as the particle may have travelled further than the straight line distance between images due to additional collisions. Thus, if possible it would be desirable to reduce this distance between images and perhaps then employ automatic detection algorithms. This possibility is currently being explored.

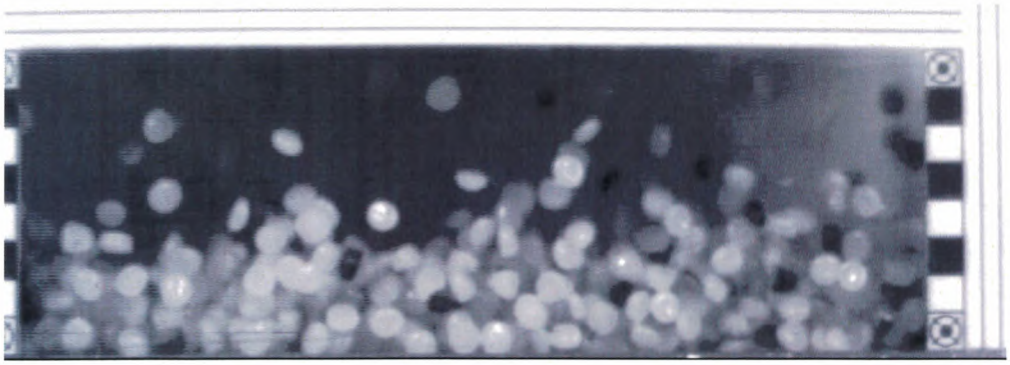

Figure. 4.2.5. A video still taken using the high-speed camera in Pavia. The flow is from right to left. The vertical density gradient in the flow is apparent. By comparing tracking particles between successive stills it is possible to infer velocity and velocity variability (granular temperature) information.

An example of an erosion experiment is provided in Fig. 4.2.6. For the majority of the time the flow passes over a rigid bed. However, within the view shown in the diagram, the flow passes over a bed of particles of similar density and diameter to those in the flow. From images of this flow it is possible to determine erosion rates and study the mechanisms of erosion in order to improve the parameterisation of mass changes in models of snow avalanche dynamics. One additional level of sophistication has been to use a wet material as the erodible substrate. This is in an attempt to simulate the cohesive behaviour of an undisturbed snow cover. One problem that has arisen with the experiments so far has been that effects introduced at the boundary between the erodible and non-erodible substrates have propagated into the image analysis area. When the proper experiments are undertaken this year, a greater size of erodible boundary will be employed in an attempt to counteract this difficulty.

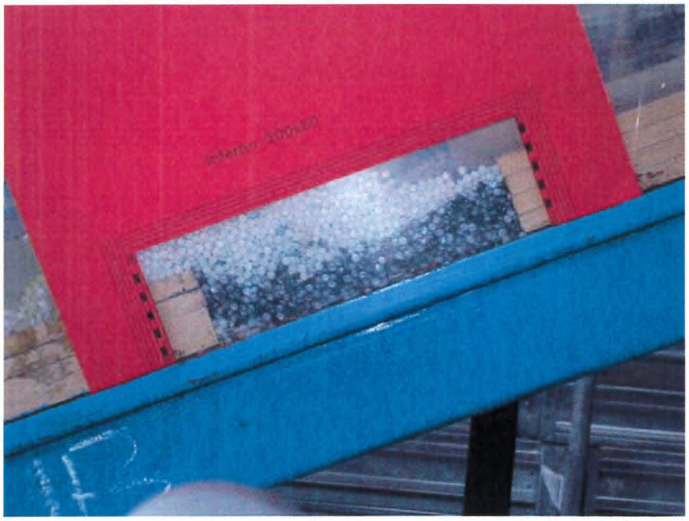

Figure 4.2.6. An image showing an erosion experiment in the Pavia chutes. The white flowing grains have entrained the darker underlying substrate, the surface of which was originally flush with the adjacent chute bed.

Main scientific results obtained in the Work Package

Velocity profiles have been successfully obtained for flowing snow at Col du Lac Blanc.

Granular flow experiments would appear to offer evidence for Froude scaling. Ongoing work will confirm if this is the case for snow and provide more robust results for the case of granular material.

Hydraulic theory would appear to explain the run-up height of granular flows against deflecting dams. However, the error increases with deflection angle and simple theory would seem to be unable to make effective predictions beyond an angle of 44°.

In the first year of the project a new analysis system has been purchased and successfully tested for the Pavia chutes. This will be employed in various experiments in the forthcoming year.

The laboratory experiments in chutes of various sizes with both dry granular materials and snow serve to study the flow dynamics under controlled conditions, systematically varying the key flow parameters.

Subtask 4.2.6 – Snow chute, Col du Lac Blanc (ETNA)

(Subtask responsible: Mohamed Naaim)

All the results presented below were obtained during the winter of 2002–2003 with flows of small rounded snow grains with various bulk densities. Only the velocity profile measurements are presented here. The velocity measurements are based on the system described in the chapter on Work Package 3.

One sample of the obtained velocity profiles is presented in Fig. 4.2.1, where the horizontal error bars are the standard deviation of the velocity distribution for each sensor during the flow and the vertical ones are the sensors' height. One notices that the velocity of the lowest sensor is non-zero. This either means that there is a highly sheared thin layer at the bottom. (the sensor is 1 cm high and is placed at the bottom of the channel, therefore the shear rate $\partial u/\partial z$ would at least be greater than $u/h \approx 500\ s^{-1}$) or that the snow slips on the bottom covered by sandpaper.

Since the vertical resolution of our sensors is limited to 1 cm, we chose to describe this situation by means of a slip condition. Above this slip, the velocity increases slightly but regularly, with an almost uniform and low shear rate. Since both these characteristics were observed for all the undertaken experiments (10 flows), we preliminarily fitted each profile with the linear function

$$u(z) = u_s + \dot{\gamma} z \,. \tag{4.2}$$

Each profile is thus described by two parameters, namely a slip velocity u_s and a uniform shear rate $\dot{\gamma}$.

Figure 4.2.7. Flow channel of the snow chute at Col du Lac Blanc.

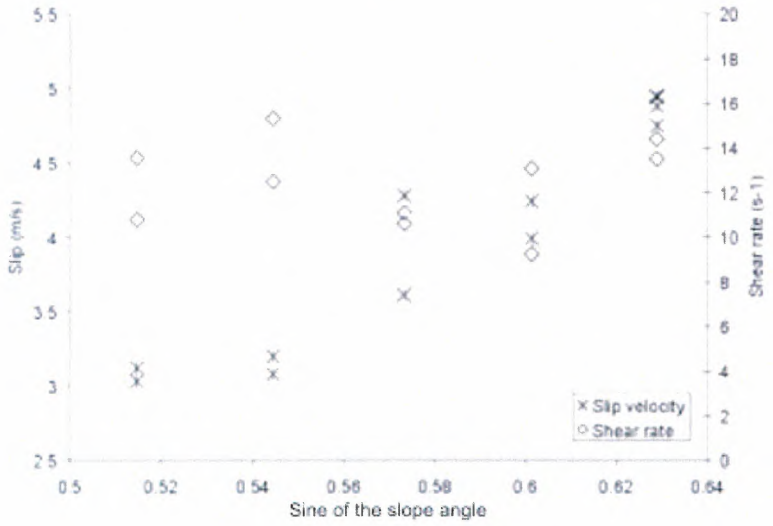

Figure 4.2.8. Col du Lac Blanc chute experiments of 2002–2003: slip velocities and shear rates as functions of the sine of the slope angle.

The characteristics (slope, height and density) of the flows and the results obtained are summarised in Fig. 4.2.8. The different shear rates $\dot{\gamma}$ obtained are all in the range 9–16 s^{-1} and no specific dependence on the slope, height or density can be observed in the range investigated. The slip velocity u regularly increases with the slope angle from 3 to 5 m s^{-1}.

Subtasks 4.2.5 and 4.2.6 – Granular flow chutes, Pavia (DIIA)

(Participants: Massimiliano Barbolini, Matteo Pagliardi, Luigi Natale)

A series of experiments with granular material have been carried out at the laboratory chutes of the Hydraulic and Environmental Engineering Department of the University of Pavia (Italy), which are described in the chapter on Work Package 3. The objective of these experi-

ments was to investigate internal properties of fast-moving granular flows such as the velocity, granular temperature and concentration profiles using high-speed camera recordings. An extensive report on the experiments carried out so far is found in the Appendix (Barbolini and Pagliardi, 2003). Therefore, only the most salient results are summarised here in two sections: (i) flow over a smooth bed; (ii) flow over a rough bed. Exploratory experiments dedicated to the study of erosive flow have also been carried out, but no firm results can be reported yet; for their description, see (Barbolini and Pagliardi, 2003).

Flow over smooth surface (metallic bed)

Froude number

The experiments were designed so that the granular flow would have a Froude number of the same order of magnitude as for a natural snow avalanche (i.e. 5 to 10). The Froude number is defined in terms of flow velocity (u) flow depth (h) and gravitational acceleration (g) as follows:

$$\mathrm{Fr} = \frac{u}{\sqrt{gh}} \,. \tag{4.3}$$

It represents the square root of the ratio of kinetic energy of the current to the potential energy of the flow. The Froude number of the experiments with smooth bed was approximately in the range $\mathrm{Fr} \cong 5 \div 7$ (depending on the part of the flow considered).

Front celerity

We made two frontal video recordings of the whole chute in two experiments, in order to measure the front celerity. The two experiments show good reproducibility. After an initial acceleration phase, about 2.5 m downstream of the opening gate (or 0.8 s from the initiation of the flow), the front attains a constant speed, approximately equal to 3.75 m/s. Therefore, at the observation reach, 4.5 m down the top of the chute (Fig. 4.2.6), the flow has already attained its terminal velocity.

Flow features

The movies show that (at least) two different flow regimes with distinct characteristics in terms of velocity, depth and concentration in the same flow coexist, at a given fixed location on the chute. In particular, at the front the particles have a large mean free path and undergo relatively few collisions. The flow shows a saltating behaviour over all its depth and the interface between the moving material and the surrounding air is not easily recognisable (Fig. 4.2.9, top image). This zone of the flow extends over about 0.5 m. After that, the flow exhibits a progressive transition (over about 0.5 m) to a regime where the material is packed more densely, the mean free path is reduced and the number of collisions increased. This zone, which we call the body (Fig. 4.2.9, bottom image), comprises the largest part of the flow length (1.5–2 m) and shows steady flow conditions. Above the body, few saltating particles are observed, and the interface between the moving material and the surrounding air can be easily recognised. Approximately one second after the arrival of the front, the body is followed by the tail showing progressively diminishing flow depth and velocity.

We made measurements of velocity and concentration in the front and the body, because they are the ones we thought more representative and practically relevant. The measurements were taken in a temporal lapse of 0.042 seconds, equivalent to ten frames.

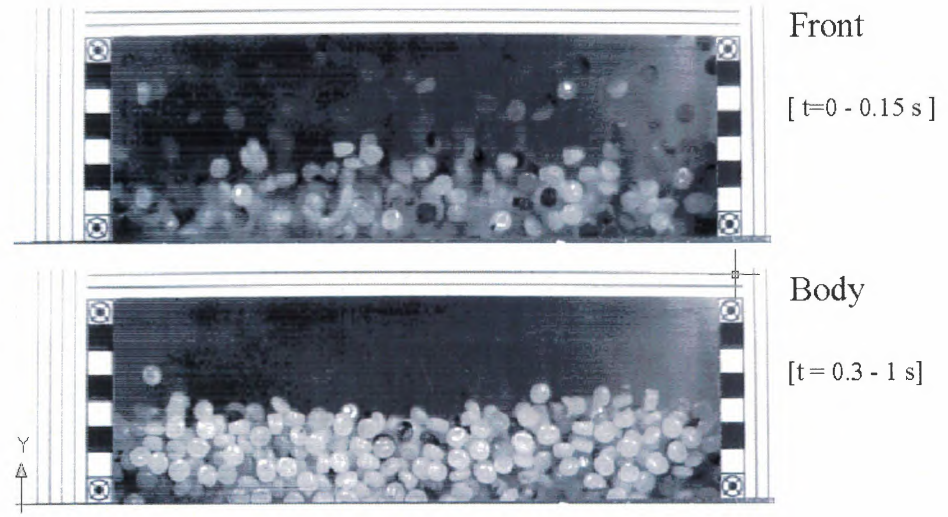

Figure 4.2.9. Distinct phases of motion in the granular flows at the Pavia chute: Dilute front with strong vertical concentration gradient, tentatively associated with the grain-inertia flow regime (top), and dense flow in the body with less pronounced density gradient and a sharp upper boundary (bottom).

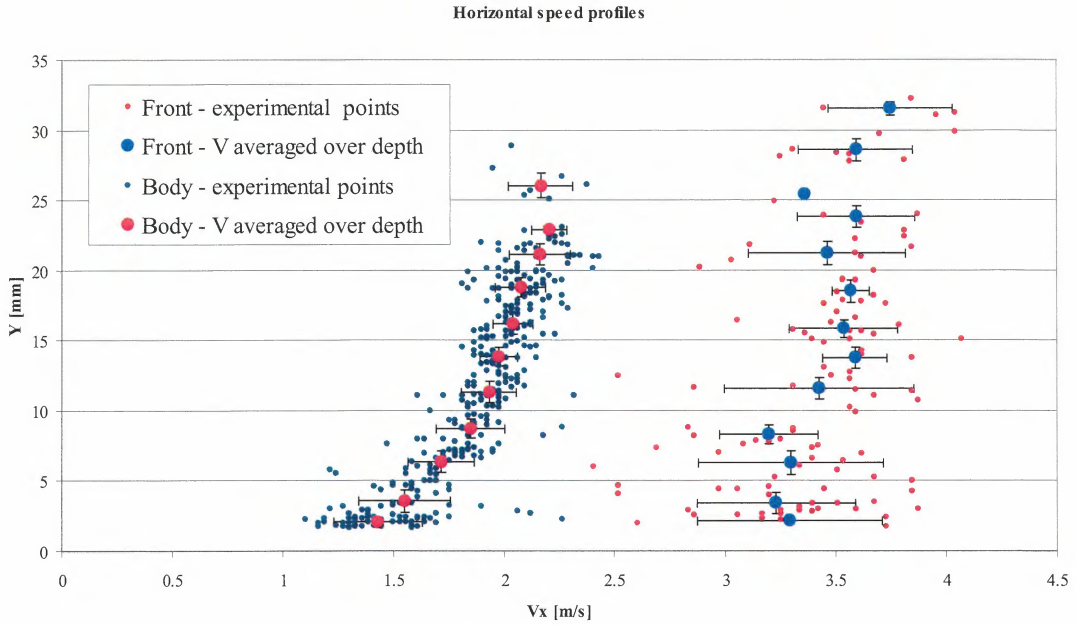

Figure 4.2.10. Velocity profiles obtained in dry granular flows over a smooth bed at the Pavia chute. Note that the profile in the body is clearly curved, in contrast to the velocity profiles obtained at the Col du Lac Blanc snow chute (Fig. 4.2.1).

Velocity profiles

Following the methods described by Barbolini and Pagliardi (2003), we have determined the velocity profiles separately for the front and the body of the flow. The results are displayed in Fig. 4.2.10. For both the two flow phases a slip velocity at the bottom of the flow was obtained, approximately 1.5 m/s for the body and 3.25 m/s for the front. Maximum velocity is reached at the flow surface in both cases, and is about 2.25 m/s and 3.5 m/s, respectively. The body shows a velocity profile that can be fitted fairly well by a second-order polynomial, with a shear rate that is decreasing from the bottom to the top of the flow; conversely, in the front the velocity is more or less constant over all the flow depth. The error bars in Fig. 4.2.10 rep-

resent the standard deviation in the velocity distribution; they should be considered more as a scattering of the measured values rather than a true error. It is interesting to notice that standard deviation is higher at the front, where the particle velocities seem to be more randomly distributed; an explanation of that comes out from the granular temperature theory.

Figure 4.2.11 compares our experimental velocity profile, obtained with dry granular material, to velocity profiles measured in experiments with snow at different scale: (i) chute scale (Bouchet *et al.*, 2003); (ii) small avalanches (Dent *et al.*, 1998); (iii) full-scale avalanche (Gubler *et al.*, 1986). For the sake of comparison, the different velocity profiles are scaled by their maximum flow depth and maximum velocity. The agreement appears quite intriguing: The profile shapes are quite similar, and even the apparent slip velocities are between 60% and 80% of the surface velocity except for one of the measurements in the snow chute. This may be seen as an indication that these flows all operated in a regime in which the material properties (density, shape, size and restitution coefficient) of the grains play a secondary role. More data and a deeper theoretical analysis is needed to corroborate this preliminary result, to determine the limits of its applicability, and to fully appreciate its dynamical significance.

Profiles of granular temperature and concentration

Particle counting and tracking also allows top evaluate the profiles of the so-called granular temperature (a measure of the velocity fluctuations in the flow) and the particle concentration. Everywhere in the head of the flow and above the body, the volumetric concentration is at most 0.15, and significantly less in most of the volume. This supports the notion of a saltation layer in the so-called grain-inertia regime or in the transition between the latter and the collisional regime. Even in the densest areas of the body, the concentration does not exceed 0.3 and is thus well below the value of about 0.5 considered to be the threshold for transition from a collisional regime to a frictional regime. More details can be found in (Barbolini and Pagliardi, 2003).

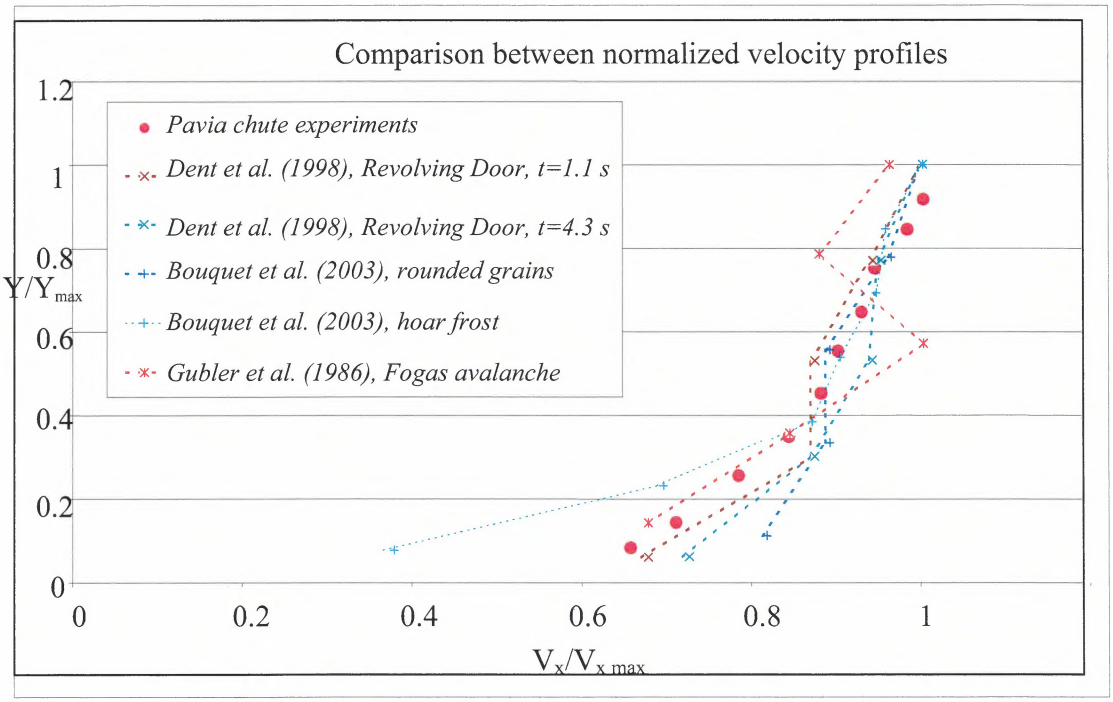

Figure 4.2.11. Comparison between normalised velocity profiles, obtained in experiments at different scales and using different materials.

Flow over rough surfaces

The experiment described above was repeated over a bed covered with no. 60 sand paper. In this case, steady flow conditions are not reached at the measurement point. In order to trace the velocity profiles, we selected six short intervals during which we measured the velocity profiles. As shown in Fig. 4.2.14, the speed and the speed profile continuously change while the flow passes the observation window. The boundary condition at the bottom of the flow changes from pronounced slip at the front (profile no. 1) to reduced slip and finally no-slip (profiles no. 2– 4); then deposition of granular material begins (profiles no. 5 and 6) at a rate of. 2–3 cm/s. It is interesting to observe that as the flow changes from slip to no-slip conditions (profiles no. 2 and 3), the shape of the velocity profile in the lower part also changes from concave to convex.

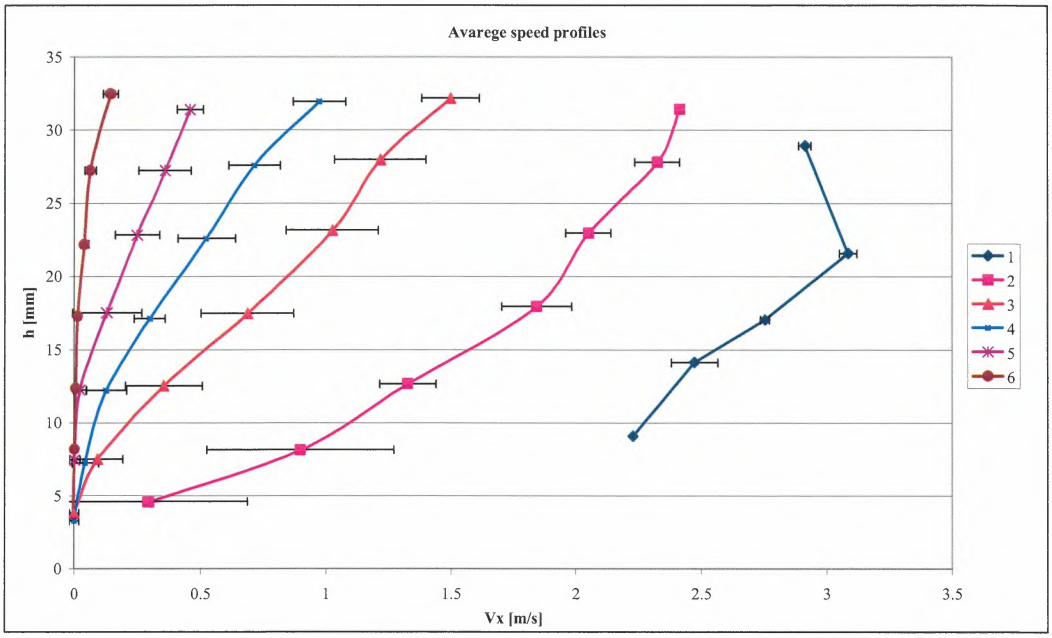

Figure 4.2.12. Pavia chute: average speed profiles for granular flow in the over a rough surface at 0.0, 0.10, 0.31, 0.52, 0.73 and 1.04 s after front arrival (measurement duration 40 ms).

We have determined the granular-temperature and concentration profiles in the same way as for the smooth-bed case and during the same six intervals as the velocity profiles shown in Fig. 4.2.12. As the flow passes from slip to no-slip boundary conditions, the concentration increases and soon exceeds 0.5, the approximate threshold for transition from the collisional to the frictional flow regime. Where deposition has occurred, the volumetric concentration is close to the one of maximum packing.

Outlook

The experiments carried out at Pavia chutes in the first year of SATSIE project gave promising results, and the technique based on high-speed recordings seems to be able to properly investigate crucial flow properties such as velocity, concentration and granular temperature profiles, as well as to better understand the processes occurring in rapid granular flows. During the next year, these experiments will be continued, varying the chute slope and the type of granular material. Furthermore, similar experiments on the longer chute will be started, using two reaches with different inclinations, in order to study also flow regime transition processes. The experiments on erosive flows will be intensively continued in the second year of SATSIE.

Studies of deflection and catching dams in granular and shallow water flows at the Bristol chute and flume (IMOR)

(Participants: Kristín Martha Hákonardóttir, Andrew Hogg, Tómas Jóhannesson)

Objectives

The experiments at the chute and flume in Bristol were designed to study the deflection of high Froude number, granular flow at a dam and to compare the flow behaviour in the interaction with the dam with the point mass theory and the shallow fluid flow theory. More precisely, the aim of the experiments was to firstly quantify the necessary height of the dam, for a given deflecting angle, to fully deflect the flow, and secondly to look at the flow behaviour if some of the flow escaped over the dam. As a limiting case, catching dams (i.e., dams positioned perpendicular to the flow) were also investigated.

In the first series of experiments with granular flows of short duration, shallow-fluid flow theory was found to be by far superior to the point-mass theory in describing the experimental results. In order to determine whether the observed deviations of the theoretical predictions were due to the granular nature or short duration of the flow, or to a more fundamental shortcoming of the theory, quasi-steady (long-duration) granular flows were compared to water flows with matching characteristic properties.

Experimental set-up

In the granular flows, glass ballotini particles of mean size 90 μm, density 2500 kg/m^3 (bulk density of 1600 kg/m^3) and approximately spherical shape were used. The flow depth was measured using an infrared optical depth sensor (ODS96), yielding time series of the depth and the flow speed. The interaction between the flow and the deflecting dams was recorded from above and from one side by video and subsequently analysed. The run-out length and distribution of the deposited particles were also measured.

In each experiment with short-duration flows, 6 kg of particles were released from the top of the chute by rapidly opening a lock gate. The experiments were designed so that the granular current had an internal Froude number of order 10.

The same setup and the same particles as in the "short" granular experiments were used in the "long" experiments, but with the channel above the dam narrowed by 10 cm, down to 22.5 cm and the particles released from a hopper. The experiments were conducted at Froude numbers 5, 12 and 14 and with dams inclined at $\gamma = 8°$, 15°, 24°, 32° and 44°. Each experiment was filmed from the side and from above. The speed was also measured inside the shock, along the deflecting dam, for $\gamma = 24°$, by tracking tracer particles. The effect of tilting the sidewalls of the dams was examined for $Fr_1 = 12$ and 14, $\gamma = 24°$ and $\alpha = 90°$, 75 °, 60° and 45°, where α is the angle between the upstream face of the dam and the slope.

Catching dam experiments were conducted for $Fr_1 = 13$. The dams had an upstream face perpendicular to the experimental chute. The height of the dams was systematically lowered and the speed of the bore travelling upstream was measured along with the depth of the flow over the dam, when overflow occurred. The aim of the experiments was to determine the height at which a bore could no longer be maintained upstream of the dam and the flow jumped over the dam in a supercritical state.

The experiments with water involved a steady stream of supercritical water flow down a 20 cm wide channel. The channel inclinations of 3°, 6° and 9° to the horizontal corresponded to

three different Froude numbers. The depth profile and deflecting angles were photographed with a digital camera through the side of the dam and from above (Fig. 4.2.14).

Results

Short duration granular flow experiments

The head of the flow was about 50 cm long, 4 cm thick and had a speed of (3.7 ± 0.8) m s^{-1}. It was very dilute and turbulent, with eddies shooting upwards. The flow immediately following was much denser with a constant depth of (0.9 ± 0.1) cm and speed of (3.5 ± 0.1) m s^{-1} (Froude number Fr_1 = 13). It was maintained for 0.6 s, or roughly 2.1 m. The flow became rapidly thinner and slower after that.

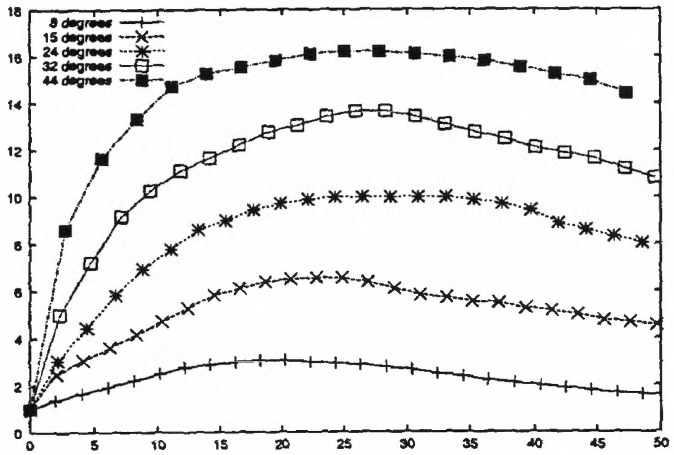

Figure 4.2.13. The run-up on the deflecting dams during the steady flow phase of short granular flows, non-dimensionalised with the thickness of the incoming stream H/h_1 and plotted as a function of the length along the dam, s (cm), for the different deflecting angles. The uncertainty in the non-dimensional run-up is estimated as ±1.

The dilute first front shot passed the deflecting dam, with the denser part immediately following and forming a semi-steady and higher profile an the dam for the smaller deflecting angles. At larger deflecting angles, the first front splashed higher up on the dam than the denser bulk of the flow.

Figure 4.2.13 shows how the maximum run-up of the granular avalanches on the deflecting dams grows with increasing deflecting angle for a fixed Froude number. The maximum run-up occurred during the semi-steady flow state and had a certain width, increasing along the dam and finally forming the airborne jet at the end of the dam.

When the deflecting dam is not high enough to fully deflect the flow, a part of the flow jumps over the dam. For low dams, the current shoots over the dam in the direction of the approaching stream. The jets are turned in the direction of the deflecting dam and the deflection of the jet approaches the deflecting angle of the dam as the dam height approaches

Steady granular flow experiments

As the front of the steady stream hits the deflecting dam, a stationary oblique shock was formed within a fraction of a second of the initial impact. The run-up profiles along the dams are plotted in Fig. 21 for the flows with three different Froude numbers. The oblique shocks were stationary for all but the largest deflecting angles, where the flow slowed down signifi-

cantly along the dam and started to pile up in front of it. This was observed for $Fr_1 = 5$ with $\gamma = 32°$ and 44° and also for $Fr_1 = 12$ and 14 with $\gamma = 44°$.

If the unsteady profiles are not considered, the run-up profiles along the dams are linear with either a constant or increasing depth along the dams (Fig. 4.2.1.4). The profiles follow the same trend as previously observed for the water and short granular flows; larger Froude numbers and deflecting angles leading to higher profiles.

Tilting the sidewalls of the dams between 45° and 90° did not affect the shock formation. The shock angle and the height (i.e. the vertical run-up) remained the same as for a vertical deflecting dam (normal to the experimental chute, $\alpha = 90°$).

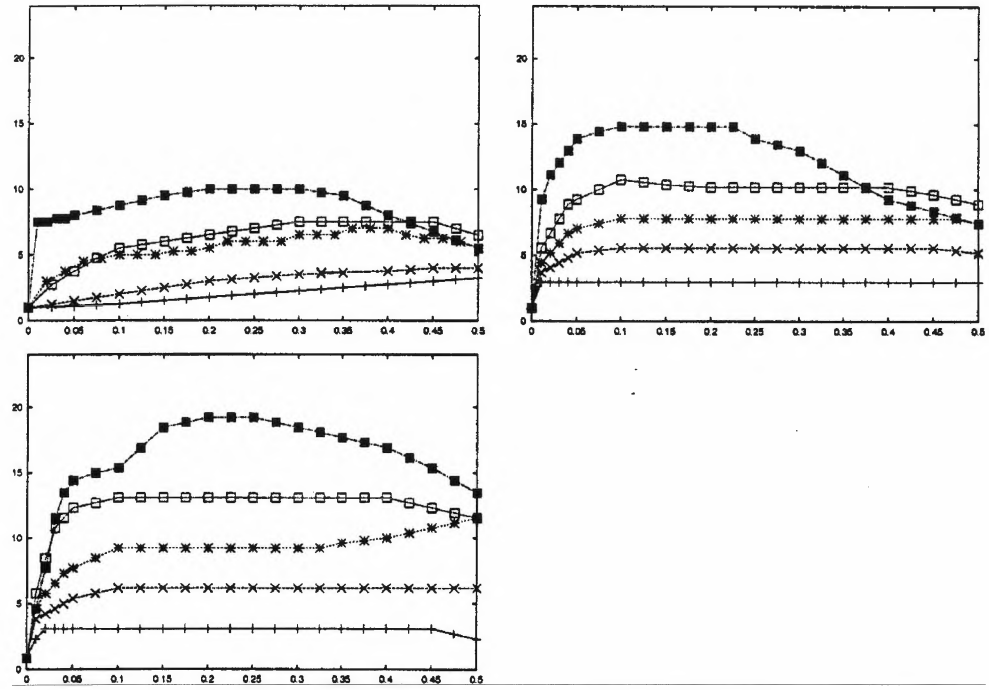

Figure 4.2.14. Non-dimensional run-up profiles, H/h_1, along the deflecting dams for steady, granular flow at three different Froude numbers, $Fr_1 = 5, 12, 14$. Each curve shows the steady shock height for a fixed deflecting angle, the different curves belonging to deflecting angles; of 8°, 15°, 24°, 32° and 44°. The shallowest profile in each graph corresponds to the 8° deflection and the deepest to the 44° deflection.

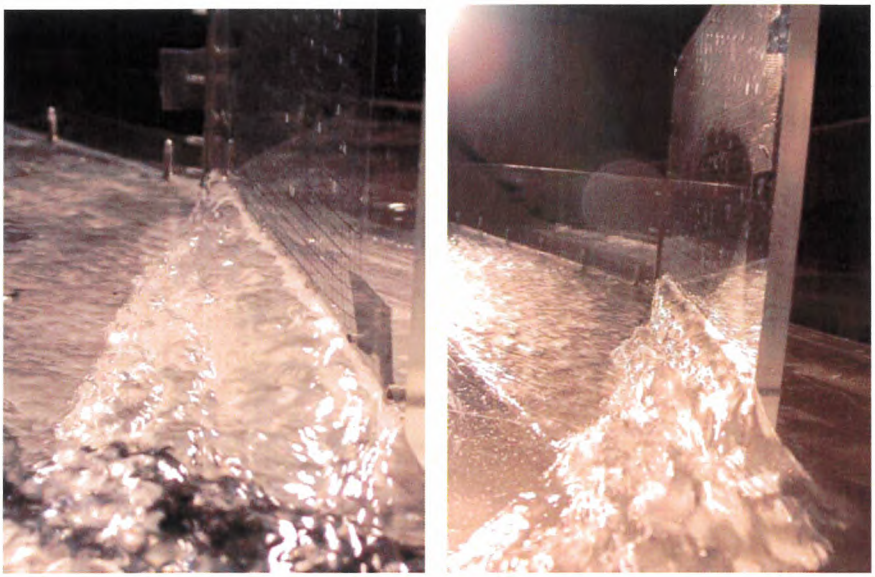

Figure 4.2.15. Photographs of the stationary, oblique shock of supercritical shallow water at $Fr_1 = 4.5$, $\gamma = 20°$ and $Fr_1 = 7$, $\gamma = 40°$, looking up into the stream along the deflecting dam. On the photograph to the right ($Fr_1 = 7$), it can be observed that the flow runs higher up on the deflecting dam at the start of the dam and then falls back on itself while the shock widens and becomes thinner

Steady water flow experiments

The run-up profiles along the dams are plotted in Figure 4.2.16. They are characterised by nearly straight lines, for $\gamma < 30°$. In all of the profiles, there was a zone at the beginning of the dam with higher run-up and overturning of the flow. The flow ran up, reached a maximum height and fell back upon the oncoming stream, much like the flow past the bow of a ship. This was more obvious for the larger deflecting angles where the largest values of the depth ratio h_2/h_1 were observed. The profile along the dam was approximately straight from the point where the flow flipped over and hit the oncoming stream for the larger deflecting angles, $\gamma > 30°$.

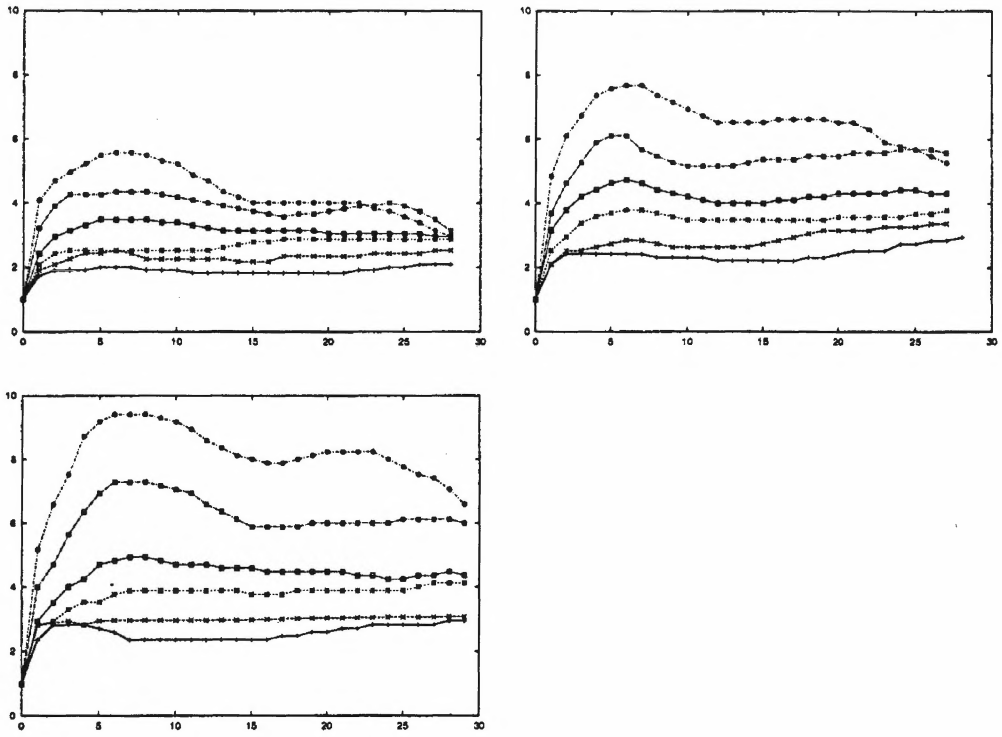

Figure 4.2.16. Non-dimensional run-up profiles along the deflecting dams of steady water flows at different Froude numbers. Each curve shows the steady shock height at a fixed deflecting angle (γ = 5, 10, 15, 20, 30 and 40°) for each Froude number. The shallowest profile on each graph corresponds to the 5° deflection and the deepest to the 40° deflection. The dams cover different proportions $l/L < 1$ of the flow path

WP 5 Model development (IMOR)

The goal of the model development work package is to improve the physical basis of currently operational snow avalanche models. Current avalanche models will be compared and tested against the results of chute experiments and field observations obtained within SATSIE and the results used to develop improved models.

Task 5.1 – Flow Regimes (ETNA)

(Task leader: Mohamed Naaim)

The snow-avalanche models currently in use are based on very simple rheological assumptions whereas a large variety of flow regimes are known to be possible in avalanching snow. The avalanche may go through a sequence of flow regimes along its downhill path, but also several flow regimes may occur simultaneously at different locations in the avalanche. There is evidence that the bottom friction experienced by the flow depends strongly on the flow regime. Conversely, the flow regime is determined by the dynamics of the flow. For this reason, it appears necessary to base a dynamical avalanche model with high predictive power on rheological assumptions that can give rise to the many observed flow regimes and also allow for transitions between them.

Characterisation of flow regimes in snow avalanches and the need for models with complex rheology

The most conspicuous appearance of different flow regimes is in mixed avalanches where the dense core (believed to be in a combined frictional and inertial regime) is shrouded in a dilute suspension of small snow grains (classifiable as the macro-viscous regime in turbulent flow). Between the two, the existence of a layer of intermediate density, consisting of particles in a wide range of diameters, has been firmly established through experiments spanning over two decades. This so-called saltation or resuspension layer may be identified with the inertial flow regime of granular flows.

Within the dense core itself, diverse flow regimes may also occur. Just after release and probably again under certain conditions in the stopping phase, the avalanche body appears to move as a flexible slab, exhibiting features of a visco-plastic material or of a granular material in the quasi-static (frictional) regime. The majority of the few velocity profiles obtained inside flowing snow show a plug-like layer overriding a relatively thin, strongly sheared layer at the bottom. However, experiments at ETNA's snow chute at Col du Lac Blanc (see WP 4) produced velocity profiles that are linear within experimental accuracy, with a significant slip velocity at the bottom.

So far, the very large density differences between the dense flow, saltation layer and suspension layer have led modellers to describe them through multi-layer models with dynamical mass and momentum exchange embodied in the interface conditions. Members of the SATSIE collaboration have extensive experience with three-layer models coupling the suspension layer either to the dense core or to the saltation layer and including the snow cover at rest to describe erosion and deposition processes. The next step, supported by the findings of a model comparison summarised below under Task 5.4, is to extend the system to four layers; this should allow a more realistic prediction of the pressure and deposit distribution in the run-out zone.

Flow-regime transitions within the dense flow itself should also be reproduced by models. The traditional approach of combining dry-friction and "turbulent", i.e., velocity-dependent, drag has been applied over several decades. It has been found to be plagued by a very wide variation of derived model parameters, which cannot be systematised in a satisfactory way. Some of this variability is probably attributable to snow entrainment—an important process neglected by most models, see Task 5.2. Nevertheless, real avalanches definitely show a much richer spectrum of behaviour than captured by the current two-parameter models.

There are several promising approaches towards a more physical rheological basis for dense avalanches. A theoretically satisfying procedure would be to treat the avalanche as an assembly of more or less elastic particles of different sizes, to simulate their interactions under some idealised but relevant flow conditions and to derive constitutive relations from the statistics of their interactions. Unfortunately, such a task cannot be tackled in the course of a short-term project like SATSIE.

Instead, laboratory experiments on granular flows with snow or substitute materials may be used to derive phenomenological friction laws that can subsequently be incorporated in continuum models. In a separate line of research, the fundamental mechanisms responsible for the observed behaviour may be investigated for better understanding of the phenomenon. This approach has been pursued at ETNA, using the experiments pioneered by Pouliquen and coworkers (Pouliquen, 1999; Pouliquen and Forterre, 2002). An outcome of this work is the model N2L, to be described below.

An alternative approach is to select, from the wide spectrum of constitutive relations developed in diverse fields, a rheological model that encompasses all types of behaviour thought to occur in avalanches and to be of practical relevance. The NIS model has been developed in this spirit and used with success in consulting by NGI for 15 years. It is based on the Criminale–Ericksen–Filbey (CEF) rheology that combines visco-plastic and granular behaviour. However, the present implementation of the model uses a much simplified rheological formulation and so foregoes much of its potential richness. Below, we discuss ways of implementing the CEF rheology in a more complete way without sacrificing the robustness and practical usability of the model as a tool in hazard mapping.

Recent granular-flow experiments and the N2L model

Flowing laws for different flow regimes have been analysed at ETNA by a combination of experimental and theoretical work. The results of this work have been implemented in a new version of the dynamical model N2L which includes entrainment and deposition of snow during the flow of the avalanche. The first experimental activities focused on the scaling law connecting the mean velocity, the flow height and the slope angle in steady uniform granular flow. Snow avalanches are generally regarded as granular materials where the ratio between the flow height and the diameter of snow grains is high. The flowing material can, therefore, be considered as a continuous medium to some approximation. The formalism of shallow fluid dynamics is furthermore adopted in N2L. The integrals of the dissipation terms are represented by an effective friction coefficient (depending of the material and flow parameters) applied at the bottom of the flow. The previous studies undertaken by Pouliquen (1999) and dealing with dry granular materials, reveal the existence of a simple linear scaling law between the Froude number and the ratio between the flow height and $h_{stop}(\theta)$, the height below which the flow stops on a given slope θ. This law is valid for low Froude numbers and dry materials. The objective of the experiments that were undertaken was to determine the limits and the possible extrapolation of this scaling law to rapid flows with high Froude numbers,

typical for natural snow avalanches, and to cohesive materials. For this purpose, a new experimental device was set-up allowing for steady uniform flows of dry and wet granular materials with a wide range of Froude numbers and cohesion.

For dry granular materials, the experiments confirmed the existence of the Pouliquen regime at low Froude numbers, $Fr \leq 2.5$. For higher Froude numbers, they showed the existence of a transition and a new regime where the Froude number tends towards an asymptotic value as the flow velocity and flow height increase. For cohesive granular materials (wet sand), the Pouliquen regime becomes unstable, and the proportionality coefficient between the Froude number and the ratio between the flow height and $h_{stop}(\theta)$, increases significantly with the cohesion. The transition and the new regime appear at approximately the same conditions as for the dry material. The asymptotic value of the Froude numer is, furthermore, roughly the same. These experiments will be continued and expanded in order to confirm these first results and explain the origin of and the conditions for the transition between the Pouliquen and constant Froude number regimes. The results of these future experiments will be used as the basis for further improvements of the N2L avalanche model.

The Criminale–Ericksen–Filbey rheology as a candidate rheological basis for a comprehensive avalanche model

A preliminary study was conducted to assess the potential of the Criminale–Ericksen–Filbey (CEF) rheology for use in an advanced model of avalanche motion that is able to describe diverse flow regimes and transitions between them. The CEF rheology encompasses Newtonian fluids, perfectly plastic materials, yielding materials of the Herschel-Bulkley type, and granular materials with Mohr-Coulomb yield criterion and dispersive pressure under shear as special cases. The Norem-Irgens-Schieldrop (NIS) model, which is successfully used in consulting at NGI, is based on the CEF constitutive equations, but fully implements only few of its attractive properties.

An interesting finding of this study is that a range of values of the dry-friction and viscoelasticity parameters leads to a decreasing effective friction coefficient with increasing shear rate, up to the point where the entire overburden is supported, not by enduring particle–particle contacts, but by the collisional dispersive pressure. Beyond this point, the friction grows again with the square of the shear rate. In this way, a so-called fast-stop mechanism (which has often been conjectured to operate in avalanches) can be implemented in a natural way. Support for such a choice of parameter values comes from recent investigations of granular flows over frictional surfaces. These questions deserve further study.

It was found that the density of an avalanche should be allowed to vary in response to the slope-normal dispersive pressure once the latter is large enough to support the overburden at high shear rates. This density reduction will limit the growth of the shear stress in accordance with measurements on granular materials, where it was found to remain nearly constant if the flow could expand in the normal direction. Further study is needed to understand whether this effect can be used to model the formation of a saltation layer if the flow of the pore and ambient air is suitably included.

A new numerical implementation of the NIS model is needed if potentially important effects such as the formation of a plug layer above the shear layer due to cohesion are to be captured and spurious mass change due to numerical artefacts is to be avoided. Among the possible ways of determining the shear-layer depth dynamically, the approach chosen in BING (a visco-plastic model originally developed for sub-aqueous debris flows) appears most attrac-

tive: Separate conservation equations are solved for the shear and plug-layer momentum. By adjusting the shear-layer depth, total flow height and plug velocity of a parabolic/constant velocity profile, momentum and mass conservation may be fulfilled. It is planned to programme a flexible and numerically stable, shock-capturing code on this basis during the second year of SATSIE and to perform extensive tests and comparisons with N2L.

Task 5.2 – Snow entrainment and mass balance (DIIA)

(Task leader: Massimiliano Barbolini)

Snow entrainment and deposition and the associated changes in the mass balance of an avalanche as is moves down the path have long been a neglected aspect of snow avalanche dynamics and numerical modelling of snow avalanches. Previous research in this field and available observations from natural scale avalanches are summarised in a report by Barbolini *et al.* (2003) about the state of the art in modelling of erosion and deposition processes, a draft of which is reproduced in Annex 2. This report, which is written as a part of SATSIE, includes a review by Margareta Eglit, Moscow State University, about Russian research in this field. Her work has been financed by a NATO fellowship, linked to but independent of SATSIE.

Overview of past experimental and theoretical research on snow entrainment in avalanche dynamics

Until recently, no data derived from direct and indirect observations of erosion and deposition have been available to guide the development of entrainment relations for use in practically usable models. Recent experiments (mainly at the Swiss test site at Vallée de la Sionne) have now yielded data on the temporal evolution of the entrainment rate at up to three different locations (upper track, lower track, upper run-out zone), combined with data on the flow height and qualitative indications of the density or particle size. From radar and video measurements, some data on the front or internal flow velocity are also available. Impact-pressure measurements near the lowermost radar location have provided insight into the structure of the measured avalanches. At the Italian test site Monte Pizzac, deposits of several avalanches were studied by means of series of cross-sectional snow pits. Careful distinction between different layers allowed reconstruction of the mass evolution of these avalanches along their path and showed that entrainment can increase the mass of avalanches by almost an order of magnitude over the release mass. It is now considered likely that the majority of medium to large avalanches could double or even triple their mass from release to run-out (Issler *et al.*, 1996); in the track, the moving mass may be more than five time the original mass (Sovilla *et al.,* 2001).

Theoretical investigation of possible mechanisms of snow erosion

The data recently obtained on snow entrainment in avalanches makes it worthwhile to investigate some candidate mechanisms in more detail and to try to obtain rough estimates of their potential contribution. A first step in this direction is made in the paper (Gauer and Issler, 2004) reproduced in the Annex.

A brief review of research on processes similar to snow erosion in fluvial hydraulics and wear and fracture mechanics suggests that direct particle-particle interactions during impacts or sliding are more important in snow avalanches than fluid-particle interactions (aerodynamic entrainment). Snow erosion and entrainment processes in avalanches are classified according to their mechanisms, the flow regimes in which they occur, and their spatial position within the avalanche. Simple, but process-specific models are proposed for erosion by impacts, ab-

rasion, ploughing, and blasting. On the basis of order-of-magnitude estimates, the first three mechanisms are clearly expected to be important. The fourth mechanism stipulates that the compaction of the snow cover ahead of the avalanche leads to the flow of escaping air just in front of the avalanche that may disrupt the snow cover and support formation of a saltation layer. The effects of this hypothetical mechanism resemble those of the ploughing mechanism. All mechanisms depend strongly on the snow properties, but with plausible parameter values, erosion rates at or above the experimentally found rates are obtained. The entrainment rate of an avalanche is most often limited by the shear stress needed to accelerate the eroded snow to avalanche speed.

Comparison of some simple entrainment laws by means of numerical simulations in a simplified topographical setting

The most relevant experimental findings on snow entrainment in avalanches are summarised in a paper with the same title as the heading of this section (Eglit and Demidov, 2003), a draft of which is found in Annex 2. The paper then gives a review of entrainment models and phenomenological formulae proposed in the literature from a variety of related fields. In particular, relevant results published only in Russian and essentially unknown in the Western scientific community are briefly summarised. Many of these approaches have been tested by the authors by means of numerical simulations under identical conditions in a somewhat idealised setting that captures the main features of typical avalanche paths. In this paper, results are presented for three classes of simple entrainment formulae:

1. *Distributed entrainment along the avalanche bottom with a fixed erosion depth per unit avalanche length.* The amount of entrained snow is proportional to the avalanche length, the erosion speed q (proportional to the decrease of the snow-cover depth per unit time) and grows linearly with the local flow velocity u:

$$q = a\,u\,.$$

   The resistance of the snow cover is indirectly taken into account by selecting the value of the entrainment coefficient, a, but there is no threshold for entrainment. Also, the entrainment depth is not limited by the stress needed to accelerate the eroded snow.

2. *Distributed entrainment proportional to the excess load.* The entrainment rate is independent of the velocity, but grows linearly with the hydrostatic pressure p (taken to be proportional the flow height h) at the bottom, provided it exceeds a minimum value p_* (corresponding to a minimum flow height h_*) that represents the compressive strength of the snow cover:

$$q = b\,(h - h_*)\,.$$

   Note that there is no explicit velocity dependence of the entrainment speed. However, the flow velocity in models of the hydraulic type considered here obeys Froude scaling, $u \propto h^{1/2}$, so that the entrainment per unit avalanche length grows as $h^{1/2}$.

3. *Entrainment speed growing with the square of the local flow velocity.* Entrainment takes place only if a threshold velocity u_* (chosen as 3 m s^{-1}) is exceeded:

$$q = \mathrm{c}\,(u^2 - u_*^2)\,.$$

Again, the entrainment depth per unit avalanche length grows with the avalanche velocity. If Froude scaling is obeyed, this model is equivalent to the previous one.

The main conclusion of this analysis is the following. For any reasonable entrainment law, the entrainment rate increases with the velocity and the flow depth. In the transition zone of an avalanche path, the maximum velocity and flow depths are usually found near the front. So in motion along steep slopes, the snow is entrained mostly by the frontal part of the avalanche. Since this frontal part is usually short in comparison to the length of the whole body of the avalanche, it can be treated from the mathematical point of view as a jump (a discontinuity) and therefore we in fact return to the first model with entrainment at the front, at least for the motion in the transition zone. Of course, in motion along a slope with a varying slope angle, the maximum values of the velocity and of the flow depth can be at a distance from the front. But it does not always mean that the entrainment rate is maximal there: all available snow could be entrained by the frontal part of the avalanche and in this case there is no entrainment anywhere except in the frontal zone.

The Cemagref erosion model

The stress caused by an avalanche on the underlying snow cover depends on the flow phase. Erosion occurs when this stress exceeds the grain stress threshold: the particles are pulled up and entrained into the flow and the total mass of the avalanche increases. On the other hand, when the friction at the bottom becomes dominant, the moving grains situated at the bottom are stopped and deposited. In this case, the total mass of the avalanche will progressively decrease. The formulation of the mass exchange used in the Cemagref N2L model is based on an assumption of similar vertical velocity profiles used in shallow fluid theory:

$$u(z,t) = \bar{\vec{u}} f(\eta) \qquad \eta = \frac{z}{h} \quad ,$$

where u is the velocity, h the flow height and z is the orthogonal coordinate to the terrain. As described in more detail by Barbolini *et al.* (2003), this assumption, together with considerations about the force balance of the lowest layers of the avalanche when the momentum increase of the entrained snow is taken into account, may be used to derive an expression for the entrainment rate $\varepsilon/\Delta t$:

$$\frac{\varepsilon}{\Delta t} = \phi_e \approx \frac{2h}{\bar{\vec{u}} \dfrac{df}{d\eta}_{\eta=0}} g \cos\theta \left[\tan\theta - \mu - \vec{\nabla} h\right] \quad ,$$

where θ is the slope of the terrain and μ is the friction coefficient between the snow and the terrain.

The Cemagref deposition model

As described above for the entrainment rate, the deposition rate may be found from force balance considerations using the velocity profile similarity assumption, see (Barbolini *et al.,* 2003) for more details, leading to the following expression for the deposition rate:

$$\frac{\varepsilon}{\Delta t} = \phi_d \approx \frac{-2h}{\bar{\vec{u}} \dfrac{df}{d\eta}_{\eta=0}} g \cos\theta \left[\tan\theta - \mu - \vec{\nabla} h\right] \quad .$$

Task 5.3 – Powder snow avalanches (DAMTP)

(Task leader: Jim N. McElwaine)

Experiments have been performed using expanded polystyrene particles and snow on steep slopes. By varying the angle it is possible to achieve different degrees of suspension ranging from none, for slopes below a critical angle, to total, for vertical slopes. The three-dimensional structure of the flows has been analysed using video cameras and the software developed in Task 2.2. The air pressure in front of and inside the flows was also measured and is being investigated as part of Task 2.3. The experimental results have been presented at the "Flow Regimes, Transitions and Segregation in Granular and Particle-Laden Flows" workshop 22–26 September 2003 in Cambridge. The theoretical analysis was presented at the "Geophysical Granular & Particle-Laden Flows" workshop 27–31 October 2003 in Bristol. The work over the next six months will include better controlled experiments with snow and the completion of two papers on the results and the theory.

Task 5.4 – Interactions with dams and impact loads (NGI)

(Task leader: Karstein Lied)

Overview of traditional descriptions of the flow of avalanches against catching and deflecting dams and the need for improvements

The dynamics of the flow of avalanches that hit obstructions, such as catching and deflecting dams or braking mounds, are poorly understood. Several methods have been used to design such structures in the past, based either on simple point-mass considerations pioneered by Voellmy (1955) and widely used in Alpine countries (Salm *et al.*, 1990), a dynamical description of the leading edge of the avalanche (Chu *et al.*, 1995) or on numerical computations of the trajectory of a point-mass on the upstream facing sloping side of the dam (Irgens *et al.*, 1998). Traditional design methods for dams are described by Salm *et al.* (1990), Norem (1994) and Lied and Kristensen (2003). In spite of some advances in the understanding of the dynamics of avalanches that hit obstructions in recent years, there is in general a substantial uncertainty regarding the effectiveness of defence structures in the run-out zones of avalanches. One of the goals of SATSIE is to improve the understanding of this problem, utilising field measurements, laboratory experiments and theoretical analysis.

The height of a catching dam is usually determined from the formula

$$H = H_v + H_s + H_f \ ,$$

where H_v is the required height due to the kinetic energy or the velocity of the avalanche, H_s is the thickness of snow on the ground on the upstream side of the dam before the avalanche falls and H_f is the thickness of the dense core of the avalanche. The terms H_s and H_f in the equation for H are usually assumed to be a few to several metres each for unconfined slopes and must be estimated based on a knowledge of the snow accumulation conditions at the location of the dam.

The term H_v is usually computed according to the equation

$$H_v = v^2/(2\lambda g)$$

for catching dams. v is the velocity of the chosen design avalanche at the site of the dam, λ is an empirical parameter and $g = 9.8$ m/s^2 is the acceleration of gravity. The empirical parameter λ is intended to reflect the effect of momentum loss when the avalanche hits the dam and

the effect of the friction of the avalanche against the upstream side of the dam during run-up. The value of λ is usually chosen to be between 1 and 2 (and sometimes even higher), with the higher values used for dams with steep upstream faces. Higher values of λ (lower dams) are chosen where the potential for large avalanches is considered rather small, whereas lower values of λ (higher dams) are chosen for avalanche paths where extreme avalanche with a large volume may be released.

The height of deflecting dams is traditionally calulated using the same equation as for a catching dam with the term H_v determined according to the equation

$$H_v = (v \sin\varphi)^2/(2\lambda g) ,$$

where v, λ and g have the same meaning as before and φ is the deflecting angle of the dam. The terms H_s and H_f are determined in the same manner as for catching dams. The λ parameter for deflecting dams is often chosen to be 1. The choice of λ equal to 1 is equivalent to neglecting momentum loss when an avalanche hits the dam and the effect of the friction of the avalanche against the dam. This leads to higher dams compared to the choice of λ higher than 1. This may partly be considered as a safety measure to counteract the uncertainty which is always present in the determination of the deflecting angle and for taking into account internal pressure forces which may lead to higher run-up than assumed in the point-mass dynamics.

There exist no accepted design guidelines for braking mounds for retarding snow avalanches although they are widely used as a part of avalanche protection measures. Laboratory experiments have recently been performed as a part of the research project CADZIE in order to shed light on the dynamics of avalanche flow over and around braking mounds and catching dams and to estimate the retarding effect of the mounds. The experiments and the design criteria for braking mounds that have been developed on the basis of them are described by Jóhannesson and Hákonardóttir (2003) and in papers and reports referenced therein.

A fundamental problem with the point-mass view of the impact of an avalanche with a deflecting dam is caused by the transverse width of the avalanche which is ignored in the point-mass description. As a consequence of this simplification, the lateral interaction of different parts of the avalanche is ignored. The point-mass trajectories corresponding to different lateral parts of an avalanche that flows along a deflecting dam must intersect as already deflected material on its way down the dam side meets with material heading towards the dam farther down. Similarly, it is clearly not realistic to consider the flow of snow in the interior of an avalanche that hits a catching dam without taking into account the snow near the front that has already been stopped by the dam. The effect of this interaction on the run-up cannot be studied based on point-mass considerations and a more complete physical description of lateral and longitudinal interaction within the avalanche body in the impact process must be developed. These flaws of the point-mass dynamics are most clearly seen by the fact that no objective method based on dynamical considerations can be used to determine the empirical parameter λ, which nevertheless has a large effect on the design of both catching and deflecting dams.

Comparison of numerical simulation models on 12 Ryggfonn avalanches

At NGI's avalanche test site Ryggfonn, extensive measurements have been carried out for two decades. When possible, the release area and depth, the front velocity between two pressure measurement locations in the lower track, the run-out distance, the extent of the deposits and a deposit depth profile along one line were recorded. The snow density was extrapolated from

measurements at a near-by automatic station for the release area and measured manually in the deposits.

From this data set, the twelve best recordings of dry-snow avalanches (with moderate to large powder-snow component) that reached or overflowed the 16 m high dam in the run-out zone were selected for a comparison of nine different avalanche dynamics models. The avalanches range from moderate-size events to very large ones, with run-out distances differing by as much as 300 m. The models comprise two quasi-analytical models, two representatives of the traditional hydraulic models currently in use for hazard mapping in Switzerland and Italy, NGI's so-called NIS model based on a simplified form of the CEF rheology (see Task 5.1 above), the PLK model with stochastic elements (popular for consulting purposes in North America), BING (a visco-plastic model originally developed for sub-aqueous mudflows), and the two-layer models SAMOS and N2L for mixed avalanches.

For each of the models and each of the twelve avalanche events, the parameter sets that best reproduced the observed run-out distances and velocities were determined. The simulated percentage of snow mass retained by the dam was then calculated and compared to the measurements. Again, for each avalanche event and model, the simulations were repeated with the optimal parameters determined before, on a model topography from which the dam was removed. This provided insight as to how the different models react to an artificial obstacle, both with regard to the run-out distance and the mass distribution above and below the dam location.

Critical cross-comparison of the simulations carried out by several team members in different countries led to repeating a number of simulations. The paper describing this work is not completely finished as this report is being written, but some of the key results could already be presented at the "International Conference on Snow and Avalanches" in Davos, and a draft of the paper is included in Annex 2. Our main findings may be summarised as follows:

- On the experimental side, careful distinction between deposits of the dense core and the saltation layer must be attempted in order to avoid misinterpretation of the measurements. Also, several velocity and/or flow-depth measurements are needed to constrain the model parameters more unequivocally.
- In all models tested, the optimum friction parameters covered a very wide range of values. Part of this spread can be attributed to the fact that the longest run-out distances in our sample most likely correspond to the reach of the saltation layer, whereas most of the dense core was stopped at the dam.
- The existing models do not adequately take into account the effect of the catching dam. In all models except PLK, its effect is underestimated, both with regard to the run-out distance and the mass distribution. An *ad-hoc* momentum reduction prescription in the PLK model is very effective in reducing the run-out, but exhibits spurious dependence on path segmentation.
- Good mapping of the pressure distribution may require multi-layer models including the saltation layer. This is also hoped to reduce the uncertainty in the choice of friction parameter values.
- Dedicated research is needed to extend presently available models so as to give a more realistic description of the energy and mass loss at obstacles like catching dams.

An experimental and numerical study of the volume retained by a dam: first results

An experimental and modelling study of the volume retained by a catching dam was undertaken by the ETNA team. The objective of the study is a better understanding of the effect of a catching dam on the flow of dense snow avalanches that partly overflow the dam. A numerical model based on shallow water theory was developed where the dense core of a snow avalanche is regarded as a thin, granular gravity current. The friction is represented by a phenomenological law based on the theory of Pouliquen (1999) as described in the previous section about Task 5.2 and in more detail in the report by Barbolini *et al.* (2003). The obtained system of equations is solved with a finite volume numerical scheme based on a simplified Riemann solver. The numerical model has been verified by comparison with analytical solutions and experimental data.

Deposits formed upstream from a catching dam located at the downstream end of a rough channel were studied in a series of laboratory experiments. The experiments were carried out for a number of different initial heights of the granular material, which was released from a reservoir at the upstream end of the channel. Two different values for the slope of the channel were used. The ratio of the retained volume to the released volume was measured. The experiments were modelled with the abovementioned numerical shallow water model. A comparison of the computed and measured retained volume showed a good agreement between the results of the experiments and the numerical computations, which are described in a report in preparation.

Shock dynamics in avalanche flow against obstructions

Recent theoretical analysis (Gray *et al.*, 2003), chute experiments (Tai *et al.*, 2001) and field observations (Jóhannesson, 2001) suggest that the interaction between avalanche flow and obstacles such as dams can, under some circumstances, be analysed within the framework of supercritical shallow fluid dynamics, by introducing discontinuities or shocks in the velocity and flow depth near the location of the obstacles. Mass and momentum conservation is then formulated through *jump conditions*, which may be used to compute the dissipation of mechanical energy caused by the obstacles. The main advantage of this dynamical approach to avalanche flow near obstructions is that the lateral and transverse dimensions of the avalanche during the interaction may be described in a dynamically consistent manner.

A series of laboratory experiments has been carried out at the University of Bristol in order to investigate shock dynamics in granular and fluid flows that hit deflecting and catching dams. The experimental findings have been compared with classical results from shock dynamics and found to compare favourably with theoretical predictions. The experimental set-up and the theoretical background is described a report by Hákonardóttir *et al.* (2003), which is reproduced in Annex 2, and summarised in Chapter 3 (experimental set-up) and 4 (results of experiments). Some of the results were presented at the "Geophysical Granular & Particle-Laden Flows" workshop in Bristol 27–31 October 2003. Further theoretical analysis and interpretation of the experiments will be carried out within SATSIE in order to formulate the results in terms of design criteria for deflecting and catching dams for protection against snow avalanches and compare these criteria to traditional design practice.

Task 5.5 – Report on the validation of new models (IMOR)

(Task leader: Tómas Jóhanesson)

Comparison of numerical models

The first phase of model validation within SATSIE must be partly based on existing data and partly on results from chute experiments since new data from SATSIE field experiments is not available. A set of 4-5 well known historical avalanches, partly based on the CADZIE data set, has been chosen for verification within Work Package 5 until data from our own tests become available. These are avalanches from Taconnaz in 1999, Ryggfonn, Flateyri in 1995 and Monte Pizzac. These avalanche will be be used to document the differences/improvements due to new physical formulations for different flow regimes and entrainment and deposition that are developed and validated within SATSIE. Numerical experiments with these avalanches are in preparation and will be carried out in the second year of SATSIE.

As described in the previous section about Task 5.4 (dam avalanche interaction), chute experiments and theoretical analysis indicates that the formation of shocks is important aspect of avalanche flow against obstructions. Model experiments with current 2D avalanche models will be carried out for flow against deflecting dams in order to investigate to what extent these models can reproduce the experimental findings and theoretical predictions based shallow fluid dynamics. These experiments will be a good test of the physical realism and the quality of the numerical implementation of these models.

Model experiments carried out at the University of Barcelona

During the first year of the project the avalanche team at the UB has actively participated in the development and application of avalanche models. Specifically, one part of our work involved the inter-comparison of the two avalanche modelling programs: *Lawsim2* (Salm *et al.*, 1990) and *AVAL-1D* (Bartelt *et al.*, 1999), with the aim of their application to the Pyrenees. The second part of our activities within the given work package dealt with the preparation of the report on simulations of dry-snow avalanches from the Ryggfonn test site.

The main goal of our modelling efforts with Lawsim2 and AVAL-1D programs was to evaluate the effect of changing input parameters, such as the dry-friction and turbulent friction coefficients, on the obtained results (e.g. the run out distance, avalanche velocity). By using the two different programs we were able to evaluate the dependence of the obtained results on the particular model. We have also attempted to establish a relationship between the different input coefficients used in the Lawsim2 and AVAL-1D since these programs were calibrated with the same data. Our final goal was to investigate whether the abovementioned programs, which were developed and calibrated with the data in the Alps, could be successfully applied to the studies of snow avalanches in the Pyrenees.

During the investigations we used data from several avalanches recorded in the Swiss Alps, together with avalanches from the Catalan part of the Pyrenees. This type of inter-comparison of data led us to the conclusion that the FL-1D and Lawsim2 programs initially developed for the Alps could be successfully applied to the studies of avalanches for land use planning in the Pyrenees.

As part of a collaborative report being prepared by Issler *at al.*, we have modelled a series of 12 well known avalanches from the full-scale test site in Ryggfonn, Norway using the dense snow avalanche module FL-1D (Bartelt *et al.*, 1999) of the AVAL-1D program. Based on the

initial data from the NGI we have introduced the topographic profiles in FL-1D, as well as specified other spatial input parameters: depth of snow, length and width of the initial snow slab and the width of the path. The dry (μ) and turbulent (ξ) friction coefficients were varied in increments within an acceptable range to study the sensitivity of the calculations to the parameters. The aim was to find the values of μ and ξ, which best reproduced the observed run out distances and velocities at monitoring points, as well as the measured impact pressures at the dam. This work, which is further described in the section about Task 5.4, is currently still in progress and the final results will be available towards the end of the year.

Main scientific results obtained in the Work Package

The main results obtained in Work Package 5 may be divided into four categories. Firstly, the state of the art in the main dynamical questions that are being considered in the work package has been reviewed, including an overview of Russian research in the field of entrainment and deposition processes in snow avalanches. Secondly, nine different avalanche dynamics models have been tested against data about 12 avalanches that hit a catching dam in the Ryggfonn avalanche path in western Norway. As expected, it was found that the computed effect of the dam varied greatly between the models. Most of the obtained differences between the models are likely to be due to effects that do not correspond to a physical description of flow of the avalanche against the dam. A fundamental improvement in the physical description of the interaction between avalanche flow and obstacles is needed in order to remedy this situation. Thirdly, chute experiments for studying granular and fluid flows against deflecting and catching dams have been interpreted theoretically in terms of shallow fluid dynamics and shocks, leading to a new understanding of the flow of avalanches against obstructions. This understanding makes it possible to consider the lateral and longitudinal dimensions of the flowing avalanche in a dynamically consistent way, which represents a large improvement over traditional derivations based on point-mass dynamics. Fourthly, new formulations for entrainment and deposition processes in snow avalanches are being developed and implemented and tested in numerical models.

WP 6 – Data sharing and dissemination of results (NGI)

(Work package leader: Karstein Lied)

This work package comprises two tasks that focus on internal communication and data exchange, one task ascertaining the safety of valuable data, and three tasks concerned with communication with the outside and dissemination of our results to avalanche professionals in Europe. Accordingly, the first group had to be started very early in the project. While the project web-site was soon operational, database design has been delayed due to external reasons detailed below.

The tasks oriented towards dissemination of results can only be started in the late phase of SATSIE when sufficiently well tested results from experiments and modelling have been obtained.

Task 6.1 – Meta-database on experimental results (DAMTP)

(Jim N. McElwaine)

After weighing various options, the consortium early in the project opted to design the planned database on experimental results as a continuation and extension of the avalanche-event database of the predecessor project, CADZIE (http://cadzie.grenoble.cemagref.fr/). It was therefore decided to wait with all work on the database until the CADZIE database was closed at the end of the project CADZIE and could be transferred to SATSIE for further maintenance and use.

However, at the end of the first year of SATSIE, the CADZIE database is still not closed and its future is unclear—not least because of legal restrictions on the topographical maps that form a central part of that database.

It has therefore been decided that SATSIE shall after all proceed to designing its own database. CDF has been chosen as the format in which all but the simplest data will be archived. The database will be designed and data transferred to it during the first months of the second project year.

Task 6.2 – Database maintenance and data back-up

(Jim N. McElwaine)

In view of the uncertainties connected to the database design (see Task 6.1 above), the majority of the partner institutions have so far not sent their experimental data to the central repository, but have themselves taken the responsibility of archiving them and keeping back-up copies. Central back-ups will be made as soon as the database has been established and the partner institutions have sent their data in the first half of the second project year.

Task 6.3 – Creation and maintenance of project website (SGUL)

(Chris Keylock)

The address for the site is http://www.leeds.ac.uk/satsie.
In the Management Progress Report covering the first six months of the project, the web-site was designed by Simon Reid (SGUL) and was populated with material submitted by project members and written by Chris Keylock (SGUL). A detailed description of the pages and their

functionality was provided in the Management Progress Report for the project. Rather than repeat that material here, we suggest that a brief navigation of the site will give an insight into the information contained therein.

We aim to continually update and add to the project's web-pages. Some examples of recently added pages include:

http://www.leeds.ac.uk/satsie/vids.html – Movie files of avalanches occurring in Catalonia (October 1st, 2003);

http://www.leeds.ac.uk/satsie/chutevids.html – Movie files of laboratory experiments in Pavia (October 12th, 2003).

Furthermore, we have added a publications page to the web-site to provide web users with information on where some of the research from the project has been published, which will hopefully expand greatly in the next two years.

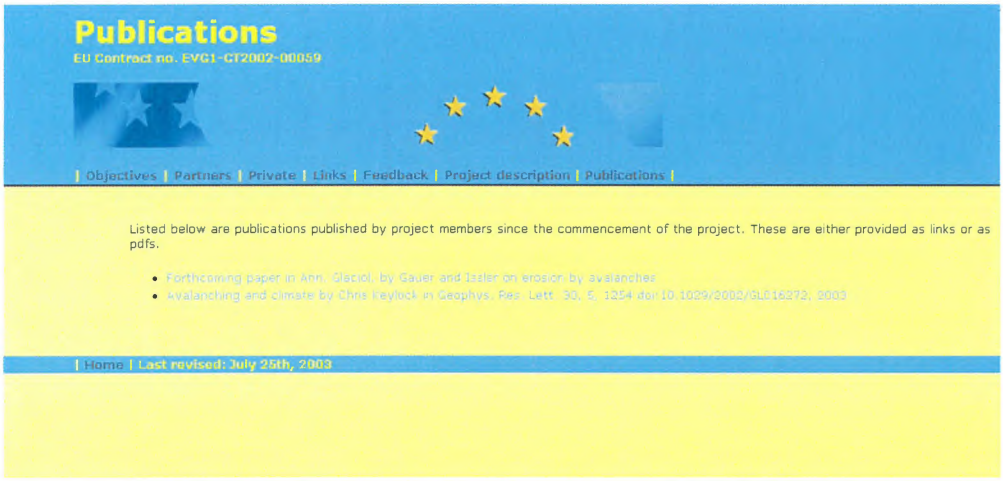

Figure 6.3.1. Publicly accessible publications page on the SATSIE web-site.

Task 6.4 – Handbook on design of protective dams (IMOR)

(Tómas Jóhannesson)

This task is scheduled to be launched only in the last year of SATSIE.

Task 6.5 – Description of new avalanche models (NGI)

(Carl B. Harbitz)

This task is scheduled to be launched only in the last year of SATSIE.

Task 6.6 – European Summer University course (ETNA)

(Mohamed Naaim)

The next natural hazards Summer University devoted to snow avalanches will be organised in September 2004 by the Institute of Natural Hazards of Grenoble (Pôle Grenoblois d'Etude des Risques Naturels, PGRN) and will be held in Courmayeur (Italy). Due to the fact that this

Summer University takes place in the middle of the project as work in SATSIE is ongoing, it is too early to base an entire course on results from SATSIE. We negotiated with the PGRN to split our contribution in two parts. The first will be one or two half-day units on the general use of numerical models in avalanche zoning and defence-structure design at the next Summer University course, i.e., in 2004. This course will be followed in 2005 or 2006 by a specialized course focusing on the new knowledge and methods developed in SATSIE. This latter course is directed towards more advanced students who have successfully attended the basic avalanche course in 2004 or earlier, and to experienced professionals in the field of avalanche hazard mapping who are familiar with the current methodology and numerical models.

Bibliography

a) Papers and reports from SATSIE team members and associates

Barbolini, M., F. Cappabianca, D. Issler, P. Gauer, M. E. Eglit, M. Naaim and R. Sailer. 2003. Erosion and deposition processes in snow avalanche dynamics: Report on the state of the art. SATSIE report, October 2003. Dipartimento d'Ingegneria Idraulica e Ambientale, Università degli Studi di Pavia, Pavia, Italy. Reproduced in the Annex.

Barbolini, M. and M. Pagliardi. 2003. Experiments with granular materials at Pavia chutes. SATSIE project report, October 2003. Dipartimento d'Ingegneria Idraulica e Ambientale, Università degli Studi di Pavia, Pavia, Italy. Reproduced in the Annex.

Eglit, M. and K. S. Demidov. 2003. The effect of snow entrainment in avalanche dynamics. Draft paper, reproduced in the Annex.

Gauer, P. and D. Issler. 2004. *Annals of Glaciology*, **38**, in print. Reproduced in the Annex.

Hákonardóttir, K. M., A. Hogg and T. Jóhannesson. 2003. A laboratory study of the interaction between supercritical, shallow flows and dams. Report G03038, November 2003, Veðurstofa Íslands, Reykjavík, Iceland. Reproduced in the Annex.

McElwaine, J. N. and Tiefenbacher, F. 2003. Calculating internal avalanche velocities from correlation with error analysis. *Surveys in Geophysics*, in print. Reproduced in the Annex.

McElwaine, J. N. 2004. Calculation of two-dimensional avalanche velocities from opto-electronic sensors. *Annals of Glaciology*, **38**, in print. Reproduced in the Annex.

Issler, D. Notes on the Criminale–Ericksen–Filbey fluid as a candidate rheology for snow avalanches. SATSIE memo, February 2003. Norges Geotekniske Institutt, Oslo, Norway.

Issler, D., M. Barbolini, F. V. De Blasio, G. Furdada, C. B. Harbitz, K. Kristensen, K. Lied, J. N. McElwaine, A. I. Mears, A. Moe, M. Naaim and R. Sailer. In preparation. Simulations of dry-snow avalanches observed in the full-scale test site Ryggfonn, Norway.

Jóhannesson, T. 2003. Satsie. Work Package 5. Meeting in Leeds on 16–18 January 2002. Thoughts to start discussion about model development and validation. Icelandic Meteorological Office, Memo TóJ-2003-02.

b) Additional literature cited

Almendros, J., B. Chouet, and P. Dawson. 2002. Array Detection of a Moving Source. *Seismological Research Letters*, **73** (2), 153–165.

Arattano, M., and F. Moia. 1999. Monitoring the propagation of a debris flow along a torrent. *Hydrological Sciences Journal - Journal des Sciences Hydrologiques*, **44** (5), 811–823.

Bartelt, P., B. Salm and U. Gruber. 1999. Calculating dense snow avalanche runout using Voellmy-fluid model with active/passive longitudinal straining, *Journal of Glaciology*, **45**(150), 242–254.

Biescas, B. 2003. Aplicación de la sismología al estudio y detección de los aludes de nieve. PhD. Thesis. University of Barcelona. ISBN: B. 46927-2003 / 84-688-3758-X. Available on-line at <http://www.tdx.cesca.es/TDX-1010103-084042/>.

Biescas, B., F. Dufour, G. Furdada, G. Khazaradze, and E. Suriñach. 2003. Frequency content evolution of snow avalanche seismic signals. *Surveys in Geophysics*, in print.

Bouquet, A., *et al.* 2003. *Surveys in Geophysics*, in print.

Chu, T. and G. Hill and D. M. McClung and R. Ngun and R. Sherkat. 1995. Experiments on granular flows to predict avalanche runup. *Canadian Geotechnical Journal*, 32, 285–295.

Dent, J. D., K. J. Burrell, D. S. Schmidt, M. Y. Louge, E. E. Adams and T. G. Jazbutis. 1998. Density, velocity and friction measurements in a dry-snow avalanche. *Annals of Glaciology*, **26**, 247–252.

Gray, J. M. N. T., Y.-C. Tai and S. Noelle. 2003. Shock waves, dead zones and particle-free regions in rapid granular free-surface flows. *Journal of Fluid Mechanics*, **491**, 161–181.

Gubler, H., M. Hiller, G. Klausegger and U. Suter. 1986. Messungen an Fliesslawinen. Zwischenbericht 1986. Mitteilung No. 41, Eidg. Institut f. Schnee- und Lawinenforschung, Weissfluhjoch / Davos, Switzerland.

Ibañez, J. M., P. E. Del, J. Almendros, R. M. La, G. Alguacil, R. Ortiz, and A. Garcia. 2000. Seismovolcanic signals at Deception Island Volcano, Antarctica; wave field analysis and source modeling, *Journal of Geophysical Research*, **105** (6), 13,905–13,931.

Irgens, F., B. Schieldrop, C. B.Harbitz, U. Domaas and R. Opsahl. 1998. Simulations of dense-snow avalanches on deflecting dams. *Annals of Glaciology*, **26**, 265–271.

Issler, D., P. Gauer, M. Schaer, and S. Keller. 1996. Staublawinenereignisse im Winter 1995: Seewis (GR), Adelboden (BE) und Col du Pillon (VD). Interner Bericht 694. Davos Dorf, Switzerland. Eidg. Inst. für Schnee- und Lawinenforschung.

Jóhannesson, T. and K.M. Hákonardóttir. 2003. Remarks on the design of avalanche braking mounds based on experiments in 3, 6, 9 and 34 m long chutes. IMO, report G03024, Reykjavík, Iceland.

Jolly, A. D., G. Thompson, and G. E. Norton. 2002. Locating pyroclastic flows on Soufriere Hills Volcano, Montserrat, West Indies, using amplitude signals from high dynamic range instruments. *Journal of Volcanology and Geothermal Research*, **118**, 299–317.

Lied, K. and K. Kristensen. 2003. *Snøskred. Håndbok om snøskred.* Vett & Viten as., Oslo.

Lied, K., A. Moe, K. Kristensen, and D. Issler. 2003. Ryggfonn: Full scale avalanche test site and the effect of the catching dam. *In:* F. Naaim-Bouvet (ed.), Proceedings of the International Seminar on Snow Avalanches Experimental Sites, November 2001, Grenoble, France. Editions du Cemagref, F–92163 Antony Cedex, France, in print.

McElwaine, J. N. 2003. Image analysis for avalanches. *In:* F. Naaim-Bouvet (ed.), Proceedings of the International Seminar on Snow Avalanches Experimental Sites, November 2001, Grenoble, France. Editions du Cemagref, F–92163 Antony Cedex, France, in print.

Norem, H. 1994. *Snow engineering for roads*. Norwegian Public Roads Administration, Oslo.

Pouliquen, O. 1999. Scaling laws in granular flows down rough inclined planes. *Physics of fluids*, **11**(3), 542-548.

Pouliquen, O. and Y. Forterre. 2002. Friction laws for dense granular flows: application to the motion of a mass down a rough inclined plane. *Journal of Fluid Mechanics*, **453**, 133-151.

Sabot, F., M. Naaim, F. Granada, E. Suriñach, P. Planet and G. Furdada. 1998. Study of avalanche dynamics by seismic methods, image-processing techniques and numerical models. *Annals of Glaciology*, **26**, 319–323.

Salm, B., A. Burkard and H.U. Gubler. 1990. *Berechnung von Fliesslawinen. Eine Anleitung für den Praktiker mit Beispielen.* Mitteilungen des Eidg. Inst. für Schnee- und Lawinenforschung, Davos, Switzerland.

Schaerer, P. A., and A. A. Salway. 1980. Seismic and impact-pressure monitoring of flowing avalanches. *Journal of Glaciology*, **26** (94), 179–187, 1980.

Scherbaum, F., and J. Johnson. 1992. PITSA, Programmable Interactive Toolbox for Seismological Analysis, *IASPEI Software Library*, 5 (http://www.seismosoc.org/publications/-IASPEI_Software.html).

Sovilla, B., F. Sommavilla, and A. Tomaselli. 2001. Measurements of mass balance in dense snow avalanche events. *Annals of Glaciology*, **32**, 230-236.

Tai, Y.-C., J. M. N. T. Gray, K. Hutter and S. Noelle. 2001. Flow of dense avalanches past obstructions. *Annals of Glaciology*, **32**, 281–284.

Tai, Y.-C., S. Noelle, J. M. N. T. Gray and K. Hutter. 2002. Shock capturing and front tracking methods for granular avalanches. *Journal of Computational Physics*, **175**, 269–301.

Voellmy, A. 1955. Über die Zerstörungskraft von Lawinen. *Schweizerische Bauzeitung*, **73**, 159–165, 212–217, 246–249, 280–285.

Appendix 1 - 7

Calculating Internal Avalanche Velocities From Correlation With Error Analysis

J. N. McElwaine (jnm11@amtp.cam.ac.uk)
Department of Applied Mathematics and Theoretical Physics, Centre for Mathematical Sciences, Wilberforce Road, Cambridge, CB3 0WA, UK, Tel: +44 1223 337858, Fax: +44 1223 337918,

F. Tiefenbacher (tiefenbacher@slf.ch)
Swiss Federal Institute for Snow and Avalanche Research, Flüelastr. 11, CH-7260, Davos Dorf, Switzerland, Tel: +41 81 4170 253, Fax: +41 81 417 01 10

Abstract. Velocities inside avalanches have been calculated for many years by calculating the cross-correlation between opto-electronic sensors using a method pioneered by Nishimura et al. (1987) and Dent et al. (1998). Their approach has been widely adopted but there has been little discussion of the optimal design of such instruments and the best analysis techniques. This paper discuses some of the different sources of error that arise and how these can be mitigated. A statistical framework that describes such instruments is developed and used to quantify the errors.

Keywords: velocity profiles, snow avalanches, granular flows, opto-electronic sensors, correlation methods

1. Introduction

Opto-electronic sensors have been used for a long time to measure the velocities inside granular flows. Some of the earliest work was done by Nishimura et al. on snow avalanches and continued in Nishimura et al. (1987). Early work was also done by Dent et al. and measurements were taken from the "Revolving Door" avalanche path near Bridger Bowl, Montana.

The basic design of these sensors is simple. An infrared LED emits light that is reflected by the passing granular material and this is detected by an infrared-sensitive photo-transistor, amplified, digitised and stored on a computer. By comparing the signals from nearby sensors its is possible to calculate the velocity of the flow.

In theory it is possible to calculate many other pieces of information about the flow since the magnitude of the back scattered light depends on the density, type, size, and orientation of the snow crystals. However, though Dent et al. (1998) tried to relate reflectivity to snow density they failed because crystal size and type are much more important than density. Some gross aspects of the flow can be determined however. For example in deposited snow the signal will be constant, in a powder cloud the signal will be very low since no light from above can reach the sensor and the density is usually too low to significantly reflect light, and above the snow a high level will be detected due to ambient lighting.

Despite the wide spread use of opto-electronic sensors there appears to have been little work done on analysing the errors and designing instruments so as to minimise them. In this paper we describe how to calculate the errors for these sensors. We then use these results to discuss how these sensors should best be designed. Some of the different variables considered are the number of sensors, sensor geometry, relative position, size and sample rate. Before we can calculate the errors it is necessary to first discuss how the data is to be processed and for this to be done a model for the behaviour of the flow field is necessary.

For convenience in this paper we ignore discretization errors in both time and space and regard functions as continuous. Only when considering the numerical implementation will a discrete time approach be used. This simplification can be made as long as the signals are properly filtered before digitisation so that there are no frequencies higher than the Nyquist frequency (half the sample frequency).

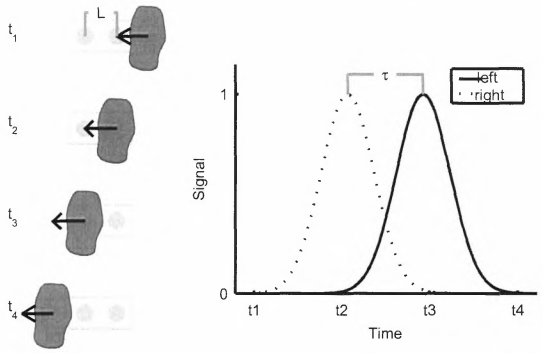

Figure 1. Schematic of a typical instrument and measurement process for a single particle. Estimated velocity is L/τ.

We start of by discussing the most frequently used method, the cross-correlation method, and explain why this method can be unreliable. Then we introduce a modified method and discuss the errors for a simple two point sensor. This shows that there are several main sources of errors. The most serious is due to the two-dimensional nature of real flow fields past a flat sensor, whereas the analysis assumes one-dimensional flow. This can be reduced by careful designing of the sensors or explicitly accounting for two-dimensional velocities. The second source of error is due to accelerations in the velocity. The correlation method assumes that the velocity is constant over the time window used for calculating the cross-correlation and when this is not true, because the flow is accelerating, errors are introduced. The acceleration errors can be reduced by improved analysis techniques where the velocity is calculated as a changing function at all times. Note that the acceleration can be caused by convective changes in velocity, that is different parts of the flow are moving with different velocities, or temporal acceleration, that is the velocity field is changing with time. Thirdly there are errors due to the inherent statistical velocity fluctuations in a granular flow. The mean velocity in a granular medium is only defined once an averaging process over individual particles has been specified. Measurements of the mean velocity based on averaging region of space or time will have statistical uncertainty. There are also errors introduced by the aperture effect, which will be explained later in greater depth. Internal changes in the flowing snow will also cause inaccurate correlations. And in a similar vein velocities normal to the mounting plane of the sensor will also introduce errors in the correlation. Since sensors are normally mounted on large walls and the normal velocity must vanish at the surface this effect will be very small unless the sensor is sensitive to a few particle diameters into the flow.

2. Errors in interpreting the lag

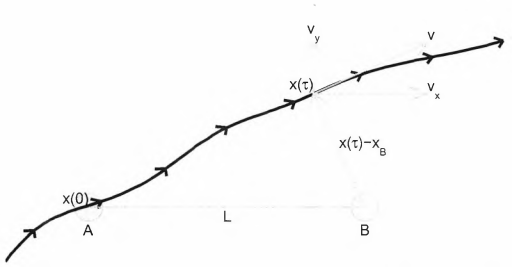

Figure 2. Particle trajectory with maximum correlation occurring at point of closest approach

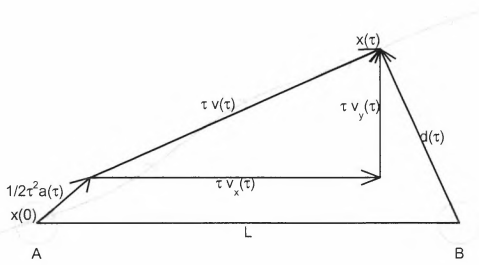

Figure 3. The dependence of τ on the particle trajectory can also be calculated geometrically. In the case when acceleration, $\mathbf{a}$, can be ignored then two applications of Pythagoras' theorem give $\tau^2 v^2 + d^2 = L^2$ and $\tau^2 v_y^2 + (L - \tau v_x)^2 = d^2$. Eliminating d^2 between the two equations gives $L/\tau = v_x + v_y^2/v_x$.

We assume that the largest cross-correlation between two sensors will occur at a time when a region of the flow which passed over the first sensor is at its closest to the second. This is discussed in more detail in McElwaine (2003) and shown to be true in the mean. This region of the flow does not have to be a particular particle, but only a region with an identifiable reflectivity signature, but for simplicity we will talk about a particle. Figure 2 shows the trajectory of this particle that is over sensor A at time 0 so that $\mathbf{x}(0) = \mathbf{x}_A$ and is closest to sensor B at time τ. Disregarding internal changes in the material and false matches the correlation between sensors A and B will be greatest at lag τ. The point of closest approach of the trajectory to sensor B occurs when the displacement between them is perpendicular to the tangent of the trajectory, which is of course the velocity. Thus

$$[\mathbf{x}(\tau) - \mathbf{x}_B] \cdot \mathbf{v}(\tau) = 0 \tag{1}$$

The same equation results algebraically by differentiating to find the minimum of the distance $|\mathbf{x}(\tau) - \mathbf{x}_B|$. We then define the effective particle acceleration $\mathbf{a}$ by

$$\mathbf{x}(t) = \mathbf{x}_A + t\mathbf{v}(\tau) + t^2\mathbf{a}(t)/2 \tag{2}$$

That is $\mathbf{a}(\mathbf{t})t^2/2$ is the difference in position between the actual position at time t and the position if the particle had moved with constant velocity $\mathbf{v}(\tau)$ (see fig. 3.) Taking the dot product of eq. 2 with $\mathbf{v}(\tau)$ and evaluating at $t = \tau$ this becomes

$$\mathbf{x} \cdot \mathbf{v} - \mathbf{x}_A \cdot \mathbf{v} = v^2\tau + \tau^2\mathbf{a} \cdot \mathbf{v}/2 \tag{3}$$

where $\mathbf{x}$ and $\mathbf{a}$ are evaluated at $t = \tau$. Then use eq. 1 to eliminate $\mathbf{x} \cdot \mathbf{v}$ and we have

$$(\mathbf{x}_B - \mathbf{x}_A) \cdot \mathbf{v} = v^2\tau + \tau^2\mathbf{a} \cdot \mathbf{v}/2 \tag{4}$$

If we take the sensors to be separated by a distance L along the x axis then this becomes $Lv_x = \tau v_x^2 + \tau v_y^2 + \tau^2(a_x v_x + a_y v_y)/2$ which can be rearranged to give

$$v_x = \frac{L}{\tau} - v_y \frac{v_y + \tau a_y/2}{v_x} - \tau a_x/2 \tag{5}$$

Thus if the particle is travelling with constant velocity $\mathbf{v}$ along the x-axis sensors so that a_y, v_y and v_x are all zero then $v_x = L/\tau$, which is the usual formula. In other cases however the velocity estimate $\hat{v}_x = L/\tau$ will be in error by $v_y(v_y + \tau a_y/2)/v_x - \tau a_x/2$. For low accelerations the main contribution will be from the velocity component v_y which biases the estimate high by v_y^2/v_x.

Equation 5 concerns point velocities at time τ and has a displacement error term $\mathbf{a}$ which is similar to the averaged particle acceleration. Another approach is to attempt to calculate the particles average velocity over the time interval τ so we define

$$\overline{\mathbf{v}} = \frac{\mathbf{x}(\tau) - \mathbf{x}(0)}{\tau}. \tag{6}$$

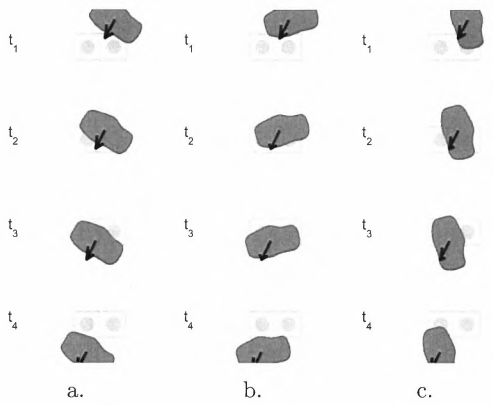

Figure 4. Different orientations of a particle with the same velocity give rise to different correlation times. In (a.) the particle is moving orthogonally to its edge and the correlation time will be positive. In (b.) the particle is rotated anti-clockwise and the correlation time will be negative. In (c.) the particle is rotated clockwise giving a larger positive correlation time.

But now the point velocity $\mathbf{v}(\tau)$ is not known and this must be approximated by defining a new pseudo-acceleration $\mathbf{a}'$ by

$$\mathbf{v}(\tau) = \overline{\mathbf{v}} + \tau \mathbf{a}' \tag{7}$$

Substituting this relation into eq. 1 and rearranging gives

$$\overline{v}_x = \frac{L}{\tau} - \overline{v}_y \frac{\overline{v}_y + \tau a'_y}{\overline{v}_x} + a'_x \left(\tau - \frac{L}{\overline{v}_x} \right) \tag{8}$$

This is very similar to eq. 5. The significant difference is that the estimate of velocity is accurate to first order in a'_x since $a'_x \left(\tau - \frac{L}{\overline{v}_x} \right) = O\left(\frac{{a'_x}^2 L^2}{\overline{v}_x^3} \right)$. This is not surprising and shows the output from these instruments will best be regarded approximations to velocity averaged over the lag time rather than point velocities.

3. Errors in Calculating the Lag

The analysis in the previous section assumed that the lag with the maximum cross-correlation occurred when the same part of the flow was identified as it passed near each sensor. This is only true on average and is not the case in general. There are two main effects to be considered, which are discussed in the following subsections.

3.1. Aperture Effect

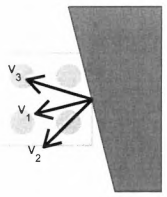

Figure 5. All three velocities v_1, v_2 and v_3 will result in the same lags between the sensors. No sensor array can distinguish between them and only the velocity component perpendicular to the edge can be measured.

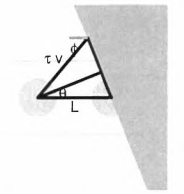

Figure 6. How the lag time τ depends on the direction of the velocity ϕ, the speed v and the direction of the edge normal θ. $L\cos\theta = \tau v\cos(\theta - \phi)$

Each photo-transistor measures the reflected intensity of the material, thus regions in the flow with the same reflectivity cannot be distinguished. Rather than seeing the correlation between different points in the flow the sensors in fact measure the correlation between contours of equal reflectivity. These contours of equal reflectivity correspond to the edges of particles. Therefore only the velocity component orthogonal to the reflectivity contours can be measured (see fig. 5). This difficulty is known as the *aperture* effect Jähne (1997) (Chapter 13).

In the case of only two sensors the problem is even worse since the normal direction $\hat{\mathbf{n}}$ can not be calculated. A simple calculation shows this effect explicitly (see fig. 6) so that

$$\hat{v}_x = \frac{L}{\tau} = \frac{v\cos(\theta - \phi)}{\cos\theta} = \frac{\mathbf{v}\cdot\hat{\mathbf{n}}}{\hat{\mathbf{x}}\cdot\hat{\mathbf{n}}}, = v_x + v_y\tan\theta \tag{9}$$

where $\hat{\mathbf{x}}$ is the unit vector along the x-axis. This shows that vertical velocities can increase or decrease the estimate $\hat{v}_x$ depending on the angle of the edge. This effect is shown in fig. 4 where the same particle approaches the sensor with same velocity but different orientations.

This subsection has discussed the relationship between the lag τ the velocity of the flow and its structure when the lag is calculated from individual events. Different approaches for calculating the lag will be discussed later, but these all calculate the lag by comparing the signal over large time intervals which therefore average over the different orientations and velocities in the flow and thus act to mitigate these effects.

3.2. Spatial Aliasing

If there are spatial variations less than the spacing between the sensors then the Nyquist limit is violated and aliasing can occur. The surface area of the sensors acts as an averaging, low-pass filter so it is not the distance between the centres of the sensors that must be small but the distance between the edges of the active part of the sensors. The requirement can be simply stated that there should be no room for particles to pass between the sensors without giving a signal. The most obvious effect of this will be when there are significant vertical velocities, and then there maybe no correlation between the sensors at all. This is shown in fig. 7. In this case the critical length between which there are no correlations L_c is the sum of the particle diameter and sensor diameter. This problem is an example of *spatial aliasing.* If there are wavelengths in the signal smaller than the sampling wavelength errors occur. To combat this problem the diameter of the sensors must be increased, which corresponds to low-pass filtering, or the sensors must be moved closer together, which corresponds to decreasing the sampling wavelength. If the particle diameter is L_c, the separation of the sensors L and the diameter of the sensors L_s the Nyquist criterion for non-aliased sampling is roughly $L_s + L_c \geq L$. If it is known that the vertical velocities will be much less than horizontal velocities this criterion can be relaxed to $L_s + L_c \geq L|v_x|/|v_y|$. This condition of small vertical velocities will be discussed in the next section.

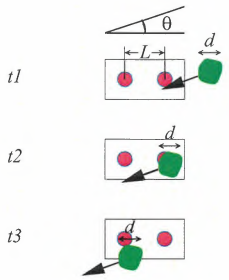

Figure 7. Vertical motion can give rise to spatial aliasing. There will only be correlations between the sensor elements if $L \sin\theta < d$.

4. Analysis Methods

4.1. Cross-correlation

This is the approach that has been used by most authors including Dent et al. (1998) and Tiefenbacher and Kern (2003). The cross-correlation of two sequences $\{x_i\}$ and $\{y_i\}$ at lag j is defined as

$$\rho(j) = \frac{\sum_{i\in A}(x_i - \overline{x})(y_{i+j} - \overline{y}_j)}{\sqrt{\sum_{i\in A}(x_i - \overline{x})^2 \sum_{i\in A}(y_{i+j} - \overline{y}_j)^2}} \tag{10}$$

The sums are taken over a time interval A of width n samples, for example $k - n/2 \ldots k + n/2$. $\overline{x}$ and $\overline{y}$ are the window averages. Sometimes it is not always clear exactly how these have been defined but for consistency this should be $\overline{x} = 1/n \sum_i x_i$ and $\overline{y}_j = 1/n \sum_i y_{i+j}$. Other variants that are symmetrical between x and y are possible. The velocity is then calculated by finding the value of j that maximises $\rho(j)$, and then the velocity is estimated using $\hat{v}_x = L\nu_s/j$, where ν_s is the sampling frequency and L the distance between the sensors. The velocity is usually thought of as being the velocity calculated at time $k\nu_s$ but a more accurate approximation would be to take it as the velocity at time $\nu_s(k + j/2)$. In either case this suggests that the velocity can only be calculated as lying in intervals of width $L\nu_s$ and that this is a fundamental design restriction. This is not the case since $\rho(j)$ can be approximated at any value of j using interpolation to gain additional precision.

A strength of this method is that it is invariant to shifts and scaling of the signal and it is straightforward. That is the same lag will be found for $ax + b$ and $cy + d$ for all non-zero constants a, b, c and d. This is useful if each combined sensor and amplifier system has different gains and offsets, since this method will automatically account for this. However the time length of any experiment is usually no more than a few minutes and over this period the electronics should be stable and show little drift. This means that the offset and gain can be chosen once for the whole sequence and should be accurate. Even if this is not possible, it would be better first to perform a filtering and transformation step, to normalise the data, and then to calculate the correlation. This will only fail if one of the sensors changes in some way as the avalanches passes, for example if some snow sticks to the front of one sensor, but not the other. This effect can easily be checked for by comparing the signal level before and after the avalanche.

Subtracting the mean from each signal before calculating the cross-correlation is similar to applying a high-pass filter and throws away an important part of the signal: its absolute value. It is easy to conduct examples where this method will perform badly. This is shown in fig. 8. The signals are identical triangular waves with a lag of 0.1 s with a very small amount (standard deviation 1×10^{-3}) of zero mean Gaussian noise. A window width of 0.3 s was used, corresponding to 1000 samples. Smaller window widths give even worse results. The search range was restricted to ± 1.5 s. Larger search ranges give larger errors.

The errors can be eliminated by choosing a window width that is greater than the period (1 s). What this figure shows is that provided the window includes a turning point from each signal, the correct lag is calculated, and the error increases smoothly with the noise. In this example the noise is so small the error is not visible. The correlation function calculated for the time a is shown in the lower left figure and shows a well defined peak at the correct lag. The middle lower figure shows the correlation function at time b. In this case the two peaks are only just contained at the edge of the window and the maximum is much less distinct. The lower right figure shows the correlation function calculated at time c. Now the two peaks are not in the window. Where neither peak is in the window the two functions match almost perfectly so the correlation function is almost 1. For large lags there is one turning point included and the correlation falls off. The reason for this behaviour is obvious. By subtracting of the mean and normalising by the mean squared deviation any two straight lines are brought into a perfect match. This means that this method is only sensitive to changes in the curvature (second derivative) of the signal.

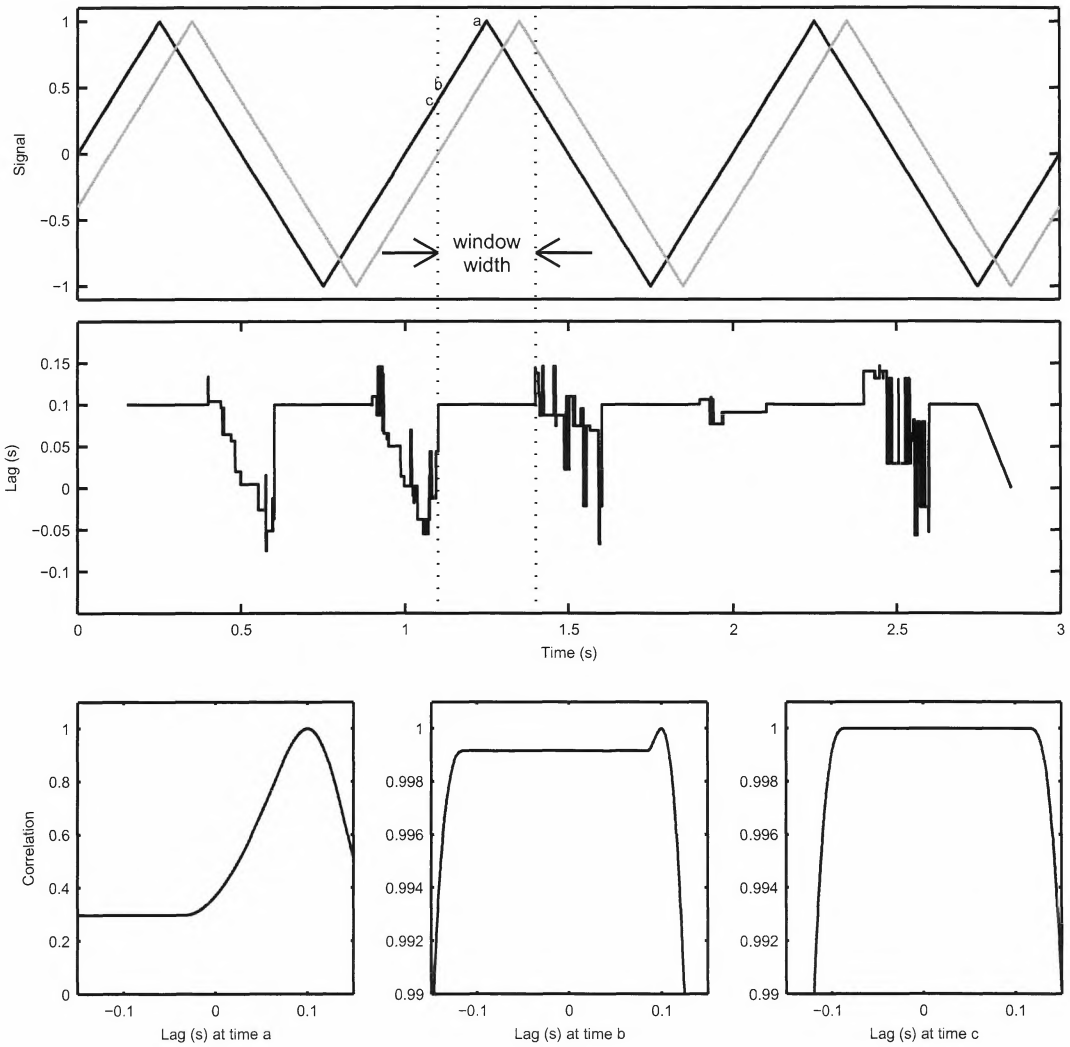

Figure 8. Failure of cross-correlation approach. The upper graph shows two nearly identical signals with a 0.1 s lag. The middle graph shows the calculated lag using maximum cross-correlation. The lower three figures show the cross-correlation function at the three points a, b and c marked in the upper figure.

4.2. Modelling the Signal

To perform any kind of analysis, the first step is understanding what we measure. Since sensors are generally fixed on approximately flat plates which are impermeable to the flow the local velocity normal to the sensor will be zero. So that to a good approximation the flows can be treated as two dimensional. Since little is known about the reflectivity of snow or other granular materials, we make no assumptions about the reflectivity field. Instead we assume a general function $f(\mathbf{x}, t)$, which depends on space and time, that specifies the signal that would be output from the sensor if it were positioned in the flow at position $\mathbf{x} = (x, y)$ at time t. This value will be a combination of the reflectivity of the snow smoothed over some volume in space according to the sensor's size, the amplification, the temporal smoothing, the digitising and finally the normalisation. This signal is then advected according the flow velocity while changing only slowly due to three-dimensional effects and physical processes between the grains. f satisfies the advection equation

$$\frac{\partial f}{\partial t} + \mathbf{v} \cdot \nabla f \approx 0. \tag{11}$$

Eq. 11 is the starting point for any analysis. In this paper we will not consider spatial variation in the velocity field $\mathbf{v}(\mathbf{x}, t)$. These can be included but considerably complicate the analysis without introducing any new features. Given this assumption, eq. 11 is easily solved. The characteristics of this equation are the trajectories of particles and since the velocity does not depend on position there is only one trajectory

$$\mathbf{x}_t(t) = \int_0^t \mathbf{v}(s) ds. \tag{12}$$

And then

$$f(\mathbf{x} + \mathbf{x}_t(t), t) = f(\mathbf{x}, 0), \tag{13}$$

or

$$f(\mathbf{x}, t) = f(\mathbf{x} - \mathbf{x}_t(t), 0). \tag{14}$$

This means that a sensor at position $\mathbf{x_i}$ will output a signal

$$f_i(t) = f(\mathbf{x}_i, t) = f(\mathbf{x}_i - \mathbf{x}(t), 0) = f(\mathbf{x}_i - \mathbf{x}(t)), \tag{15}$$

where f is evaluated at $t = 0$ when no time argument is given.

Since the f_i are normalised to have mean zero, we can assume that the mean of f is zero and define the auto-correlation function as

$$c(\mathbf{x}) = E[f(\mathbf{x} + \mathbf{y}, t) f(\mathbf{y}, t)] = \frac{1}{A} \iint_A f(\mathbf{x} + \mathbf{y}, t) f(\mathbf{y}, t) \mathbf{dy} = \frac{1}{T} \int_0^T f(\mathbf{x} + \mathbf{y}, t) f(\mathbf{y}, t) dt \tag{16}$$

The auto-correlation function can be defined as an average over different fields f realised in different experiments, or as an average over space at one point in time, or as an average over time for two fixed points. If we assume ergodicity, stationarity and homogeneity these will be equivalent. These conditions will not be exactly true, but one can hope that they will be approximately true and check the accuracy later. The success of the method does not rely on them holding, but they are useful simplifying assumptions for the analysis. We also assume isotropy so that $c(\mathbf{x})$ is a function only of $|x|$. These rather technical assumptions considerably simplify the analysis and are natural. If more data becomes available they can be tested. Different degrees of variation in downslope and slope-normal directions can easily be incorporated by scaling the coordinates.

Since a drawback of the cross-correlation method in section 4.1 was that it was invariant under independent transformations of the functions, we consider a new method that is only

invariant when both signals are transformed identically. This means that variations in mean levels and gradients will give a signal. We work in the continuous domain for convenience but it is straightforward to convert to the discrete domain using Fourier series.

4.3. Minimum Squared Discrepancy

A general approach to constructing analysis methods would attempt to have some of the properties of maximum likelihood estimation, that is minimising residuals. In this paper we will only consider two element sensors but the method can be generalised. Then for two sensors separated by a distance L we would expect $f_1(t+\tau/2) - f_2(t-\tau/2)$ to be small when $\tau = L/v_x$. Thus we consider the method that minimises

$$e(\tau) = \int [f_1(t+\tau/2) - f_2(t-\tau/2)]^2 w(t) dt, \tag{17}$$

where $w(t)$ is a weight function. Note that this is symmetric with respect to f_1 and f_2. If the integrand were unsymmetric with only one of the functions lagged, for example $f_1(t) - f_2(t-\tau)$, it can be shown that there are extra errors introduced that can be significant. The weight function $w(t)$ determines not only the width of the region over which the data is used but also its relative importance.

We will consider only gradual variations in the velocity, so we write

$$\mathbf{x}_t(t) = \mathbf{v}t + \mathbf{a}t^2/2 \tag{18}$$

where $\mathbf{v}$ is the velocity at $t = 0$ and $\mathbf{a}$ the acceleration. Using eq. 15

$$f_i(t) = f(\mathbf{x}_i - \mathbf{v}t - \mathbf{a}t^2/2). \tag{19}$$

Combining this with eq. 16 gives

$$E[\{f_1(t+\tau/2) - f_2(t-\tau/2)\}^2] = 2c(0) - 2c(d(t,\tau)), \tag{20}$$

where

$$\begin{aligned} d(t,\tau) &= |\mathbf{x_1} - \mathbf{x}_2 - \mathbf{v}(t+\tau/2) + \mathbf{v}(t-\tau/2) - \mathbf{a}(t+\tau/2)^2/2 + \mathbf{a}(t-\tau/2)^2/2| \\ &= |\mathbf{x_1} - \mathbf{x}_2 - \mathbf{v}\tau - \mathbf{a}t\tau|. \end{aligned} \tag{21}$$

Therefore using eq. 16

$$\begin{aligned} E[e(\tau)] &= \int E[\{f_1(t+\tau/2) - f_2(t-\tau/2)\}^2] w(t)\, dt \\ &= \int [c(0) - c(d(t,\tau))] w(t)\, dt. \end{aligned} \tag{22}$$

It is clear that this will be approximately minimised by choosing τ so as to minimise $d(t,\tau)$, thus justifying the earlier assumption that the maximum cross-correlation occurs at the point of closest approach.

In order to calculate the errors and the probability of failure (see appendix A) we need to calculate $E[\dot{e}(\tau)]$ and $E[\ddot{e}(\tau)]$. Differentiating eq. 21 with respect to τ we have

$$\frac{d}{d\tau} d(t,\tau) = \frac{d}{d\tau} |\mathbf{x_1} - \mathbf{x}_2 - \mathbf{v}\tau - \mathbf{a}t\tau| \tag{23}$$

$$= -\frac{(\mathbf{v} + t\mathbf{a}) \cdot (\mathbf{x_1} - \mathbf{x}_2 - \mathbf{v}\tau - \mathbf{a}t\tau)}{d(t,\tau)}, \tag{24}$$

and

$$\frac{d^2}{d\tau^2} d(t,\tau) = \frac{|\mathbf{v} + t\mathbf{a}|^2}{d(t,\tau)} + \frac{[(\mathbf{v} + t\mathbf{a}) \cdot (\mathbf{x_1} - \mathbf{x}_2 - \mathbf{v}\tau - \mathbf{a}t\tau)]^2}{d(t,\tau)^3}. \tag{25}$$

Thus

$$E[\dot{e}(\tau)] \;=\; 2\int (\mathbf{v}+t\mathbf{a})\cdot(\mathbf{x_1}-\mathbf{x}_2-\mathbf{v}\tau-\mathbf{a}t\tau)\frac{\dot{c}(d(t,\tau))}{d(t,\tau)}w(t)dt. \tag{26}$$

Now we Taylor expand in $a=|\mathbf{a}|$ and make the first choices about $w(t)$. If $w(t)$ is an even function of t that is $w(t)=w(-t)$ then odd powers of t in the integral disappear and

$$E[\dot{e}(\tau)] \;=\; 2\int \frac{[\mathbf{v}\cdot(\mathbf{x_1}-\mathbf{x}_2-\mathbf{v}\tau)\dot{c}(|\mathbf{x_1}-\mathbf{x}_2-\mathbf{v}\tau|)+O(a^2)]}{|\mathbf{x_1}-\mathbf{x}_2-\mathbf{v}\tau|}w(t)dt. \tag{27}$$

Terms of order a would remain here if an unsymmetric method in τ were used. Nothing in the integral now depends upon t except for $w(t)$ so

$$E[\dot{e}(\tau)] \;\approx\; 2[\mathbf{v}\cdot(\mathbf{x_1}-\mathbf{x}_2-\mathbf{v}\tau)\frac{\dot{c}(|\mathbf{x_1}-\mathbf{x}_2-\mathbf{v}\tau|)}{|\mathbf{x_1}-\mathbf{x}_2-\mathbf{v}\tau|}\int w(t)dt. \tag{28}$$

At the minimum of $e(\tau)$, $\dot{e}(\tau)=0$,so we need to look for solutions of eq. 28 equal to zero. Suppose that the sensors are a distance L apart along the x-axis then eq. 28 becomes

$$E[\dot{e}(\tau)] \;\propto\; [\tau(v_x^2+v_y^2)-Lv_x]\frac{\dot{c}\left(\sqrt{(L-v_x\tau)^2+v_y^2\tau^2}\right)}{\sqrt{(L-v_x\tau)^2+v_y^2\tau^2}}. \tag{29}$$

If $\dot{c}\left(\sqrt{(L-v_x\tau)^2+v_y^2\tau^2}\right)\approx 0$ for all τ in eq. 28 this means that there are no correlations between the sensors. This is the case discussed in subsection 3.2. This occurs if the minimum value of $d(0,\tau)=Lv_y/\sqrt{v_x^2+v_y^2}$ is so large that $c(d(0,\tau))\approx 0$. When there are no appreciable correlations between the sensors it is of course impossible to calculate the velocity by any method. This failure can be minimised by reducing L, ensuring that the sensors are aligned with the flow so that v_y is as small as possible or by increasing the correlation length by using sensors that average over a large spatial area.

If $\dot{c}\neq 0$ then eq. 28 is zero when

$$\tau=\frac{\mathbf{v}\cdot(\mathbf{x_1}-\mathbf{x_2})}{|\mathbf{v}|^2}+O(a^2)=\frac{v_xL}{v_x^2+v_y^2}. \tag{30}$$

This means that if we estimate the x-axis velocity by $\hat{v}_x=L/\tau$ we in fact calculate

$$\hat{v}_x=\frac{L}{\tau}=L\frac{v_x^2+v_y^2}{v_xL}=v_x+\frac{v_y^2}{v_x}. \tag{31}$$

Thus direct maximisation of the correlation between two sensors does not measure the velocity in the direction of the sensors but this more complicated function. If v_y is small this will be a good approximation, but in other cases the results can be severely biased and the estimated velocity will be larger than the true velocity by v_y^2/v_x. The problem is discussed in section 2 and illustrated in the left two parts of figure 4. Even though the horizontal speeds are different in these two figures the output signals are identical. This is the major problem with one-dimensional arrays of sensors. If there is some way of calculating the vertical velocity v_y then the bias can be eliminated by solving for v_x as a function of $\hat{v}_x$ and v_y in equation eq. 31. The obvious way to do this is to build a two-dimensional sensor array with closely spaced vertical sensors so that v_y can be separately estimated. A simple sensor that can do this is shown in fig. 10. If it is not feasible to install a new sensor another approach is to alter the vertical length scale by averaging vertically. If the sensors averages over a large vertical region so that the vertical dimensions are λL

such as in fig. 9 then the effective vertical velocity is reduced by a factor λ so that eq. 31 becomes

$$\hat{v}_x = v_x + \frac{v_y^2}{v_x \lambda^2}. \tag{32}$$

Thus if the aspect ratio is 4 the error will be reduced by a factor of 16. Building a sensor with such an aspect ratio could be achieved by using a lens, appropriate choice of sensor and orientation, or by stacking sensors and combing their output.

Figure 9. One-dimensional array of two sensors designed to reduce bias from vertical velocities. The active region of the sensors averages over a large vertical region to reduce bias.

4.4. Gaussian Correlation

In this section we assume that the correlation function $c(x)$ is Gaussian and we also use a Gaussian weight function $w(t)$. This choice is made because the calculation are then easy to perform and it is sufficient to demonstrate the dependence of the errors on the design parameters and the properties of the flow. Analysis could also be performed with correlation functions for hard disc systems or using correlation functions measured from the data. We do not expect this would significantly change the conclusions.

We precede as in the previous section to analyse the method using the expectation of the derivative of $e(\tau)$. We define $d_0(t) = d(t+\tau_0, t-\tau_0)$, where τ_0 is the lag that minimises the squared discrepancy. Thus

$$d_0 = \frac{L v_y}{v}, \tag{33}$$

which has a simple interpretation. d_0 is the point of closest approach to sensor 2 of a point moving with the flow that passes over sensor 1 at around time 0. Expanding in powers of a and removing terms odd in t

$$E[e(\tau_0)] = 2W_0 \left[c(0) - c(d_0)\right] + O(a^2), \tag{34}$$

$$E[\dot{e}(\tau_0)] = O(a^2), \tag{35}$$

$$E[\ddot{e}(\tau_0)] = -2W_0 v^2 \frac{\dot{c}(d_0)}{d_0} + O(a^2), \tag{36}$$

where $W_0 = \int w(t)\, dt$. More complicated expressions can be calculated for the variances, $V[\dot{e}(\tau_0)]$ and $V[\ddot{e}(\tau_0)]$, but these will not be included here. Instead we illustrate how these results can be used by taking $w(t)$ to be a Gaussian function of time scale T and assuming that the correlation function c is also a Gaussian with length scale given by L_c.

$$w(t) = \frac{e^{-\frac{t^2}{2T^2}}}{2T} \qquad c(t) = C_0 \frac{e^{-\frac{t^2}{2L_c^2}}}{\sqrt{2\pi}} \tag{37}$$

This choice is made because the integrals for the expectations $E[e]$, $E[\dot{e}]$ and $E[\ddot{e}]$ can all be performed exactly and the integrals for the variances $V[e]$, $V[\dot{e}]$ and $V[\ddot{e}]$ can be easily approximated by expanding in powers of a. What this approximation corresponds

to is assuming that Ta/v is small, where $v = |\mathbf{v}|$. This is a natural assumption since methods of this type will not work well if the velocity varies significantly over the window. In the following analysis we generally work to the lowest non vanishing term. There is no significant difference between a direct correlation method and a residual method.

The probability of failure is given by

$$p(\text{fail}) \approx \frac{3}{4} \frac{1 + \exp\left(\frac{L^2 v_y^2}{L_c^2 v^2}\right)}{\sqrt{1 + 4T^2 v^2 / L_c^2}} \tag{38}$$

The numerator contains a positive exponential term with argument $\frac{L^2 v_y^2}{L_c^2 v^2} = d_0^2 / L_c^2$. In order for the failure probability to be small this must be of order 1. Since the exponential term is added to 1 there is little advantage in making it very small. The term will be order one in two situations. If the spacing of the sensors is sufficiently close that no spatial aliasing occurs for all v_x and v_y (sec. 3.2) that is $L \leq L_c$. Or when the angle of the velocity to the sensor axis is sufficiently small, that is $v_y/v \leq L_c/L$. For most sensors built so far the spacing is at least 5 mm which is well above the smallest correlation lengths which will be of the order of the particle diameters around 1 mm. Thus there will be no detectable correlations except for velocities with angle less than $\approx \tan^{-1}(1/5)$. However, the large scale features of a snow avalanche may be many metres in size (Nishimura et al. (1987)) and these will be detected as a correlation between both sensors for any velocity direction.

This result is exactly what would be expected. Eq. 36 contains a factor $\dot{c}(d_0)$ and it is one over this that appears as the numerator in eq. 38 (since $d_0^2/\dot{c}(d_0)^2 \propto \exp(d_0^2/L_c^2)$). For many correlation function $\dot{c}(d) = 0$ for all d greater than some critical value and in that case eq. 38 diverges and failure becomes a certainty.

Given that the numerator of eq. 38 is order 1 the probability of failure can only be small if the denominator is large, which occurs if Tv/L_c is large. This also has a natural interpretation. Tv is the length of material that has passed over the sensor. Dividing this by the correlation length L_c give the approximate number of independent samples. And this is the usual reduction in variance with sample size. If this is large and the exponential is limited then eq. 38 becomes

$$p(\text{fail}) \approx \frac{3}{4} \frac{L_c}{Tv} \tag{39}$$

We focus on the case where the vertical velocities are small and consider $u_y = O(a^{1/2})$. The probability of failure, from eq. 38, will then be small if $T = O(a^{-1/2})$. This is the most interesting gearing because the leading order terms contain vertical velocity terms and acceleration terms. Using the results in the appendix and Gaussian correlation and weighting functions we get.

$$p(\text{fail}) \approx \frac{3}{4}\frac{L_c}{uT} + \frac{3}{16}\frac{[L^2(7a_x^2 + 3a_y^2) - L_c^2(2a_x^2 + 5a_y^2)]T}{u_x^3 L_c} + \frac{3}{8}\frac{u_y^2}{u_x^2}\frac{L^2 - L_c^2}{L_c u_x T} - \frac{3}{32}\frac{L_c}{u_x^3 T^3} \tag{40}$$

$$E[\hat{v}_x] - v_x = \frac{v_y^2}{v_x} + \frac{T^2 a^2}{v_x} \tag{41}$$

$$V[\hat{v}_x] = \frac{L_c v_y^2}{4 v_x T} + \frac{L_c(a_y^2 + 3a_x^2)T}{8 v_x} \tag{42}$$

Now that the acceleration terms are included it is clear that there is a value of T that minimises $p(\text{fail})$, which scales like v_x/a if $L \approx L_c$. For such large T however the bias would be of order v_x, so that though the method would be likely to find a minimum in the correct region, the error would be unacceptable. This illustrates part of the tradeoff

between large T maximising the chance of finding a minimum, but large T also coupling to accelerations and increasing the errors. This is also shown in the variance equation 42. Large T decreases the first term in proportional to the number of *independent samples* Tv_x/L_c, but increases the second term because of acceleration. The variance term will be minimised by a T approximately v_y/a which is order $a^{-1/2}$ as we assumed. If $T = v_y/a$ then the bias term will just be of the same order v_y^2/v_x. This choice of T thus provides a compromise between vertical velocity errors and acceleration errors. The bias equation 41 also shows that the all the errors to this order increase the apparent mean velocity.

Once the velocity estimate $\hat{v}_x$ has been formed we can use these equations to estimate the errors. This can be done as follows. The expected residual will be

$$E[e(\tau_0)] = C_0 \frac{L^2(v_y^2 + a^2T^2)}{2L_c^2 v_x^2}, \tag{43}$$

and the curvature

$$E[\ddot{e}(\tau_0)] = \frac{C_0 v_x^2}{L_c^2}. \tag{44}$$

If we equate the measured residual $\hat{e}(\tau_0)$ and curvature $\hat{\ddot{e}}(\tau_0)$ to these equations we can estimate the errors. Using eqs. 43 and 44

$$\frac{E[e(\tau_0)]}{E[\ddot{e}(\tau_0)]} = \frac{L^2(uy^2 + T^2a^2)}{2u_x^4} \tag{45}$$

Thus the bias can be estimated as

$$-\frac{2u_x^3}{L^2} \frac{\hat{e}(\tau_0)}{\hat{\ddot{e}}(\tau_0)} \tag{46}$$

The beauty of this is that it is not necessary to directly estimate C_0 or L_c. Thus our revised estimate of the velocity is

$$\hat{v}_x' = \frac{L}{\tau_0} - \frac{2u_x^3}{L^2} \frac{\hat{e}(\tau_0)}{\hat{\ddot{e}}(\tau_0)} \tag{47}$$

which is bias free to this order.

The variance equation eq. 42 can be similarly estimated if we approximate $(a_y^2 + 3a_x^2) \approx 2a^2$ it becomes

$$V[\hat{v}] = L_c \frac{v_y^2 + T^2a^2}{4v_xT} = \frac{L_c u_x^3}{2TL^2} \frac{E[e(\tau_0)]}{E[\ddot{e}(\tau_0)]} \tag{48}$$

Unfortunately it is not possible to estimate the variance without also estimating the correlation length L_c, but this can be done using standard techniques. Eq. 48 is the variance estimate of $\hat{v}$ not of the bias corrected velocity $\hat{v}'$. The variance of this will be larger since there is the variance of the correction term to consider. For this reason it is probably best to regard the bias correction as an error estimate rather than performing it directly. The one standard deviation confidence interval will then be roughly

$$\left[\frac{L}{\tau_0} - \frac{2u_x^3}{L^2} \frac{\hat{e}(\tau_0)}{\hat{\ddot{e}}(\tau_0)} - \frac{v_x}{L}\sqrt{\frac{L_c v_x}{2T} \frac{\hat{e}(\tau_0)}{\hat{\ddot{e}}(\tau_0)}}, \quad \frac{L}{\tau_0} + \frac{v_x}{L}\sqrt{\frac{L_c v_x}{2T} \frac{\hat{e}(\tau_0)}{\hat{\ddot{e}}(\tau_0)}}\right], \tag{49}$$

A check on the assumptions could also be performed by using the calculated $\hat{v}_x$ to estimate the acceleration a_x.

The design criterion for correlation sensors can thus be summarised as follows in decreasing order of importance

$L \approx L_c$ Eliminates spatial aliasing and allows correlations at all velocity angles. If this is not possible then the sensor can only be operated in the range $\frac{v_y}{v}\frac{L}{L_c} = O(1)$

$f_s > 2v/L_c$ The sampling frequency must be high enough to prevent temporal aliasing
$\frac{Tv}{L_c} \ll 1$ Good sample statistics
$\frac{Ta}{v^2} \ll 1$ Low bias and variance
$\frac{v_y}{v} \ll 1$ Low bias and variance
Confidence intervals should be calculated according to eq. 49

The next two sections discuss how to reduce and eliminate the errors induced by vertical velocities and accelerations.

4.5. 2D FLOW

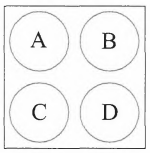

Figure 10. Two-dimensional array of four sensors designed to measure vertical and horizontal velocities. The active region of the sensors is as large as possible to reduce spatial aliasing.

A full discussion of design criteria for two-dimensional sensors is contained in McElwaine (2003), but a rough approach is straightforward. The most important criterion for a 2d sensors is that $L \approx L_c$ or smaller so that there are always the appropriate correlations between the sensors. Figure 10 shows a sensor with four photo-transistors arranged on a square. The optimal lag τ can be calculated between six pairs (AB, AC, AD, BC, BD, CD) in a similar way as for 1D sensors. Let τ_x and τ_y minimise the respective expressions

$$e_x(\tau_x) = \int w(t)\left\{[f_A(t+\tau_x/2) - f_B(t+\tau_x/2)]^2 + [f_C(t+\tau_x/2) - f_D(t+\tau_x/2)]^2\right\} dt$$
$$e_x(\tau_y) = \int w(t)\left\{[f_A(t+\tau_y/2) - f_C(t+\tau_y/2)]^2 + [f_B(t+\tau_y/2) - f_D(t+\tau_y/2)]^2\right\} dt,$$

where f_A, f_B, f_C and f_D are the signals from each photo-transistor. By combining the signals in this way, rather than calculating separate lags for each pair, the errors can be reduced. Diagonal correlation lags τ_{AD} and τ_{CB} can also be calculated between AD and CB respectively. If we let τ_x and τ_y be the minimising correlation lags then

$$\frac{L}{\tau_x} = \frac{v_x^2+v_y^2}{v_x} \quad \frac{L}{\tau_y} = \frac{v_x^2+v_y^2}{v_y} \tag{50}$$
$$\frac{L}{\tau_{AD}} = \frac{v_x^2+v_y^2}{v_x+v_y} \quad \frac{L}{\tau_{CB}} = \frac{v_x^2+v_y^2}{v_x-v_y} \tag{51}$$
$$\tag{52}$$

The bias and variance of each of the τ's can be calculated using the previous methods. Then they can then be suitably combined to produce an estimate of v_x and v_y with minimum error. Suppose that σ_x, σ_y, σ_{AD} and σ_{CB} are the expected root mean squared errors. Then the minimum expected root mean squared error estimates can be calculated by minimising

$$\frac{\left[\frac{L}{\tau_x} - \frac{v_x^2+v_y^2}{v_x}\right]^2}{\sigma_x^2} + \frac{\left[\frac{L}{\tau_y} - \frac{v_x^2+v_y^2}{v_y}\right]^2}{\sigma_y^2} + \frac{\left[\frac{L}{\tau_{AD}} - \frac{v_x^2+v_y^2}{v_x+v_y}\right]^2}{\sigma_{AD}^2} + \frac{\left[\frac{L}{\tau_{CD}} - \frac{v_x^2+v_y^2}{v_x-v_y}\right]^2}{\sigma_{CB}^2} \tag{53}$$

The expression is complicated to minimise analytically especially as the estimated squared errors, σ_x^2 etc., will be functions of v_x and v_y. It is however easy to minimise numerically.

If the the flow were between directions AD and AB, then σ_y and σ_{CD} would be large and the solution would be weighted towards τ_x and τ_{AD}. The result would roughly be

$$v_x = \frac{L\tau_x}{\tau_x^2 + (\tau_{AD} - \tau_x)^2} \quad v_y = \frac{L(\tau_{AD} - \tau_x)}{\tau_x^2 + (\tau_{AD} - \tau_x)^2}. \tag{54}$$

4.6. Continuous velocity estimation

The errors due to accelerations in the previous analysis are caused by assuming a fixed velocity over the window width. If instead of this we try to estimate the varying function $v(t)$ at all times it is possible to eliminate or at least reduce this source of error. Eq. 17 can be naturally generalised to

$$e[\tau] = \int [f_1(t + \tau(t)/2) - f_2(t - \tau(t)/2)]^2 dt, \tag{55}$$

where $\tau(t)$ is a function of time for the whole measurement period, $e[\tau]$ is now a functional and the integration is to be performed over the whole sample. In order for this to be a well posed problem it is necessary to constrain $\tau(t)$ and this is done by introducing a penalty functional term

$$\lambda \int \left(\frac{d\tau(t)}{dt}\right)^2 dt \tag{56}$$

where λ determines the degree of smoothing enforced on τ. The Euler-Lagrange equation for this system is

$$\lambda \frac{d\tau(t)^2}{dt^2} = [\dot{f}_1(t + \tau(t)/2) + \dot{f}_2(t - \tau(t)/2)][f_1(t + \tau(t)/2) - f_2(t - \tau(t)/2)]. \tag{57}$$

This equation can be efficiently solved using multi-grid techniques and the velocity calculated as $v_x(t) = L/\tau(t)$. A full discussion will be included in future work.

5. Results

Experiments were carried out at the SLF chute in Davos. Preliminary results and three different methods of analysis will be briefly mentioned. A full analysis will appear in a later paper.

The velocity sensor array consists of a 5×5 matrix of photo diode/photo transistor pairs. First we analyse the data using the traditional method of Dent (eq. 10). For each row of the sensor array, the cross correlation function can be computed for 10 pairs of signals corresponding to 10 combinations of each two time shifted sensor signals related to 10 different stream-wise sensor spacings.

Assuming that the velocity of the flow does not change significantly while passing the sensor array which has a stream-wise extension of 2 cm, the accuracy of the velocities obtained from one row of the sensor array can be estimated by statistical analysis of the velocities measured by all possible sensor pair combinations of the row. Previous experimental setups of optical correlation velocity measurements in avalanches Nishimura et al., Dent et al. (1993, 1998) were using only one pair of signals and therefore did not allow such an error analysis.

Figure 11 shows a plot of the mean velocities obtained from all 5 sensors of row 3 and 5 of the sensor array where the error bars indicate the standard deviation of the mean velocity, $\bar{v}$, which is an average of the velocities obtained by correlation of each of the 10

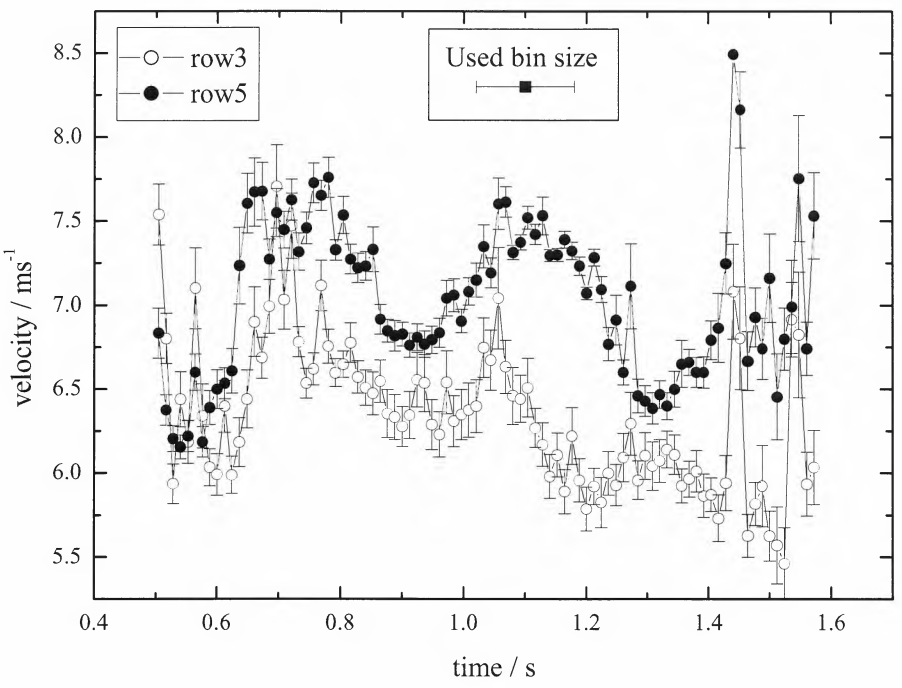

Figure 11. Velocity measurements by row 3 and 5 of the sensor array performed at April 3, 2002.

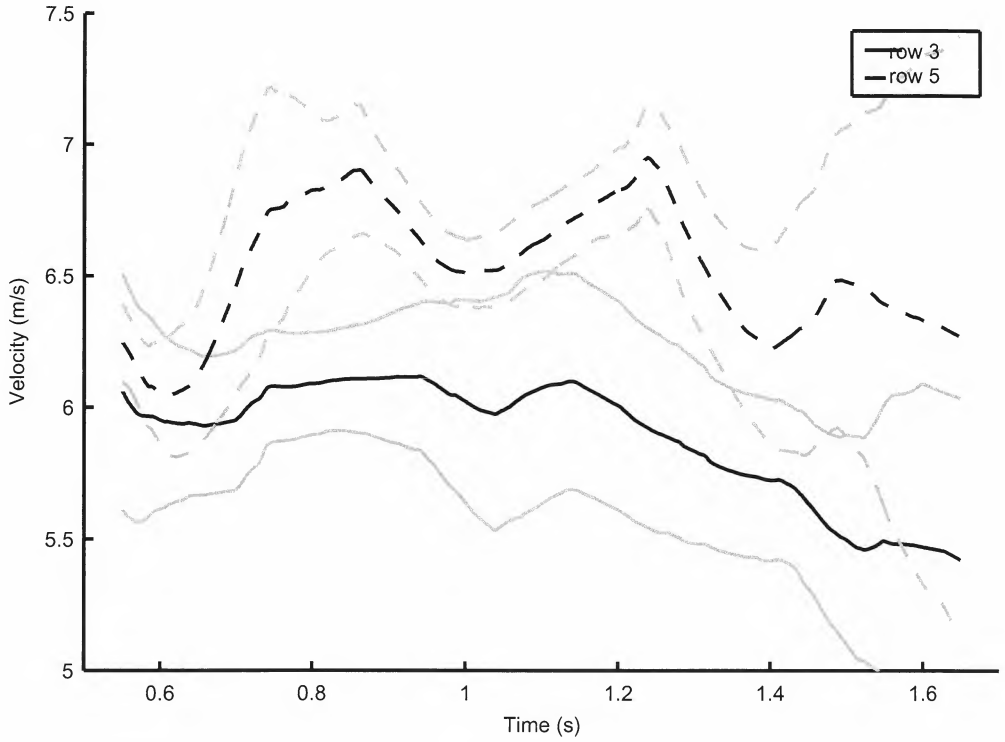

Figure 12. Continuous velocity estimates with populations standard deviations (grey).

sensor pairs of a row of the sensor array. The correlation functions have been evaluated using a 0.16 s interval every 0.012 s.

The vertical distance between row 3 and 5 of the sensor array is 2.1 cm where row 3 is situated 2.1 cm above the sliding surface. Taking into account the errors mentioned above, the velocities obtained by the two sensor rows are significantly shifted as is shown in fig.11. Interpreting the plot with respect to the vertical spacing of the rows, the shear can be estimated to be approximately 25 s^{-1} in the flow layer between 2.1 cm and 4.2 cm above the sliding surface.

Figure 12 shows the velocities calculated using the continuous approach of section 4.6. The standard deviations are calculated from the ten different velocity measurements pairs at each row height. The gross features of the two results are clearly similar but the overall velocities are considerably lower. So much so that the error intervals of the estimates do not overlap. This is not that surprising as these are not true error estimates, but instead highly correlated estimates of the variance in the velocity. That is they do not account for any bias effects resulting from vertical velocities, so the true horizontal velocities maybe considerably lower. Secondly the sensors are all closely positioned so that the errors between the sensors cannot be assumed to be independent. Roughly speaking if the correlation between the errors is ρ then the true standard deviation will be larger by a factor $1/(1-\rho)$.

6. Conclusions

The work in this paper is still ongoing and is by no means complete. In particular a detailed analysis of the auto-correlations should be performed and also an explanation of the large differences in the results of the two analysis methods in the last section. Though correlation sensors are a very useful tool great care should be exercised in interpreting the data and particular care taken to understand the uncertainties in the estimations. In particular the usual estimate of velocity $\hat{v}_x = L/\tau$ is in fact an estimate of

$$v_x + \frac{v_y^2}{v_x} + \frac{T^2 a^2}{v_x}, \tag{58}$$

and will therefore be considerably larger then the true velocity v_x unless v_y^2/v_x^2 and T^2a^2/v_x^2 are small. The analysis also demonstrates that it should be possible to greatly reduce the errors by using closely spaced two-dimensional arrays of sensors that are as small as the smallest correlation lengths which are of the order of the grain size (1 mm).

Acknowledgements

J. N. McElwaine was supported by a University Research Fellowship from the Royal Society. The authors would like to thanks to Martin Kern for help with carrying out the experiments and building the sensor and Rick Munro for many helpful comments.

Appendix

A. Estimating Parameters

It is a well known result of classical statistics that the best asymptotic estimators are maximum likelihood estimators (MLE). Unfortunately to apply these methods the probability density function of the reflectivity would have to be specified by a parametric model.

If this could accurately be done this would provide the best method of analysis. If a bad parametric model is applied however the estimators may be very poor indeed so until more data is available we use a non-parametric approach which attempts to be similar to MLE methods, but without requiring a complete probabilistic description. Our methods are based on minimising a sum of residuals and if these residuals are regarded as independent and Gaussian then this is equivalent to an MLE estimate.

Suppose that we estimate the speed of the flow $\hat{v}_x = L/\hat{\tau}$ by minimising a function $e(\tau)$. To estimate the accuracy of the method we wish to find the *bias* or expected error $E[\hat{\tau}]$, the variance in the estimate $V[\hat{\tau}] = E[\hat{\tau}^2] - E[\hat{\tau}]^2$ and the probability that there is a minimum close to the true value. In this appendix expressions for these values are derived.

Let $e(\tau)$ be a function of the data and assume that the true minimum occurs at τ_0. Due to noise and other inaccuracies when we attempt to minimise $e(\tau)$ we will find the minimum at some other value $\hat{\tau} \neq \tau_0$. Taylor expanding to second order

$$e(\tau) = e(\tau_0) + \tau\dot{e}(\tau_0) + 1/2\tau^2\ddot{e}(\tau_0) \tag{59}$$

Thus the minimum will be found at at $\hat{\tau} = -\dot{e}(\tau_0)/\ddot{e}(\tau_0)$ provided that $\ddot{e}(\tau_0) > 0$. That is the method will succeed if $p(\ddot{e}(\tau_0) < 0)$ is small and the error will be $-\dot{e}(\tau_0)/\ddot{e}(\tau_0)$. The probability of failure can be bounded using Chebychev's inequality. Let $\mu = E[\ddot{e}(\tau_0)] > 0$ and $\sigma^2 = E[\ddot{e}(\tau_0)^2] - \mu^2$. Then

$$P(\ddot{e}(\tau_0) < 0) = P(a - \ddot{e}(\tau_0) > a) \leq P(|\ddot{e}(\tau_0) - a| > a) \leq \frac{E[|\ddot{e}(\tau_0) - a|^2]}{a^2} = \frac{\sigma^2 + (\mu - a)^2}{a^2}. \tag{60}$$

This upper bound is true for all a and is minimised by $a = (\sigma^2 + \mu^2)/\mu$ so

$$P(\ddot{e}(\tau_0) < 0) \leq \frac{\sigma^2}{\sigma^2 + \mu^2} \approx \frac{\sigma^2}{\mu^2} \tag{61}$$

This shows that the the method will have a high probability of success if $V[\ddot{e}(\tau_0)]/E[\ddot{e}(\tau_0)]^2$ is small. This bound is conservative and in many cases $\ddot{e}(\tau_0)$ will be well approximated by a normal distribution since it is the sum of many random variables. In this case the probability of failure will be estimated as $P(W \leq 0) = 1 - \mathrm{erf}\left(\frac{\mu_W}{\sigma_W}\right)$, where $\mathrm{erf}(x)$ is the error function. The bias of the method is $E[\hat{\tau}] = E\left[\frac{\dot{e}(\tau_0)}{\ddot{e}(\tau_0)}\right]$. Approximating $\dot{e}(\tau_0)$ and $\ddot{e}(\tau_0)$ as independent gives $E[\hat{\tau}] = E[\dot{e}(\tau_0)]E[1/\ddot{e}(\tau_0)]$. The method only finds a local minima when $\ddot{e} > 0$ and since this occurs with high probability only when σ^2/μ^2 is small we can write $E[1/\ddot{e}(\tau_0)] \approx 1/E[\ddot{e}(\tau_0)]$ so that $E[\hat{\tau}] = E[\dot{e}(\tau_0)]/E[\ddot{e}(\tau_0)]$. The variance of the estimate $V[\hat{\tau}]$ can be calculated using the same approximations as before

$$V[\hat{\tau}] = \frac{V[\dot{e}(\tau_0)]}{E[\ddot{e}(\tau_0)]^2} = \frac{V[\dot{e}(\tau_0)]}{E[\ddot{e}(\tau_0)]^2}. \tag{62}$$

Since the velocity is estimated using the rule $\hat{v}_x = L/\hat{\tau}$ the mean error in the estimated velocity is

$$\begin{aligned} E[\hat{v}_x - v_x] &\approx \frac{L}{E[\hat{\tau}]} - \frac{L}{v_x} \approx \frac{L}{\tau_0 - E[\dot{e}(\tau_0)]/E[\ddot{e}(\tau_0)]} - \frac{L}{\tau_0} \\ &\approx \frac{L}{\tau_0^2}\frac{E[\dot{e}(\tau_0)]}{E[\ddot{e}(\tau_0)]} = \frac{v_x^2}{L}\frac{E[\dot{e}(\tau_0)]}{E[\ddot{e}(\tau_0)]}. \end{aligned} \tag{63}$$

This assumes that the error is small compared to the true velocity. The variance in the estimated velocity can be estimated similarly

$$V[\hat{v}_x] \approx \frac{v_x^4}{L^2}\frac{E[\dot{e}(\tau_0)^2]}{E[\ddot{e}(\tau_0)]^2}. \tag{64}$$

These two eqs. 63 and 64 in conjunction with the following equation which gives the probability that the method fails

$$P(\ddot{e}(\tau_0) < 0) = \frac{V[\ddot{e}(\tau_0)]}{E[\ddot{e}(\tau_0)]^2} \tag{65}$$

give a means to quantatively evaluate different sensor designs and analysis algorithms. They can also be used to estimate the degree of uncertainty in a measurement, that is to calculate confidence limit or error intervals. To do this we need a means of estimating the various expectations in terms of the observed data. $E[\ddot{e}(\tau_0)]$ can be approximated as $\ddot{e}(\hat{\tau})$ in the same way as maximum likelihood estimation. This cannot be done however for $E[\dot{e}(\tau_0)]$ since at the minimum of course $\dot{e}(\hat{\tau}) = 0$. There is no general method for approximating this or the variances $V[\dot{e}(\tau_0)]$ and $V[\ddot{e}(\tau_0)]$, but given a model for the underlying data these can be approximated in terms of the total residual $e(\hat{\tau})$.

References

Dent, J. D., K. J. Burrel, D. S. Schmidt, M. Y. Louge, E. E. Adams, and T. G. Jazbutis: 1998, 'Density, Velocity and Friction Measurements in a Dry-snow Avalanche'. *Ann. Glaciol.* **26**, 247–252.

Jähne, B.: 1997, *Digital Image Processing. Concepts, Algorithms, and Scientific Applications.* Berlin: Springer, 4 edition.

McElwaine, J. N.: 2003, 'Calculation of Two-Dimensional Avalanche Velocities From Opto-Electronic Sensors'. To appear Ann. Glac.

Nishimura, K., N. Maeno, and K. Kawada: 1987, 'Internal Structures of large-scale avalanches revealed by a frequency analysis of impact forces.'. *Low. Temp. Sci., Ser. A* **46**, 91–98. In Japanese with English Summary.

Nishimura, K., N. Maeno, F. Sandersen, K. Kristensen, H. Norem, and K. Lied: 1993, 'Observations of the Dynamic Structure of Snow Avalanches'. *Ann. Glaciol.* **18**, 313–316.

Tiefenbacher, F. and M. A. Kern: 2003, 'Experimental devices to determine snow avalanche basal friction and velocity profiles'. *Cold Reg. Sci. Tech.* to appear.

Calculation of Two-Dimensional Avalanche Velocities From Opto-Electronic Sensors

J. N. McElwaine*

*Department of Applied Mathematics and Theoretical Physics,

Centre for Mathematical Sciences, University of Cambridge,

Wilberforce Road, Cambridge, CB3 0WA, UK

International Symposium on Snow and Avalanches

Davos, Switzerland, 2–6 June 2003

24th June 2003

Abstract

Opto-electronic sensors using infrared LEDs and photo-transistors have been used for measuring velocities in snow avalanches for more than ten years in America, Europe and Japan. Though they have been extensively used, how they should be designed and how the data should be processed has received little discussion. This

*jnm11amtp.cam.ac.uk

paper discusses how these sensors can be applied to measure two-dimensional velocities. The effects of acceleration and structure in the underlying field of reflectance are carefully accounted for. An algorithm is proposed for calculating the continuous velocity vector of an avalanche and a sketch of the mathematical analysis given. The paper concludes by suggesting design criteria for such sensors.

1 Introduction

Opto-electronic sensors have been used for a long time to measure the velocities inside granular flows. Some of the earliest work was done by (Nishimura et al., 1987) on snow avalanches and continued in (Nishimura et al., 1993). Early work was also done by (Dent et al., 1998) and measurements were taken from the "Revolving Door" avalanche path near Bridger Bowl, Montana.

The basic design of these sensors is simple. An infrared LED emits light that is reflected by the passing granular material and this is detected by an infrared-sensitive photo-transistor, amplified, digitised and stored on a computer. By comparing the signals from nearby sensors its is possible to calculate the velocity of the flow.

In theory it is possible to calculate many other pieces of information about the flow since the magnitude of the back scattered light depends on the density, type, size, and orientation of the snow crystals. However, though (Dent et al., 1998) tried to relate reflectivity to snow density he failed because crystal size and type are much more important than density. Some gross aspects of the flow can be determined however. For

example in deposited snow the signal will be constant, in a powder cloud the signal will be very low since no light from above can reach the sensor and the density is usually too low to significantly reflect light, and above the snow a high level will be detected due to ambient lighting.

Despite the wide spread use of opto-electronic sensors there appears to have been little work done on how these sensors can be applied to two-dimensional measurements. In (McElwaine and Tiefenbacher, 2003) a detailed analysis is developed for two element sensors and the standard cross-correlation algorithm is analysed in detail. The main results of this work are that the measured velocities are consistently too high by

$$\frac{v_y^2 + T^2 a_x^2 + T^2 a_y^2}{v_x} \tag{1}$$

where v_x is the velocity parallel to the sensor, v_y the perpendicular velocity, a_x and a_y the corresponding accelerations and T the width of the correlation window. The paper also shows that T must be sufficiently large so that $L_c/(Tv)$ is small, where L_c is the correlation length of the snow, in order that the minimum of the cross-correlation can be located and that $L_c v_y/(Lv)$, where L is the sensor element separation, must be small so that there are correlations between the sensor elements. These requirements that the bias is low, and that the correlation exists and can be found cannot be simultaneously satisfied unless v_y/v_x, Ta_x/v_x and Ta_y/v_x are all small. A novel analysis method is briefly presented that changes the time leading to acceleration errors T, the width of the correlation window, to L/v_x the transit time over the sensor. This dramatically reduces the acceleration induced bias, but the bias from v_y

cannot be eliminated satisfactorily from a one-dimensional sensor. This paper begins by discussing how a four element sensors will perform with different flow fields. This insight is used to develop a continuous estimation procedure for two-dimensional velocity which is introduced and analysed.

For convenience in this paper we ignore discretisation errors in time and regard functions as continuous. This simplification can be made as long as the signals are properly filtered before digitisation so that there are no frequencies higher than the Nyquist frequency (half the sample frequency). Continuous functions are then defined by their Fourier interpolation.

2 Interpretation of Lag Times

2.1 Effect of Acceleration

One of the simplest situations is shown in figure 1. An edge is moving past four photo-transistors with centres at $\mathbf{x}_i$. Only the velocity and acceleration normal to the edge, that is in the direction $\hat{\mathbf{n}}$, can be resolved. This is known as the aperture effect (Jähne, 1997) (Chapter 13). We write $v = \hat{\mathbf{n}} \cdot \mathbf{v}$ and similarly for the acceleration $a = \mathbf{n} \cdot \mathbf{a}$. If $\mathbf{a}$ is constant, then the arrival time of the edge at each sensors τ_i will be given by

$$y + v\tau_i + a\tau_i^2/2 = \hat{\mathbf{n}} \cdot \mathbf{x}_i \tag{2}$$

There are four equations, one for each sensor, and four unknowns, which are v the normal velocity, a the normal acceleration, y the position of the

edge at $t = 0$ and $\hat{\mathbf{n}}$ the normal direction to the edge. A convenient choice of coordinates is $\mathbf{n}\cdot\mathbf{x}_1 = L/2\cos\theta$, $\mathbf{n}\cdot\mathbf{x}_2 = -L/2\cos\theta$, $\mathbf{n}\cdot\mathbf{x}_3 = L/2\sin\theta$ and $\mathbf{n}\cdot\mathbf{x}_4 = -L/2\sin\theta$ so the the diagonal length between the sensors is L. Equation 2 for each i can now be solved to give

$$\begin{aligned}
\theta &= \phi + \tan^{-1}\left(\frac{\lambda^2\tan 2\phi}{1-\lambda^2}\right), \\
v &= -\frac{L}{\delta}\frac{4\lambda\overline{\tau}/\delta + \cos(2\phi)}{\sqrt{\cos(2\phi)^2 - 2\lambda^2\cos(2\phi)^2 + \lambda^4}}, \\
a &= \frac{L}{\delta^2}\frac{4\lambda}{\sqrt{\cos(2\phi)^2 - 2\lambda^2\cos(2\phi)^2 + \lambda^4}}, \\
y &= L\frac{16\lambda\overline{\tau}^2 + 8\overline{\tau}\delta\cos(2\phi) - 2\lambda\delta^2 - \lambda^3\delta^2}{8\delta^2\sqrt{\cos(2\phi)^2 - 2\lambda^2\cos(2\phi)^2 + \lambda^4)}},
\end{aligned} \tag{3}$$

where the following auxiliary variables have been defined

$$\begin{aligned}
\overline{\tau} &= (\tau_1 + \tau_2 + \tau_3 + \tau_4)/4, \\
\delta_1 &= \tau_1 - \tau_2, \\
\delta_2 &= \tau_3 - \tau_4, \\
\delta &= \sqrt{\delta_1^2 + \delta_2^2}, \\
\phi &= \tan^{-1}(\delta_2/\delta_1), \\
\overline{\lambda} &= \frac{\tau_1 + \tau_2 - \tau_3 - \tau_4}{\delta}.
\end{aligned} \tag{4}$$

Using y, v and a from eqs. 3 we know that at time t the position of the edge projected in the direction $\hat{\mathbf{n}}$ is $y + vt + 1/2at^2$ and the velocity is $v + at$. A natural choice is to calculate the time t_0 when the edge is over the centre of the sensor and then calculate the velocity at this time. This

gives a quadratic equation for t_0 which has the following solution.

$$t_0 = \overline{\tau} - \frac{\delta}{4} \frac{\lambda(\lambda^2+2)\,\mathrm{sgn}(\cos 2\phi)}{|\cos 2\phi| + \sqrt{\cos(2\phi)^2 + 2\lambda^2 + \lambda^4}}. \tag{5}$$

This has been written so that the correct solution is chosen regardless of the sign of $\cos(2\phi)$. The velocity at this time is

$$v(t_0) = \frac{L}{\delta}\sqrt{\frac{\cos(2\phi)^2 + 2\lambda^2 + \lambda^4}{\cos(2\phi)^2 - 2\lambda^2\cos(2\phi)^2 + \lambda^4}}. \tag{6}$$

The acceleration a and angle θ, given by eqs. 3, are both independent of time in this model. Thus these two equations along with eq. 6 can give an estimate of the flow properties at the time t_0 given by eq. 5.

There are several salient features of these equations. First they are exact for all accelerations, angles and velocities. The mean time $\overline{\tau}$ only occurs in eq. 5 specifying the time at the centre of the measurement. The angle, velocity and acceleration only depend on the differences between the lag times τ_i. To understand these equations it is helpful to invert them.

$$\begin{aligned}
\lambda &= \frac{\left[\sqrt{1+\sqrt{1-\epsilon^2\sin^2\theta}} - \sqrt{1+\sqrt{1-\epsilon^2\cos^2\theta}}\right]^2}{2 - \sqrt{1-\epsilon^2\cos^2\theta} + \sqrt{1-\epsilon^2\sin^2\theta}} \approx 1/4\epsilon\cos 2\theta + O(\epsilon^3) \\
\delta_1 &= \frac{L}{v}\frac{\sqrt{2}\cos\theta}{1+\sqrt{1-\epsilon^2\cos^2\theta}} \approx \frac{L\cos\theta}{v}\left[1 + 1/8\epsilon^2\cos^2\theta + O(\epsilon^4)\right], \\
\delta_2 &= \frac{L}{v}\frac{\sqrt{2}\sin\theta}{1+\sqrt{1-\epsilon^2\sin^2\theta}} \approx \frac{L\sin\theta}{v}\left[1 + 1/8\epsilon^2\sin^2\theta + O(\epsilon^4)\right],
\end{aligned} \tag{7}$$

where v is the velocity at the centre point and $\epsilon = aL/v^2$ is the relative velocity change over the size of the sensor. For $\epsilon > 1$ the velocity can

change direction so that the edge will not reach the sensor for certain angles, and this is shown in the above equations by the square roots becoming imaginary. By considering small relative accelerations the nature of λ as a measure of relative acceleration and δ_1 and δ_1 as velocities along the axis is clear. The above expansions in ϵ are uniformly valid for $|\epsilon| < 1$, but the inverse expansions treating λ as a small parameter breakdown when $\cos 2\theta$ is small. This is because when the edge is moving parallel to the sides of the square it is no longer possible to calculate the acceleration. This problem will be expanded upon when we discuss the errors.

To calculate the effect of errors in the four τ_i we assume that they are random variables with mean μ_i and independent mean squared errors with variance σ^2. These errors arise from quantisation, statistical fluctuations, electronic noise and deviations by the reflectance field from our model. Allowing the errors to be dependent only effects the results by a small factor and is not important.

Consider an estimate of some property $\hat{g} = g(\tau_i)$. The mean squared error about the exact value $g(\mu_i)$ can then be calculated as follows.

$$V[\hat{f}] = E[(\hat{g}-g)^2] = E\left[\left(\sum_i (\tau_i - \mu_i)\frac{\partial g}{\partial \tau_i}\right)^2\right] = \sum_i \left(\frac{\partial g}{\partial \tau_i}\right)^2 E[(\tau_i-\mu_i)^2] = \sigma^2 \sum_i \left(\frac{\partial g}{\partial \tau_i}\right)^2 \tag{8}$$

Using this formula for each of $\hat{v}$, $\hat{a}$ and $\hat{\theta}$ the errors can easily be calculated. The expressions are rather long however so we only consider

the case of small ϵ and expand.

$$\begin{aligned} V[\hat{v}] &= \frac{\sigma^2 v^4}{L^2}\left[2+\epsilon^2\frac{4+9\cos^2(2\theta)+5\cos^4(2\theta)}{4\cos^2(2\theta)}+O(\epsilon^4)\right] \\ V[\hat{\theta}] &= \frac{\sigma^2 v^2}{L^2}\left[2+5/4\epsilon^2\sin^2(2\theta)+O(\epsilon^4)\right] \\ V[\hat{a}] &= \frac{\sigma^2 v^6}{L^4}\left[\frac{64}{\cos^2(2\theta)}+\epsilon^2\frac{2(13\cos(2\theta)^2-16)}{\cos^2(2\theta)}+O(\epsilon^4)\right] \end{aligned} \tag{9}$$

These equations show that there is a very strong dependence of the error on the angle for the acceleration and the velocity. For small $\cos(2\theta)$ the expansions break down and the errors can be arbitrarily large in calculating v and a. This breakdown occurs for any size of ϵ though the equations are not included here. Different estimations that avoid this breakdown will be discussed in the following subsections. These results also show that the size of the errors is determined by the dimensionless grouping $\sigma v/L$. This is exactly the uncertainty one would expect if the sampling period is σ and the lag times τ_i can be located to this accuracy. If this is the case then the larger L is the smaller the errors will be. In general however, this is wrong for two reasons. If a feature or edge is diffuse the lags can be calculated with a precision that is much greater than the sampling period. Also as L increases the correlation between the sensors will decrease and may disappear, so that σ increases without bound. A different approach is needed to include these effects, which will be discussed later. First however two different modelling assumptions will be introduced.

2.2 Effect of Curvature

The previous subsection considered the case when the curvature of the flow was constant over the scale of the sensors but the velocity was allowed to vary. In this subsection we consider the case of constant velocity, but with curvature. This would correspond to the case where the size of the sensor is comparable with that of the particles. A four element sensor does not give enough information to resolve particle centre, curvature and velocity as this has five unknowns, but it is possible to solve for the normal velocity. The four equations for the lags at each sensor are

$$|\mathbf{y} + \mathbf{v}\tau_i - \mathbf{x}_i|^2 = R^2 \tag{10}$$

where $\mathbf{y}$ is the centre of curvature at $t = 0$ and R is the radius of curvature. using the normal approximation so that $\mathbf{y} = y\hat{\mathbf{n}}$ and $\mathbf{v} = v\hat{\mathbf{n}}$ and the same definition of the sensor element sensors $\mathbf{x}_i$ the equation for each lag time is

$$(y + v\tau_i - \hat{\mathbf{n}} \cdot \mathbf{x}_i)^2 + (\hat{\mathbf{m}} \cdot \mathbf{x}_i)^2 = R^2 = 1/\kappa^2, \tag{11}$$

where $\hat{\mathbf{m}}$ is the unit vector normal to $\hat{\mathbf{n}}$ For a straight edge R is infinite so it is more convenient to work with the curvature $\kappa = 1/R$.

The four equations can be solved to give

$$v = \frac{L}{\delta} \tag{12}$$

$$\theta = \phi \tag{13}$$

$$y = -L\frac{\overline{\tau}}{\delta} + L\frac{\cos(2\phi)}{4\lambda} \tag{14}$$

$$\kappa = \frac{4\lambda}{L\sqrt{\cos^2(2\phi) + 2\lambda^2 + \lambda^4}} \tag{15}$$

These are considerably simpler than those involving acceleration because the curvature gives a linear time shift and thus has no effect on the velocity or normal angle. The effect of acceleration is nonlinear and more complicated. In the case of small acceleration, the results give the same estimates for v and θ. Since this model includes no acceleration the velocity and angle estimate are for all times. A sensible choice is to regard them as applying at the mean time $\overline{\tau}$.

If we use eq. 12 as our estimate $\hat{v}$, and eq. 13 as our estimate $\hat{\theta}$, then the errors in the estimates can be calculated as before. They are

$$\begin{aligned} V[\hat{v}] &= \frac{2v^4\sigma^2}{L^2} \\ V[\hat{\theta}] &= \frac{2v^2\sigma^2}{L^2} \end{aligned} \tag{16}$$

These equations are exact and have no dependence on angle or curvature. Thus the velocity and normal angle can be equally well calculated in any direction. The estimates for the errors in κ and y do depend on the angle and are also unstable for small $\cos 2\theta$. Thus again showing that the sensor will be most effective when aligned with the diagonal in the flow direction.

Suppose now we use the estimates given by eq. 12 and eq. 13 in the case of acceleration. The total squared error will now consist of a bias

term and an uncertainty in τ term. The bias errors are

$$\begin{aligned}
\hat{v} - v &= \frac{v\epsilon}{4 - 2\sqrt{1-\epsilon^2\cos^2\theta} - 2\sqrt{1-\epsilon^2\sin^2\theta}} - v \\
&= -1/16 v\epsilon^2[1+\cos^2(2\theta)^2] + O(\epsilon^4) \\
\hat{\theta} - \theta &= \tan^{-1}\left(\cos(\theta)\sin(\theta)\frac{\sqrt{1+\sqrt{1-\epsilon^2\cos^2\theta}} - \sqrt{1+\sqrt{1-\epsilon^2\sin^2\theta}}}{\sin^2\theta\sqrt{1+\sqrt{1-\epsilon^2\cos^2\theta}} + \cos^2\theta\sqrt{1+\sqrt{1-\epsilon^2\sin^2\theta}}}\right) \\
&= -1/32\epsilon^2\sin(4\theta) + O(\epsilon^4)
\end{aligned}$$

The variance of these estimates can also be calculated as before, but is now much simpler than for the unbiased estimates including acceleration.

$$V[\hat{v}] = \frac{\sigma^2 v^4}{L^2}\frac{2\epsilon^4}{(4 - 2\sqrt{1-\epsilon^2\cos^2\theta} - 2\sqrt{1-\epsilon^2\sin^2\theta})^2} \quad (17)$$

$$= \frac{\sigma^2 v^4}{L^2}\left[2 - 1/2\epsilon^2(1+\cos^2(2\theta)) + O(\epsilon^4)\right] \quad (18)$$

$$V[\hat{\theta}] = \frac{\sigma^2 v^2}{L^2}\frac{2\epsilon^2}{4 - 2\sqrt{1-\epsilon^2\cos^2\theta} - 2\sqrt{1-\epsilon^2\sin^2\theta}} \quad (19)$$

$$= \frac{\sigma^2 v^2}{L^2}\left[2 - 1/4\epsilon^2(1+\cos^2(2\theta)) + O(\epsilon^4)\right] \quad (20)$$

These mean squared errors do depend on the angle θ, but they are always finite, so provided that the velocity does not vary too much over the size of the sensor so that ϵ is small, the estimators derived from the curvature model in eqs. 12 and 13 will be more accurate. Only if the flow is very closely aligned with the sensor and accelerations are very large and the curvature can be neglected, will the estimators based on the acceleration model prove better.

2.3 Closest approach

In this subsection we consider another interpretation of the lag times when there is structure in the flow field over length scales smaller than the sensor size. In the next section when the complete statistical description is given this is also seen to arise from averaging over many edge events.

We consider a trajectory given by $(\tau - t)\mathbf{v} + 1/2(\tau - t)^2\mathbf{a}$ so that it passes through the centre of the sensor. The lag time τ_i for sensor i is the point of closest approach, so that

$$([\mathbf{v} + (\tau - t)\mathbf{a}] \cdot [(\tau_i - t)\mathbf{v} + 1/2(\tau_i - t)^2\mathbf{a} - \mathbf{x}_i] = 0. \tag{21}$$

Each of these equations is a cubic in τ_i which can be solved exactly, but for simplicity we only consider series solutions for small acceleration a. In this case we interpret θ as the direction of the velocity $\mathbf{v}$, let $a = |\mathbf{a}|$ and let ω be the angle between $\mathbf{v}$ and $\mathbf{a}$, so that $\mathbf{a} \cdot \mathbf{v} = av\cos\omega$. Expanding in terms of the non dimensional ϵ and substituting the τ_i into eqs. 4

$$\delta = \frac{L}{v} + \frac{L\epsilon^2}{128v}[4 - 4\cos(4\theta) + 8\cos(2\omega) - \cos(4\theta + 2\omega) + 9\cos(4\theta - 2\omega)] + O(\epsilon^4) \tag{22}$$

$$\phi = \theta + 1/128\epsilon^2[4\sin(4\theta) + \sin(4\theta + 2\omega) - 10\sin(2\omega) - 9\sin(4\theta - 2\omega)] + O(\epsilon^4) \tag{23}$$

$$\overline{\tau} = t - \epsilon\frac{L\cos\omega}{16v}\epsilon + O(\epsilon^3) \tag{24}$$

$$\lambda = -1/8\epsilon[3\cos(2\theta - \omega) - \cos(2\theta + \omega)] + O(\epsilon^3) \tag{25}$$

Eq. 24 shows that the mean time is only effected to lowest by acceleration in the direction of the velocity as would be expected. Substituting these results into the simple estimators $\hat{v} = L/\delta$ and $\hat{\theta} = \phi$ we can calculate

the bias and variance as before.

$$\hat{v} - v = -1/128\epsilon^2 v[4 - 4\cos(4\theta) + 8\cos(2\omega) - \cos(2\omega + 4\theta) + 9\cos(4\theta - 2\omega)] + O(\epsilon^4) \quad (26)$$

$$\hat{\theta} - \theta = 1/128\epsilon^2[(4\sin(4\theta) + \sin(2\omega + 4\theta) - 10\sin(2\omega) - 9\sin(4\theta - 2\omega)] + O(\epsilon^4) \quad (27)$$

$$V[\hat{v}] = \frac{\sigma^2 v^4}{L^2}\left[2 - 1/16\epsilon^2[4 - 4\cos(4\theta) + 8\cos(2\omega) - \cos(2\omega + 4\theta) + 9\cos(4\theta - 2\omega)] + O(\epsilon^4)\right]$$

$$V[\hat{\theta}] = \frac{\sigma^2 v^2}{L^2}\left[2 - 1/32\epsilon^2[4 - 4\cos(4\theta) + 8\cos(2\omega) - \cos(2\omega + 4\theta) + 9\cos(4\theta - 2\omega)] + O(\epsilon^4)\right]$$

What these results show are that under the assumptions of this section the simple estimators for v (eq. 12) and θ (eq. 13) also perform well. That is, the bias and the variance will be small for all angles provided that the velocity does not change too much across the width of the sensor and the lag times can be accurately calculated. In the next section we describe how to calculate the lag times and perform a complete statistical analysis of the approach.

3 Continuous Time Estimation

The continuous time estimation approach was described briefly in (McElwaine and Tiefenbacher, 2003) for two element sensors. In this paper we show how the same method can be applied to four element sensors. The field of reflectance $f(\mathbf{x})$ is regarded as constant in time and corresponds to the value one element of our sensor would output if placed at a location $\mathbf{x}$. For simplicity we do not include temporal variation in f, but this is not significant as the differences are very similar to changes in velocity. Let $f_i(t)$ be the signal received by sensor i at time t which is $F(\mathbf{y}(t))$ where $\mathbf{y}(t)$ is the relative trajectory of the centre of the sensor to

the flowing medium. The method consists of minimising the Lagrangian

$$\mathcal{L} = \sum_i \int [f_i(\tau_i(t)) - f(t)]^2 \, dt + 2\gamma \sum_i \int \left(\frac{d\tau_i(t)}{dt} \right)^2 dt. \qquad (28)$$

The variables to solve for are τ_i, the lags at each sensor, and $f(t)$, the estimated underlying value at the centre of the sensor. The first terms of $\mathcal{L}$ penalises the discrepancy between the lagged sensor signals and the estimated signal f. If there were no constraint on the lag functions then these could be made zero but the lags would be unphysical. For this to be well posed, certainly the $\tau_i(t)$ must have no frequencies higher than the sampling frequencies. In fact we expect only slow changes in the velocity so a simple term that enforces this has been chosen, which has nice features. It is analytically tractable and corresponds to linear interpolation when there is little information present in the signal. γ is a parameter that determines the strength of this smoothing. At least one additional constraint on the $\tau_i(t)$ is also necessary. Using our results from the previous section which show that estimators based only on $\delta_1 = \delta \cos\phi$ and $\delta_2 = \delta \sin\phi$ give good results we use $\tau_1(t) = t + \delta_1/2$, $\tau_2(t) = t - \delta_1/2$, $\tau_3(t) = t + \delta_2/2$ and $\tau_4(t) = t - \delta_3/2$. It would also be possible to try to calculate curvature, but imposing an additional constraint simplifies the numerical implementation and means the the residuals $f_i(\tau_i(t)) - f(t)$ contain much useful information about the accuracy of the method. The Lagrangian (eq. 28) then becomes

$$\begin{aligned} \mathcal{L} \;=\; & 1/2 \int \Big\{ [f_1(t + \delta_1/2) - f(t)]^2 + [f_2(t - \delta_1/2) - f(t)]^2 + [f_3(t + \delta_2/2) - f(t)]^2 \\ & + [f_4(t - \delta_2/2) - f(t)]^2 + \gamma \left(\frac{d\delta_1)}{dt} \right)^2 + \gamma \left(\frac{d\delta_2)}{dt} \right)^2 \Big\} \, dt \end{aligned} \qquad (29)$$

where the dependence of δ_i on time has been dropped. Solving this variational problem is straightforward. The estimated field value f is simply the average of the lagged measurements

$$f(t) = 1 - 4\left[f_1(t+\delta_1/2) + f_2(t-\delta_1/2) + f_3(t+\delta_2/2) + f_4(t-\delta_2/2)\right] \quad (30)$$

If there is additional knowledge about the underlying field f this could be incorporated here, but failing that the mean field can be eliminated. The Euler-Lagrange equations for δ_i are then

$$\gamma\ddot{\delta}_1 = \dot{f}_1(3f_1 - f_2 - f_3 - f_4)/4 - \dot{f}_2(3f_2 - f_1 - f_3 - f_4)/4 \quad (31)$$

$$\gamma\ddot{\delta}_2 = \dot{f}_3(3f_3 - f_1 - f_2 - f_4)/4 - \dot{f}_4(3f_4 - f_1 - f_2 - f_3)/4 \quad (32)$$

where each f_i is evaluated at the appropriate lagged time $t \pm \delta_i$. This can be solved efficiently numerically using an implicit multi-grid scheme.

A rigorous analysis of these equations will not be given here, but an indication of the nature of the solutions and the errors involved will be briefly discussed. The reading at each sensor $f_i(t) = f(\mathbf{x}_i - \mathbf{y}(t))$. Taylor expanding each f_i in eq. 31 to lowest order about $-\mathbf{y}(\mathbf{t})$ gives

$$\gamma\ddot{\delta}_1 = 1/2(\mathbf{v}\cdot\nabla f)^2\delta_1 - 1/2L(\mathbf{v}\cdot\nabla f)(\hat{\mathbf{x}}\cdot\nabla f) \quad (33)$$

$$\gamma\ddot{\delta}_2 = 1/2(\mathbf{v}\cdot\nabla f)^2\delta_2 - 1/2L(\mathbf{v}\cdot\nabla f)(\hat{\mathbf{y}}\cdot\nabla f) \quad (34)$$

where $\mathbf{x}_1 - \mathbf{x}_2 = L\hat{\mathbf{x}}$ and $\mathbf{x}_3 - \mathbf{x}_4 = L\hat{\mathbf{y}}$. The equations for δ_i are now decoupled. letting $g(t) = |\nabla f(-\mathbf{y}(t))|^2$, the signal power, and $g(t)\hat{\mathbf{n}}(t) =$

$\nabla f(-\mathbf{y}(t))$, the equation for δ_1 can then be written

$$\ddot{\delta}_1 = \frac{g(\mathbf{v}\cdot\hat{\mathbf{n}})^2}{2\gamma}\left[\delta_1 - L\frac{(\hat{\mathbf{x}}\cdot\hat{\mathbf{n}})}{(\mathbf{v}\cdot\hat{\mathbf{n}})}\right]. \tag{35}$$

The right hand side of this vanishes when $\delta_1 = L\frac{(\hat{\mathbf{x}}\cdot\hat{\mathbf{n}})}{(\mathbf{v}\cdot\hat{\mathbf{n}})}$, which is precisely the condition (neglecting acceleration) in eq. 7, that is the lag time for the arrival of an edge with normal direction $\hat{\mathbf{n}}$ travelling with velocity $\mathbf{v}$. Departures away from this value are governed by the size of $\frac{g(\mathbf{v}\cdot\hat{\mathbf{n}})^2}{2\gamma}$. When this is large, δ_1 will closely match the lag. When it is smaller, larger deviations will be allowed and δ_1 will be an average of this and be approximately linear. This equation can be analysed by splitting up the multiplier into its mean part and its varying part. If f is isotropic, then g and $\hat{\mathbf{n}}$ are independent, and $\hat{\mathbf{n}}$ is distributed uniformly on the unit circle. So defining $\alpha^2(t) = E\left[\frac{g(\mathbf{v}\cdot\hat{\mathbf{n}})^2}{2\gamma}\right] = \frac{v^2(t)E[|\nabla f|^2]}{4\gamma}$, which depends only weakly on t through changes in v, and $\beta(t) = \frac{g(\mathbf{v}\cdot\hat{\mathbf{n}})^2}{2\gamma} - \alpha^2$. Eq. 35 becomes

$$\ddot{\delta}_1 - \alpha^2\delta_1^2 = \beta\delta_1 - Lg(\hat{\mathbf{x}}\cdot\hat{\mathbf{n}})(\mathbf{v}\cdot\hat{\mathbf{n}}). \tag{36}$$

The Greens function for the left hand side (that decays for large $|t|$) is $G(s,t) = -\frac{e^{-\alpha|s-t|}}{2\alpha}$, neglecting variation in α. So we can write

$$\delta_1(t) = \int_{-\infty}^{\infty} \frac{e^{-\alpha(t)|s-t|}}{2\alpha(s)}\left[Lg(s)(\hat{\mathbf{x}}\cdot\hat{\mathbf{n}}(s))(\mathbf{v}(s)\cdot\hat{\mathbf{n}}(s)) - \delta_1(s)\beta(s)\right] ds \tag{37}$$

This equation can be used to calculate the statistics of $\delta_1(t)$. It is mostly easily understood in the frequency domain. The Fourier transform of the Greens function is $\alpha^2/(\alpha^2+\omega^2)$, that is, it is a low pass filter with cutoff frequency α. If the dominant frequencies in $\hat{\mathbf{n}}(t)$ are above this

then they can be averaged to give

$$\delta_1(t) \approx \int_{-\infty}^{\infty} \alpha/2 e^{-\alpha|s-t|} L \frac{\hat{\mathbf{x}} \cdot \mathbf{v}(s)}{v^2(s)} \, ds \approx L \frac{\hat{\mathbf{x}} \cdot \mathbf{v}(s)}{v^2(s)} \tag{38}$$

The approximation for δ_2 is similar, so that up to terms in acceleration, we have the same results as in eqs. 22 and 23, thus the velocity can be estimated as

$$\mathbf{v} = L \frac{\hat{\mathbf{x}}\delta_1 + \hat{\mathbf{y}}\delta_2}{\delta_1^2 + \delta_2^2}. \tag{39}$$

The above heuristic justification can be made precise and the errors quantified, but the analysis is complicated and the brief discussion above contains the salient features.

Though the analysis and implementation for the continuous method described in eq. 28 are more complicated than for the traditional approach of calculating lags at fixed times using a fixed window there are several important advantages of this approach.

1. The primary errors due to acceleration enter through the time scale defined by the traverse size of the sensor L/v, not the window width needed to calculate the cross correlation. The acceleration errors will therefore be an order of magnitude smaller. The smoothing needed to overcome the aperture effect acts as a low pass filter removing high frequencies in the velocity, rather than introducing bias. If there is prior information about the wavelengths in $f(\mathbf{x})$, for example if the particle size distribution is known, the regularisation term $\gamma\dot{\delta}^2$ (equivalent to ω^2 in the frequency domain) can be changed so as to produce any desired filter.

2. The effective smoothing width $1/\alpha$ depends inversely on the signal strength, so that velocity is automatically interpolated where the signal is weak and errors are reduced where the signal is strong.

3. The cross correlation approach can fail by finding an incorrect global maximum that is unrelated to the lag time (McElwaine and Tiefenbacher, 2003), resulting in effectively infinite expected mean squared error. The errors in this continuous approach will only increase gradually as the signal degrades and the mean squared error will always be finite until there is total lack of correlation.

4 Design Criteria for Sensors

The design of a sensor to calculate velocities depends on several factors. In order to calculate velocities it is necessary to average over several incident edges at different angles, but as the averaging time increases, higher frequencies in velocity are filtered out. Thus maximum sensitivity will be achieved by considering the smallest wavelengths, L_c, that exist in the reflectance field $f(\mathbf{x})$. This will be similar to the size of the smallest particles. For the sensor elements to detect these wavelengths the diameter of the elements should be the same or smaller. The area of the element acts as a low-pass spatial filter, so in order to satisfy the Nyquist criterion and prevent aliasing, the sensors spacing should be the same. That is, there should be no gaps between the active parts of the elements that are larger than the smallest wavelength. For flowing snow the smallest particles may be less than 1 mm in size and it may not be possible to build such a small sensor, though this might be achievable us-

ing fibre optic cables to connect to the photo-transistors. The sampling frequency should also be chosen to satisfy the Nyquist requirement. The highest frequencies that will be observed are $\approx v_{\max}/(d + L_C)$, where d is the diameter of the active part of a sensor element. (If the sensors elements are not round this should be the smallest dimension through the element centre). The sampling frequency should be chosen to be at least twice this, but going much higher will add no further information. The lag times can easily be calculated with super-resolution (accuracy greater than the sampling frequency) by interpolating (over-sampling) the signal. Finally if the flow has a preferred direction, such as parallel to the ground it is best to orient this as shown in fig. 2, which is optimised for horizontal or vertical directions. This has several advantages. Most of the errors are minimised in this direction. The acceleration or curvature can be calculated as the same part of the flow passes over sensors at three different times. The spatial aliasing also depends on the angle as it is less likely that particles will pass through the gaps. Another countermeasure, if spatial aliasing cannot be prevented, is to reduce this vertical dimension L_y as shown in fig. 3. This will reduces most errors when $|v_x| > |v_y|$, but increase errors when the velocity is closer to vertical.

These design criteria can easily be summarised in terms of the power spectrum (the energy at different wavelengths) of the reflectance field f. Energy at wavelengths less than the averaging diameter d of each photo-transistor is filtered out. Energy at wavelengths between d and the sensors spacing L appears as noise. Energy at wavelength greater than the spacing L is the useful signal energy. Since there are also

fixed sources of error, the maximum signal to noise ratio is obtained by having $d = L = L_c/2$. The sampling frequency needs to be at least $2L_c/v$. For laboratory chute experiments with snow $L_c \approx 1\,\mathrm{mm}$ and $v < 10\,\mathrm{m}^{-1}$, so that the sampling frequency should be around 20 KHz and the sensors 1 mm in size. For a real snow avalanche the sampling frequency would need to be higher — around 50 kHz. Photo-transistors are generally larger than 1 mm, but by using fibre optic cables, or a ccd chip rather than photo-transistors, it should be possible to build such a sensor. If existing sensors are to be used the best choice would be to mount four photo-transistors as close together as possible, perhaps with a defocussing lens in order to spatial average over the sensor spacing L.

5 Conclusions

There are many possible sources of error in calculating velocities from opto-electronic sensors. This paper has described how the careful design of such instruments and analysis procedures can reduce and quantify the errors. Further improvements could be made by investigating in detail the nature of the reflectance field $f(\mathbf{x})$ and constructing a parametric model that incorporates information such as the particle size distribution. In a flow of identical granular particles this would be straightforward and estimates of the local flow density could easily be made, by reducing the smoothing γ and calculating individual normal velocities and angles, rather than attempting to find the velocity averaged over several particles and orientations. Using a sensor with five elements would allow the curvature and size of the particles also to be reliably

estimated, which would be important for a more complicated material such as snow when the sizes are not known.

6 Acknowledgements

The author was supported by a University Research Fellowship from the Royal Society. Part of this work was undertaken at the Federal Institute for Avalanche Research in Davos supported by a grant from the Swiss National Science Foundation. The author would like to thank Felix Tiefenbacher for making data available from correlation sensors and Barbara Turnbull and Perry Bartelt for arranging the visit.

References

Dent, J. D., Burrel, K. J., Schmidt, D. S., Louge, M. Y., Adams, E. E., and Jazbutis, T. G. (1998). Density, velocity and friction measurements in a dry-snow avalanche. *Ann. Glaciol.*, 26:247–252.

Jähne, B. (1997). *Digital Image Processing. Concepts, Algorithms, and Scientific Applications.* Springer, Berlin, 4 edition.

McElwaine, J. N. and Tiefenbacher, F. (2003). Calculating internal avalanche velocities from correlation with error analysis. proceedings of EGS 2002 session Snow Avalanche Dynamics .Special issue of Surveys in geophysics on Snow and Avalanche.

Nishimura, K., Maeno, N., and Kawada, K. (1987). Internal structures of large-scale avalanches revealed by a frequency analysis of impact

forces. *Low. Temp. Sci., Ser. A*, 46:91–98. In Japanese with English Summary.

Nishimura, K., Maeno, N., Sandersen, F., Kristensen, K., Norem, H., and Lied, K. (1993). Observations of the dynamic structure of snow avalanches. *Ann. Glaciol.*, 18:313–316.

List of Figures

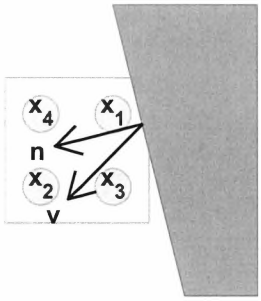

Fig. 1: Schematic of a four element sensor with a straight edge

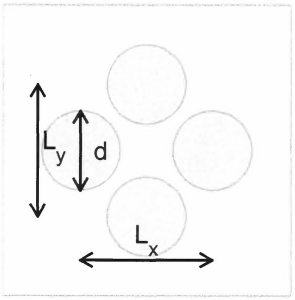

Fig. 2: Schematic of a symmetric four element sensor, where $L = L_x = L_y$ and the elements are diameter d

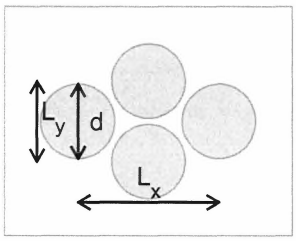

Fig. 3: Schematic of an asymmetric four element sensor, optimised for horizontal flow

Experiments with granular materials at Pavia chutes

M. Barbolini and M. Pagliardi 2003

1. INTRODUCTION

A series of experiments with granular material have been carried out at the laboratory chutes of the Hydraulic and Environmental Engineering Department of the University of Pavia (Italy). The aim of such experiments was to investigate - using high-speed camera recordings - the internal properties of fast moving granular flows (velocity, granular temperature and concentration profiles). The experimental set-up and the measurements techniques are described at §'s 2 and 3, respectively; the results are presented at § 4., in two distinct sections: (i) flow over smooth bed; (ii) flow over rough bed.

2. EXPERIMENT SET-UP

2.1 Chute

The channel (see Figure 1) has rectangular shape and is 35 cm wide and 6 m long, with a constant slope which can vary from 0° up to about 45°. The bed of the channel is metallic and the lateral walls (50 cm high) are made of Plexiglas. A pneumatic gate is installed at the beginning of the channel. The reservoir is 0.8 m long, has a volume of about 0.15 m^3, and must be loaded manually.

Section shape	Rectangular
Length	6 m
Width	35 cm
Height of the lateral walls	50 cm
Roughness with water	N=1 (*Manning*)

Table 1 - Mean features of the chute

Figure 1 - View of the experimental chute

In the experiments the inclination of the chute was set to 30°, and was held fixed. The video-recordings were made in a window located about 4.5 meters downstream from the release gate (see figure 2 and 7).

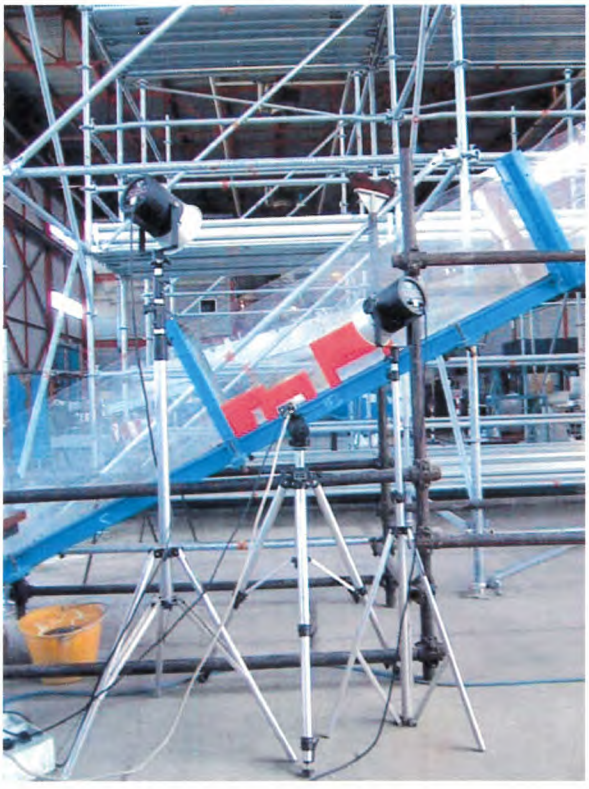

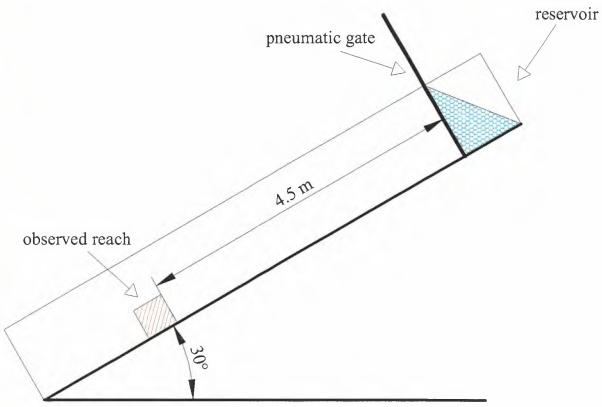

Figure 2 - Side view of the chute, with indication of the recording area

In addition to the metallic bed (see § 4.1), in order to vary the frictional properties of the sliding surface, we made up two rough surface that can be used as chute bed (see § 4.2): one was made rough by gluing a layer of particles onto a board and the other using sand paper (n°60), Figure 3.

Figure 3 - Sand paper bed (left) and glued particles bed (right)

2.2 High speed camera

Even though high-speed capture system exists from some time now, they are characterized by really high costs of the hardware and software parts used to set-up the system. Our main aim was to build a system with a frame rate that was higher than usual analogue cameras, but with a comparable cost. We thought we could achieve this goal by using off-the-shelf components and avoiding, when possible, special purpose parts that raise the cost of the system significantly. Moreover all the software had to be open-source so it was easily adaptable to our needs and it carried no direct additional costs.

The heart of the system is a progressive camera with digital interface made by Pulnix. It is capable of a sustained rate of 30 million pixels per second that may be arranged into different frame-rates as shown in table 2.

	Width	Height	Frequency
Full height	640	480	120 Hz
Half height	640	198	240 Hz
Quarter height	640	10	350 Hz

Table 2 - Image sizes and frame frequencies available

The camera has an electronic shutter able to manage exposure times from 60 s^{-1} up to 32'000s^{-1}; for this experiments we used a lens with a focal length of 14.5mm and F1.4. In order to illuminate the stage two photographic light, with the power of 1250 watt each one, has been used. In table 3 are summarized the mean feature of the shots.

Frame width [pixel]	640
Frame high [pixel]	198
Definition	8 bit / pixel
Movie length [s]	1.25
Frames/s	240
Frames/movie	300
Shutter speed	1/8000s

Table 3 - Mean feature of the shot

2.3 Polyethylene beads.

To simulate the avalanche we used a granular material with a density similar to the water and size sufficient to be recognized in the movie; particularly we employed high density polyethylene (Eraclene) beads (see Figure 3), which main features are summarized in table 4. The beads are similar to cylinders 3 mm wide and 2 mm high. For a better particles recognition we painted about the 20% of these (see Figure 4).

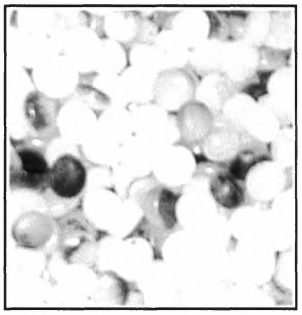

Figure 4 - Granular material used in the experiments

Size	Diameter [mm]	2, 3
Density	ρ [g/cc]	0.88
Bulk concentration	c^* [-]	0.7
Angle of repose	ϕ [°]	22.6

Table 4 Granular beads features

3. MEASUREMENT TECHNIQUES

3.1 Front celerity

The front celerity was measured using frontal video recordings (see Figure 5). Putting marks along the chute (every 50 cm), and evaluating from the records the time the front needs to travel the distance from a mark the successive one (Δt) the front celerity (V_{fr}) may be simple evaluated as:

$$V_{fr} = \frac{0{,}5}{\Delta t} \qquad (m/s) \tag{1}$$

Figure 5 - Front view of the chute; the white marks on the bed are used to measure front position versus time, i.e. front celerity

3.2 Particle's speed and speed profiles

Using a high speed camera we obtained movies in which the paths of every bead are simply recognizable (figure 6). Analysing two consecutive frames it is possible to extract the length travelled by every single particle in 1/240 of second. In this way we obtained the particles speed (and speed components) at a given position (see relations 2a-b), as well as speed profiles and particles trajectories. A device used in the movie display program permits us to save the particle position in a text file, but we have to recognize with the mouse each beads.

$$\begin{cases} X = \dfrac{(x'_n - x''_n)}{2} \\ Y = \dfrac{(y'_n - y''_n)}{2} \end{cases} \tag{2a}$$

$$\begin{cases} V_{x_n} = \dfrac{(x'_n - x''_n)}{(1/240)} \\ V_{y_n} = \dfrac{(y'_n - y''_n)}{(1/240)} \end{cases} \tag{2b}$$

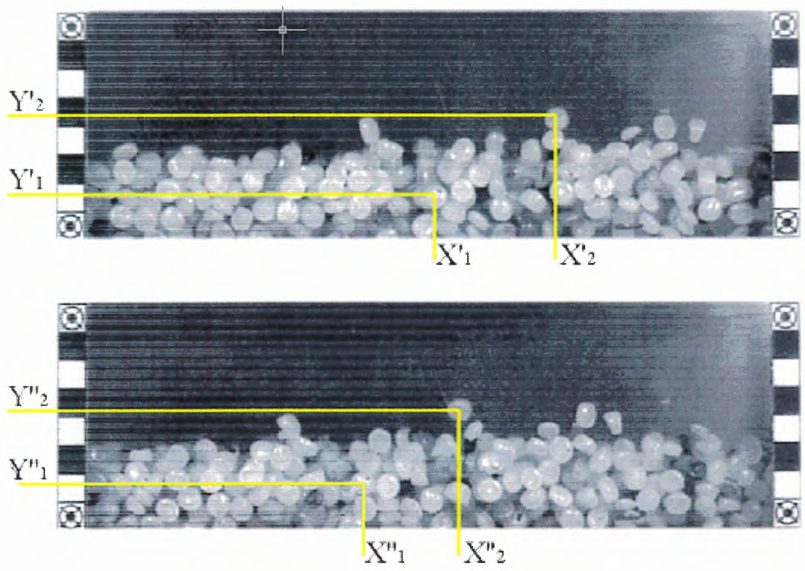

Figure 6 - Particle path in two consecutive frames.

In order to frame more easily the flow a mask with a metric graduation, shown in figure 7, was stuck on the chute wall (see also figure 2).

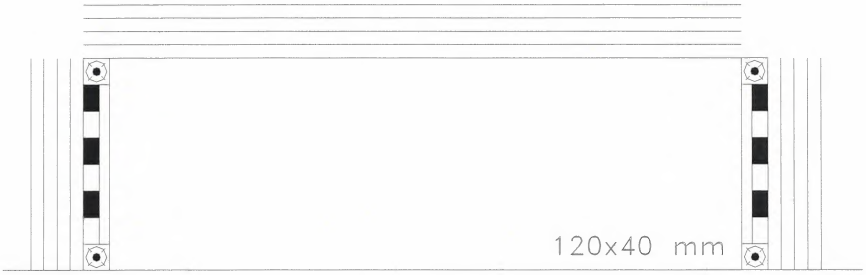

Figure 7 - Metric guide mask

To mediate the measurement errors a large number of particles had been considered inside the mask for each frame, as well as e large number of frames; furthermore each experiment has been replayed five times to be validated.

We didn't take in account the transversal component of the speed, so far; for the future, we intend to do some experiments for evaluating also this component, shooting the flow from the top of the chute.

3.3 Volumetric concentration

Behaviour of granular flows depends also from concentration, so it's important to know its evolution during the flow. Many authors proposed methods to evaluate the concentration by digital image analysis techniques and also we are working in this direction. At the moment, using manual methods, the simplest way of obtaining estimates for volumetric concentration is to subdivide the

viewing area into arbitrary spatial partitions (see Figure 8) and then to count the number particle n_i falling in each box. The concentration in a given box can then be evaluated as:

$$c = \frac{n_i \cdot c^*}{n_b} \tag{3}$$

where n_b is the estimated number of particle in the box at the bulk density condition, and c* is the bulk density. According to this method, the density has been calculated as the average of the density values relative to the same sequence of frames used to measure the velocity profiles.

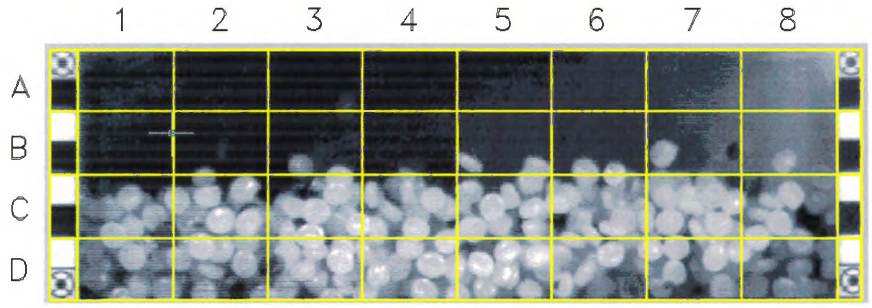

Figure 8 - Boxes used to calculate the volumetric concentration

Knowing speed and concentration profiles we are able to estimate also the flow rate as follows:

$$Q = h \cdot 0{,}35 \cdot \rho \cdot \sum_{1=1}^{N} c_i \cdot v_i \tag{4}$$

where h is the height of the boxes (0,35 is the width of the channel), ρ is the polyethylene density and c_i and v_i the average volumetric concentration and velocity at the considered depth. The flow rate Q given by (4) is expressed in kg s^{-1}.

4. RESULTS

4.1 Flow over smooth surface (metallic bed)

4.1.1 Froude number

The experiments were designed so that the granular flow could have a Froude number of the same order of magnitude as for a natural snow avalanche (i.e. 5 to 10). The Froude number is defined in terms of flow velocity (*u)* flow depth (*h)* and gravitational acceleration (*g)* as follows:

$$Fr = \frac{u}{\sqrt{gh}} \tag{5}$$

It represents the square root of the ratio of kinetic energy of the current to the potential energy of the flow. The Froude number of the experiments with smooth bed was approximately in the range: $Fr \cong 5 \div 7$ (depending on the considered part of the flow, see § 4.1.3).

4.1.2 Front celerity

We made two frontal shots of the whole chute for two experiments, in order to measure the front celerity (figure 9). The two experiments show a good reproducibility. After an initial acceleration phase, about 2,5 m downstream the opening gate (about 0,8 second from the initiation of the flow) the front attain a constant speed, approximately equal to 3,75 m/s (dotted line in Figure 9). Therefore, at the observation reach, 4.5 down the top of the chute (see figure 2), the flow has already attained its terminal velocity.

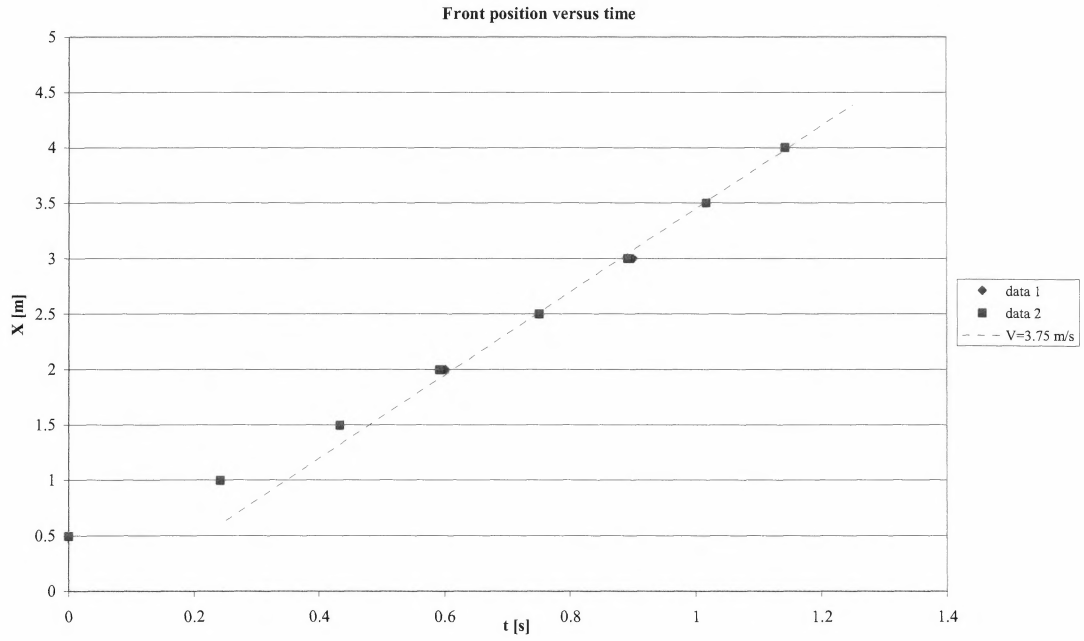

Figure 9 - Front position versus time

4.1.3 Flow features

The movies show that into the same flow, for a fixed section, coexist (at least) two different stages of motion with distinct characteristics in term of velocity, depth and concentration. In particular the initial part of the flow (what we call the "front") is represented by a very dispersed material, with particles having large mean free path and relatively few collisions, so that the flow shows a saltating behaviour over all the depth and the interface between the moving material and the surrounding air is not easily recognisable (Figure 10). This phase of flow takes about 0,15 second. After that, the flow exhibit a progressive transition (that takes about 0,15 seconds) to a regime where the material comes to an increased packing, reduced mean free path and increased number of collisions. This phase of motion, that we call the "body" (see Figure 10), is the main one, takes the majority of time

(about 0,7 seconds) and shows steady flow conditions. During the flow of the body few saltating particles can be observed, and the interface between the moving material and the surrounding air can be easily recognised. After the passage of the body (approximately after one second since the beginning of the flow) the flow ends up with a tail showing progressively reduced flow depth and velocity.

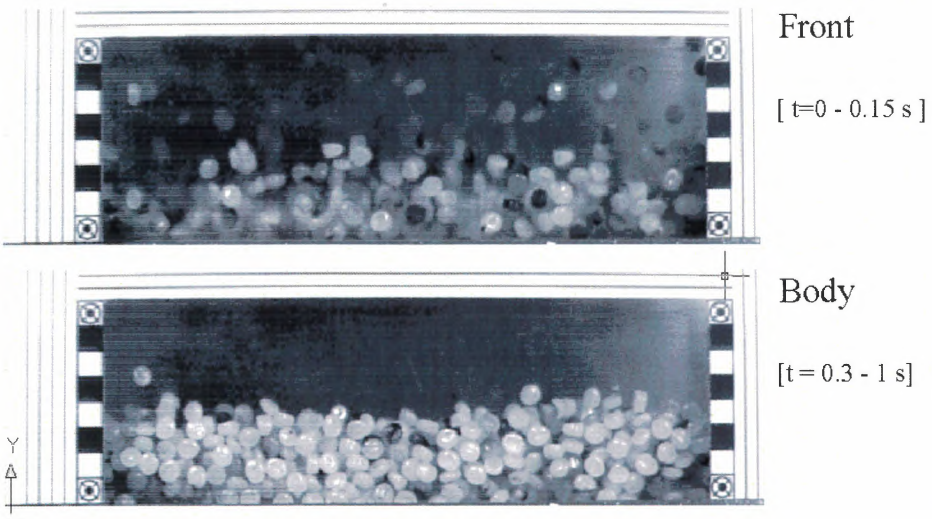

Figure 10 - Distinct phases of motion

We made measurements of velocity and concentration for the front and the body, because they are the ones we thought more representative. The measurements were taken in a temporal lapse of 0.042 seconds, equivalent to ten frames.

4.1.4 Velocity profiles

According to the methods described at § 3.2 (equations 2), we have determined the velocity profiles for either the "front" and the "body" of the flow. The results are displayed in Figure 11. For both the two flow phases a slip velocity at the bottom of the flow was obtained, approximately 1,5 m/s and 3,25 m/s for the body and the front of the flow, respectively. Maximum velocity are reached at the flow surface in both cases, and are about 2,25 m/s and 3,5 m/s for the body and the front of the flow, respectively. The body shows a velocity profile that can be fitted fairly well by a second order polynomial, with a shear rate that is decreasing from the bottom to the top of the flow; conversely, in the front the velocity is more or less constant over all the flow depth. The error bars in Figure 11 represents the standard deviation in the velocity distribution; they should be considered more as a scattering of the measured values rather than a true error. It is interesting notice that standard deviation is higher at the front, were the particle velocities seems to be more random; an explanation of that comes out from the granular temperature theory.

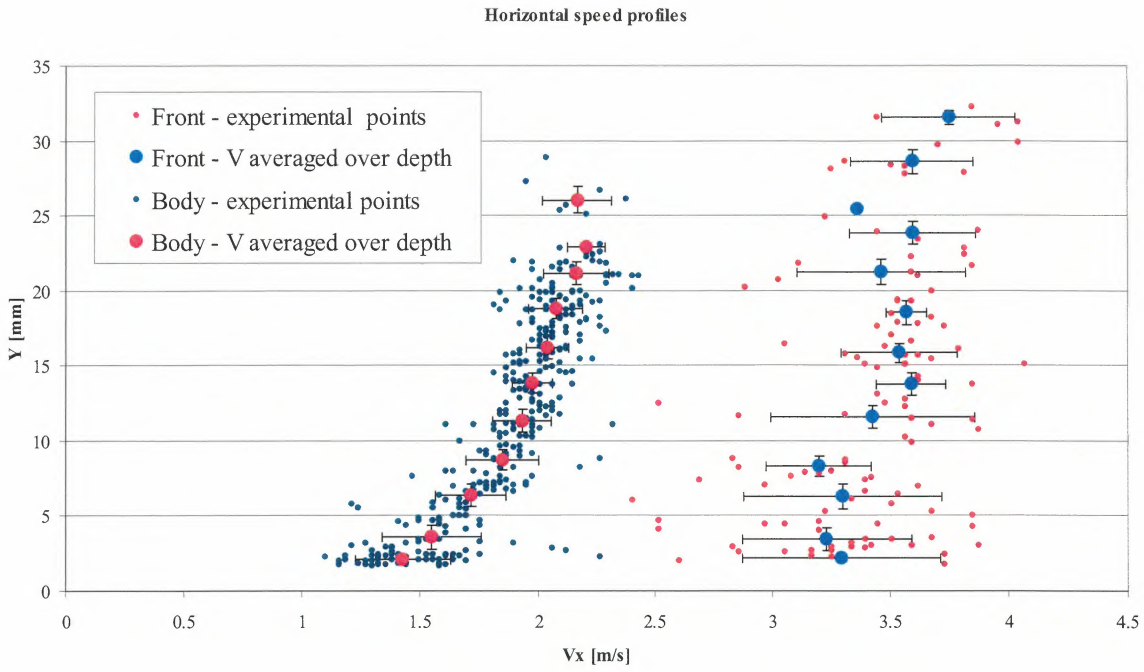

Figure 11 - Velocity profiles

In Figure 12 is presented a comparison of our experimental profile of velocity, obtained with dry granular material, with velocity profiles measured in experiments with snow carried out at different scale: (i) chute scale (Bouchet et al., 2003); (ii) small avalanches (Dent, 1998); (iii) full-scale avalanche (Gubler, 1996). For sake of comparison the diffewrent velocity prtofiles are rescaled accoding to maximum flo depth and maximum velocity. The agfreement appears quite incouraging.

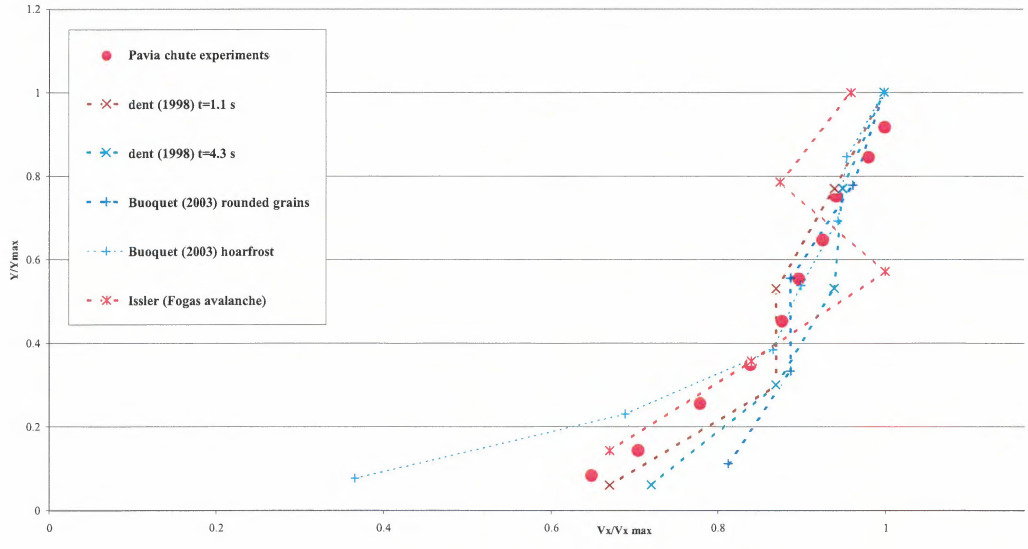

Figure 12 - Comparison between normalised velocity profiles, obtained in experimentsat different scales and using different materials

4.1.5 Granular temperature profiles

Some physical similarities between granular flows and gases has led to adapt kinetic theories to granular materials; in particular, the analogy among the random motion of grains and molecules is so strong that it is possible to define a "granular temperature" according to the kinetic theory of gases. According to Ogawa (1978), which first introduced the concept of granular temperature, the velocity of each particle may be decomposed into the sum of a mean velocity and a random component, taking into account for the relative motion of the particle compared with the mean velocity of the flow. This random component is similar to the "thermal temperature" in the kinetic theory of gases, and can be written as:

$$T = \frac{1}{2}\left\langle \left(u_i - \bar{u}\right)^2 + \left(v_i - \bar{v}\right)^2 \right\rangle \tag{6}$$

where u_i and v_i are the horizontal and vertical velocity of the i^{th} particle and $\bar{u}$ and $\bar{v}$ are the horizontal and vertical average velocity of the flow. In figure 13 is represented the granular temperature measured in our experiments, including the distinction between the two phases of motion previously identified ("front" and "body", respectively, see § 4.1.3).

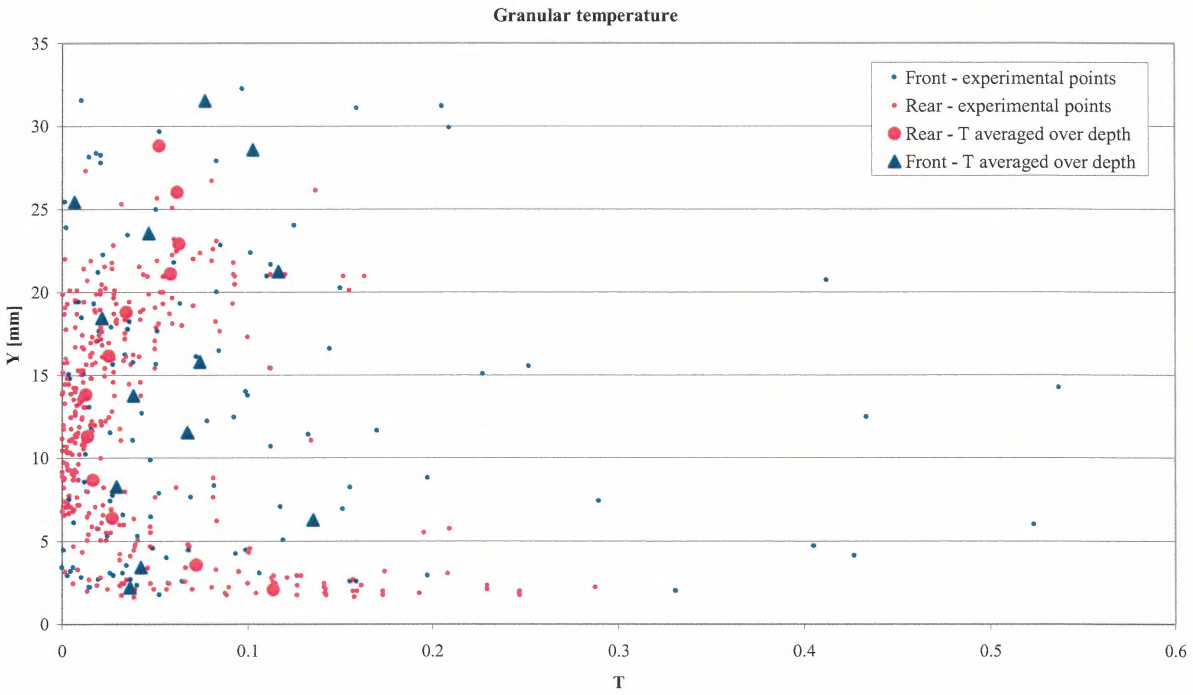

Figure 13 - Granular temperature profiles

Campbell (1990) describes two distinct mechanisms of granular temperature generation. The first, referred to as "collisional temperature generation", is a by product of interpalticle collisions in the sense the two colliding particle will have a resultant velocities depending not only on their initial velocities, but also on the type of collision they experience, therefore will contain apparently random velocities. The second mode of temperature generation, referred to as "streaming temperature generation", is a product of the velocity gradient because the temperature is proportional to the difference between the local velocity and the mean one.

From our experiments results that:

- the "front" has a uniform velocity distribution, similar to a plug flow, and the granular temperature is almost constant all over the depth and is mostly generated from the collision between the particles.
- the "body" has a clear velocity gradient and the granular temperature is proportional to that except for the upper layer, where even if the velocity gradient is decreasing the granular temperature raises again; this can be partly explained by the fact that close to the free surface of the body, the grains show a saltating behaviour and generate flow condition similar to the one in the front of the flow, therefore also the granular temperature accords to that flow condition.

4.1.4 Concentration profiles

According to the methods described at § 3.3 (equations 3), we have determined the concentration profiles for either the "front" and the "body" of the flow. The results are displayed in Figure 14.

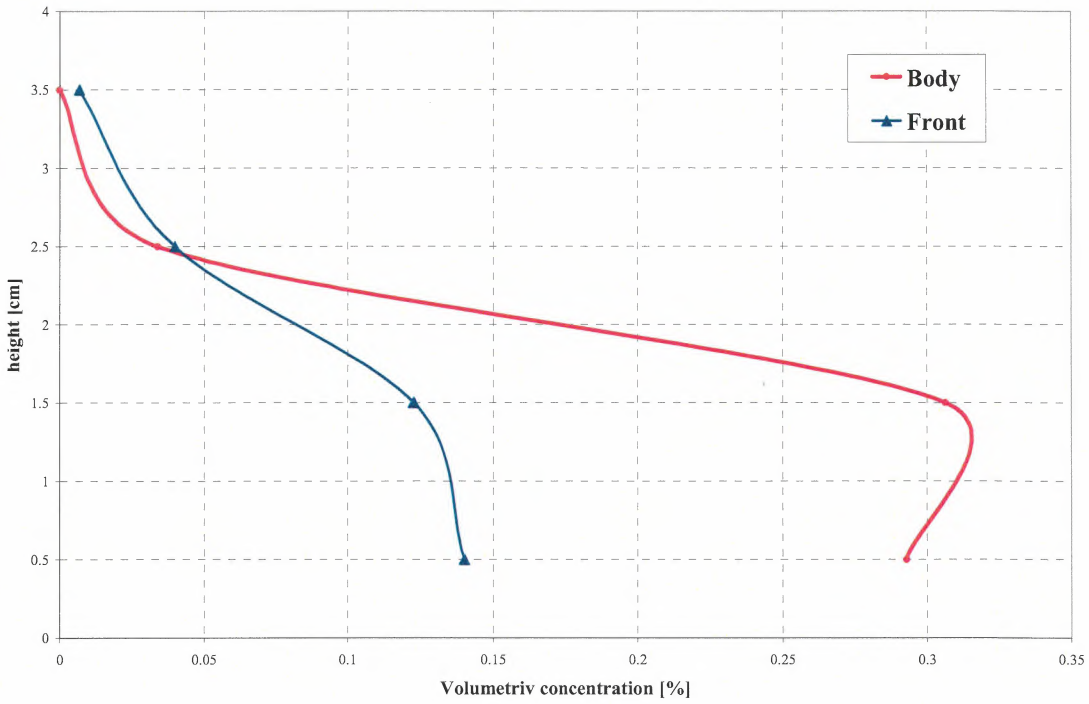

Figure 14 - Volumetric concentration profiles

It can be observed that, as expected, the concentration in the front is lower than in the body of the flow. Furthermore, whereas in the body the concentration goes to zero above 3 cm, in the front we have a non-null value of concentration (even if small) also between 3 and 4 cm, due to few particles suspended at the top of the flow that results in higher flow depth for the front. In the front the concentration decrease progressively from about 0,15 at the bottom of flow to zero at the top of the flow. Conversely in the body of flow we have a concentration approximately constant in the first two centimetres of the flow, set to a value of about 0,3 (that means a value that is well below the one - that is 0,5 -considered to be a threshold for transition from a collisional regime to a frictional regime); at the top layer of the body, which is basically a saltation layer, the concentration decreases abruptly to about 0,05.

4.2 Flow over rough surfaces

The same experiment as to one described at § 4.1 was made covering the chute bed with sand paper n°60 (see Figure 15). In this case at the recording section (see Figure 2) the flow continues to vary without get to a steady flow condition.

Figure 15 - View of the chute covered with sand paper in the area of the recording section (up to about 1 meter upstream)

In order to trace the velocity profiles we fixed six instants in which measure the speed profiles (table 5). As shown in figure 16 the speed and the speed profile change all over the flow. The condition at the bottom of the flow, as the front travel trough the recording area, present a slip condition (see profile n. 1 in Figure 16). The slip velocity then decreases up to reach a no-slip condition at the bottom (see profile n. 2, 3 and 4 in Figure 16); then deposition of granular material starts (see profile n. 5 and 6 in Figure 16). From the speed profiles of Figure 16 it is possible to calculate the deposit rate, estimated roughly in 2-3 cm/s. It is interesting to observe that when the flow change the bottom condition from slip to no-slip (profile n. 2 and n. 3 respectively, Figure 16), also the shape of the velocity profile in the lower part change from concave to convex.

n. of profile	1	2	3	4	5	6
frame	0	25	75	125	175	250
t [s]	0.00	0.10	0.31	0.52	0.73	1.04

Table 5 - Instant at which speed profiles have been measured (the n. of profiles refer to those in Figure 16 and 17)

Also in this case we traced the granular temperature profiles, shown in figure 17. Except for the profile n. "1", the granular temperature seems to be mainly produced by the "streaming temperature generation", and is therefore proportional to the velocity gradient. Increase of granular temperature

at the top of the flow is observed, according to saltation of particles in that zone and to what found in Figure 13 for the smooth bed case. Using the sand paper bed, the granular temperature appears to be higher than in the case with the metallic bed, excluding the cases where a no-slip condition at the bottom is observed. As expected, in the area where deposition of granular material occurs the granular temperature approximate to a null value.

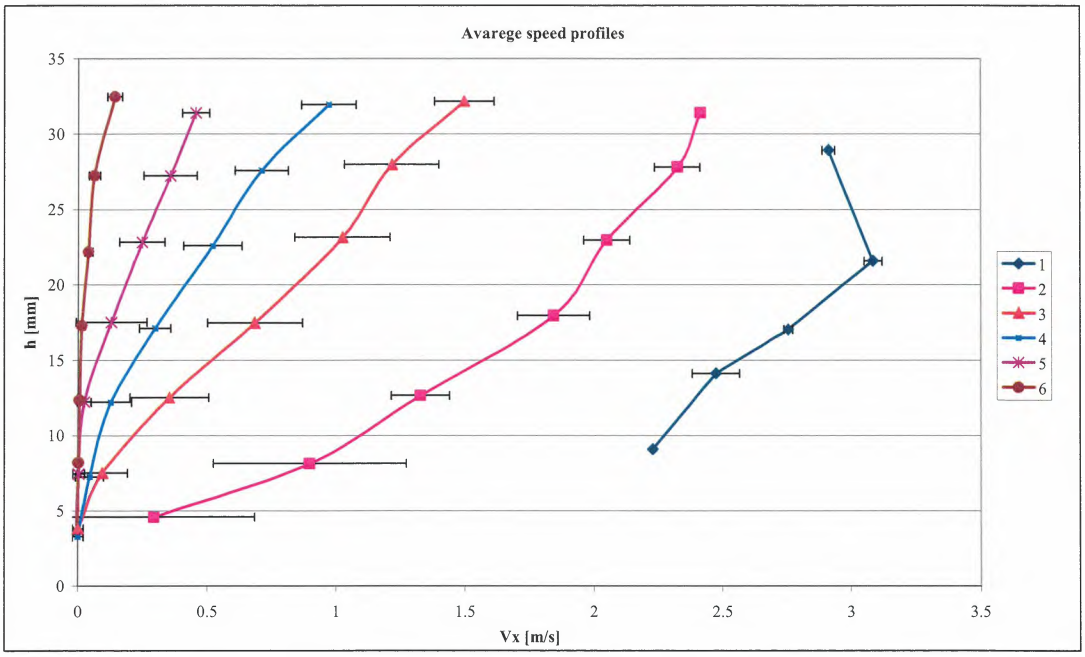

Figure 16 - Average speed profiles: the number in the legend refers to those in table 5

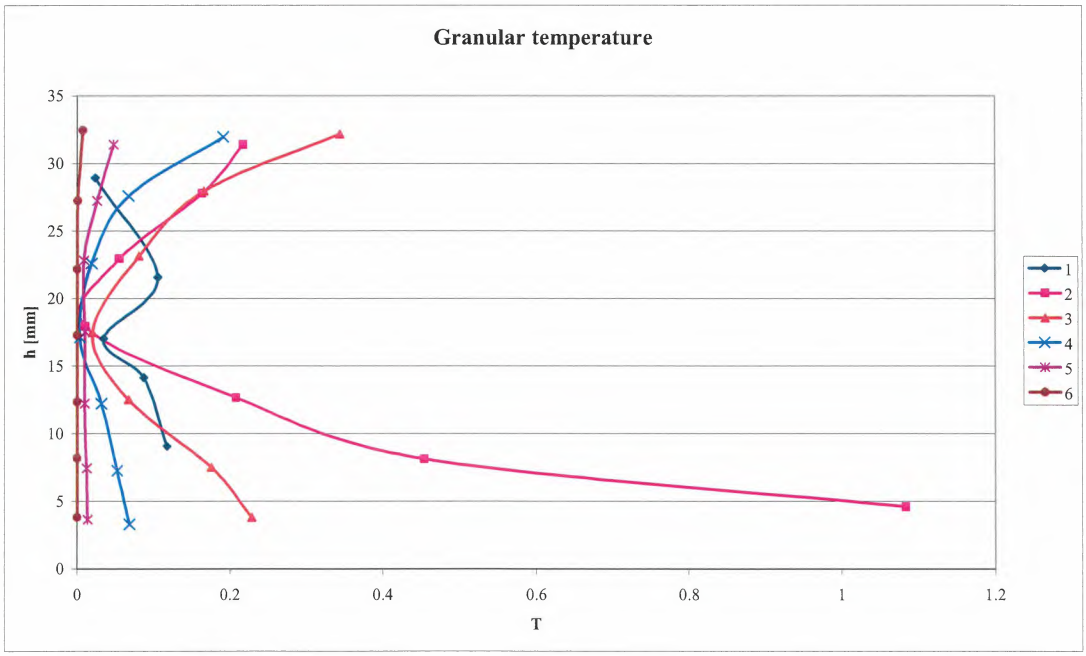

Figure 17 - Granular temperature profiles: the number in the legend refers to those in table 5

According to the methods described at § 3.3, also for these type of flow we have determined the concentration profiles; given the unsteady features of the flow, we have done it for different instant of motion, as shown in Figure 18.

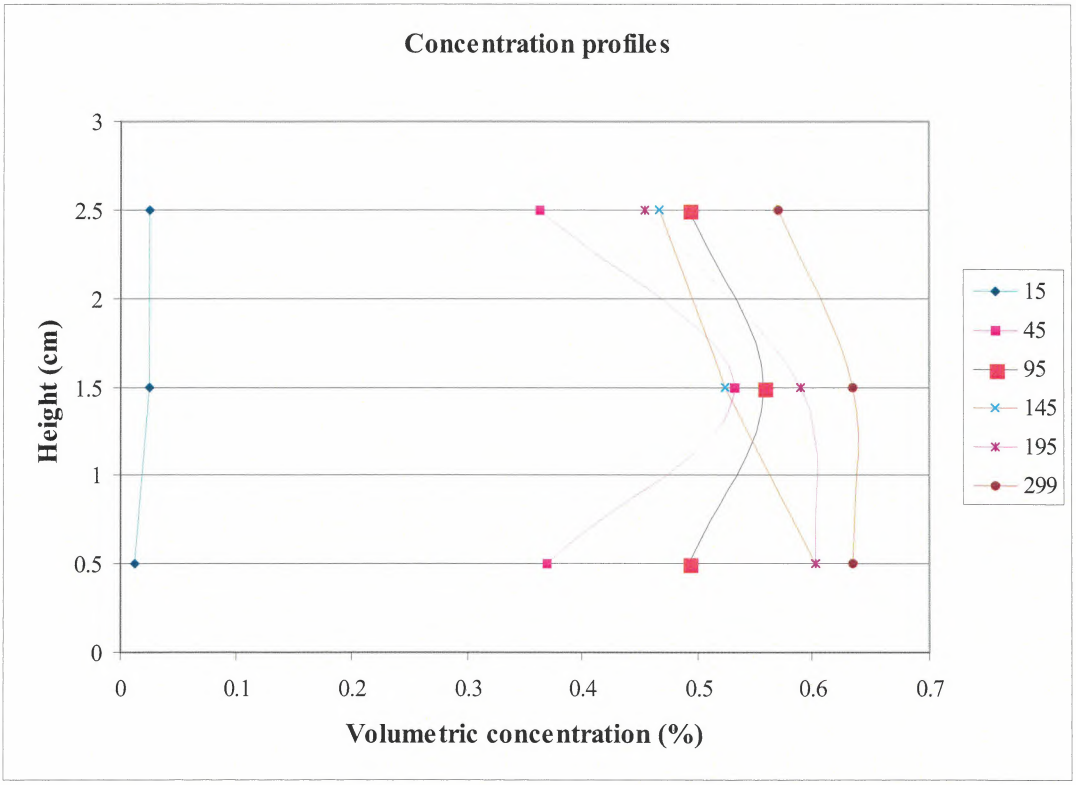

Figure 18 - Volumetric concentration profiles: the number in the legend indicate the frame to which the profiles refer (see also table 5)

It is interesting to observe that at the bottom of the flow, passing from a slip to a non-slip condition, the concentration increases, and overcome the threshold indicative of a transition from collisional to frictional flow regime - that is abut 0,5. In particular, in the part of flow where deposition has occurred the volumetric concentration is close to the one of maximum particles packing.

5. OUTLOOK

The experiments carried out at Pavia chutes in the first year of SATSIE project gave promising results, and the technique based on high-speed recordings seems to be able to properly investigate crucial flow properties such as velocity, concentration and granular temperature profiles, as well as to better understand the ongoing processes in rapid granular flows. Next year these experiments will be continued, varying the chute slope and the granular material type. Furthermore, similar experiments on the longer chutes will be started, using two reaches with different inclinations, in order to study also flow regime transition processes. Beside experiments on flows over smooth and rough bed, also investigations on erosive flow were started; such experiments are presently in progress and the first result under analysis. Such investigations will be carried out in the next year of project as well.

VEÐURSTOFA ÍSLANDS

Report
03038

Kristín Martha Hákonardóttir
Andrew Hogg, CEGF
Tómas Jóhannesson

A laboratory study of the interaction between supercritical, shallow flows and dams

VÍ-ÚR27
Reykjavík
November 2003

Abstract

We report on a series of laboratory experiments to study the deflecting and retarding effect of avalanche defence measures. We find that incompressible, shallow-layer shock dynamics can be used to describe the interaction of high Froude number, steady, dense, granular flows with obstacles, such as deflecting and catching dams. Stationary, oblique shocks are formed in the interaction of the flows with deflecting dams, while a travelling bore is formed upstream of a catching dam when none of the flow over-tops the dam. As the height of the dam is lowered compared with the depth of the approaching flow, the bore slows down and finally the flow jumps ballistically over the dam and a shock is not formed upstream of the dam.

Contents

1 Introduction

The traditional design of dams used to deflect or stop dense snow avalanches has been based on simple considerations of the energy of a small part of the flow or the run-up of a point-mass on the upstream facing, sloping side of a deflecting or a catching dam (Irgens *et al.*, 1998). McClung and Mears (1995) consider the run-up onto a catching dam and by accounting for the pressures in the flow, conclude that the point mass theory underestimates the run-up by a factor of two. Both of the approaches, however, may be too idealised. Chu *et al.* (1995) have performed small-scale experiments and tested the theory of McClung and Mears against their observations. Both theories suggest that energy is lost in the impact of the current with the dam and McClung and Mears hypothesise that the flow loses the normal component of its approach velocity in the interaction. A fundamental diffi culty with the point-mass view of the impact of an avalanche on a deflecting dam is caused by the fi nite width of the avalanche, since the lateral interaction of different parts of the avalanche is ignored. The point-mass trajectories corresponding to different lateral parts of the avalanche must intersect as already deflected material on its way down the dam side meets with material heading towards the dam farther down. The effect of this interaction on the run-up cannot be studied easily using a point-mass consideration and a more complete physical description of lateral interaction in the impact process must be developed.

More recent chute experiments and theoretical analysis (Tai *et al.*, 2001, and Gray *et al.*, 2003) suggest a different flow behaviour in the impact of dense supercritical granular flow with obstacles. The experiments indicate that a shock (or a jump) is formed upstream of an obstacle and in the direction normal to the shock, a jump from a supercritical flow state to a subcritical one occurs which may be modelled by 'shallow-water' jump conditions, see for example (Whitham, 1999). Observations of two natural, snow avalanches hitting deflecting dams above the village Flateyri in western Iceland (Jóhannesson, 2001) reveal the same phenomena as these laboratory experiments. The avalanche debris that was left behind showed that the impact had channelised a part of, or the whole of the width of both the avalanches into thicker streams, travelling parallel to the dam and thereby increased the run-out of the avalanches signifi cantly. These observations suggest that a shock was formed near the dams in the interaction.

The fundamental difference between the theoretical approaches described above indicates that further investigations of the behaviour of granular flows interacting with dams are needed. Such studies provide a better understanding of the dynamics of the flows. Small-scale laboratory experiments, larger-scale experiments with snow as well as observations of natural avalanches that hit dams are needed as a part of such investigations.

Three sets of experiments in small-scale laboratory chutes are described in this report. The experiments involve supercritical, dry, dense, granular flows, short and long in duration, on steep slopes and supercritical flow of water on shallow slopes. The experiments were scaled with the internal Froude number of the flows, $\mathrm{Fr} = u/\sqrt{g^{\star}h}$, where u is the flow speed, $g^{\star} = g\cos\xi$ is the component of the gravitational acceleration perpendicular to a

slope inclined at an angle ξ to the horizontal and h is the depth of the flow. The Froude numbers of the flows were in range of 5–15. The experiments at the lower Froude numbers are comparable with experimental results of flows interacting with dams reported by Gray *et al.* (2003). Those can then be compared with the higher Froude number flows in order to draw conclusions about the expected flow behaviour in the interaction of the dense core of a natural, dry-snow avalanche with dams.

The dense core of a natural, dry-snow avalanche has a Froude number of the order 10 (Hopfinger, 1983 and Issler, 2003). The compressibility of the dense core, characterised by the Mach number of the flow, Ma, is not well understood (Issler, 2003). The Mach number represents the ratio between the flow speed and the speed of pressure disturbances in the flow (speed of sound in the flow, c), $\mathrm{Ma} = u/c$. In relatively incompressible and shallow free surface flows, pressure disturbances travel as gravity waves on the free surface of the flow with a speed of $\sqrt{gh}$, and the flow is characterised by the Froude number. The shock angle of the avalanche that was partly channelised by the deflecting dam in Flateyri was small and the channelised part of the shock was considerably thicker than the undisturbed part of the flow. The increased flow depth of the shock indicates that the dense core of the avalanche was not highly compressible and the small shock angle is consistent with a high Froude number flow ($\mathrm{Fr}_1 \sim 10$). We therefore study the behaviour of the dense core by analogy with high Froude number, incompressible flows, though that may not apply to all natural, dry-snow avalanches.

The report starts with a short review and discussion of incompressible, shallow-layer shock dynamics, needed to explain the experimental results (§ 2), followed by a description of the three experimental series. The first series (§ 3) involves an initial set of experiments of granular flows at Froude numbers of the order 10, conducted to identify the flow behaviour in the interaction with a deflecting dam. The avalanches in this series had a short flow duration, that is the length to depth ratio of the currents was approximately 200. The experimental observations gave rise to questions that were addressed in the following two experimental sets where avalanches with a longer flow duration were used (a length to depth ratio of over 10000). Steady water experiments of flows on shallow slopes with Froude numbers close to 5 are described in § 4. They were designed to investigate how well the shallow-water model and the jump conditions agreed with shallow-water experiments. The final set of experiments is described in § 5. The experiments involved steady granular flows at three different Froude numbers; 5, 12 and 14, linking the previous two experimental sets. The three experimental sets are finally compared in § 6 and some general conclusions are drawn from the combined experiments.

2 Shock theory

One approach to modelling the interaction of an avalanche with a dam involves viewing the avalanche motion as a stream of supercritical shallow-water that undergoes changes in flow state (hydraulic jump) when interacting with dams. Jumps between flow states have been observed experimentally with dense granular flows down channels (Savage, 1979) and as a result of the interaction with catching and deflecting dams in the laboratory (Gray *et al.*, 2003) and in nature when a snow avalanche of volume 10^5 m^3 hit a deflecting dam in Flateyri, Iceland, in 1999 (Jóhannesson, 2001).

The description of the interaction between granular flow and an obstacle in terms of the dynamics of shallow-water flow involves a dramatic simplification of the physical processes that may not provide an accurate description of flows of natural snow avalanches. The theory is developed below in considerable detail in order to provide a consistent framework for the interpretation of the experiments that have been carried out. Deviations from the predictions of this theory can then provide a starting point for a more realistic theoretical description.

2.1 Classical hydraulic jump

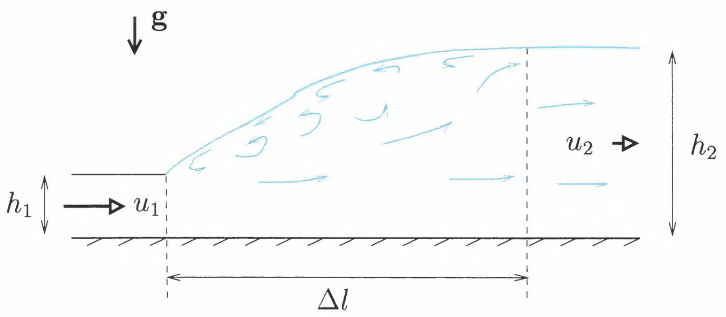

Figure 1: Schematic diagram of a classical hydraulic jump.

Hydraulic jumps are regions where shallow-water flows change from a supercritical to a subcritical state and thereby dissipate mechanical energy. The transition between the two states does not occur abruptly, but rather over a finite length, Δl, illustrated in Figure 1, hereafter referred to as the 'transition zone'.

The characteristics of the hydraulic jump are highly dependent on the Froude number of the approaching flow, Fr_1. Hager (1992) classifies hydraulic jumps according to the magnitude of Fr_1 as follows: The hydraulic jump is termed pre-jump for $1.7 < \mathrm{Fr}_1 < 2.5$. A series of small rollers develop on the surface for $\mathrm{Fr}_1 \sim 1.7$, and are slightly intensified for increasing Froude numbers. The water surface is quite smooth, and the velocity distribution in the tailwater is fairly uniform. Transition jumps correspond to Froude numbers between 2.5 and

4.5. This type of jump has a pulsating action. The entering jet oscillates heavily from the bottom to the surface. Each oscillation produces a large wave of an irregular period. Jumps for $4.5 < \mathrm{Fr}_1 < 9$ are stabilised jumps with the since they have a limited tailwater wave action, a relatively high energy dissipation, and a compact and stable appearance. For extremely high speed flows at Froude numbers above 9, the high velocity jet is no longer able to remain near the underlying boundary. Slugs of water rolling down the front face of the jump intermittently fall into the high-velocity jet and generate additional tailwater waves. The surface of the jump is usually very rough and contains a considerable amount of spray.

According to the classical analysis of two-dimensional hydraulic jumps of a fluid with isotropic, hydrostatic pressure distributions, mass and momentum fluxes are conserved across the jump but mechanical energy is dissipated, see *e.g.* (Whitham, 1999). The analysis describes the conditions on either side of the transition zone but does not resolve the complicated three-dimensional structure of the transition zone. Jump brackets, $[\![\ ]\!]$, are commonly used to indicate differences in flow states upstream and downstream of the jump. The conservation of mass and momentum fluxes across the stationary jump in Figure 1 can be written as

$$\begin{aligned} [\![uh\rho]\!] &= 0, \\ \left[\!\!\left[h\rho u^2 + \frac{1}{2} g^\star \rho h^2 \right]\!\!\right] &= 0. \end{aligned} \tag{1}$$

2.2 Normal shocks: Catching dams

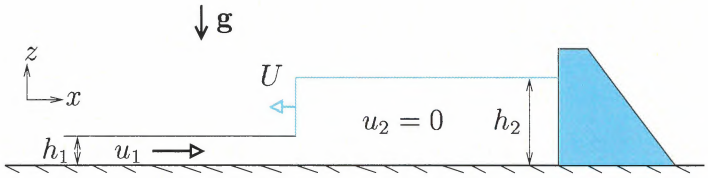

Figure 2: Schematic diagram of a two-dimensional bore travelling upstream from a catching dam.

When supercritical flow passes over an obstacle that is high enough so that the flow state changes to a subcritical state, fluid starts to pile up upstream of the obstacle. The transition between a supercritical flow and a subcritical flow is accomplished in a hydraulic jump, as mentioned above. Figure 2 shows a hydraulic or a granular jump formed when the approaching flow hits a catching dam. A bore travels upstream from the dam and the dam is higher than the depth of the bore. By choosing a reference frame travelling with the bore at speed U to the left, conservation of mass- and momentum fluxes across the jump becomes

$$(u_1 + U)\, h_1 \rho_1 = U h_2 \rho_2, \tag{2}$$

$$h_1 \rho_1 \left(u_1 + U\right)^2 + \frac{1}{2} g^\star \rho_1 h_1^2 = h_2 \rho_2 U^2 + \frac{1}{2} g^\star \rho_2 h_2^2, \tag{3}$$

where $g^\star = g$ is the acceleration due to gravity and ρ is the density of the flow. For incompressible jumps, such as hydraulic jumps, $\rho_1 = \rho_2$. For granular materials we expect, on the other hand, the stationary material downstream of a jump to be somewhat more closely packed than the dilated flowing material implying $\rho_2 > \rho_1$. An expression, relating the ratio of the shock depth and the depth of the approaching stream to the Froude number of the oncoming flow and the density ratio, ρ_2/ρ_1, is given by

$$\mathrm{Fr}_1 = \frac{h_2}{h_1}\sqrt{\frac{1}{2}\left(\rho_2/\rho_1 - \frac{1}{h_2/h_1} - \left(\frac{1}{h_2/h_1}\right)^2 + \left(\frac{1}{h_2/h_1}\right)^3 \frac{1}{\rho_2/\rho_1}\right)}. \tag{4}$$

The ratio, h_2/h_1, is plotted in Figure 3 (a) as a function of Fr_1 for different density ratios. Increased density difference lowers the height of the bore. The Froude number of the incoming flow can, furthermore, be obtained as a function of the ratio of the bore speed and the speed of the approaching flow and the density ratio

$$\mathrm{Fr}_1 = \frac{1}{U/u_1}\sqrt{\frac{1 + 2U/u_1 - (\rho_2/\rho_1 - 1)\,(U/u_1)^2}{2\rho_2/\rho_1(1 + U/u_1)}}. \tag{5}$$

The function is plotted in Figure 3 (b) for different density ratios. We note that at high upstream Froude numbers, the bore speed is slow compared with the speed of the incoming flow and the increased density difference slows the bore down.

The same set of equations with $g^\star = g\cos\xi$ (the component of gravity normal to a slope inclined at an angle ξ to the horizontal) may be used to describe flow down an inclined plane,

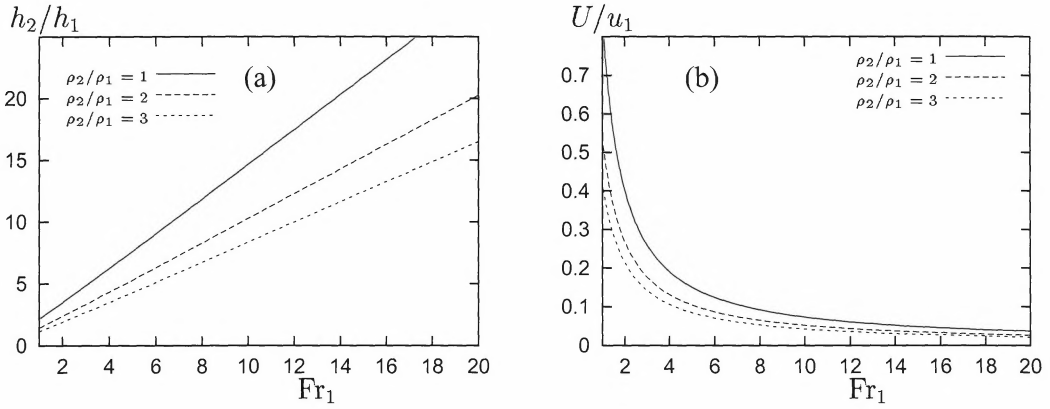

Figure 3: The ratio between the bore speed and the speed of the incoming flow as a function of the Froude number. The density ratios between 1 and 3 are chosen to correspond to possible density ratios in snow avalanches. Issler (2003) suggests that the dense core of a flowing dry-snow avalanche has a density in the range ρ_1 =250–500 kg m^3 while the density of avalanche debris hardly exceeds ρ_2 =500–600 kg m^3.

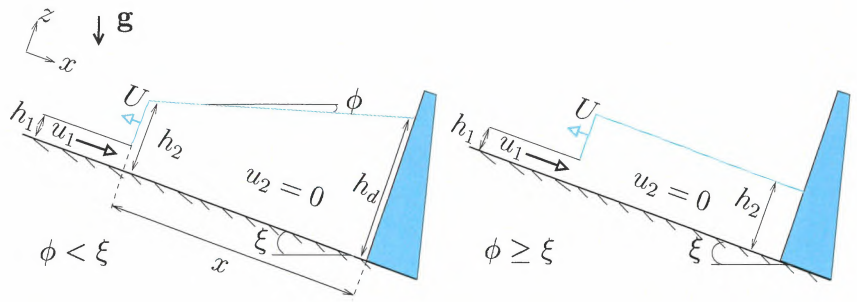

Figure 4: Schematic diagram of a bore travelling up an inclined plane, away from a catching dam, for material with different internal friction angles ϕ.

interacting with a dam, when the internal friction angle of the stationary material is larger than or equal to the slope angle, $\phi \geq \xi$. This will be the case if the transition zone is thin enough so that the component of gravity along the slope (the additional accelerative term, $g \sin \xi$) will not affect the conservation of momentum flux over the bore, see Figure 4. The free surface of a stationary pile of material is stable at angles up to the internal friction angle of the stationary pile, this angle is also termed the angle of repose of the material, ϕ. The free surface of the stationary material downstream of the shock is therefore stable at the slope angle ξ if $\phi \geq \xi$ and arrests on the slope downstream of the bore with the surface inclined at ξ. That implies that the depth of the stationary material in front of the dam is h_2 everywhere. In the case of material with $\phi < \xi$ ($\phi = 0$ for fluids), the stationary material (fluid) arrests on the slope downstream of the bore with the free surface inclined at the angle of repose and the depth of the stationary material just in front of the dam, h_d, increases the further upstream the bore travels. The mass flux, previously described by equation (2), needs to be adjusted in order to account for the the redistribution of the mass that is stopped in front of the dam

$$\begin{aligned} u_1 h_1 \rho_1 + \frac{\partial}{\partial t}\left(\rho_1 h_1 x\right) &= \frac{\partial}{\partial t}\left(\left[h_2 + \frac{h_d - h_2}{2}\right]\rho_2 x\right), \\ \left(u_1 + U\right) h_1 \rho_1 &= U \rho_2 \left(h_2 + x \tan\left(\xi - \phi\right)\right), \end{aligned} \tag{6}$$

where x is the position of the front of the bore, $h_d = h_2 + x \tan\left(\xi - \phi\right)$ and $\partial x / \partial t = U$.

As the height of the catching dam decreases relative to the depth of the approaching stream, some flow will escape over the dam and reach a critical state at the top of the dam, see *e.g.* (Gerhart *et al.*, 1993), while a hydraulic/granular jump is still present upstream of the dam, see Figure 5 (a). More of the flow escapes over the dam if the height of the dam is decreased further and finally a bore can no longer be maintained upstream of the dam and the flow jumps supercritically over the dam, as shown in Figure 5 (b).

The hydraulic/granular jump upstream of a dam with overflow, positioned on a slope inclined at an angle ξ with $\phi \geq \xi$ can be calculated by considering the conservation of mass and

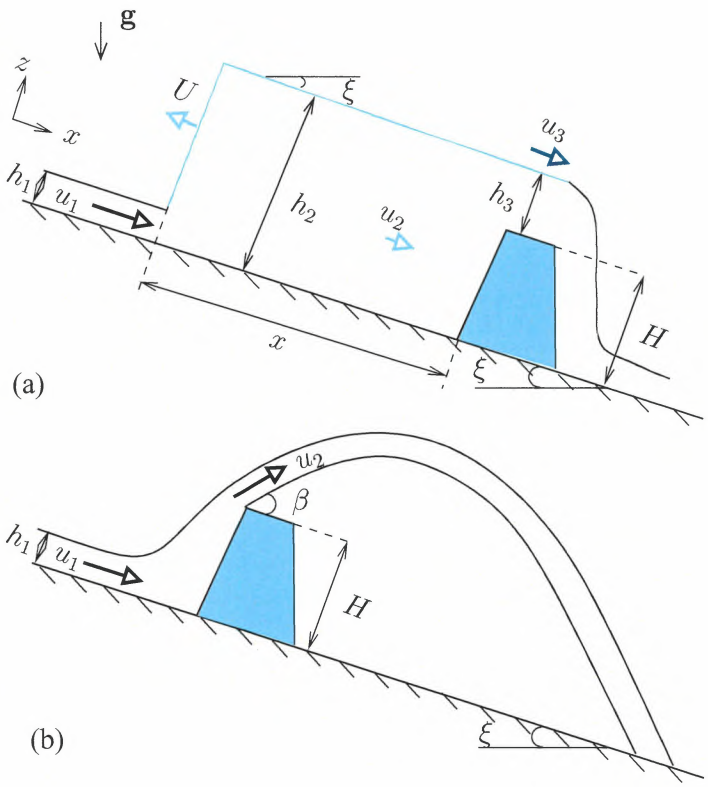

Figure 5: The top fi gure (a) is a schematic diagram of a granular jump formed upstream of a dam, when supercritical fbw interacts with the dam, some of the fbw escapes over the dam. The fbw over the dam is critical, $\mathrm{Fr}_3 = 1$, $U > 0$, $\phi \geq \xi$. The bottom fi gure (b) shows supercritical fbw jumping over a dam, $U < 0$.

momentum fluxes across the bore in a reference frame travelling with the bore

$$(u_1 + U)\, h_1 = (u_2 + U)\, h_2, \tag{7}$$

$$\frac{1}{2} g^\star h_1^2 + (u_1 + U)^2\, h_1 = \frac{1}{2} g^\star h_2^2 + (u_2 + U)^2\, h_2. \tag{8}$$

We have assumed that $\rho_1 = \rho_2 = \rho_3$ for simplicity, since the fbw does not stop completely in front of the dam and will therefore not be as closely packed as in the case of no over-topping. Conservation of mass fux over the dam in a stationary frame of reference becomes

$$h_2 u_2 = h_3 u_3 \qquad \text{where} \qquad h_3 = h_2 - H, \tag{9}$$

by, for simplicity, assuming that the fbw is in a constant, uniform state downstream of the jump, *i.e.* the downslope component of gravity is balanced by friction. The fbw goes through

another transition of state as it passes over the dam. It is subcritical upstream of the dam and supercritical downstream of the dam. We therefore find that the flow over the dam is critical, leading to a final constraint on the flow:

$$\mathrm{Fr}_3 = 1, \qquad \text{which implies that} \qquad u_3 = \sqrt{g^\star h_3}. \tag{10}$$

In the case of material with $\phi < \xi$, the free surface of the granular material is stable at the angle of repose if u_2 is sufficiently small and equation (9) becomes

$$(h_2 + x\tan(\xi - \phi))\, u_2 = h_3 u_3 \qquad \text{where} \qquad h_3 = h_2 + x\tan(\xi - \phi) - H, \tag{11}$$

and x is the distance from the front of the bore to the catching dam, see Figures 4 and 5 (a).

A hydraulic/granular jump can no longer be maintained upstream of the dam when the computed speed of the bore becomes negative and the flow jumps over the dam in a supercritical flow state. The jet takes a ballistic trajectory over the dam as described by Hákonardóttir *et al.* (2003a and 2003b) for flows with braking mounds and catching dams in which the obstacles have a height comparable to the depth of the approaching flow.

2.3 Oblique shocks: Deflecting dams

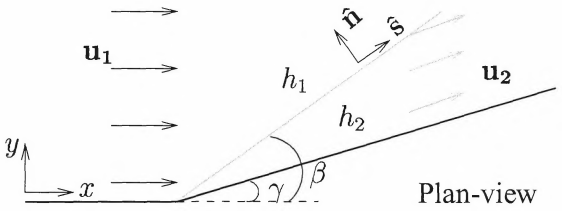

$$\mathbf{u_1} = (u_1, 0)$$
$$\mathbf{u_2} = (u_2\cos\gamma, u_2\sin\gamma)$$
$$\hat{\mathbf{n}} = (-\sin\beta, \cos\beta)$$
$$\hat{\mathbf{s}} = (\cos\beta, \sin\beta)$$

Figure 6: Uniform fluid flow hits a deflecting dam at an angle γ and a stationary, oblique shock is formed at an angle β to the incoming flow. Unit vectors normal and tangential to the shock are denoted by $\hat{\mathbf{n}}$ and $\hat{\mathbf{s}}$. The flow downstream of the shock is parallel to the dam.

Shock conditions can be formulated for fluid flow hitting a deflecting dam and forming an oblique, stationary shock that is flowing with a constant speed in a direction parallel to the dam. These conditions can be obtained in most text books on gas dynamics, *e.g.* (Whitham, 1999), and adapted to shallow-water flow. We assume that $\rho_1 = \rho_2$ in the granular flow, since the flow on both sides of the shock is in a dilated flowing state. The conservation of mass flux across the jump takes the form

$$[\![\, h\mathbf{u}\cdot\hat{\mathbf{n}} \,]\!] = 0,$$

which leads to

$$h_2 u_2 \sin(\beta - \gamma) = h_1 u_1 \sin\beta. \tag{12}$$

Conservation of momentum flux across the jump can be written as

$$\left[\!\left[h\mathbf{u}\left(\mathbf{u}\cdot\hat{\mathbf{n}}\right)+\frac{1}{2}g^{\star}h^{2}\hat{\mathbf{n}}\right]\!\right]=0,$$

which in the directions normal and tangential to the shock becomes

$$\frac{1}{2}g^{\star}h_2^2+h_2u_2^2\sin^2\left(\beta-\gamma\right) = \frac{1}{2}g^{\star}h_1^2+h_1u_1^2\sin^2\beta, \tag{13}$$

$$h_2u_2^2\sin\left(\beta-\gamma\right)\cos\left(\beta-\gamma\right) = h_1u_1^2\sin\beta\cos\beta. \tag{14}$$

Equation (14) together with (12) implies that the speed along the shock must be continuous

$$u_2\cos\left(\beta-\gamma\right)=u_1\cos\beta.$$

By solving (12), (13) and (14) for a given incoming speed and flow depth, the outgoing flow speed and depth can be calculated along with the oblique shock angle, β. An expression, relating the shock angle to the known flow parameters (the Froude number of the flow and the deflecting angle of the dam) is given by

$$\mathrm{Fr}_1=\frac{1}{\sin\beta}\sqrt{\frac{\tan\beta}{2\tan\left(\beta-\gamma\right)}\left(\frac{\tan\beta}{\tan\left(\beta-\gamma\right)}+1\right)}. \tag{15}$$

For a given Froude number and a given deflecting angle, there are two possible shock angles. The smaller angle corresponds to a weak shock and the larger one to a strong shock. As $\gamma\to 0$ the weak shock tends to $\beta=\sin^{-1}\left(1/\mathrm{Fr}_1\right)$ and the strong shock tends to a normal shock, for which $\beta=90°$. The flow speed downstream of a weak shock is nearly always supersonic, while the speed becomes subsonic through a strong shock. We restrict our discussion to weak shocks since those are the ones that usually occur in practice. Using equation (15), we plot the behaviour of the shock angle relative to the dam as a function of the Froude number for constant deflecting angles in Figure 7 (a) and as a function of the deflecting angle for constant Froude numbers in Figure 7 (b). The plots indicate that the shock angle is highly dependent upon the Froude number of the flow and becomes smaller with increasing Froude number. We furthermore note that for high Froude numbers, the shock angle is relatively independent of the deflecting angle of the dams. The ratio between the shock height and the depth of the approaching stream is plotted as a function of the Froude number for constant deflecting angles in Figure 7 (c) and as a function of the deflecting angle for constant Froude numbers in Figure 7 (d). The plots show that the shock depth increases with increasing deflecting angles and Froude numbers.

In this analysis, the pressure in the granular material has been assumed to be hydrostatic and isotropic. There is a debate in the granular flow literature about whether the assumption of an isotropic pressure field is appropriate for granular flows such as snow avalanches. For

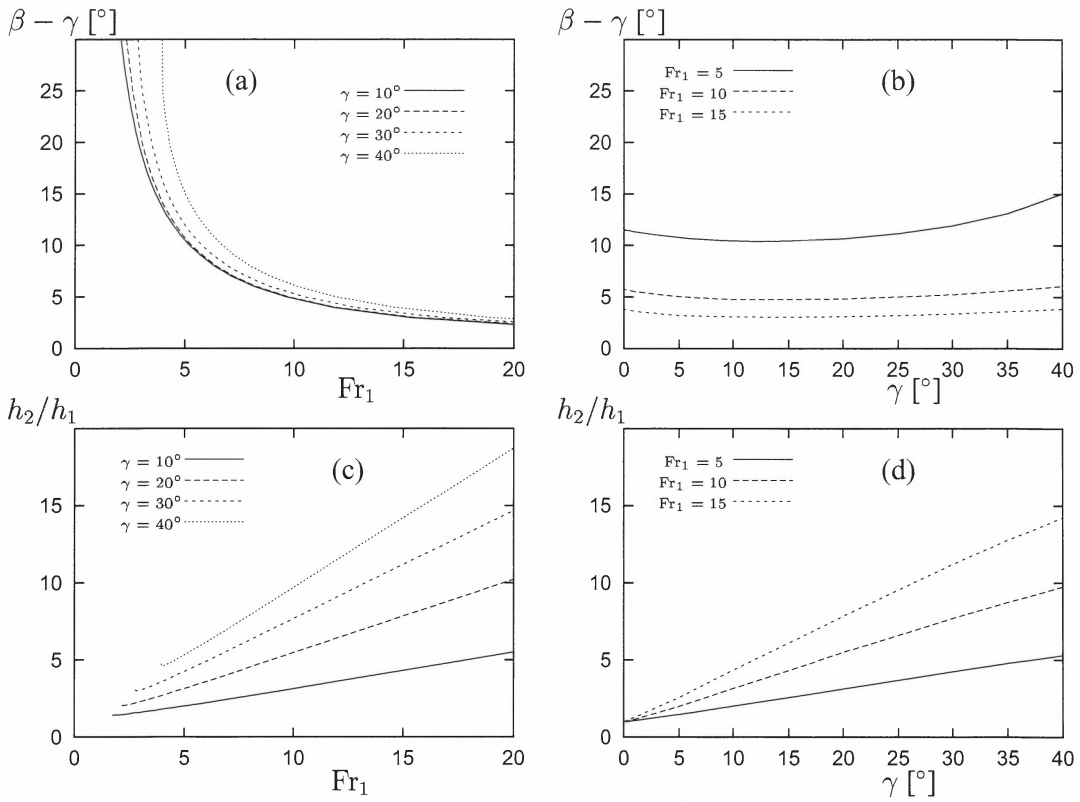

Figure 7: The shock angle relative to the deflecting dam plotted: (a) as a function of the Froude number for constant deflecting angles and (b) as a function of the deflecting angle for constant Froude numbers. The shock height non-dimensionalised by the depth of the approaching flow plotted: (c) as a function of the Froude number for constant deflecting angles and (d) as a function of the deflecting angle for constant Froude numbers.

example, Savage and Hutter (1989) link the components of the pressure field parallel with and normal to the slope, p_{xx} and p_{zz}, through an earth pressure coefficient, defined by

$$K = \frac{p_{xx}}{p_{zz}}.$$

Values of the earth pressure coefficient may be derived assuming a Mohr-Coulomb plastic behaviour for the cohesionless yield on the basal sliding surface,

$$K = \begin{cases} K_{\text{act}} & \text{for} \quad \partial u/\partial x > 0, \\ K_{\text{pass}} & \text{for} \quad \partial u/\partial x < 0, \end{cases}$$

with

$$K_{\text{act/pass}} = 2\left(1 \mp \sqrt{1 - \cos^2\phi/\cos^2\delta}\right)\sec^2\phi - 1,$$

where ϕ is the internal friction angle of the granular material and $\mu = \tan\delta$ is the dynamic friction coeffi cient at the bed. If the jump conditions (1) are implemented with anisotropic pressure, then the conservation of momentum flux across the bore becomes

$$\left[\!\left[h\rho u^2 + \frac{1}{2}K_{\text{pass}}g^\star\rho h^2 \right]\!\right] = 0. \tag{16}$$

Gray *et al.* (2003) and Pouliquen and Forterre (2002) treat the pressure in granular flows as isotropic and hydrostatic and obtain better agreement with the experimental results than when using an earth pressure coeffi cient. Gray *et al.* also argue that the discontinuity in the pressure, introduced through the earth pressure coeffi cient, is unphysical and should lead to a discontinuity in the flow depth. They base their theoretical model on older models of avalanches, developed by Russian scientists, see *e.g.* (Eglit, 1983), where direct analogy is made between granular avalanches and shallow-water flows.

3 Laboratory experiments of short duration, steady granular flows interacting with deflecting dams

The experiments were designed to study the deflection of high Froude number granular flow by a dam and to compare the flow behaviour in the interaction with the dam with the point mass theory and the shallow-water theory, described in § 2. The necessary height of a deflecting dam at a constant deflecting angle, needed to fully deflect the oncoming flow, was quantified and the flow behaviour if some of the flow escaped over the dam was studied.

3.1 Experimental setup and design

The experiments were performed on a 6 m long wooden chute consisting of two straight sections, one inclined at 38° to the horizontal and the other one horizontal, see Figure 3.1. The sections were connected by a thin plywood sheet, positioned 2.32 m downslope from the gate, to obtain a smooth transition between the sections. The chute had 0.20 m high side walls made of perspex to allow for recording from the sides.

The deflecting dams were constructed of plywood and positioned at the upper section of the chute, 1.69 m downslope from the gate perpendicular to the base of the chute, at five different deflecting angles to the flow; $\gamma = 8\ °$, 15°, 24°, 32° and 44°, see Figure 8. The dams had a flow depth to dam height ratio from 1 to 20, or up to the dam height needed to fully deflect the flow for each deflecting angle.

The experiments were designed so that the granular current had an internal Froude number of the order 10. Glass beads (ballotini) of mean size 90 μm, density 2500 kg m^{-3} (bulk density of 1600 kg m^{-3}) and an approximately spherical shape were used. In each experiment, 6 kg of particles were released from the top of the chute by the rapid opening of a lock gate. The interaction between the flow and the deflecting dams was recorded from above and from the side with two video cameras. The evolution of the depth profile on the deflecting dams was measured by analysing the side-view video footage of the experiments. The angles of the deflected and the overflowing parts of the stream to the deflecting dam were analysed from the video footage provided by the camera that was positioned above the dams. The run-out length and distribution of the deposited particles were also measured.

The speed of the flow in front of the dams was measured over a length of 0.40 m by tracking the first front of the flow and tracer particles for interior speeds. The maximum flow depth was measured by fixing a gate in the flow path at a known distance from the base of the chute. The distance of the gate from the chute was then increased systematically until all of the current flowed under the gate without touching it.

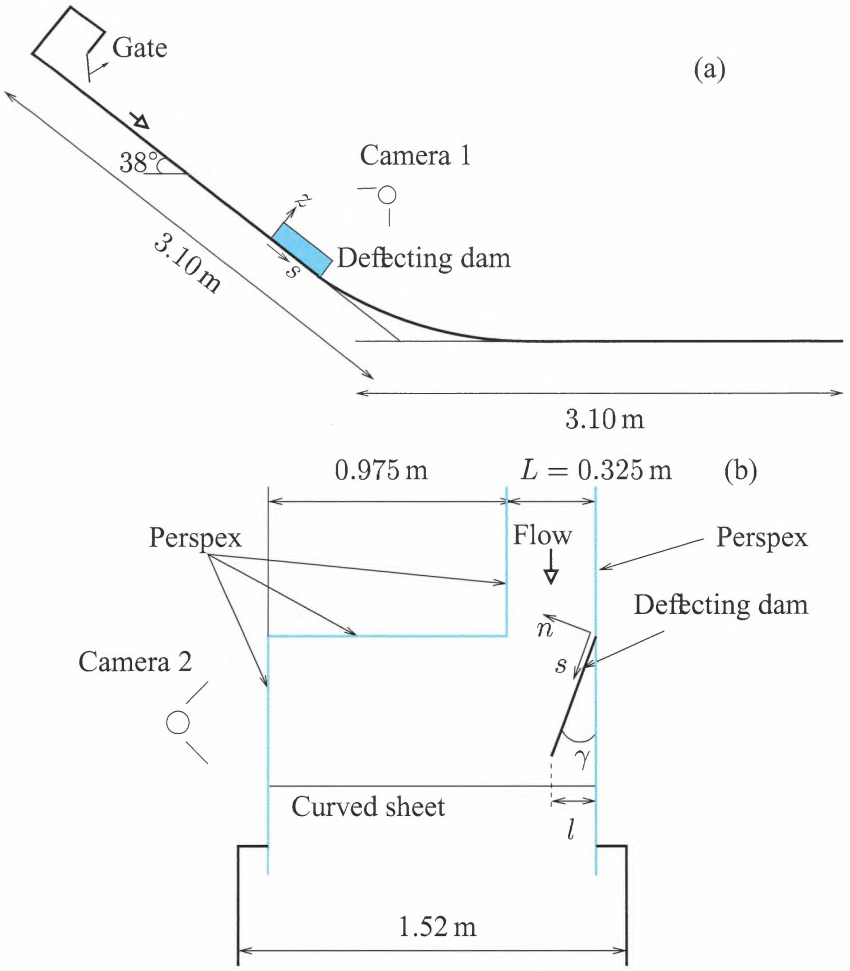

Figure 8: Schematic diagrams of the experimental chute, (a) shows a side-view of the chute and (b) a plan-view of the chute section next to the deflecting dam. The run-out zone starts were the slope angle changes, at the curved sheet. The channelled section of the chute is approximately 1.70 m long, measured from the lock gate.

3.2 Flow description

The flow quickly reached a terminal velocity on the upper section of the chute and flowed down the chute with a constant speed and a constant depth. The head of the flow was about 0.50 m long, 0.04 m thick and had a speed of $(3.7 \pm 0.8)\,\mathrm{m\,s^{-1}}$. It was very dilute (it could be seen through when looked at from above) and turbulent, with eddies suspending the glass beads. The flow immediately following was much denser with a constant depth of

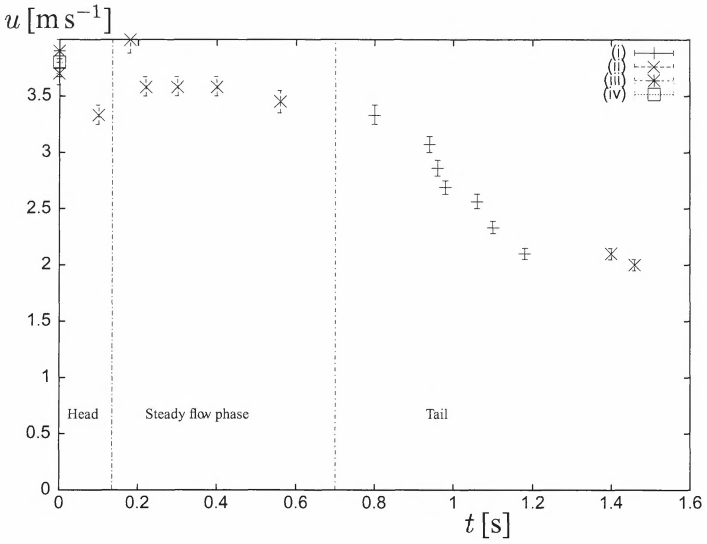

Figure 9: Flow speeds plotted as a function of time for experiments number (i) 83 to (iv) 86. The speed was measured at a fixed position, in front of the deflecting dams.

(0.009 ± 0.001) m and speed of $(3.5 \pm 0.1)\,\mathrm{m\,s^{-1}}$, resulting in a Froude number of 13. The dense flow phase was maintained for 0.6 s, so the flow was roughly 2.1 m long. This flow phase will be referred to as the steady flow phase. The flow rapidly thinned and slowed down after that, see Figure 9.

During the experimental period the particles changed slightly in character, leading to increased mobility of the flow. The run-out lengthened linearly by approximately 5% during the period, measured from the start of the run-out zone. The front speed of the flow was also found to increase linearly through the experimental period, see Figure 10. The interior speeds (the speed of the steady flow phase) were only measured at the end of the experimental period. It was thus assumed that the steady interior speed increased throughout the experimental period in the same fashion as the front speed, but with a $0.2\,\mathrm{m\,s^{-1}}$ lower speed as Figure 9 suggests. A summary with the exact values of the interior speeds that were used for the different deflecting angles is given in Table 1.

3.3 Results: Flow completely deflected by the dams

The dilute first front splashed onto the deflecting dam up to a similar height as the denser part immediately following and forming a semi-steady profile on the dam. The width of the stream flowing along the dam increased downstream and finally formed a jet at the end of the dam in a direction parallel with the dam. Figure 11 shows that the maximum run-up of the granular avalanches on the dams grew with increasing deflecting angles.

The effect of subjecting larger and smaller proportions of the avalanches to the deflect-

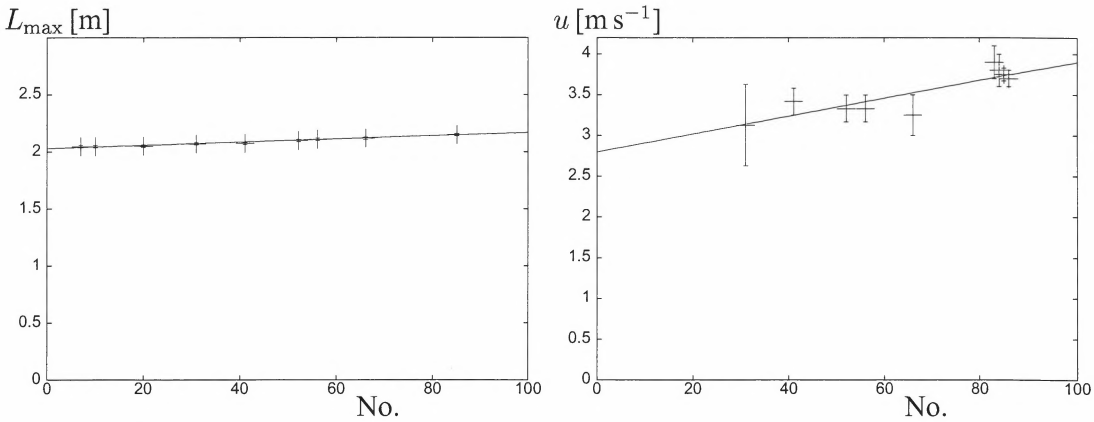

Figure 10: The maximum run-out and the front speed plotted as a function of the sequential number of the experiment performed (+) with a linear fit through the observations. The maximum run-out was measured from the start of the run-out zone (the curved sheet).

γ[°]	No.	u [m s^{-1}]
8.0 ± 0.5	65	3.3
15.0 ± 0.5	60	3.3
24.0 ± 0.5	47	3.1
32.0 ± 0.5	39	3.0
44.0 ± 0.5	55	3.2
90.0 ± 0.1	11	2.7

Table 1: The estimated interior speed of the flow, u, during the steady flow phase for the different deflecting angles, γ. The number of each experiment is denoted by No.

ing dams on the run-up on the dams (long and short dams) was examined for three different deflecting angles. Figure 12 shows a plot of the locus of the maximum run-up onto the deflecting dams for deflecting dams covering different proportions of the width of the avalanche, $0.2 \leq l/L \leq 1.1$, where L is the width of the avalanche and l is the deflected width defined in Figure 8. The maximum flow depth along the dams was always reached after a distance that was shorter than the length of the dams. Changing the length of the dams did therefore not alter the maximum flow depth in front of the dams. It was furthermore concluded that the end of the dams, where the pressure suddenly drops, did not affect the run-up profiles on the dams significantly, which is consistent with the flow being in a supercritical flow state along the dams.

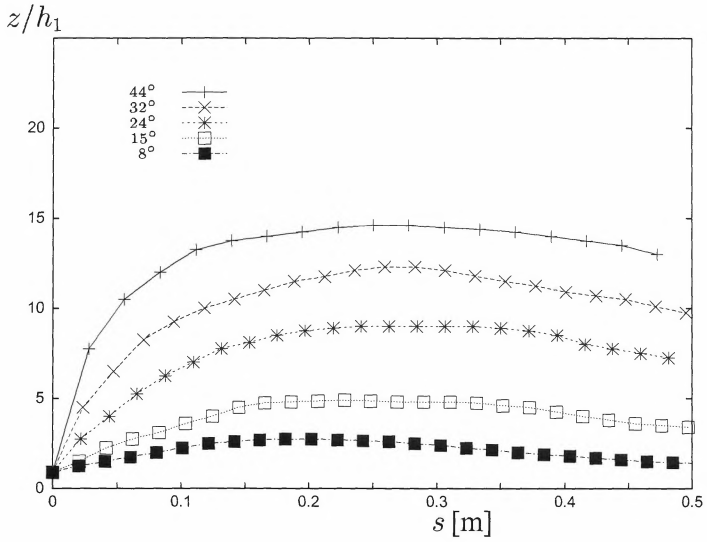

Figure 11: The locus of the maximum run-up on the deflecting dams non-dimensionalised with the thickness of the incoming stream plotted as a function of the length along the dams for the different deflecting angles. The uncertainty in the non-dimensional run-up is estimated ± 1 due to the short duration of the steady flow phase and an inaccuracy in drawing/visualising the curves from the video recordings.

3.3.1 Comparison with existing theories

The point mass model (PM), developed by Irgens *et al.* (1998), was used to calculate the path of a point-mass along a deflecting dam, assuming no loss of energy in the impact with the dam. The Coulomb friction parameter in the model, μ, was taken to be $\mu = \tan\delta$, where δ is the dynamic friction angle between the flow and the base of the experimental chute which was measured to be about 20°, implying $\mu \approx 0.4$. The dimensional coefficient representing turbulent dissipation, M/D, can be determined from the steady state of the momentum equation, see Irgens *et al.* (1998)

$$u^2 = (M/D)g(\sin\xi - \mu\cos\xi). \tag{17}$$

By substituting the measured, steady flow speed and depth on the chute into equation (17) we obtain $M/D \approx 4\,\mathrm{m}$. The physical range of these parameters for snow is discussed by Perla (1980).

Figure 13 shows that for small deflecting angles, the point mass model predicts the run-up on the deflecting dams well, but overshoots when the deflecting angle increases. No parameter values, within a reasonable physical limit of the two parameters, μ and M/D, could reproduce all the observed curves at once. The reason might be that dissipation of the mechanical energy of the flow takes place when the current impacts the dams. The dissipation can be assumed to increase with larger deflecting angles as the velocity component normal to the dams increases.

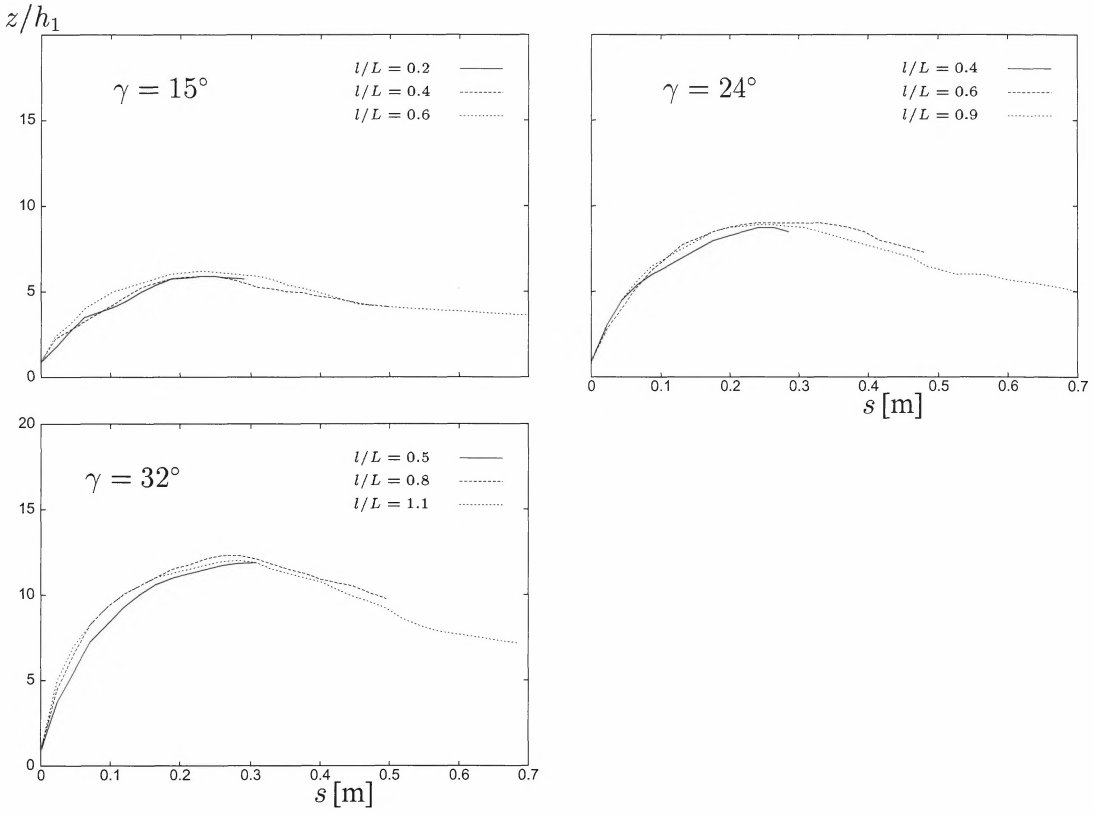

Figure 12: The non-dimensional run-up profiles of the avalanches on the deflecting dams plotted as a function of the length along the dams. The deflecting dams covered different proportions of the width of the avalanches, l/L (see Figure 8 for definition), between 0.2 and 1.1. The maximum run-up was reached during the steady flow phase.

If that is the case, tilting of the dams should affect the dissipation and the run-up on the dams. McClung and Mears (1995) account for internal pressure in the flow, which is neglected in the point-mass theory. They find that the run-up onto catching dams becomes twice as high as the point-mass theory predicts. The experiments reported here show the opposite, at least when no additional dissipation is incorporated. McClung and Mears, furthermore, suggest that the flow should lose its velocity component normal to the dam in the impact. That implies that there should not be run-up onto dams that have an upstream face normal to the slope on which they are positioned and is therefore not in agreement with our experimental results. The point mass theory developed by Irgens *et al.* and the more advanced theory by McClung and Mears do not seem to capture the physics of the interaction correctly.

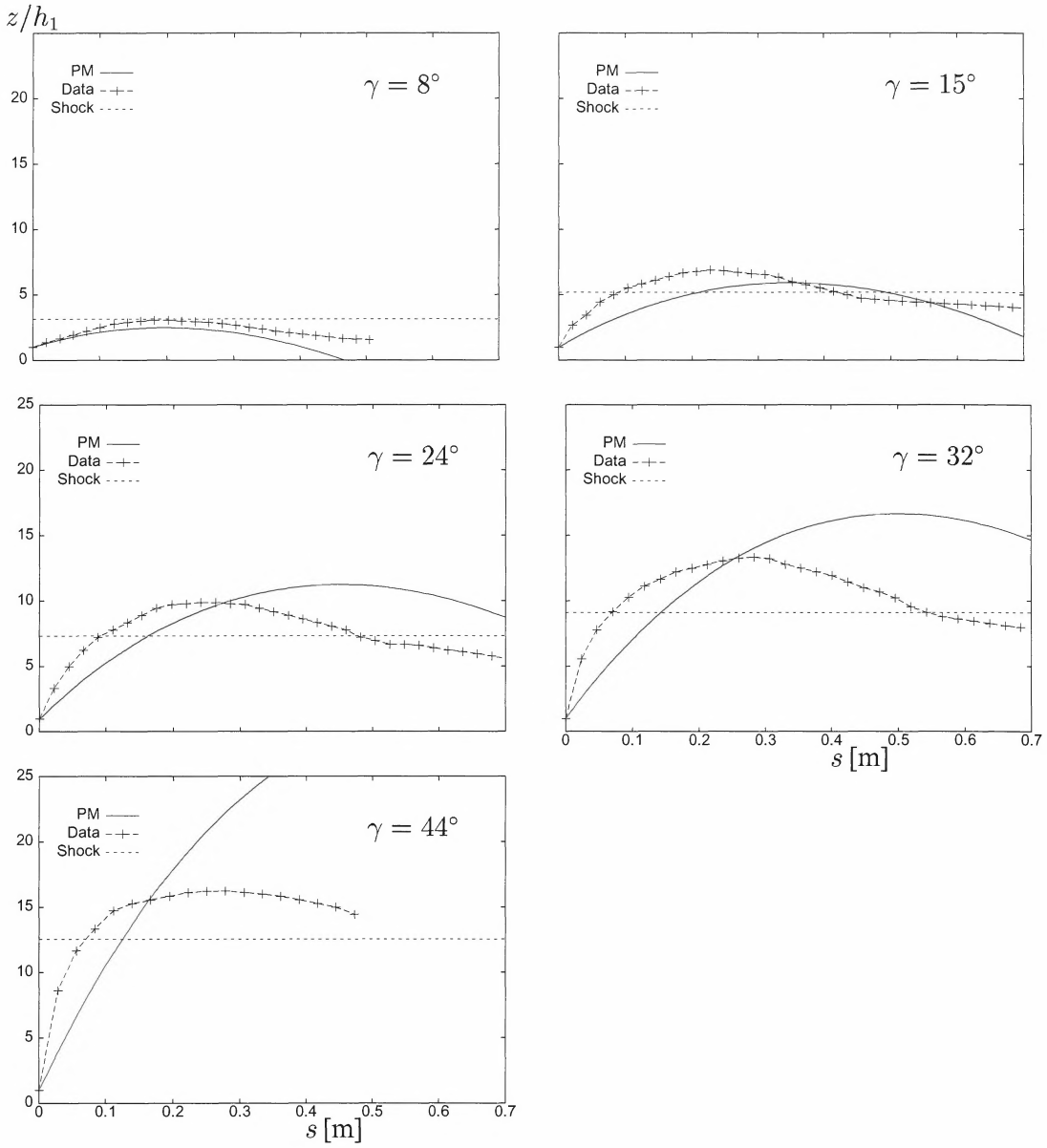

Figure 13: Non-dimensional run-up profiles for granular flows at $\mathrm{Fr}_1 = 13$. Each graph shows the observed depth profile along the deflecting dams, non-dimensionalised with the depth of the approaching stream, for a fixed deflecting angle, γ (+). The theoretical non-dimensional run-up of a point mass is shown with a solid curve and the theoretical non-dimensional shock height with a dashed line.

The granular flow consists of a thin, dense layer of numerous interacting point masses and can therefore be viewed to some approximation as a fluid or gas-like current. The flows are shallow, supercritical and not highly compressible, which gives rise to the possibility of shocks in the flow depth forming upstream of the dams (granular jumps) see the theoretical overview in § 2. The shock height, h_2, was calculated from the shallow-water jump conditions, equations (12), (13), and (14), and is plotted in Figure 13 as a straight line. We see that the observed run-up (+) is initially higher than the predicted shock height. The run-up then decreases along the dams and the theoretically derived shock height predicts the run-up close to the end of the deflecting dams. By introducing an earth pressure coefficient, K, into the jump conditions (equation (16)) the theoretical shock height is lowered, since $K_{\text{act/pass}} > 1$, and worse agreement with the experimental observations is obtained. The theoretical shock angle is plotted in Figure 14 along with the observed widening of the stream along the deflecting dams for the different deflecting angles.

The agreement of the shock theory with the experimental observations indicates that a shock forms upstream of the deflecting dams as is expected for supercritical flow of incompressible fluids interacting with deflectors. What still remains unclear from these experiments is why the flow ran higher up on the dams than the jump conditions predicted and had a tendency to turn over in a backwards rotating motion along the first 0.4–0.5 m of the dams. It is also unclear whether gravity disturbs the shock formation or influences the shock height along the dams, since the experiments were conducted with steady flows on a sloping surface, whereas the theory was derived for fluid flow on a horizontal plane where the flow states on

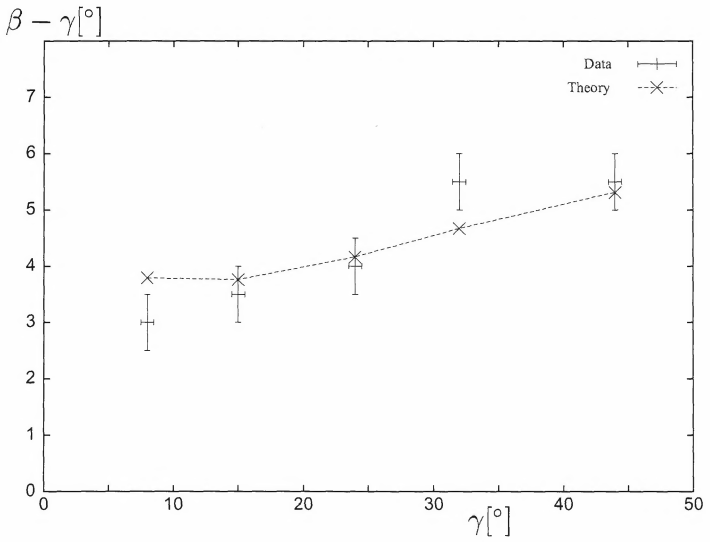

Figure 14: The shock angle relative to the dam, $\beta - \gamma$, plotted as a function of the deflecting angle, γ, for the theory (dashed line) and the experimental observations (+).

both sides of the shock are constant. There is furthermore a possibility that friction at the side of the dam affects the relatively narrow shock. The steady state flow phase was also quite short ($\sim$ 0.6 s) and one wondered whether the run-up onto the dams would develop further for a longer steady flow phase.

3.4 Results: Flow over-topping the dams

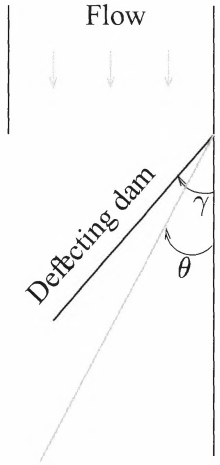

Figure 15: Plan-view of the experimental chute defining the overflow angle, θ.

The over-topping of flow interacting with deflecting dams was investigated by measuring the overflow angle, θ, defined in Figure 15, during the steady flow phase for dams of different heights, H, and at different deflecting angles, γ. When the deflecting dams were not high enough to fully deflect the flow, a part of the flow over-topped the dams. The experiments showed that for very low dams the current shot over the dams in a direction close to that of the approaching stream, $\theta \approx 0$. The jets were then turned more in the direction of the deflecting dams as the dams became higher and the overflow angle of the jets approached the deflecting angles of the dams as the height of the dams approached the height needed to fully deflect the current, *i.e.* $\theta \rightarrow \gamma$ for $H \rightarrow h_2$, if a shock is formed upstream of the dams. This effect is illustrated in Figure 16 where θ/γ is plotted as a function of H/h_2 for the five deflecting angles.

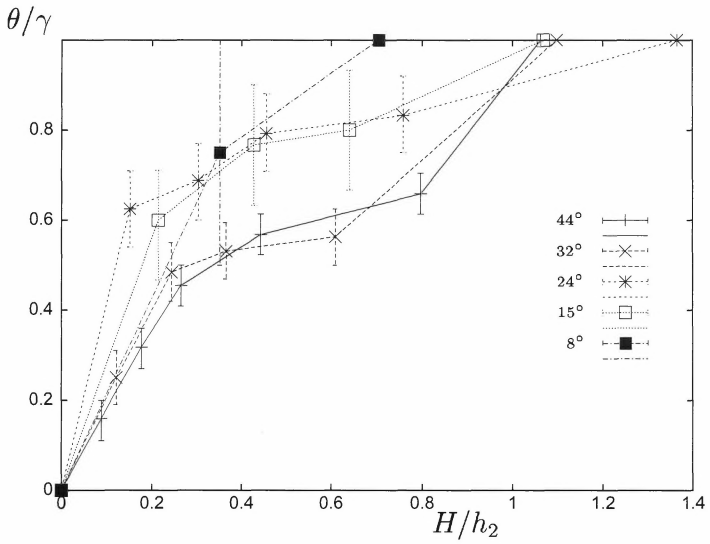

Figure 16: The overflow angle, θ, non-dimensionalised with the deflecting angle, γ, plotted as a function of the ratio between the dam height, H, and the calculated shock height, h_2.

4 Laboratory experiments of steady water flows interacting with deflecting dams

Two series of water experiments were conducted to study how well shallow water shock theory agreed with observations of rapid, shallow water flow.

4.1 Experimental setup and design

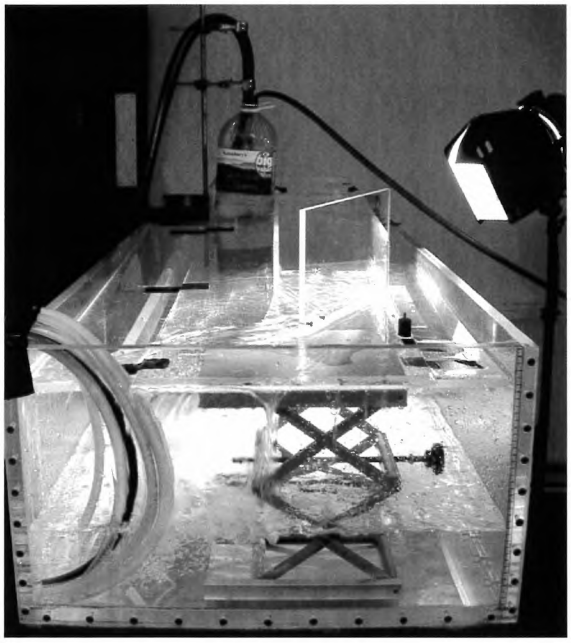

Figure 17: A photograph of the experimental setup for rapid flows of water. A steady stream of water was supplied through 3 hoses and stored in a reservoir. The water flowed over a weir and under a gate to minimise turbulence and wave action, and continued down a 0.2 m wide perspex channel before finally hitting a deflecting dam, also made of perspex. The deflecting dams were 0.3 m long and did never completely cover the width of the channel.

The experiments involved a steady stream of supercritical water flow down a 0.2 m wide channel at a speed u_1 and a depth h_1. This stream hit a deflecting dam and formed a steady hydraulic jump of height h_2 with speed along the dam, u_2, see Figure 17. The flow ended up in a large tank that gradually filled during the experiments, since the draining system did not fully cope with the flux of water into the tank. It was therefore necessary to split the experiments into two series: one to measure the height of the hydraulic jump and another to

measure the deflecting angle. The depth profiles on the dams and the deflecting angles were photographed with a digital camera, through the side of the dams and from above (Figure 18). The depth profiles and shock angles were measured for water flow on three different slopes, inclined at 3°, 6° and 9° to the horizontal. The flow speed, u_1, and depth, h_1, upstream of the dams were different for the different channel slopes, and consequently the oncoming flow had different Froude numbers in each of the three different experimental setups.

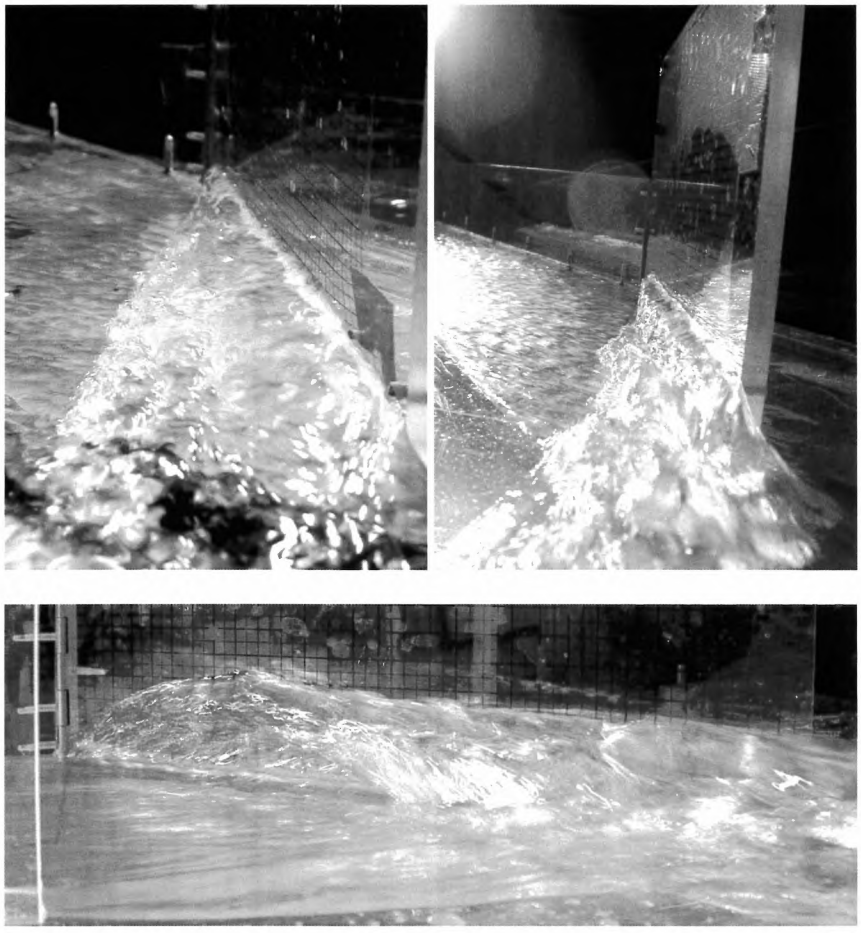

Figure 18: Photographs of stationary, oblique shocks of supercritical shallow water at $\mathrm{Fr}_1 = 4.5$, $\gamma = 20°$ (first figure) and $\mathrm{Fr}_1 = 7$, $\gamma = 40°$ (second figure), looking up into the streams along the deflecting dam. The bottom photograph shows a close-up of the second photograph, looking onto the side of the deflecting dam. It can be observed that the flow runs higher up on the deflecting dam at the start of the dam and then falls back on itself and the shock widens and becomes thinner.

4.2 Results

The incoming flow speeds and depths along with the Froude numbers in the two experimental series are summarised in Table 2. The first front of the flows splashed up higher on the dams than the steady hydraulic jumps. All of the experimental sets involved stabilised hydraulic jumps ($4.5 < \mathrm{Fr}_1 < 9$) that are relatively free of wave action, apart from the experiments on the 3° slope where the hydraulic jump is on the boundary of being a stabilised jump and might be categorised as a transitional jump with pulsating action (Hager, 1992). The Reynolds number is defined by $\mathrm{Re} = \rho u h/\mu$, where ρ is density and μ is viscosity. In the experiments, we find that Re is sufficiently large that viscous effects may be neglected.

The run-up profiles along the dams are plotted in Figure 19. The flow depth along the dams was found to be nearly constant, for dams at $\gamma \leq 20°$. For dams at the largest deflecting angles, $\gamma > 20°$, there was a zone at the beginning of the dams with higher run-up and overturning of the flow. The flow ran up, reached a maximum height and fell back upon the oncoming stream in a rotating motion. The flow depth in front of the dams was approximately constant further along the dams.

A possible explanation for the higher run-up and overturning of the flow at the beginning of the dams lies in the finite width of the highly turbulent transition zone. The width of the transition zone is denoted by Δl in Figure 20. The higher run-up occurs when the transition zone intersects with the beginning of the dams. The turbulence in the transition zone pushes the water higher up on the dams than the depth of the hydraulic jump along the dams. The region along the dam where the dam and the transition zone intersect will be referred to as the 'adjustment region'. The length of the adjustment region should increase with firstly smaller shock angles and secondly a wider transition zone. Figures 7 (a) and (b) show that the shock angle decreases with increasing Froude number, and for Froude numbers above 5 the shock angle is relatively independent of the deflecting angle. There should therefore be an increase in the length of the adjustment region with higher Froude number flows. Furthermore, studies of hydraulic jumps show that the transition zone widens as the shock height increases for Froude

Series	ξ [°]	u_1 [m s^{-1}]	h_1 [m]	Fr_1	Re
I	3	1.05 ± 0.05	0.00575 ± 0.00025	4.4 ± 0.3	6100
	6	1.25 ± 0.08	0.00475 ± 0.00025	5.8 ± 0.5	6000
	9	1.4 ± 0.1	0.00425 ± 0.00025	7.0 ± 0.8	6100
II	3	0.95 ± 0.05	0.0055 ± 0.0005	4.1 ± 0.4	5200
	6	1.18 ± 0.07	0.0045 ± 0.0005	5.6 ± 0.7	5300
	9	1.25 ± 0.08	0.004 ± 0.0005	6.4 ± 0.8	5000

Table 2: A description of the steady stream of the incoming flow for the two experimental series. Series I was used to measure the depth profile along the dam and series II to measure the shock angle.

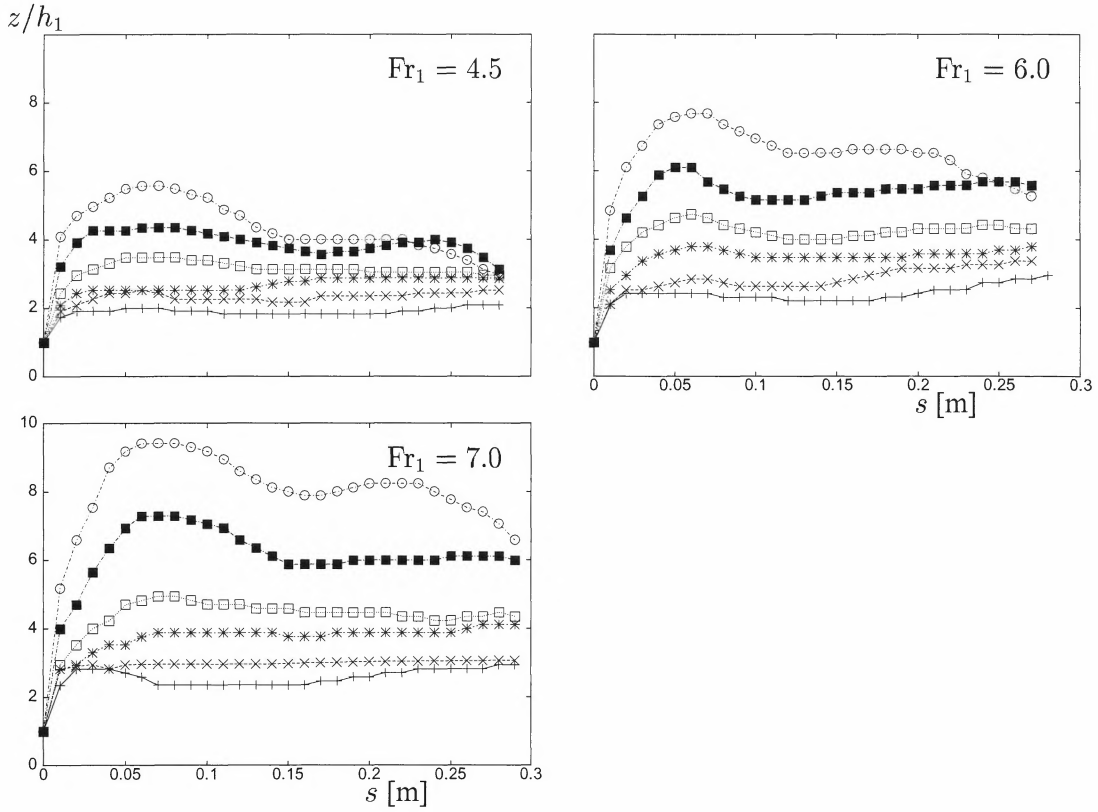

Figure 19: Non-dimensional run-up profiles along the deflecting dams of steady water at different Froude numbers. Each curve shows the steady shock height at a fixed deflecting angle. The deflecting angles tested were: $\gamma = 5\,°$, 10°, 15°, 20°, 30° and 40°. The shallowest profile on each graph corresponds to the 5° deflection and the deepest to the 40 ° deflection.

numbers up to around 7. (For $1 < \mathrm{Fr}_1 < 7$, $4 < \Delta l/h_2 < 6$, see for example (Gerhart *et al.*, 1993).) Figures 7 (c) and (d) show that the shock height increases with increasing deflecting angles for flows at fixed Froude numbers. The adjustment region should therefore also lengthen with wider deflecting angles. The shock height furthermore increases with higher Froude numbers for fixed deflecting angles, see Figure 19. That enhances the lengthening of the adjustment region for higher Froude number flows.

An increase in the length of the adjustment region with higher Froude number flows is not obvious from the run-up profiles in Figure 19 due to the narrow range of the Froude numbers. The transition zone in the experiments was observed to widen as a function of the deflecting angle (and consequently as a function of the flow depth of the hydraulic jump) from being just under 0.01 m for $\gamma = 5°$ to about 0.03 m for $\gamma = 40°$. A longer adjustment region for the larger deflecting angles is observable from the run-up profiles in Figure 19 due to this effect.

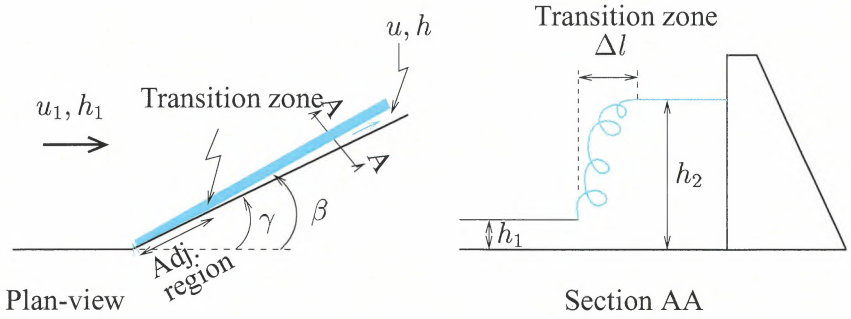

Figure 20: Schematic diagram of the adjustment region along a deflecting dam, caused by the intersection of the turbulent transitions zone with the deflecting dam.

The run-up at the beginning of the dams is observed to increase with increasing deflecting angles. That may be caused by the increase in the velocity component of the approaching flow normal to the dams, $u \sin \gamma$, since the pressure distribution in the turbulent adjustment region is far from being hydrostatic and the flow may follow ballistic trajectories along the side of the dam in this region.

We now compare the experimental results with the predictions of the steady-state shock theory in some detail. The system of equations (12), (13) and (14) was solved numerically for the shock depth, h_2, speed, u_2, and angle, β, for a given incoming flow depth, h_1, speed, u_1, and deflecting angle, γ. The shock angle relative to the dam, $\beta - \gamma$, is plotted in Figure 21 as a function of the deflecting angle. There is good agreement between the experimental results and the theory for the three experimental series. The predicted shock height is plotted as a straight line on Figures 22, 23 and 24 along with the observed run-up profile. The agreement is fairly good apart from the observed higher run-up at the beginning of the dams.

We conclude that the hydraulic jumps on shallow slopes are well described by the shallow-water jump conditions where constant flow states are assumed on both sides of the hydraulic jump. There is, however, a region close to the beginning of the dams where the flow runs higher up on the dams than the theory predicts, due to turbulence in the transition zone. This adjustment region lengthens, and the flow depth in front of the dams in the adjustment region increases relative to the surface of the constant hydraulic jump further down stream, with higher Froude number flows and larger deflecting angles.

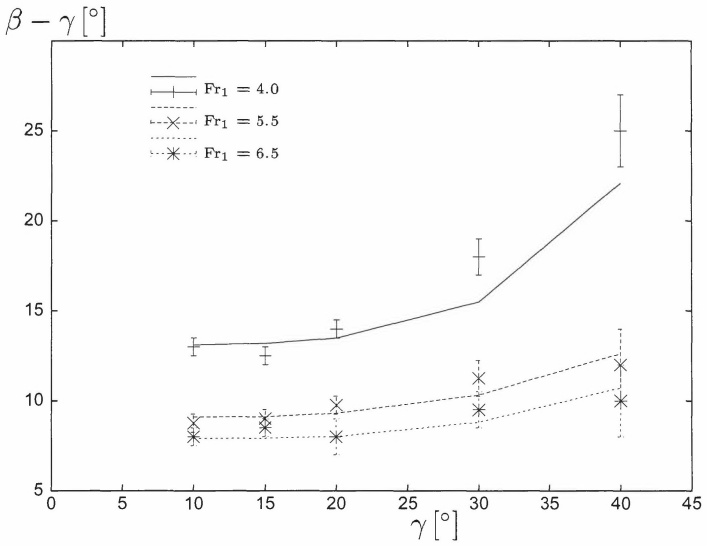

Figure 21: The shock angle relative to the dam plotted as a function of the deflecting angle for the three different Froude numbers. The lines show the theoretical predictions and the points are the experimental results.

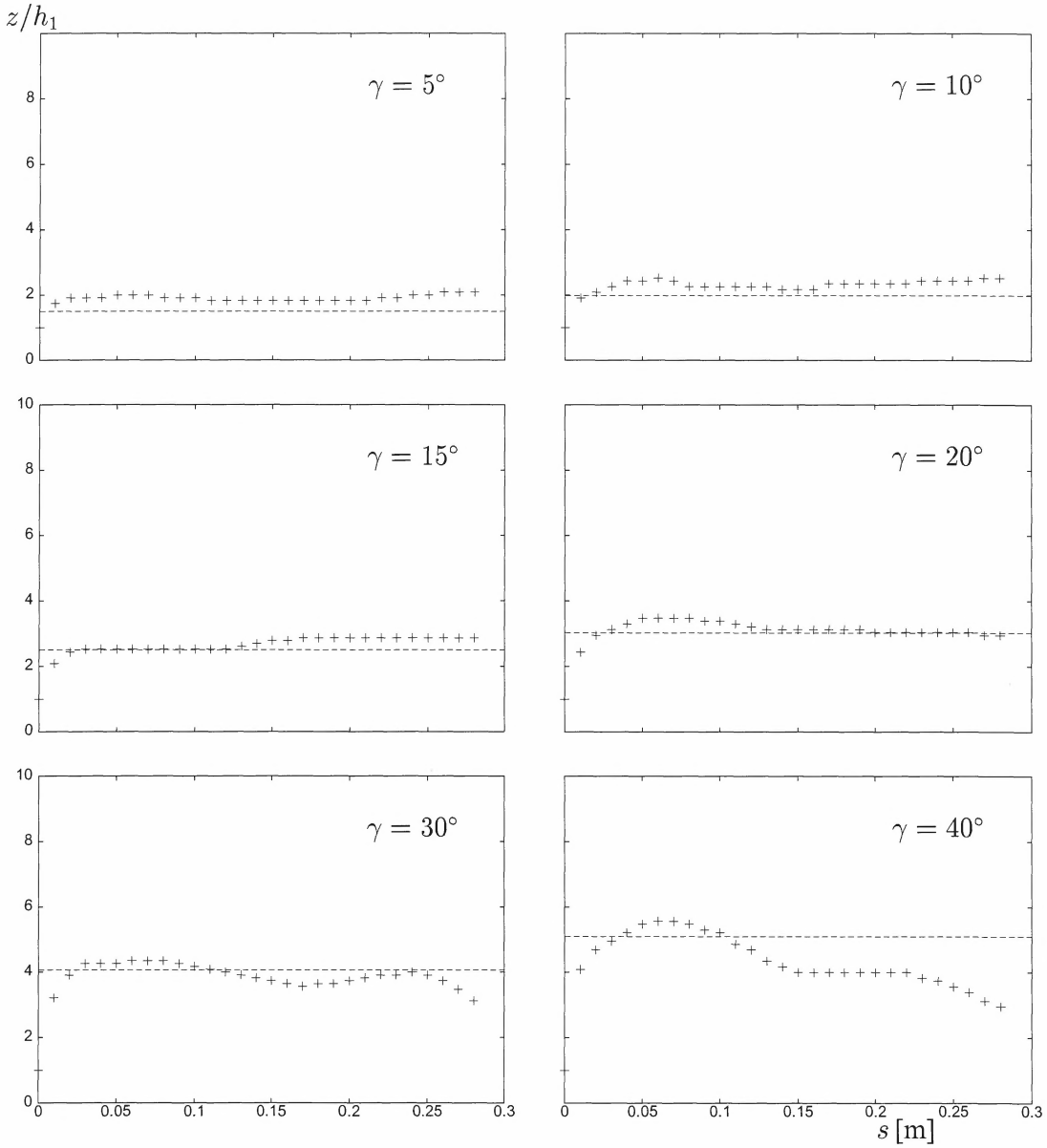

Figure 22: Non-dimensional run-up profiles for water flow at $\mathrm{Fr}_1 = 4.5$. Each graph is a plot of the observed depth profile along the deflecting dam, non-dimensionalised with the depth of the incoming stream at a fixed deflecting angle, γ (+). The theoretical non-dimensional shock height, h_2/h_1, is shown with a dashed line.

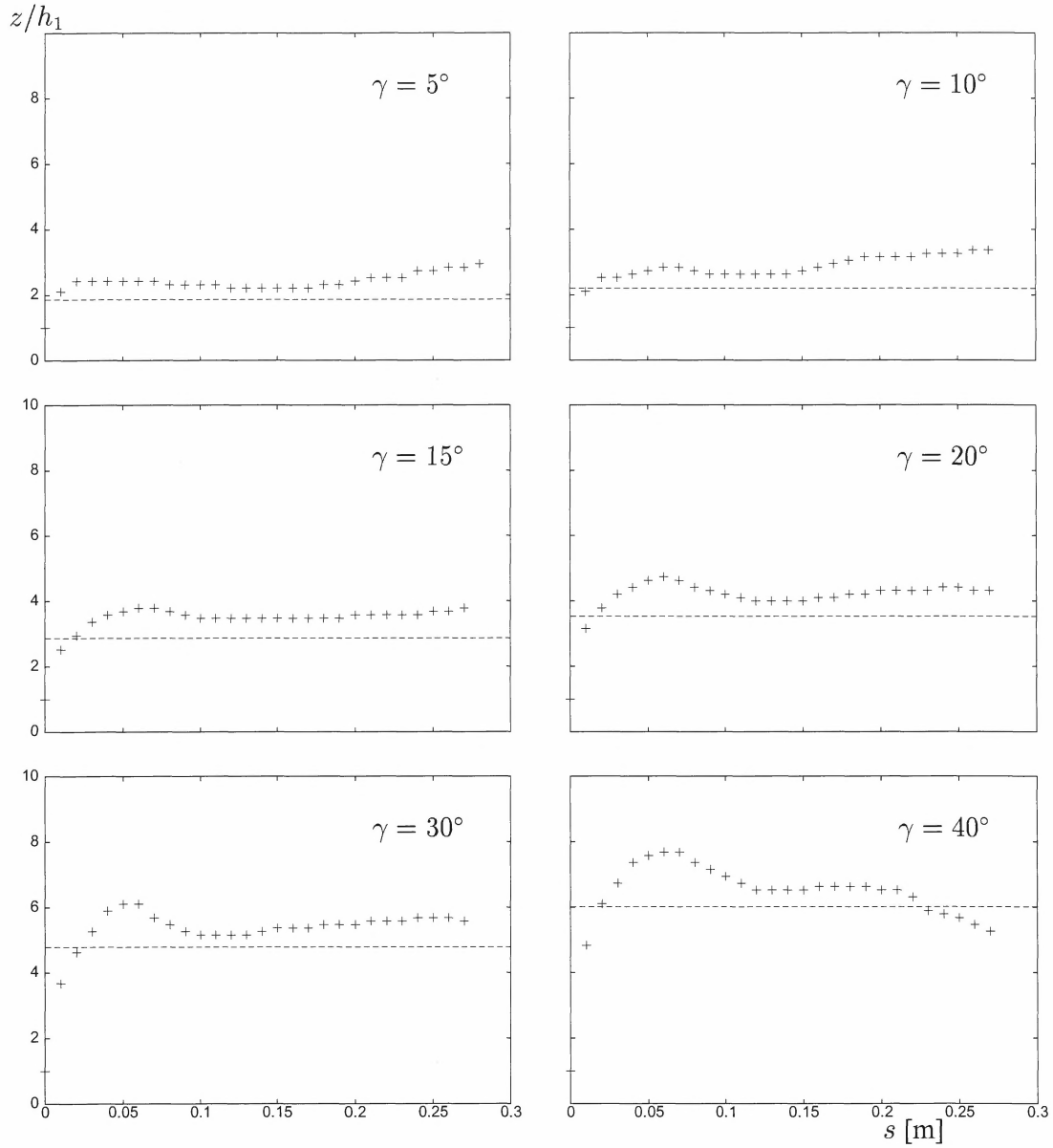

Figure 23: Non-dimensional run-up profiles for water flow at $\mathrm{Fr}_1 = 6.0$. Each graph is a plot of the observed depth profile along the deflecting dam, non-dimensionalised with the depth of the incoming stream, for a fixed deflecting angle, γ (+). The theoretical non-dimensional shock height, h_2/h_1, is shown as a dashed line.

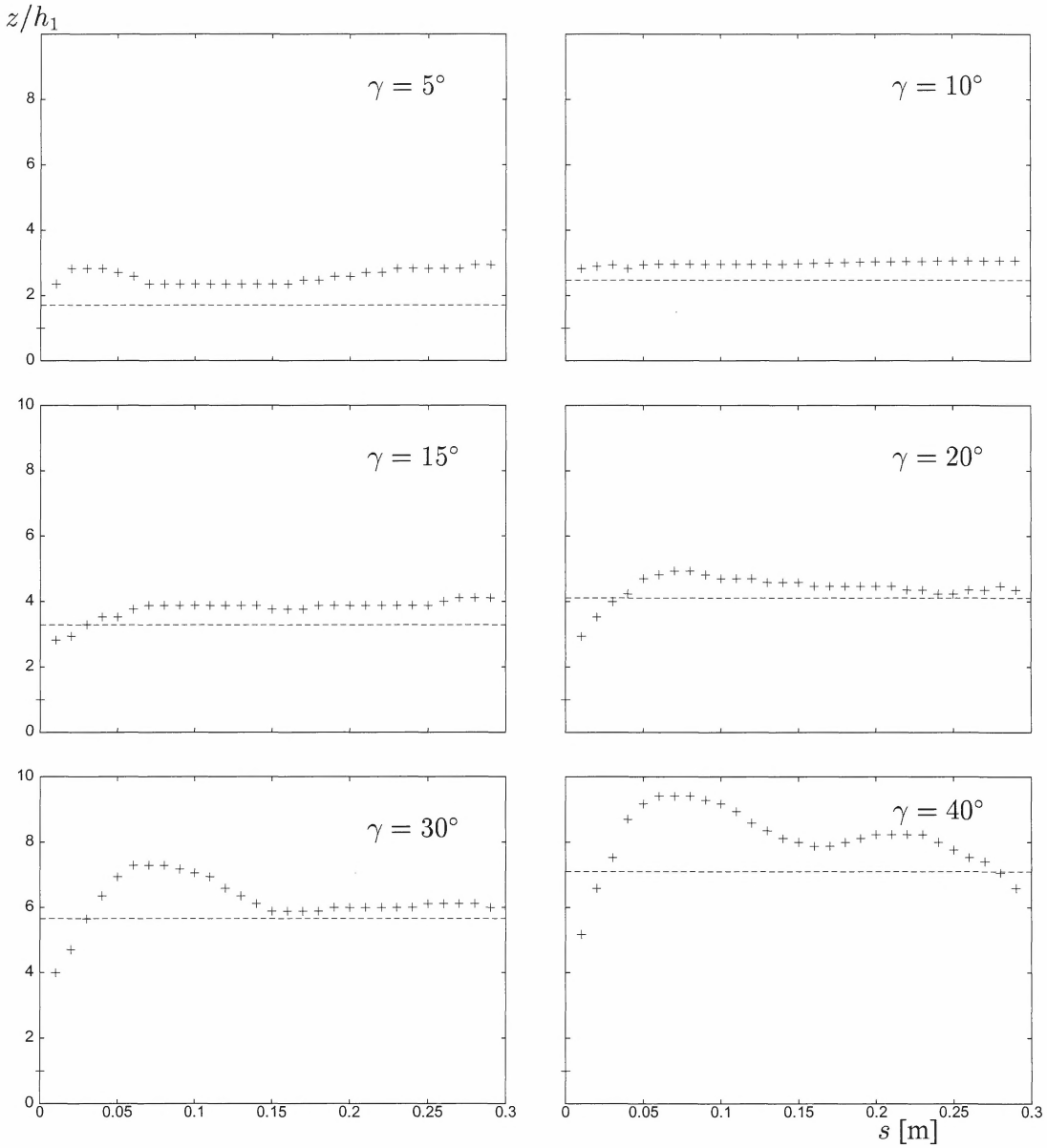

Figure 24: Non-dimensional run-up profiles for water flow at $\mathrm{Fr}_1 = 7.0$. Each graph is a plot of the observed depth profile along the deflecting dam, non-dimensionalised with the depth of the incoming stream, for a fixed deflecting angle, γ (+). The theoretical non-dimensional shock height, h_2/h_1, is shown as a dashed line.

5 Laboratory experiments of steady granular flows interacting with deflecting and catching dams

A series of experiments at three different Froude numbers was designed to study the formation of a steady, oblique, granular shock along a deflecting dam, positioned on a sloping chute. The objective of the experiments was to maintain a steady flow for a few seconds in order to link the granular jumps on steep slopes, described in § 3, to the hydraulic jumps on shallow slopes, described in § 4. The effect that tilting of the upstream dam faces had on the oblique shocks was also investigated. The formation of a granular jump upstream of a catching dam was then explored and the height of the catching dam at which a bore could no longer be maintained upstream of the dam was determined.

5.1 Experimental setup and design

Figure 25: A photograph of the steady, granular experimental setup.

The same setup and the same particles were used as in the short granular experiments described in § 3.1, but with the channel narrowed by 0.1 m, to 0.225 m. The release mechanism was adjusted so that it was possible to control the depth of the flow out of the hopper. As before, the flow was released by abruptly opening a lock gate, see Figure 25.

The experiments within each series were conducted during a 12 hour period to minimise the effect of changes of the humidity in the laboratory on the ballotini beads. The flow speed and depth were measured at the start and end of each experimental set. The flow speed was measured by tracking tracer particles that were thrown into the flow and the flow depth was measured using an optical depth sensor (ODS96) that uses infrared light to measure the distance to a surface.

The deflecting dam experiments were conducted at three different Froude numbers: 5, 12 and 14, overlapping the values in the previous experiments with water and granular flows, and for five different deflecting angles: $\gamma = 8°$, 15°, 24°, 32° and 44°. The dams had an upstream face perpendicular to the experimental chute, $\alpha = 90°$, where α is the angle between the upstream dam face and the chute. The dams were 0.5 m long and covered different proportions of the flow path, l/L, see Figure 8 (b) for definitions. For $\gamma = 8°$, 15° and 24°, $l/L < 1$, but for $\gamma = 32°$, $l/L = 1.1$ and for $\gamma = 44°$, $l/L = 1.5$, which means that the dams extended out of the flow-path for the two largest deflecting angles.

The flow depth along the dams and the shock angles at the dams were measured from video footage of the experiments. The flow speed was measured inside the shock, along the deflecting dam, for $\gamma = 24$ °, by tracking tracer particles that were thrown into the flow. The effect of tilting the sidewalls of the dams was examined for $\mathrm{Fr}_1 = 12$, $\gamma = 24°$ and $\alpha = 90°$, 75°, 60° and 45°, again by measuring the steady shock angle and flow depth along the dam for each value of α.

Catching dam experiments were conducted for flows at $\mathrm{Fr}_1 = 12$ and 14. The dams had an upstream face perpendicular to the experimental chute. The height of the dams was systematically lowered and the speed of the bore travelling upstream was measured along with the depth of the bore and the depth of the flow over-topping the dam when overflow occurred. The effect of tilting the upstream face of the dams to $\alpha = 60°$ was also explored.

5.2 Results: Deflecting dams

The characteristics of the steady stream are given in Table 3. The flow reached a steady, uniform state (constant flow speed and depth) very quickly (within the first tens of centimetres from the release) on the steep section of the experimental chute. The steady stream hit the deflecting dam approximately 2 m further down and a stationary oblique shock was formed within a fraction of a second of the initial impact, see Figure 26. The dilute first front of the flow splashed up to a similar height on the dams as the shock.

The run-up profiles along the dams are plotted in Figure 27 for the three different Froude number flows. The oblique shocks were stationary for all but the largest deflecting angles. The dams for the 32° and 44° deflections extended out of the flow path of the avalanches leading to the slowing down of the current along the end of the dams and the subsequent pile up of material in front of the dams. This was observed for $\mathrm{Fr}_1 = 5$ with $\gamma = 32°$ and 44° and also for $\mathrm{Fr}_1 = 12$ and 14 with $\gamma = 44°$. The plotted profiles of the unsteady flows are those that were observed before the material started to pile up in front of the dams.

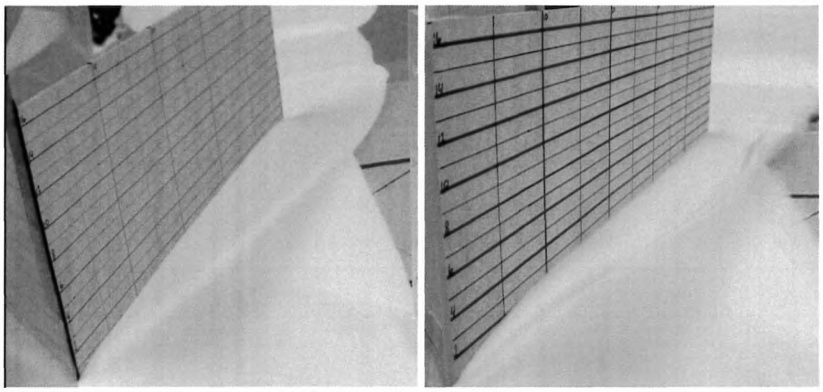

Figure 26: Photographs of oblique, granular shocks for $\gamma = 24°$ for two different Froude numbers, $\mathrm{Fr}_1 = 5$ and 12, on slopes inclined at $\xi = 26°$ and 30°, looking downstream onto the deflecting dams. The shock is narrower on the photograph to the right ($\mathrm{Fr}_1 = 12$) and the flow flips over and falls back on the oncoming stream at the beginning of the dam.

ξ [°]	u_1 [m s^{-1}]	h_1 [m]	Fr_1
26.5 ± 0.5	0.7 ± 0.01	0.0020 ± 0.0002	5
30.3 ± 0.5	1.85 ± 0.07	0.0027 ± 0.0002	12
30.3 ± 0.5	1.52 ± 0.05	0.0013 ± 0.0002	14

Table 3: A description of the steady stream of granular flow for the three different experimental setups.

If these unsteady profiles are not considered, the run-up profiles along the dams show an approximately constant depth along the dams. The profiles follow the same trend as previously observed for the water and granular flows; larger Froude numbers and deflecting angles lead to higher run-up on the dams.

The turbulent transition zone intersected with the upper most part of deflecting dams in the water experiments and the flow ran higher up on the dams in this region relative to the hydraulic jump further downstream. This effect is less profound in these granular experiments since higher run-up on the dams is not observable from the run-up profiles. The flow was, nevertheless, observed to turn over and fall back on itself at the start of the deflecting dams for the the higher Froude number flows, $\mathrm{Fr}_1 = 12$ and 14, see Figure 26. The transition zone was observed to be much thinner than in the water experiments (less than 0.01 m wide for all of the deflecting angles).

The experimental results can be compared with the shallow-water jump conditions. Equations (12), (13) and (14) were solved numerically for the shock depth, speed and angle: h_2, u_2 and β, for a given incoming flow depth, speed and deflecting angle: h_1, u_1 and γ. The shock

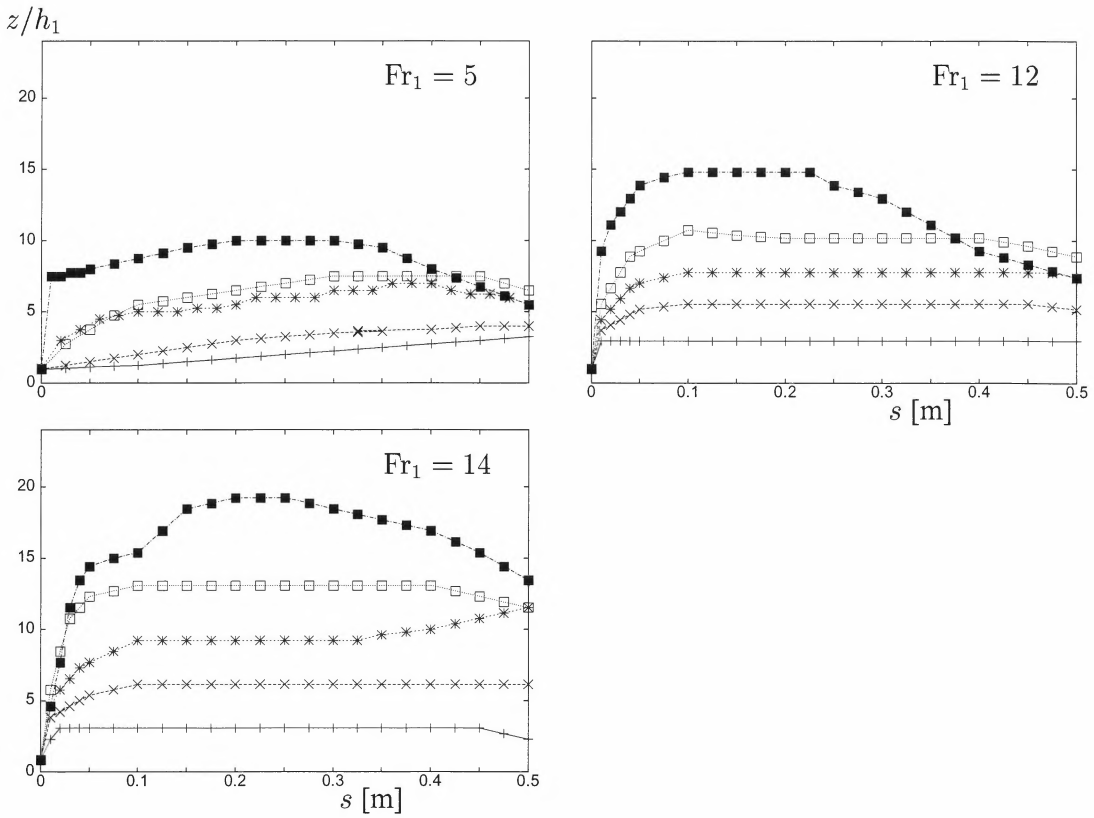

Figure 27: Non-dimensional run-up profiles along the deflecting dams for steady, granular flow at three different Froude numbers, $\mathrm{Fr}_1 = 5, 12, 14$. Each curve shows the steady shock height for a fixed deflecting angle, the different curves belong to different deflecting angles; 8 °, 15°, 24°, 32° and 44°. The shallowest profile on each graph corresponds to the 8° deflection and the deepest to the 44° deflection. The profiles for $\mathrm{Fr}_1 = 5$ with $\gamma = 32°$ and $44°$ and for $\mathrm{Fr}_1 = 12$ and 14 with $\gamma = 44°$ were unsteady.

angle is plotted as a function of the deflecting angle in Figure 28. The shallow-water theory accurately predicts the experimental results for all three Froude numbers. The observed depth profiles along the dams are plotted in Figures 29, 30, 31, and show good agreement with the predicted shock height after the short distance along the dams that it takes the flow to reach the depth of the hydraulic jump. The depth profiles for the $\mathrm{Fr}_1 = 5$ show a slight increase in the flow depth along the dams while there is no increase in the flow depth for the higher Froude number flows.

The effect of tilting the sidewalls of the dams between $\alpha = 45°$ and $\alpha = 90°$ for $\mathrm{Fr}_1 = 12$

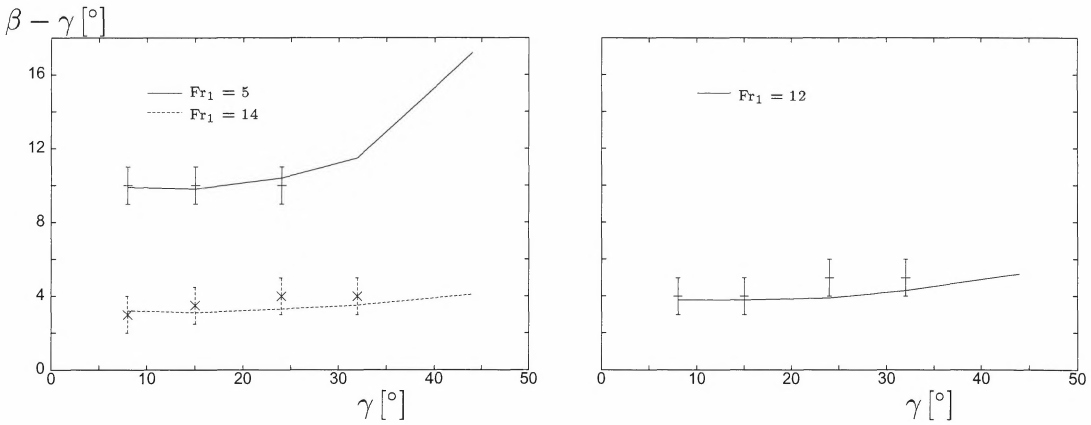

Figure 28: The shock angle relative to the dam, $\beta - \gamma$, plotted as a function of the deflecting angle for the three different Froude numbers. The lines show the theoretical predictions and the points are the experimental results. The shocks were unsteady for $\mathrm{Fr}_1 = 5$ and $\gamma = 32°$ and $44°$; $\mathrm{Fr}_1 = 12$ and 14 and $\gamma = 44°$, so that no shock angle was observed.

did not affect the shock formation. The shock angle and the depth, measured normal to the chute, remained the same as for a deflecting dam normal to the chute, $\alpha = 90\,°$. The area per unit width of the dam over which the normal pressure acts is $h_2/\sin\alpha$, where h_2 is the flow depth at the dam, measured normal to the chute. The total normal force on a unit width of the dam thus becomes $\rho g^{\star} h_2^2/(2\sin\alpha)$ and increases by a factor of $\sqrt{2}$ for dams at $\alpha = 45°$ compared with dams at $\alpha = 90°$. The Coulomb friction force on the dams is proportional to the normal force on the dams, and thus increases by tilting the dams. If Coulomb friction affects the run-up onto the dams, there should be a visible difference in the run-up profiles on the dams for dams tilted at different angles. This does, however, not seem to be the case in these high Froude number experiments.

We conclude that shallow-water jump conditions that assume constant flow states on both sides of the jump can be used to describe granular jumps along deflecting dams on non-accelerative slopes (the flows were steady). Coulomb friction at the side of the dams is not observed to affect the characteristics of the shock for the high Froude number flows, $\mathrm{Fr}_1 = 12$, that were studied.

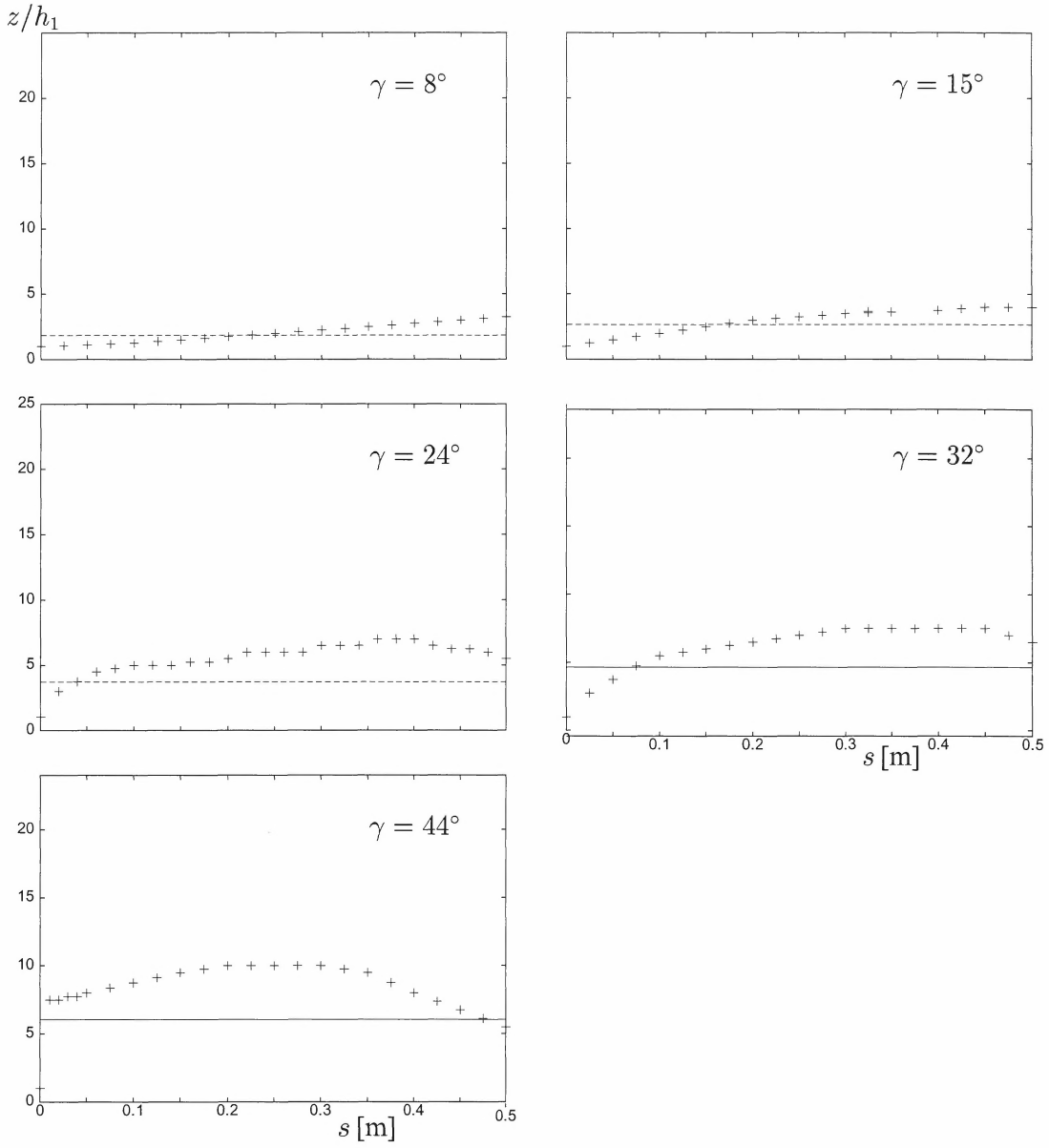

Figure 29: Non-dimensional run-up profi les for granular fbw at $\mathrm{Fr}_1 = 5$. Each graph is a plot of the observed depth profi le along the deflecting dam, non-dimensionalised with the depth of the approaching stream, for a fi xed deflecting angle, γ (+). The theoretical non-dimensional shock height, h_2/h_1, is shown as a dashed line. The shocks were unsteady for $\gamma = 32°$ and $44°$ where the shock height is drawn as a solid lines.

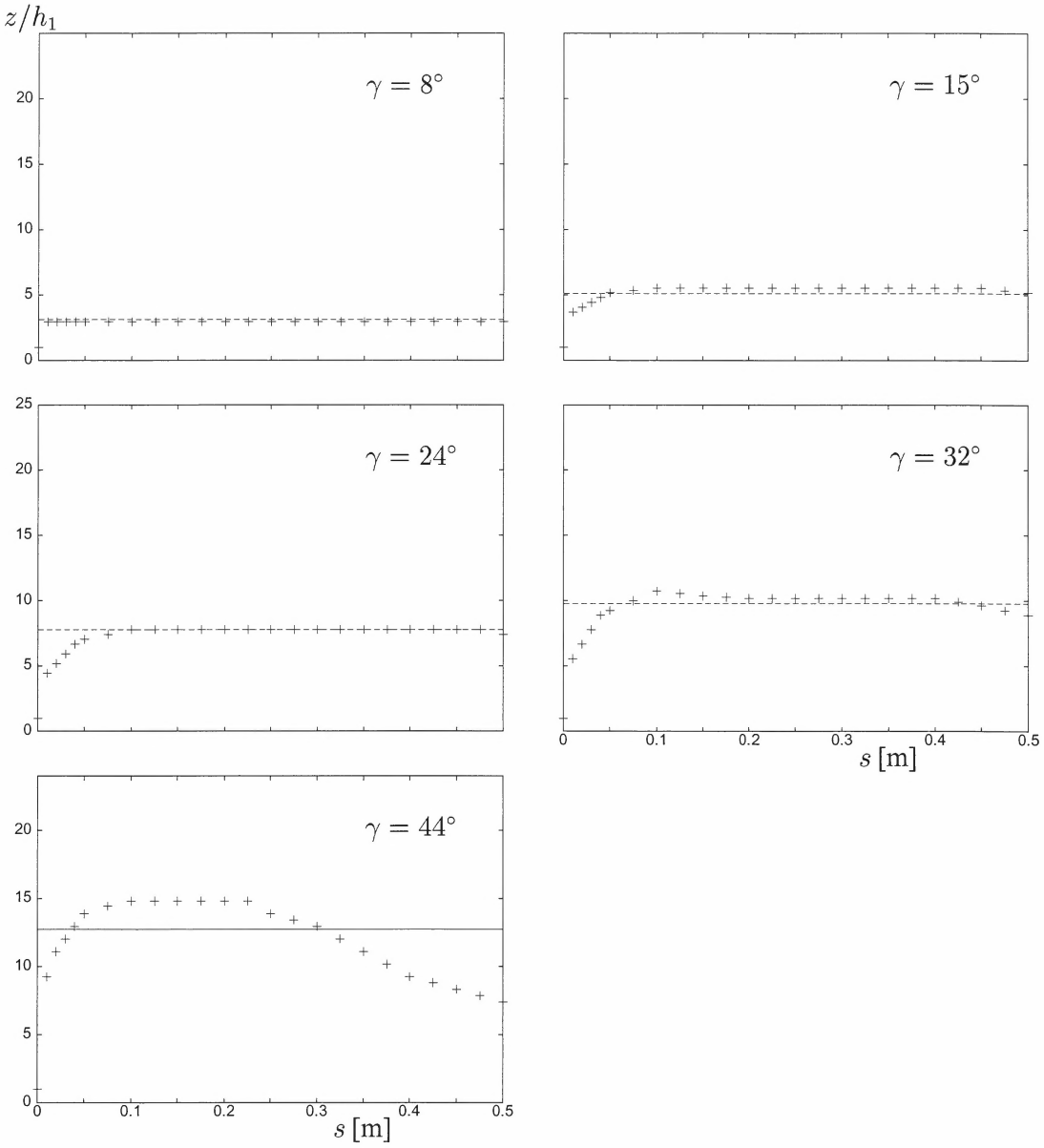

Figure 30: Non-dimensional run-up profi les for granular flow at $\mathrm{Fr}_1 = 12$. Each graph is a plot of the observed depth profi le along the deflecting dam, non-dimensionalised with the depth of the approaching stream, for a fi xed deflecting angle, γ (+). The theoretical non-dimensional shock height, h_2/h_1, is shown as a dashed line. The shock was unsteady for $\gamma = 44°$ where the shock height is drawn as a solid line.

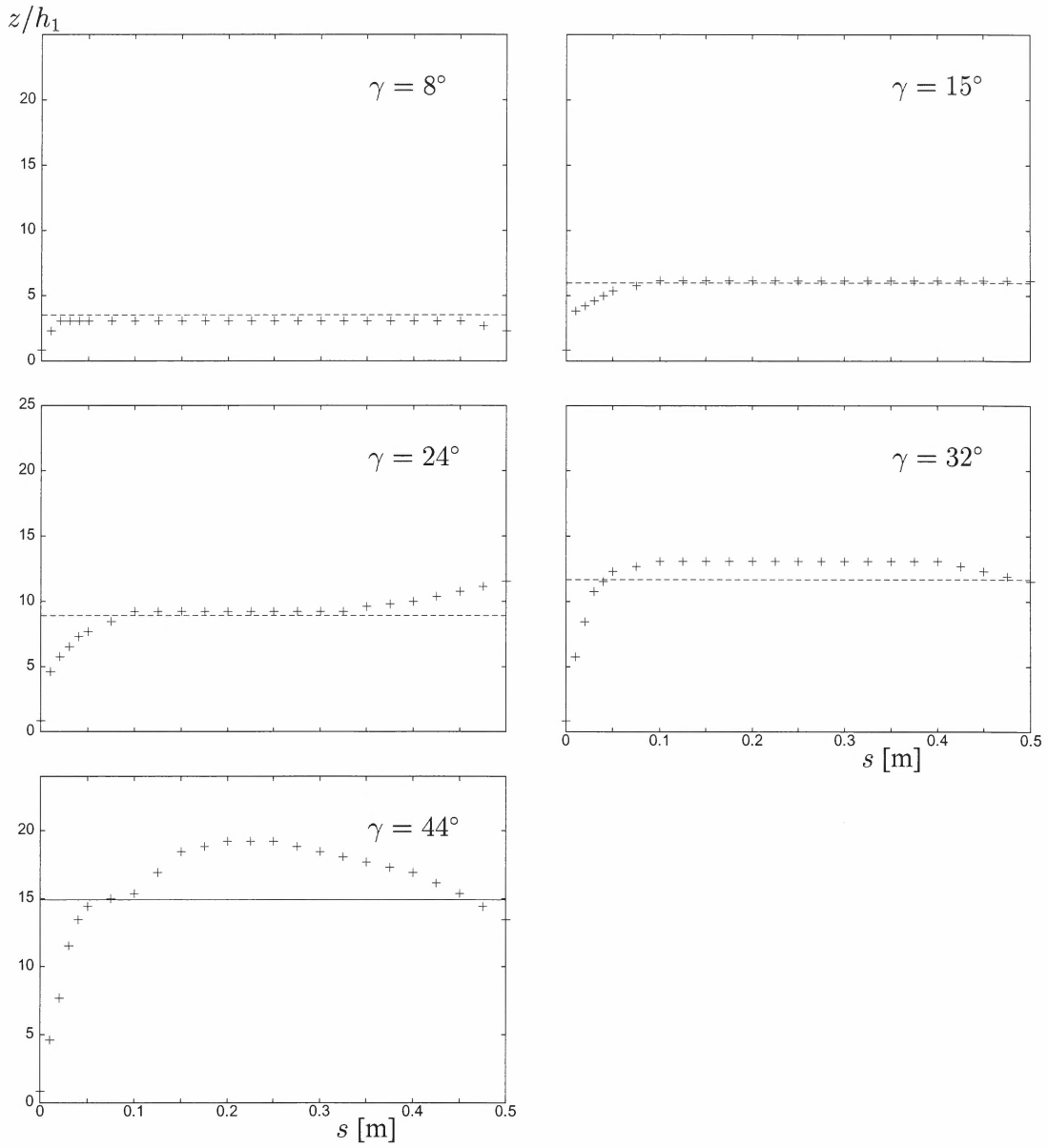

Figure 31: Non-dimensional run-up profi les for granular flow at $\mathrm{Fr}_1 = 14$. Each graph is a plot of the observed depth profi le along the deflecting dam, non-dimensionalised with the depth of the approaching stream, for a fi xed deflecting angle, γ (+). The theoretical non-dimensional shock height, h_2/h_1, is shown as a dashed line. The shock was unsteady for $\gamma = 44°$ where the shock height is drawn as a solid line.

5.3 Results: Catching dams

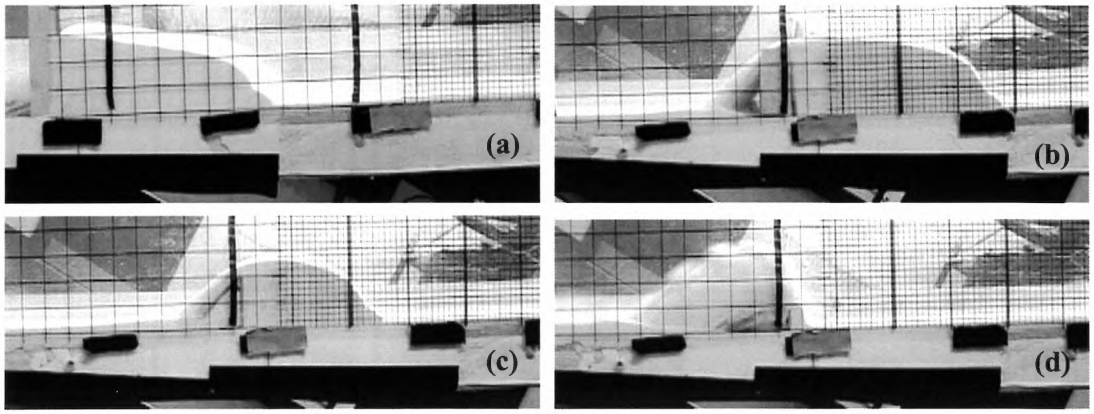

Figure 32: Photographs of granular flow at $\mathrm{Fr}_1 = 12$, travelling from right to left down a 30° incline and interacting with (a) a high catching dam (on the left) and forming a bore that travels upstream; (b) a lower catching dam, $H/h_1 = 18$, with some of the flow over-topping the dam and a stationary bore upstream of the dam; (c) an even lower catching dam, $H/h_1 = 15$, where the stationary bore is closer to the dam; (d) a lower still catching dam, $H/h_1 = 11.5$, where all of the flow over-tops the dam. Note that the incoming flow is only 0.002 m thick and hardly visible on the photographs. The dimensions of the larger grid-cells are (0.02×0.02) m.

Experiments with flows at Froude numbers 12 and 14 revealed that granular bores travelling upstream were formed in front of catching dams (see Figure 32). The dilute first front of the flow splashed higher up on the dams than the granular jump. The angle of repose of the granular material (ballotini beads) was smaller than the slope of the chute, $\phi = 21° < \xi = 30°$. The free surface of the stationary material in front of the dam (downstream of the shock) was intermittently levelled out to the angle of repose of the ballotini beads by thin avalanches on the free surface, propagating from the start of the bore and down to the catching dam. The bore slowed down during the upstream propagation, as more material avalanched down to the dam in order to level out the lengthening free surface of the bore. An upstream propagating bore was still present in front of the dam, when the height of the dam was lowered, so that some of the flow over-topped the dam. The bore propagated upstream until the mass flux over the bore balanced the mass flux over the dam at which point the bore stopped. The distance travelled upstream by the bore shortened when the dam was lowered, until a granular jump upstream of the dam disappeared and all of the flow was launched over the dam.

The scenario where a shock is formed upstream of a catching dam and the dam is high enough so that no part of the flow over-tops is described by equations (3) and (6) when $\phi < \xi$.

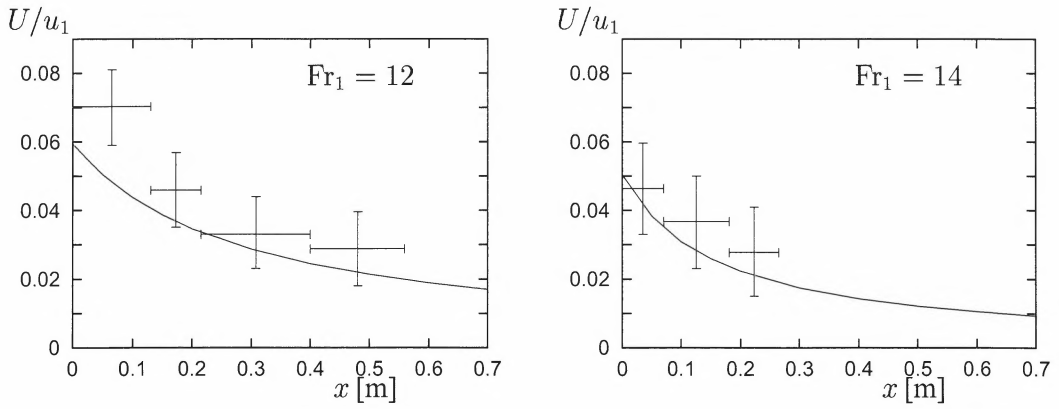

Figure 33: The borespeed non-dimensionalised with the speed of the approaching flow, U/u_1, plotted as a function of the distance travelled upstream by the bore, x, for $\mathrm{Fr}_1 = 12$ and 14. The theoretical prediction for material with $\phi \geq \xi$ is plotted as a straight line. The observed bore speed for $\xi - \phi = 9°$ is averaged over the distance indicated by the x-error bars (+).

The shock height and the time dependent position of the bore front were accurately predicted by the theory by using the same density on both sides of the bore, $\rho_2 = \rho_1$, see Figure 33. Gray *et al.* (2003) have conducted similar catching dam experiments using material with a larger internal friction angle than the angle of the slope on which their flows take place. They find that the system of equations referred to above predicts the speed and the depth of the upstream propagating bore. (Gray *et al.* furthermore conduct their experiments at slope angles that balance the basal friction angle of the flow so that gravity does not affect the conservation of momentum flux over the bore, but they do not comment on the results when gravity is not matched by Coulomb friction.)

When the catching dam was lower than the shock height, some of the flow over-topped the dam. The setup is described by the system of equations (7), (8), (10) and (11), for $\phi < \xi$ and a constant flow state downstream of the shock. For a given approaching flow depth and speed: h_1, u_1, the bore height, bore speed, overflow height and overflow speed: h_2, U, h_3, u_3, can be determined.

Experiments with flows at $\mathrm{Fr}_1 = 12$ showed that the bores travelled a certain distance upstream where they then stopped. The flow was in a constant flow state upstream of the shock and may to some approximation be regarded as being in a constant flow state downstream of the shock. The shock depth and overflow depth, h_2 and h_3, were well predicted by the theory. The theory also predicted the position of the stationary bore, see Figure 34. The dam height leading to no shock formation upstream of the dam was furthermore accurately predicted by the theory, *i.e.* the dam height resulting in a computed negative bore speed. The ratio between the dam height leading to no shock formation and the initial shock height for no overflow was found to be $H/h_2 \approx 0.65$. Equation (4) with $\rho_2/\rho_1 = 1$ can be used to approximate the dam

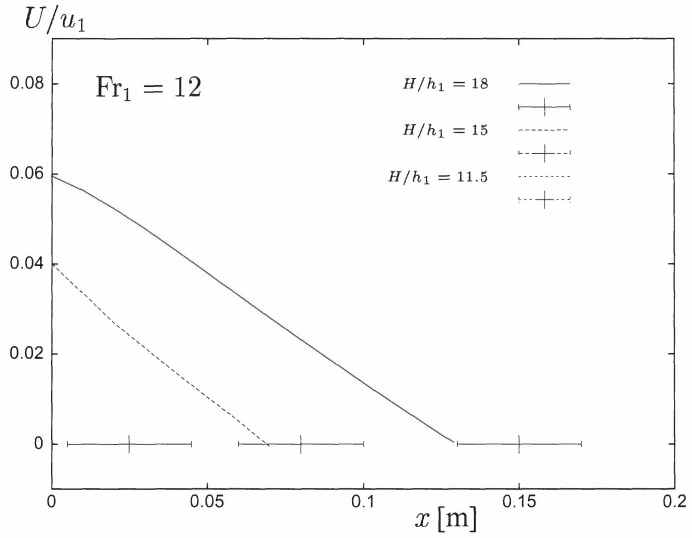

Figure 34: The theoretically predicted bore speed non-dimensionalised with the speed of the approaching flow, U/u_1, plotted as a function of the distance travelled upstream by the bore, x, for different dam heights, H. The speed $U = 0$ indicates that the bore has stopped and the experimental observations of the stopping position of the bore are plotted for the three different dam heights (+). For $H/h_1 = 11.5$, the theory predicts that the bore would only travel half a millimetre upstream. The theoretical line is therefore not visible on the plot.

height corresponding to no shock formation as a function of the depth of the incoming flow and the Froude number.

$$H \approx 0.65\, h_2 \approx 0.65\sqrt{2}\mathrm{Fr}_1 h_1 \approx 11 h_1.$$

The effect of tilting the upstream face of the catching dam had no effect on the shock height and bore propagation. It was observed, however, in the experiments that the first front splashed up higher on the dams than the immediately following shock and the angle at which the first front took off from the top of the dams coincided with the angle of the upstream dam face.

We conclude that the shallow-water framework gives accurate predictions of the granular jumps, while the splash-up of the dilute and compressible first front of the flow onto the dams remains a subject of future work.

6 Discussion

The experimental study has considered steady, supercritical flow of water and dry, granular material interacting with dams. The flows were at different Froude numbers, were of different physical scales (different flow depth and speed) and took place on steep and shallow slopes. The experiments revealed that the dry, dense, granular free surface flows scale with the internal Froude number of the flow as do flows of water. Features such as shocks were observed upstream of the dams in the granular flows as well as in the water flows. A better agreement between theory and experiments was obtained for the granular flows if the pressure was taken to be isotropic and hydrostatic, instead of linking the longitudinal and normal stresses through an earth pressure coeffi cient.

Stationary, oblique shocks were formed in the interaction of the flows with deflecting dams. They were well described by incompressible, shallow-layer shock theory, derived on a horizontal plane, assuming constant flow states on both sides of the shock. Less intense wave action and turbulence were observed in the granular flows than in the water, presumably owing to dissipation in inelastic collisions between grains and this may account for a sharper transition zone in the granular material. The structure of the granular jumps was not observed to depend on the Froude number of the approaching flow for the Froude number range that was studied, $5 < \mathrm{Fr}_1 < 14$, as is the case in hydraulic jumps. Higher run-up than the jump conditions predicted and turn-over of the flow was observed close to the upstream end of the deflecting dams for the higher Froude number granular flows and for water flow at the largest deflecting angles and for all Froude numbers. This effect was more obvious for the water because of a more turbulent and wider transition zone.

A travelling bore was formed upstream of the catching dams when none of the flow overtopped the dams. For lower dams with some overflow, a shock could still be observed. As the height of the dams was gradually lowered, the bores stopped closer to the dams and fi nally the flow shot ballistically over the dams in a supercritical flow state and a shock did not form upstream of the dams. The granular jumps were well described by the shallow-water jump conditions. The internal friction angle of dry snow is suggested by Salm (1993) to be close to 25°. In most cases avalanche protection dams will be positioned in the run-out zone of an avalanche path and not at angles steeper than 25°. The theoretical consideration for $\phi \geq \xi$ would therefore in most cases be appropriate for the analysis of snow avalanches. The snow stopped by a catching dam may furthermore be more densely packed than the flowing avalanche leading to a density difference over the shock (mostly in the range $1 < \rho_2/\rho_1 < 3$) and a lower shock height at the dam than for an incompressible jump, such as a hydraulic jump.

Highly compressible flows with Mach numbers larger than one were not considered in the experiments (excluding the fi rst front of the flows). There is a possibility that the dense core of some natural dry-snow avalanches is slightly supersonic (Briukhanov *et al.*, 1967) which may give rise to the formation of compression shocks in the interaction with dams. Such compression shocks have been observed experimentally in dilute granular flows (Rericha *et*

al., 2002).

The higher splash-up of the first front of the flows onto the catching dams is consistent with high pressures (impulse pressures) measured during the first few milliseconds of the impact of an avalanche with a catching dam (Bozhinskiy and Losev, 1998; Schaerer and Salway, 1980; Kotlyakov, *et al.*, 1977; and Salm, 1964) and also pressure records and observed splash-up of steep water waves on walls, see Peregrine (2003) for an overview.

The results presented here are a step towards a better understanding of the dynamics of dense granular flows, such as snow avalanches, that hit deflecting and catching dams. These results may be used to formulate new design criteria for such dams. They might also be useful for implementing deflection dynamics in numerical models that could be used to evaluate the effectiveness of dams as protection measures for settlements, communication lines and other properties and infrastructure. An important consideration in the application of our results to pratical design of protection dams is the question of the formation of the shock in the initial impact with the dam. In order for the shock to form, the flow must undergo a change in flow state from a supercritical flow to a subcritical flow as it passes over the dam. The presence of a shock is assumed in the derivation of the theoretical shock relations in section §2. The dam height needed for a hydraulic jump to occur in the first place will be larger than the theoretical bore height if the loss of energy across the granular jump is larger than the energy loss in the impact of the flow with the catching dam. This will, however, not be further discussed here.

7 Acknowledgements

This study was carried out with support from the European Commission (the research project *Satsie*, grant EVG1-CT-2002-00059) and the Icelandic Avalanche Fund. KMH acknowledges the financial support of the University of Bristol and the Icelandic Research Council. Thanks are due to Dieter Issler who provided useful comments on a draft of this report.

References

Bozhinskiy, A. N. and Losev, K. S. (1998). The Fundamentals of Avalanche Science. *Mitt. Eidgenöss. Inst. Schnee- Lawinenforsch.*, 55:280 S.

Briukhanov, A. V., Grigorian, S. S., Miagkov, S. M., Plam, M. Y., Shurova, I. Y., Eglit, M. E., and Yakimov, Y. L. (1967). On some new approaches to the dynamics of snow avalanches. In *Physics of Snow and Ice*, volume 1, part 2, pages 1223–1241. Proc. of the Intl. Conf. on Low Temperature Science, Sapporo 1966, The Institute of Low Temperature Science, Hokkaido University, Sapporo Japan.

Chu, T., Hill, G., McClung, D. M., Ngu, R., and Sherkat, R. (1995). Experiments on granular flow to predict avalanche runup. *Canadian Geotechnical Journal*, 32:285–295.

Dias, F. and Christodoulides, P. (1991). Ideal jets falling under gravity. *Physics of Fluids A*, 3(7):1711–1717.

Eglit, M. E. (1983). Some mathematical models of snow avalanches. In Shahinpoor, M., editor, *"Advances in the Mechanics and the Flow of Granular Materials"*, volume 2, pages 577–588. Clausthal-Zellerfeld and Gulf Publishing Company.

Gerhart, P. M., Gross, R. J., and Hochstein, J. I. (1993). *Fundamentals of Fluid Mechanics*. Addison-Wesley, 2 edition.

Gray, J. M. N. T., Tai, Y.-C., and Noelle, S. (2003). Shock waves, dead-zones and particle-free regions in rapid granular free surface flows. *Journal of Fluid Mechanics*, 491:161–181.

Hager, W. H. (1992). *Energy Dissipators and Hydraulic Jump*. Kluwer Academic Publishers.

Hager, W. H. and Vischer, D. L. (1995). *Energy dissipators*. Balkema Publishers.

Hákonardóttir, K. M., Hogg, A. J., Batey, J., and Woods, A. W. (2003a). Flying avalanches. *Geophysical Research Letters*, in press.

Hákonardóttir, K. M., Hogg, A. J., Jóhannesson, T., and Tómasson, G. G. (2003b). A laboratory study of the retarding effect of braking mounds on snow avalanches. *Journal of Glaciology*, in press.

Hopfinger, E. J. (1983). Snow avalanche motion and related phenomena. *Ann. Rev. Fluid Mech.*, 15:47–76.

Irgens, F., Schieldrop, B., Harbitz, C. B., Domaas, U., and Opdahl, R. (1998). Simulations of dense-snow avalanches on deflecting dams. *Annals of Glaciology*, 26:265–271.

Issler, D. (2003). Experimental information on the dynamics of dry-snow avlanches. In Hutter, K. and Kirchner, N., editors, *Response of granular and porous materials under large and catastrophic deformations*, volume 11 of *Lecture notes in applied and computational mechanics*, pages 109–160. Springer (Berlin).

Jóhannesson, T. (2001). Run-up of two avalanches on the deflecting dams at Flateyri, northwestern Iceland. *Annals of Glaciology*, 32:350–354.

Kotlyakov, V. M., Rzhevskiy, B. N., and Samoylov, V. A. (1977). The dynamics of avalanching in the Khibins. *Journal of Glaciology*, 19:431–439.

McClung, D. M. and Mears, A. I. (1995). Dry-flowing avlanche run-up and run-out. *Journal of Glaciology*, 41:359–372.

Peregrine, D. H. (2003). Water-wave impact on walls. *Annual Review of Fluid Mechanics*, 35:23–43.

Perla, R., Cheng, T. T., and McClung, D. M. (1980). A two-parameter model of snow-avalanche motion. *Journal of Glaciology*, 26:197–207.

Pouliquen, O. and Forterre, Y. (2002). Friction law for dense granular flows: application to the motion of a mass down a rough inclined plane. *Journal of Fluid Mechanics*, 453:133–151.

Rericha, E. C., Bizon, C., Shattuck, M. D., and Swinney, H. L. (2002). Shocks in Supersonic Sand. *Phys. Rev. Lett.*, 88(014302).

Salm, B. (1964). Anlage zur Untersuchung dynamischer Wirkungen von bewegtem Schnee. *ZAMP*, 15:357–375.

Salm, B. (1993). Flow, flow transition and runout distances of flowing avalanches. *Annals of Glaciology*, 18(1):221–226.

Savage, S. B. (1979). Gravity flow of cohesionless granular materials in chutes and channels. *Journal of Fluid Mechanics*, 92 part 1:53–96.

Savage, S. B. and Hutter, K. (1989). The motion of a finite mass of granular material down a rough incline. *Journal of Fluid Mechanics*, 199:177–215.

Schaerer, P. A. and Salway, A. A. (1980). Seismic and impact-pressure monitoring of flowing avalanches. *Journal of Glaciology*, 26:179–187.

Tai, Y.-C., Noelle, S., Gray, J. M. N. T., and Hutter, K. (2001). An accurate shock-capturing finite-difference method to solve the Savage-Hutter equations in avalanche dynamics. *Annals of Glaciology*, 32:263–267.

Whitham, G. B. (1999). *Linear and Nonlinear Waves*. John Wiley & Sons, Inc.

EROSION AND DEPOSITION PROCESSES IN SNOW AVALANCHE DYNAMICS: REPORT ON THE STATE OF THE ART

Editors: **M. Barbolini and F. Cappabianca**
Contributors: D. Issler and P. Gauer
M. Eglit
M. Naaim
R. Sailer

Pavia, 20 October 2003

1 Introduction

A few centuries ago, snow avalanches were depicted as big snowballs rolling down the mountainsides and growing to gigantic proportions by picking up snow from the snow cover on their perilous way (see Figure 1). As naive as this concept of avalanching may appear today, one aspect of it has been vindicated by recent observations and measurements: the entrainment of snow has now been recognised as a major factor in the dynamics of snow avalanches. The majority of medium to large avalanches could double or even triple their mass from release to runout (Issler *et al.*, 1996); in the track, the moving mass may be more than five times the original mass (Sovilla *et al.*, 2001). From measurements with profiling radar, erosion rates above 200 kg m^{-2} s^{-1} have been inferred during the very rapid removal of up to 1 m of fresh snow at the avalanche front, while they were found in the range 10–50 kg m^{-2} s^{-1} during episodes of more gradual entrainment in the head of dry-snow avalanches (Issler, 2003). In papers on modelling, snow entrainment has often been mentioned as a potentially important process, strongly influencing the estimate of avalanche deposition depths as well as of velocities and runout distances, but few models actually include it in a meaningful way.

Figure 1 - Wood engraving of H. Schäufelein showing an avalanche fall, contained in the poem "Theuerdank" (1517)

The purpose of the present report is to summarise the state of the art with respect to the study of erosion/deposition processes in snow avalanche dynamics. Available observations and measurements will be presented (§ 2), possible conjectured mechanism will be discussed (§ 3) and the models so far proposed will be briefly described (§ 4).

2 Observations and measurements

Observations on avalanche paths just after the passage of an avalanche show that the snow cover is changed: Part of the snow cover, and sometimes the entire snow cover, is eroded and deposits are found along the avalanche path. Analysing the variation of avalanche mass during its motion therefore appears crucial to describe the dynamics of avalanches in a more precise way.

Field measurements have been carried out on three experimental avalanche sites (Issler, 1999): the Italian Monte Pizzac test site (Sommavilla *et al.*, 1998), the Swiss Vallée de la Sionne test site (Ammann, 1999) and the Norwegian Ryggfonn test site (Lied *et al.*, 2002). The data from these three sites permit to collect information about the erosion/deposition processes in relation to different avalanche types. Avalanches at Ryggfonn and Valleé de la Sionne typically are large mixed avalanches (wet-snow avalanches in spring) and move mainly on open slopes. Conversely, the avalanches at Monte Pizzac are channelled dense avalanches of small dimensions. The influence of mass variation on the dynamics of snow avalanches has also been analysed with data from the catastrophic events of winter 1999 (Sovilla and Gruber, 2002). Recently, also laboratory investiga-

tions on granular erosive flows have been carried out at Pavia chutes (Barbolini, personal communication).

2.1 Mass balance measurements at Mt. Pizzac test site

The Monte Pizzac avalanche site is located in the Venetian Dolomites, and has been operative since the winter 1993/94 (Sommavilla *et al.*, 1998; Issler, 1999). The path has a vertical drop of about 500 m and an average slope of 31°. Typical events at this site are either dry or moist dense-flow avalanches in early- and mid-winter and wet dense-flow avalanches at the end of winter. The avalanches are of small size, with typical release volumes of 1500–2000 m^3. The dynamical evolution of the avalanches can be studied by means of arrays of mechanical flow height switches coupled with impact sensors on poles placed at six locations along the avalanche track. These instruments permit to calculate the mean velocity along different track segments as well as the time evolution of the flow depths and pressures at specific points along the avalanche path.

During the winter 1997/98, the avalanche mass balance was determined for four events (5 and 21 December 1997 and 14 and 28 April 1998 - Sovilla *et al.*, 2001). Each event was studied by recording snow-cover profiles across a number of cross-sections along the slope from the release zone to the deposition zone. In each cross-section the eroded and deposited mass were evaluated with manual measurements. Then, the avalanche mass that had flowed through the cross-section was estimated by adding the eroded mass to the initial mass and subtracting the snow deposited by the avalanche. The results of these mass-balance measurements are summarised in Table 1. In spite of greatly different initial masses and snow water content, in all surveyed avalanches the erosion peaks were found in the first part of the track where the slope angle is greater than 30° (with an avalanche mass increase up to 720% with respect to the release mass); the avalanches attained their maximum moving mass near the middle of the path where the slope angle drops below 30°. Except for the smallest event, which met a rough bed surface in early winter and lost mass from the beginning, appreciable deposition also began near this point, where the avalanches begin to decelerate. The mass balance of these events seems to be primarily governed by the path slope. The erosion rates seem to be correlated also with the initial mass, which in turn correlates with the new-snow depth in the path. A relevant correlation with velocity seems to be present only for the biggest and fastest dry avalanche. The ratio between the density of deposited and released snow was found to be in the range 2–3, excluding the case of the wet-snow avalanche which did not show substantial density increase from release to runout. Two examples of mass balance are given in Figure 2, whereas a comparison between erosion and deposition along the track, the avalanche speed and the track inclination is shown in Figure 3.

Event	*Typology*	*Release mass (Rm)* kg	*Maximum mass (Mm)* kg	*Mm/Rm*	*Average speed* $m\ s^{-1}$	*Runout* m	*Release density (Rd)* $kg\ m^{-3}$	*Deposit density (Dd)* $kg\ m^{-3}$	*Dd/Rd*
5 December 1997	Dry	33700	61600	1.8	11	547	135	280	2.1
21 December 1997	Dry	84400	505850	7.2	17.9	680	140	270–430	1.9–3.1
14 April 1998	Moist	30900	126800	4.1	12.3	530	115	290–345	2.5–3
28 April 1998	Wet	90000	296700	3.3	7.6	580	500	500–560	1.0–1.1

Table 1 - Summary of the mass-balance measurements carried out at the Monte Pizzac site in the winter 1997/98 (from Sovilla et al., 2001)

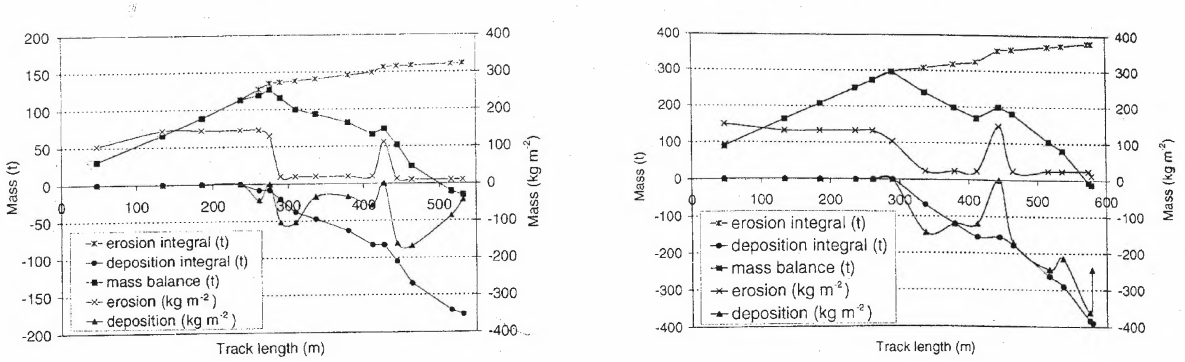

(a) (b)

Figure 2 - Mass balance for the events of 14/04/1998 (a) and 28/04/1998 (b) (from Sovilla et al., 2001)

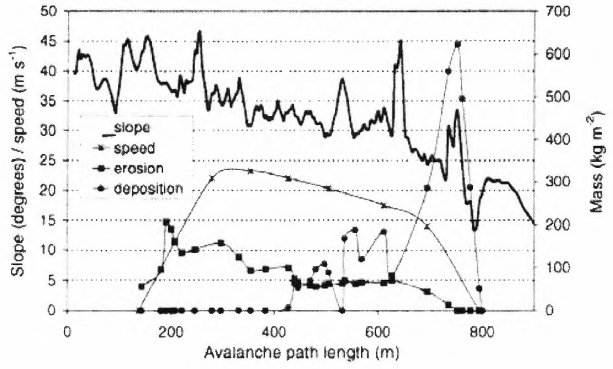

Figure 3 - 21 December 1997 avalanche event: comparison between eroded and deposited mass, avalanche speed and path slope (from Sovilla et al., 2001)

2.2 Mass-balance and local erosion-rate measurements at Vallée de la Sionne

During the winter 1999 three large avalanche events (30 January 1999, 10 February 1999, 25 February 1999) were artificially triggered at the Valleé de la Sionne test site, Canton of Valais, Switzerland (Vallet *et al.*, 2001). The site extends from 2650 m a.s.l. to 1450 m a.s.l., with an average slope of 27°. Photogrammetry and field measurements were used to precisely map the boundaries of the avalanche events and to measure the surface of the snow cover before and after the triggering of an avalanche. The purpose of these measurements was to obtain detailed information about the released and deposited snow volumes. The data obtained from the photogrammetric surveys are given in Table 2.

	30 January 1999	10 February 1999	25 February 1999
Released volume (m^3)	84000	220000	520000
Released snow density (kg m^{-3})	200	220	250
Released mass (t)	16800	48400	130000
Deposition volume (m^3)	40000	467000	876000
Deposition snow density (kg m^{-3})	400	440	500
Deposition mass (t)	16000	205480	438000
Erosion rate (-)	1	4.2	3.4

Table 2 - Summary of the photogrammetric surveys carried out at Vallée de la Sionne in the winter 1999 (from Vallet et al., 2001)

The first avalanche, i.e. the smallest, did not show erosion, probably because of the larger spontaneous avalanche that preceded it and eroded and compacted most of the fresh snow. Conversely, the second avalanche quadrupled its initial mass, eroding the entire fresh snow over large parts of the path (with an estimated total erosion of about $1{,}5\times10^5$ tons); similarly, the third avalanche tripled its initial mass by eroding almost all the fresh snow (about 1,5 m deep) and some of the highly compacted deposits from the previous avalanche in the gently sloped runout zone. These measurements clearly showed that almost the whole new snow cover below the release area can be picked up by large avalanches under extreme conditions.

At Vallée de la Sionne, the FMCW radar system (Gubler and Hiller, 1984), installed at three locations along the avalanche path (upper and lower track and upper runout zone), gives information about the time evolution of the erosion rate and the flow depth (Dufour e*t al.*, 2000). The three dry-snow avalanches triggered in winter 1999 produced fairly similar patterns in the time-distance-intensity plots, see Figure 4.

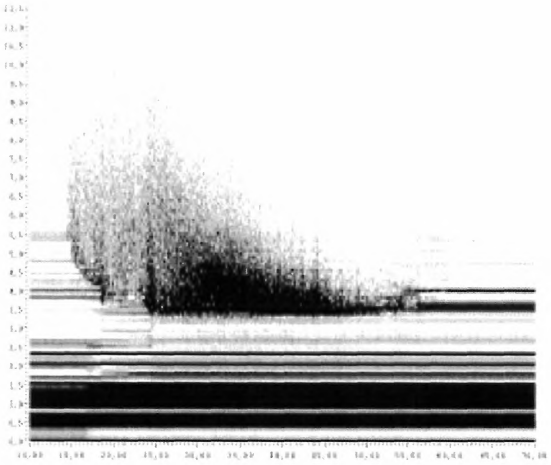

Figure 4 - FMCW radar echo intensity as a function of time (horizontal axis) and electromagnetic distance from the ground (vertical axis). Vallée de la Sionne, 25/02/1999 event, uppermost radar location (from Issler, 2003).

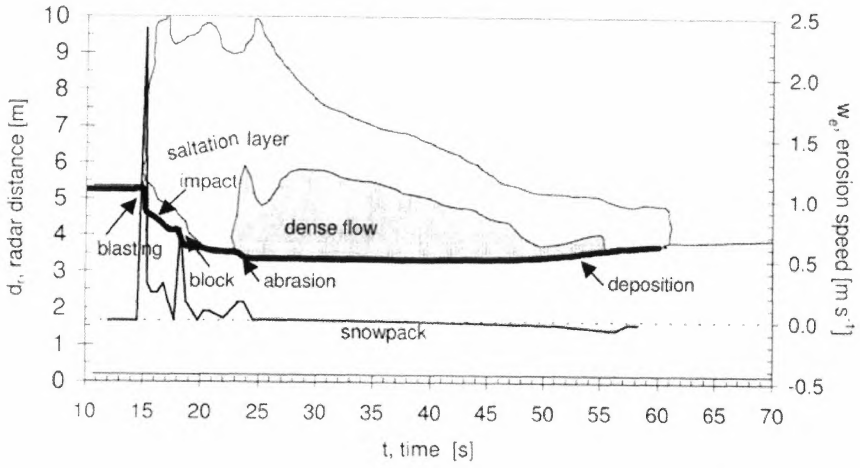

Figure 5 - Radar distance of the snow surface from the ground vs. time (thick line) and the corresponding erosion speed (thin line). Vallée de la Sionne test site, uppermost radar location, 25/02/1999 event (from Gauer and Issler, 2003).

For the avalanche of 25/02/1999, Figure 5, obtained from the radar plot of Figure 4, shows quasi-instantaneous erosion of about 0.7 m of snow at the leading front of the saltation layer, with an erosion speed of approximately 2.5 m s^{-1}. In the following 5 s, erosion is more gradual, the erosion velocity decreases from 0.25 m s^{-1} to near zero, and the radar echo intensity shows a layer (about 0.5 m thick) with higher density and larger block size than in the upper part of the saltation layer. Then the erosion speed reaches a second peak, which is tentatively interpreted as a snow block ripped out of a stronger layer. After that, the average erosion speed is about 0.05 ms^{-1}. Only then the dense core arrives. During the first second of its passage, the erosion speed has a value of 0.15 ms^{-1}; afterwards no further erosion is observed in this case. Snow deposition takes place during the last 10 s of the passage of the dense core.

All three events observed at Vallée de la Sionne exhibit similar features: In each event, the upper layer of snow is quasi-instantaneously, i.e. within less than 1 s, removed by the avalanche front (by a sort of "ploughing" or "gobbling" mechanism). Typical values of the ploughing depths are 0.8–1.0 m for all avalanches, corresponding to 8–14 t $m^{-1}s^{-1}$ were incorporated into these avalanches per unit width. A second phase, lasting about 1–10 s, follows. In this phase snow is eroded more gradually and the erosion rate diminishes from 0.3 ms^{-1} to about one third of this rate. After this phase the avalanche flows without eroding or depositing appreciably from about 30 s to about 1 minute in the two largest events. The formation of the deposit occurred quite abruptly in all cases.

It has been observed (Sovilla *et al.*, 2001) that, at a given location or instant, erosion at the front may coexist with deposition at the tail, where the velocity is smaller. Moreover, FMCW measurements show that front entrainment seems to dominate over basal erosion. However, the dominating process depends on the snow cover characteristics and avalanche dimensions. If the snow cover is made up by fresh snow during the impact between the avalanche front and the snow cover, the avalanche could collects "immediately" a relevant amount of snow at the front (ploughing, see § 3.2), but if the superficial layer of the snow cover is hard, the avalanche tends to slide over it and may scrape mass from its bottom surface (abrasion, see § 3.1).

2.3 Mass balance measurements at Ryggfonn

The Ryggfonn avalanche test site, located in South-western Norway, has been in operation since the winter 1980. The Ryggfonn avalanche path has a vertical drop of about 900 m and a horizontal length of 2100 m. The avalanches range in volume from 10,000 m^3 to 500,000 m^3, with maximum velocities up to 60 m s^{-1}. The avalanches are both naturally released and triggered by pre-placed explosives. The installations in the lower part of the path consist of (Issler, 1999; Lied *et al.*, 2002):

- A 16 m high and 100 m wide catching dam located at the lower end of the path.
- A 6.5 m high steel mast, instrumented with strain gauges in two sections, located on the top of the dam.
- A 4.5 m high concrete structure instrumented with three load plates, situated 230 m up-slope from the dam.
- A 5.5 m high cylindrical steel mast, diameter 1.3 m, instrumented with two load plates, identical to the load plates at the concrete structure, located 320 m up-slope from the dam.
- 5 geophones placed in the ground, 3 at the dam and 2 up-slope from the dam at distances of 18 and 65 m.
- An instrumented shelter near the run-out area with recording equipment.

Even if measurements on this site have been mainly focused on the effect of the dam on avalanches, mass-balance measurements have been made on 12 major dry snow avalanches. All the avalanches hit the dam and either were stopped by the dam or over-topped it. Estimates of the release area, fracture depth, deposits area and volume were obtained through aerial and field surveys; the snow density in the release area was extrapolated from NGI's snow measurement station located a few kilometres away (the average density in the starting zone was about 300 kg m^{-3}), and the snow density of the deposits near the dam was measured manually (average density of about 430 kg m^{-3}). All these data permitted to calculate the initial and deposited mass of each avalanche and subsequently to estimate the net entrainment between release and deposit. The net entrainment from release to deposit was found to be variable from –15% to +220%, with an average value of about 100% (that means a doubling of initial mass); actually, among the 12 avalanches, only one event (27/03/1993) showed a mass decrease from release to run-out. The data measurements on the 12 avalanches are summarised in Table 3.

Date	*Overrun (m)*	*Freeboard (m)*	*Release volume (10^3 m^3)*	*Velocity ($m\ s^{-1}$)*	*Type*	*Release mass (kt)*	*Entrainment (%)*
1983/01/10	148	14	100	46	Dry	33.9	+33
1983/03/08	-22	13	45	23	Dry	7.1	+220
1985/02/13	48	16	20	34	Powder	4.6	+100
1987/01/28	203	14	70	48	Dry	14.5	+100
1988/04/11	23	16	40	38	Dry	5.5	+190
1988/12/23	38	15	75	31	Dry	13.6	+150
1990/03/07	48	15	30	43	Powder	4.6	+160
1993/03/27	151	6	20	35	Powder	9.4	-15
1994/01/24	29	16	40	33	Dry	11.2	+60
1995/03/03	58	15	20	35	Powder	5.5	+60
1997/02/08	173	5	100	45	Dry	31.7	+60
2000/02/17	311	5	80	49	Powder	11.4	+180

Table 3 - Data measurements on the 12 avalanches analysed. The overrun length is measured from the downstream base of the dam, the front velocity is measured between the tower and the concrete structure. Entrainment is expressed as the difference between deposited and released mass relative to the released mass (from Issler et al., 2003).

2.4 The catastrophic events of winter 1999

The winter 1999 is remembered as a catastrophic winter for its extraordinary avalanche activity throughout the Alps. In Switzerland, more than a thousand avalanches damaged structures, blocked transport routes and killed 17 people. One of the most severely struck areas in the Swiss Alps was the Obergoms (uppermost part of the Rhone valley, located in Canton of Valais). In particular, four events that occurred between the villages of Geschinen and Oberwald were analysed (Sovilla and Gruber, 2002).

In order to obtain information about the release and deposit area of each event and the snow volumes on the ground, aerial stereo-photographs of the areas affected by avalanches were taken immediately after the avalanche events and again during the summer. Moreover, photogrammetry allowed to determine the snow height along profiles parallel to the avalanche trajectories, giving information on the distribution of erosion and deposition along the avalanche path. A summary of the measurements collected by photogrammetry and analysis of geo-referenced aerial photographs is given in Table 4.

Avalanche	Type	Exposition	Release altitude	Release area, m^2	Release volume Rv, m^3	Deposition average height, m	Deposition volume Dv, m^3	Ratio $\bar{Dv}/\bar{Rv}$	Potential eroded area, m^2	H eroded snow, m $\rho = 300 kgm^{-3}$
Jungstafel	Open slope	SE	2080-1920	(72000) 85800	(144000) 171612	1.52	(216950)* 325425	1.9	608239	0.25
Cheer	Open slope	NW	2115-1960	(70900) 80180	(141800) 160360	2.02	(340650)* 510975	3.2	568037	0.62
Cheer_w	Channel	NW	2180-2120/ 2040-1920	(22580) 28100	(45160) 56200	1.91	(123040)* 184560	3.3	245190	0.59
Loeuewenbach	Channel	NW	2120-1980	(51875) 60180	(103750) 120360	2.82	(274550)* 411825	3.4	392481	0.74

Table 4. Overview of the measurements for the 1999 avalanches, Numbers in parentheses are from planimetric measurements. ( ): measured volume; the actual volume has been calculated multiplying the real volume by a factor of 1.5 in order to take into account snow compression in the deposition zone (from Sovilla and Gruber, 2002).*

The ratio between the deposit volume *Dv* and the release volume *Rv* shows that all four avalanche eroded snow along the path. Three of the four avalanches have a ratio between 3.2 and 3.4, whereas the ratio is only 1.9 for the Jungstafel avalanche. The difference between the release and deposit volumes divided by the potential erosion area, i.e. the total area affected by the avalanche passage, allowed the determination of the average eroded snow height. Values between about 0.6 m and 0.75 m were found for all avalanches exposed to NW; conversely, for the Jungstafel avalanche the average erosion height was found to be only 0.25 m. This is probably due to the different snow water content of that event. A high water content in the snow, as was the case for the Jungstafel avalanche, decreases the capacity of the avalanche to erode snow along the avalanche path and erosion occurs particularly on the steeper parts of the track, whereas a large quantity of snow is left on the more gentle parts of the track (see Figure 6). An example of the results obtained from the observations of these events is shown in Figure 6, which reports, for the Jungstafel avalanche, the snow height along the track and in the deposit zone before and after the avalanche passage. The horizontal line indicates the average snow depth before the avalanche passage.

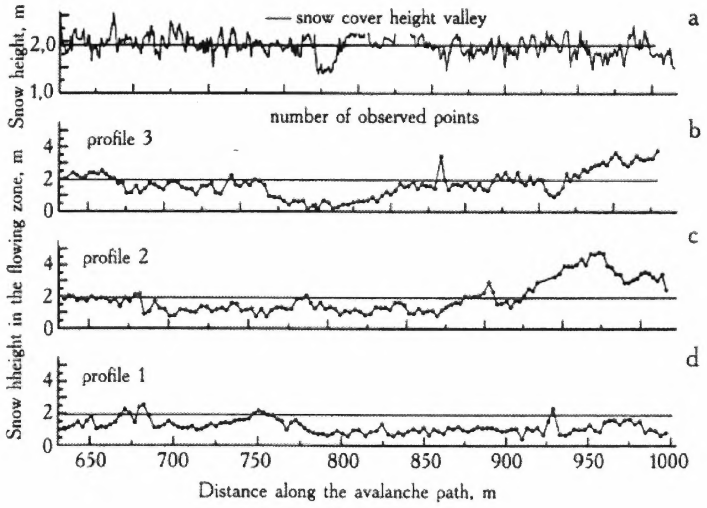

Figure 6 - Jungstafel avalanche (22/02/1999).(a): Snow depth in the deposit zone before the avalanche passage. (b), (c) and (d): Snow depth in the flowing zone after the avalanche passage along 3 different profiles (from Sovilla and Gruber, 2002).

3 Possible erosion mechanisms

There are different erosion mechanisms that may contribute to the increasing of the mass of an avalanche from the release area to the deposit zone. Simple but process-specific models have been recently proposed by Gauer and Issler (2003), to describe erosion by impacts, abrasion, fluidisation and ploughing. All these erosion mechanisms may occur simultaneously in different parts of the avalanche body and their relative importance is mainly determined by the avalanche flow parameters and snow cover properties.

3.1 Erosion by direct particle–particle interaction

Measurements with profiling radar (see Figure 4) show relatively long episodes with gradual erosion at moderate rates, indicating the importance of snow erosion due to particles impinging on the snow cover surface within the saltation layer of the avalanches. Each particle impact on the snow pack causes a displacement of the surface particles within the impact crater, partly leading to a densification of the snow pack, partly to loosening of the snow and its entrainment by the ambient flow. The impacting particle itself may rebound from the surface or penetrate it and get stuck. The particle sizes range from grains with a diameter of approximately 0.25 mm to blocks with a size of a few decimetres. At the base of the dense avalanche core the particles are in continuous contact and slide over one-another. Hard particles will plough grooves in the softer snow pack under their own weight and the overburden load. The snow cover is partly compacted, partly loosened and entrained by the avalanche. This process is commonly known as abrasion.

3.1.1 Impact erosion

For a first estimate of potential impact erosion speeds, the impact of snow particles on the snow cover is treated as the impact of a rigid sphere (the snow particle) on a porous, rigid and perfectly plastic material with compressive yield stress Y (the snow pack). Based on the tests of Abele and Gow (1975), the following relation may be assumed to hold between Y (in kPa) and the snow cover density ρ_s (in kg m^{-3}):

$$Y = 2.1 \times 10^{\frac{\rho_s - 100}{150}} \tag{1}$$

The impacting particle is decelerated and deflected upwards while it compacts and displaces the snow cover (provided the particle is not completely submerged into the snow cover). If the impact angle α (measured from the x-axis, see Figure 7) is sufficiently small, the particle will not be stopped completely but will leave the snow cover again. The equation of motion for the impinging snow particle reads:

$$\ddot{x} = -g\sin\phi - \frac{P_L}{m_p}(\sin(\alpha+\beta) + \mu\cos(\alpha+\beta)) \tag{2}$$

$$\ddot{z} = -g\cos\phi + \frac{P_L}{m_p}(\cos(\alpha+\beta) - \mu\, sin(\alpha+\beta)) \tag{3}$$

where ϕ is the slope angle, m_p is the mass of the snow particle, $P_L = p_d A_e$ is the force due to the plastic flow pressure acting in the line of motion and μP_L is the contribution of the Coulomb friction tangential to the motion. A_e is the projection of the instantaneous contact area onto the plane defined by $\overline{AB}$ and the y-axis (Figure 7). The plastic flow pressure p_d is approximated as $p_d \approx c_p Y$. For solids $c_p \approx 3$ in the fully plastic stage; c_p is close to unity for porous media in the fully plastic stage and for small indentation;, it increases with increasing indentation and reaches a maximum value of about 3, reflecting strain hardening.

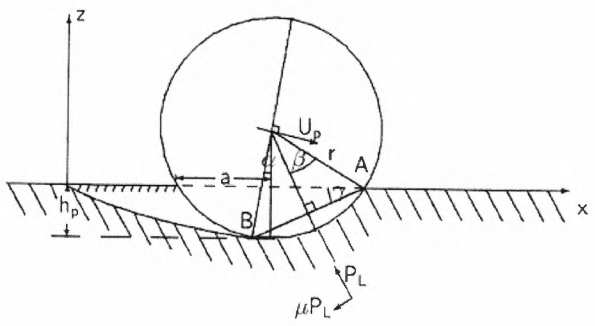

Figure 7 - Rigid snow particle impacting onto the plastic snow pack (from Gauer and Issler, 2003).

The erosion speed is given by:

$$w_{ie} = N_i V_e \tag{4}$$

where V_e is the volume of an impact crater (calculated numerically by solving equations 2 and 3 and using proper geometrical relations, see Rickerby and MacMillan, 1980), and N_i is the number of particle impacts per unit time and unit area, approximated as:

$$N_i \approx \frac{cW_f \cos\phi}{2V_p} \tag{5}$$

where $c/2$ is the volume concentration of particles in downward motion, W_f is the terminal velocity of the particles and V_p their volume. Simulations presented in Gauer and Issler (2003) have shown that the impact erosion speed w_{ie} is mainly affected by the snow cover density: in particular, it decreases exponentially with increasing snow cover density. Another important controlling factor is the impact angle α; the erosion speed grows with increasing impact angle and thus with particle size because larger particles have a higher fall velocity W_f and thus tend to impact under a steeper angle. Note that the growth of the erosion speed with increasing impact angle is sharply limited by the

maximum angle (depending on the impact velocity) beyond which the particle gets absorbed in the snow pack.

3.1.2 Abrasion

The methods developed for impact erosion may also be applied to estimating the abrasion speed. Consider now a snow particle indenting the snow pack and sliding parallel to the surface ($\alpha = 0$). The particle equations of motion (2) and (3) are supplemented with an overburden load L and with the traction exerted on the particle by the avalanche :

$$\ddot{x} = \left(g + \frac{L}{m_p} \right) \sin\phi - \frac{P_L}{m_p} \left(\sin\beta + \mu \cos\beta \right) + \frac{F_D}{m_p} \tag{6}$$

$$\ddot{z} = -\left(g + \frac{L}{m_p} \right) \cos\phi + \frac{P_L}{m_p} \left(\cos\beta - \mu \sin\beta \right) \tag{7}$$

L is determined by the effective pressure transferred through the particle lattice within the avalanche. We assume that each snow block at the interface carries the load $L = \rho_{av} g h_{av} \cos\phi / N_b$, with N_b the number of blocks per unit footprint area. For simplicity, the traction is expressed as a drag:

$$F_D \approx \frac{C_D}{2} \rho_{av} \pi r^2 \left| u_{av} - U_{pe} \right| \left(u_{av} - U_{pe} \right) \tag{8}$$

where C_D is the drag coefficient (which depends on the flow regime), ρ_{av} and u_{av} the avalanche density and velocity, U_{pe} the velocity of the sliding particle and r the particle radius. In the present case of surface-parallel sliding the left-hand side of eq. 7 vanishes, and the plastic-flow pressure times the z-component of A_e balance the load due to the particle and its overburden. At the same time, the plastic-flow pressure times the x-component of A_e acts as the retarding force in eq. 6.

The material eroded by one block per unit time is proportional to the penetrating cross-sectional area, A, perpendicular to the flow direction and the mean velocity of the block, $\overline{U}_p$. Hence the erosion speed due to abrasion may be expressed as:

$$w_{ea} = N_b A \overline{U_p} \tag{9}$$

Simulations presented in Gauer and Issler, 2003 show that the determining factors for the abrasion erosion w_{ea} speed are the snow density and the effective overburden of the particle at the base; conversely, only a weak particle-size dependence was found.

3.2 Erosion at the avalanche front

3.2.1 Fluidisation

Fluidisation of the snow pack occurs when an air pressure gradient in the pores of the snow cover generates a stress gradient in the matrix that counteracts the cohesive and gravitational forces. A pore air pressure gradient can arise at the snow avalanche front as an effect of two mechanisms:

- The rapid flow of the dilute snow–air mixture causes a pressure drop above the snow cover;
- The snow cover is rapidly compacted by the avalanche and pore air tries to escape through the undisturbed snow cover.

Fluidisation due to the first mechanism may operate in the upper part of the head of the dense core and contribute to the formation of the saltation layer. Fluidisation due to the second mechanism may occur only in the frontal part of the avalanche, where the pore pressure should attain several kPa at the compression front. Snow fluidised just ahead of the avalanche front will be easily entrained and might be the major source feeding the saltation layer. Estimations of the pressure necessary to initiate fluidisation (for details see Gauer and Issler, 2003) indicate that erosion by fluidisation may occur in relatively large and fast avalanches. However, even if complete fluidisation is not reached, this mechanism contributes to the weakening and destruction of the snow pack.

3.2.2 Ploughing

It has been observed that the front of the avalanche may behave like a plug, shearing part of the snow cover off. A part of the snow cover is entrained into the avalanche flow, a part is compacted underneath the avalanche where the avalanche may either slide over it or eventually erode it through abrasion or impact erosion (Figure 8).

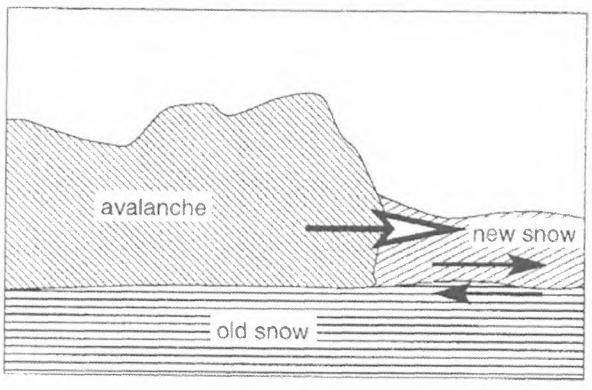

Figure 8. Part or all the snow cover is sheared off the substrate and incorporated in the flow (from Issler et al., 2000)

The erosion depth and the compression of the snow underneath the avalanche are determined by the interplay of various factors. The weight of the avalanche head largely determines the compression of the snow cover that is not eroded, but the upward deflection of the eroded snow increases that pressure. In order to describe the compaction and erosion process, one may consider a prismatic control volume bounded by three jump surfaces (see Fig. 9). Surface *b* forms the shear surface, surface *c* is the boundary towards the avalanche, and surface *a* forms the boundary to the air flow above. Across each of these surfaces, the jump conditions for mass and momentum must be fulfilled:

$$[\![\rho_r(\mathbf{u}_r - \mathbf{C}_r)\cdot\mathbf{n}_r]\!] = 0 \tag{10}$$

$$[\![\rho_r\mathbf{u}_r(\mathbf{u}_r - \mathbf{C}_r)\cdot\mathbf{n}_r]\!] - [\![\mathbf{t}_r\cdot\mathbf{n}_r]\!] = 0 \tag{11}$$

where *r* indicates the surfaces *a*, *b* and *c* respectively. $\mathbf{C}_r$ is the velocity of the (non-material) surfaces, and $\mathbf{t}_r\cdot\mathbf{n}_r$ is the normal stress onto the surfaces. The erosion depth d_e is strongly influenced by the normal stresses at the shear plane *b;* the determining quantities are the compressibility of the snow pack and the overburden load from the avalanche head. The difficulty connected with these equations consists in specifying the stresses on the boundaries of the volume; further studies are needed in order to obtain approximate solutions that can be compared to measurements.

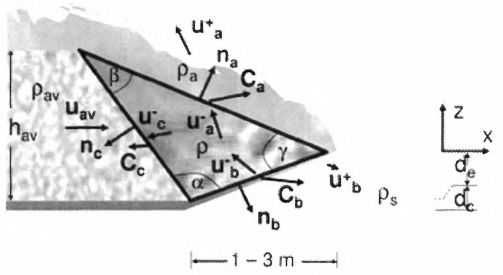

Figure 9. Schematic representation of the head region of a dense-flow avalanche ploughing through the snow pack (from (Gauer and Issler, 2003)).

The four erosion mechanisms briefly described above may all contribute to entrainment. They occur in different parts of avalanches and under different circumstances. It is very likely that the flow regime determines which mechanism is dominant; ploughing and abrasion need a dense avalanche body, whereas impact erosion seems to be limited to a more dilute flow. Fluidisation occurs only if the avalanching snow is sufficiently hard and dense, but the process itself tends to dilute the avalanche front.

All the erosion mechanism need to be further investigated either via theoretical studies or through a series of experiments both carried out in the laboratory and in full-size test sites. Once the mechanisms are better understood, they have to be formulated in terms of the dynamical variables and parameters of the models they should be incorporated in.

4 Mathematical models

4.1 Briukhanov *et al.*, 1967

The two equations used by the authors to describe the avalanche motion along the slope are:

$$\frac{\partial h}{\partial t}+\frac{\partial hv}{\partial x}=0 \tag{12}$$

$$\frac{\partial v}{\partial t}+v\frac{\partial v}{\partial x}=g\sin\psi-\frac{1}{2h}\frac{\partial}{\partial x}\left(h^2 g\cos\psi\right)-\left(f_1+f_2\right) \tag{13}$$

where f_1 and f_2 are the dry and hydraulic friction, respectively, v is the velocity of the flow, h is the thickness of the flow and ψ is the slope angle. This model describes entrainment at the flow front as a hydraulic jump. The boundary between the moving avalanche snow and the static snow is idealised as a shock wave perpendicular to the flow. It has been observed that the larger the velocity and the flow depth are, the larger is the entrainment rate. Usually in the transition zone of an avalanche path, the maximum velocity and flow depth occur near the front. Since this frontal part is usually short in comparison to the length of the whole body of the avalanche, it can be treated as a discontinuity such as in the above model.

In the equations (12) and (13) there are no terms responsible for mass entrainment; all the entrainment is assumed to occur at the front and is taken into account by applying proper boundary conditions ensuring mass and momentum conservation at the front:

$$\rho\,\bar{h}\left(w-\bar{v}\right)=\rho_0 h_0 w \tag{14}$$

$$\rho_0 h_0 w\bar{v}=\frac{1}{2}\rho\bar{h}^2 g\cos\psi-\sigma^* h_0\equiv P\quad at\quad P\geq 0 \tag{15}$$

where w is the speed of the avalanche front, $\bar{h}$ and $\bar{v}$ are the snow height and velocity of the avalanche body, respectively, σ^* is the compression strength of the entrained snow-pack layer, h_0 and ρ_0 are the thickness and the density of the snow cover, and P is the force exerted on the snow cover by the avalanche.

The thickness of the layer that is being entrained depends on the strength of the snow in this layer and on the value of the force with which the avalanche acts on it; the maximum erodible snow height is assumed to be known in advance. When $P < 0$ (i.e., the avalanche force is insufficient to disrupt the snow cover), the relation (15) is replaced by one of the following conditions:

$$w=\bar{v}=0 \qquad \text{(stop of the front)} \tag{16}$$

$$h_0=\frac{\rho\,\bar{h}^2 g\cos\psi}{2\sigma^*} \qquad \text{(partial entrainment of the snow cover)} \tag{17}$$

$$w=\bar{v},\ \bar{h}=h_0=0 \qquad \text{(absence of snow entrainment)} \tag{18}$$

4.2 Grigorian and Ostroumov, 1977

These authors considered a flow in a chute with rectangular cross-section. They proposed a model for gradual entrainment from the bed, assuming that the boundary of the moving avalanche and the underlying static snow layer is a shock front at which the snowpack is disintegrated and entrained into the flow. This shock front is assumed to be inclined to the bed, in contrast to the previous model.

The continuity equation is:

$$\frac{\partial F}{\partial t}+\frac{\partial (uF)}{\partial S}=q \tag{19}$$

where F is the cross-sectional area of the flow, S the co-ordinate along the flow path and q the entrainment rate, i.e., the volume of entrained snow per unit time and unit footprint area.

The quantity of eroded snow is proportional to the load p (the sum of hydrostatic and dynamic pressure) generated by the moving snow on the undisturbed snow:

$$p=\rho\left(ah+Cu^2\cdot\sin\alpha\right) \tag{20}$$

where ρ is the avalanche average density, a is the sum of the slope-normal component of gravity and the centripetal acceleration, h is the local flow depth, α the front entrainment slope, defined in terms of the local snow-cover depth δ by $\alpha=\arctan(\partial\delta/\partial S)$, u the avalanche speed, and C is an empirical constant.

At the front, the mass and momentum conservation give:

$$\omega\rho_0=(\omega-v)\rho_1 \tag{21}$$

$$\omega v\rho_0=\begin{cases} p-p_*, if\ p>p_* \\ 0, if\ p\le p_* \end{cases} \tag{22}$$

where ρ_0, ρ_1 are the densities of undisturbed snow and of the snow after the entrainment, ω is the propagation velocity of the shock front where the snow cover is broken up and mixed into the moving snow mass, v is the average velocity of the avalanche body, and p_* is related to the compressive strength of the snow cover. It is assumed that the thickness of the snow cover, its density and p_* are known. It follows that:

$$\omega=\sqrt{\frac{p-p_*}{\rho(1-\rho_0/\rho_1)}}\equiv\sigma\cdot\sqrt{\frac{p-p_*}{\rho_0}} \tag{23}$$

where the parameter σ is a constant characterising the compacting of the snow during the breaking process (Grigorian and Ostroumov (1977) assumed $\rho_1 = \rho_0$). The mass source parameter (the volumetric entrainment rate) q is:

$$q = \omega \frac{\rho_0}{\rho} L = \begin{cases} \dfrac{\sigma L}{\rho} \sqrt{(p - p_*)\rho_0} & p > p_0 \\ 0 & p \le p_0 \end{cases} \tag{24}$$

where L is the width of the chute.

4.3 Eglit, 1983

Eglit (1983) gives the equations describing the motion of avalanches consisting of two layers (a lower dense layer and an upper powder layer) as well as of powder avalanches. The two-layer model includes mass exchange between the two layers as well as between the dense part of the avalanche and the motionless snow cover.

Let ρ_1, v_1, h_1 and ρ_2, v_2, h_2 be the density, velocity and thickness of the dense layer and the powder layer, respectively, and ρ_0, h_0 the density and thickness of the underlying snow cover. The formulae for mass exchange between the layers are:

$$V_{10} = \begin{cases} m_{01} |v_1| \dfrac{\sqrt{\rho_1 \rho_0}}{\rho_1 + \rho_0} & (h_0 > 0) \\ 0 & (h_0 = 0) \end{cases} \tag{25}$$

$$V_{21} = \begin{cases} m_{12} |v_2 - v_1| \dfrac{\sqrt{\rho_2 \rho_1}}{\rho_2 + \rho_1} & (h_1 = 0 \quad or \quad x < x_f) \\ m_{02} |v_2| \dfrac{\sqrt{\rho_2 \rho_0}}{\rho_2 + \rho_0} & (h_1 = 0 \quad or \quad x > x_f) \end{cases} \tag{26}$$

where V_{10} and V_{21} are the volume exchange rate between the dense core and the underlying snow cover and the volume exchange rate that corresponds to the snow entrained by the powder layer, m_{10}, m_{12} are coefficients that may depend on the corresponding Richardson numbers, and x_f is the co-ordinate of the leading front of the dense layer of the avalanche.

The rate of the volume influx to the core from the powder layer is denoted here by V and consists of two terms: the first is V_{21} and the second is connected with sedimentation in the powder layer:

$$V = -V_{21} + V_S \tag{27}$$

$$V_S = v_S \cos\psi \tag{28}$$

where ψ is the slope angle and v_S is the settling velocity of the snow particles in the powder layer.

4.4 Brugnot and Pochat, 1981

The flow equations of the model are the continuity and the momentum equation:

$$\frac{\partial S}{\partial t}+\frac{\partial P}{\partial x}=0 \tag{29}$$

$$\frac{\partial P}{\partial t}-\frac{2P}{S}\frac{\partial S}{\partial t}+\left[\frac{gh}{n}-\frac{P^2}{S^2}\right]\frac{\partial S}{\partial x}=gS\sin\psi+\frac{gh}{n}\left(\frac{\partial S}{\partial x}\right)h$$

$$=const-\left[f_s gS\cos\psi+f_l g\frac{P}{R^2}+f_t g\frac{P^2}{SR}\right] \tag{30}$$

where:

- $S=s\rho$ [kg/m] with s the transversal section of the flow and ρ the snow density (during the flow, the snow density varies with the speed and the snow depth; the authors proposed the following form of variation: $\rho=\frac{\rho_0}{1+\alpha(V-V_0)}$, ρ_0 is the density at rest, V_0 the threshold speed at which ρ varies and α the coefficient of variation);
- P [kg/s]is the snow flow rate;
- h is the flow depth;
- g is the gravity acceleration;
- ψ is the slope angle;
- n is a variable used to describe the wet area of a section ($s=kh^n$);
- f_s, f_l and f_t are coefficients of static, laminar and turbulent friction, respectively.

The equations above are applied to the entire flow domain; at the front of the avalanche, the authors use boundary conditions of the "mobile jump" type:

$$W(S-S_0)=P \tag{31}$$

$$P(W-V)=\frac{g}{n+1}(Sh-S_0h_0) \tag{32}$$

where V is the avalanche average velocity, W is the front velocity, S_0 the entrained snow mass per unit travelling distance and h_0 the erodible snow depth.

The phenomenon of snow entrainment up-stream of the avalanche front is not well known and the *mathematical* model proposed by the authors schematises the entrainment of snow with the hypothesis that a given snow depth h_0, provided by the user in each section, is completely entrained at the avalanche front (Figure 10).

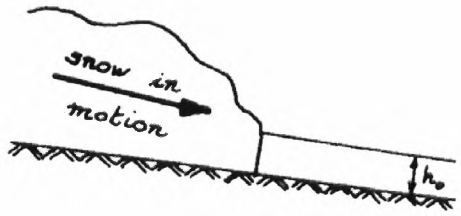

Figure 10: Treatment of snow entrainment as a hydraulic jump at the avalanche front in the model of Brugnot and Pochat (1981).

4.5 Hungr, 1995

The avalanche mass (Hungr's model applies to rapid flow slides, debris flows and avalanches) is represented by a series of blocks contacting each other, free to deform and with a constant volume. The model is based on a Lagrangian finite difference solution of the equations of motion, which are formulated in curvilinear co-ordinates and for a moving mesh, as illustrated in Figure 11.

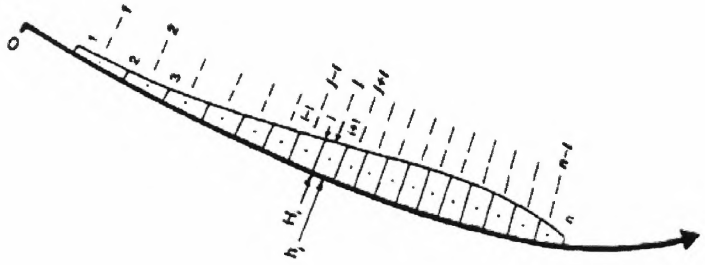

Figure 11: The Lagrangian mesh in curvilinear co-ordinates. Boundary blocks are numbered i = 1 to n, mass blocks J = 1 to n–1 (Hungr, 1995).

At the end of each time step, the integration of Newton's second law leads to:

$$v_i = v_i' + \frac{g\left(F\Delta t - M\right)}{\gamma H_i B_i ds} \tag{33}$$

v_i' is the initial velocity of the ith block and v_i is the velocity of the block at the end of a time step, F is the net driving force acting on a boundary block, Δt is the time step interval, γ is the bulk unit weight of the boundary block, g the gravitational acceleration and M the momentum flux due to erosion.

The deposition and entrainment of material at the base or sides of the flow can be simulated by changing the volume of each boundary and mass block in each time step, in assigned entrainment or deposition zones along the path, by a prescribed amount. The momentum flux M is set to reflect momentum changes caused to the mass changes. Considering a streamline, representing the flux integrated over the entire cross-section, Newton's second law in terms of momentum is:

$$F = \frac{\Delta(mv)}{\Delta t} \tag{34}$$

where m and v are the mass and the velocity of a boundary block and Δ signifies a change in a time step. The momentum of a block, equal to mv, changes in the course of a time step in response to changes of both the mass and the velocity of the block. Neglecting the second-order term, the momentum after a time step is:

$$mv + \Delta(mv) = mv + (\Delta m)v + m(\Delta v), \tag{35}$$

from which

$$m(\Delta v) = \Delta(mv) - (\Delta m)v = F\Delta t - (\Delta m)v \tag{36}$$

4.6 Sovilla and Bartelt, 2002

The model proposed permits to analyse the effect of the snow bed stratification on the erosion process. The avalanche increase its mass by eroding a snow layer with characteristics specified by the user. The erodible snow may be built up of different layers with a heights and density equal to those of the real avalanche event.

Experimental measures realised on the Swiss test site Vallée de la Sionne with the use of a FMCW radar showed that the erosion process at the avalanche front (*ploughing*) seems to dominate over basal erosion.

The model equations are:

$$\frac{\partial A}{\partial t} + \frac{\partial Q}{\partial x} = \dot{S}_e + \dot{S}_d \tag{37}$$

$$\frac{\partial Q}{\partial t} + \frac{\partial}{\partial x}\left[\alpha \frac{Q^2}{A}\right] = A\left[gF_0 + gF_f + gF_e\right] - \lambda gA\frac{\partial h}{\partial x}\cos\varphi \tag{38}$$

where:

- $\dot{S}_e$ e $\dot{S}_d$: volumetric snow entrainment and deposition rates [m^2/s] which represent the volumetric variation of the avalanche caused by the entrainment and deposition of material along the avalanche path;
- gF_0: gravitational acceleration along the track;
- F_f: flow friction;
- F_e: entrainment friction;
- φ : terrain inclination;
- Q: avalanche flow rate;

- A: transversal section of the avalanche.

F_e is considered to be negligible in comparison to the other friction sources.

In the Voellmy-fluid model the erosion processes are introduced using Grigorian and Ostroumov theory (Grigorian and Ostroumov, 1977). The friction introduced by the new mass (the eroded mass incorporated into the avalanche at the avalanche velocity) have to be taken into account by a variation of the model parameters (turbulent and kinematic friction, ξ and μ) and by the coefficient of active/passive pressure λ.

The events mentioned above from Monte Pizzac and Valleé de la Sionne were simulated using two different dynamical models: the Voellmy-fluid model and the NIS model (Sovilla and Bartelt., 2002). For both models, two different entrainment mechanisms were tested:

- "Front entrainment" (the eroded mass is instantaneously accelerated to the avalanche velocity);
- "Distributed entrainment" over the avalanche path (the acceleration of the eroded mass requires a specified amount of time).

Distributed entrainment near the front gave the best fit to the experimental data for both test sites. The authors claim that the distribution of mass inside the avalanche (the dislocation of the entrained snow in the avalanche), can influence the dynamics of the avalanche more than the quantity of the eroded mass.

4.7 The SOMOS erosion module (Sailer *et al.*, 2002)

The simulation model SAMOS (Sampl and Zwinger, 1999) distinguishes between the dense and the powder component of a dry-snow avalanche. Because of the completely different features of the two components, different models have been developed to describe their motion. The two models are coupled by an additional model which describes the mass and momentum exchange between the two components of the avalanche. The snow entrainment module was added later by the two authors, but a detailed description of the underlying theory has not yet been published. The input parameters of the model are: (i) snow mass (given as the height, density and extension of the release area); (ii) the mean diameter of snow particles that are transported in the powder layer of the avalanche; (iii) the density of the dense layer. In the latest version of the model, the erodible areas along the avalanche path are defined by specifying the snow density, depth and width of the erodible layer.

The entrainment process considered is not erosion at the sliding surface of the avalanche but a "ploughing-in" of the resting snow in front of the dense-flow avalanche layer. The erodible snow depth and its density have to be imposed as boundary conditions of the model. The snow eroded at the front is deflected parallel to the front surface (Figure 10) and the eroded mass-flow is:

$$\dot{m} = \rho u w h_s \tag{39}$$

where ρ is the density of the eroded snow, w the flow width, h_s the erodible snow depth and u the velocity of the eroded snow hitting the avalanche front. Part of the eroded snow is incorporated into the dense part of the avalanche and the remaining by the powder part:

$$\dot{m} = \dot{m}_d + \dot{m}_p \tag{40}$$

$$\dot{m}_d = f_d \cdot \dot{m} \tag{41}$$

f_d is a parameter that takes into account the fraction of eroded snow entrained in the dense flow. f_d=1 if the entire eroded snow is incorporated into the dense flow. f_d is determined heuristically and is a function of:

- the ratio between the flow height and the erodible snow height;
- the ratio between the density of the dense flow and of the erodible snow cover;
- the Froude number $F_r = \dfrac{u}{\sqrt{g h_d}}$.

The authors have decided to use the following ratio to determine f_d:

$$f_d = \min\left(\frac{z'_b}{z'_{\max}}, 1\right) \tag{42}$$

where z'_b and z'_{max} are the vertical height of the point B and the maximum height of the entrained snow flux, respectively (Figure 12).

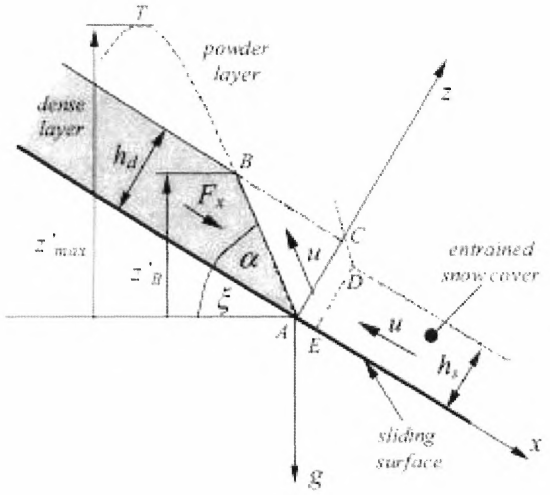

Figure 12. Snow entrainment at the front of the dense avalanche layer (Sailer et al., 2002).

The force that acts as resistance to the dense layer flow, necessary to deflect the entrained mass, is obtained from the momentum equation applied to the control volume A-B-C-D-E-A shown in Figure 12:

$$F_x w h_d = \dot{m}\left(u - u_B \cos\alpha\right) - w A_{ABCDE} g \rho \sin\alpha \tag{43}$$

where u_B is the velocity in B of the deflected/entrained snow and α is shown in Figure 12.

4.8 CEMAGREF erosion and deposition models (Naaim *et al.*, 2003)

4.8.1 The erosion model

Depending on the flow phases, the avalanche flow applies more or less high stress on immobile snow cover . When this exceeds the grain stress threshold, erosion occurs: the particles are pulled up and entrained into the flow: the total mass of the avalanche increases. On the other hand, when the friction at the bottom becomes dominant, the moving grains situated at the bottom are stopped and deposited. In this case, the total mass of the avalanche will progressively decrease.

Before tackling the formulation of the mass exchanges, it is necessary to recall one of the main hypotheses used in shallow water theory related to velocity profile similarity:

$$u(z,t) = \bar{\vec{u}} f(\eta) \qquad \eta = \frac{z}{h} \tag{44}$$

where u is the velocity, h the flow height and z is the orthogonal coordinate to the main slope. At an altitude b, the velocity can be written as:

$$u(b) = \bar{\vec{u}} f(\frac{b}{h}) = \bar{\vec{u}} \left\langle f(0) + \frac{b}{h}\frac{df}{d\eta}(0) + .. \right\rangle \tag{45}$$

if b is small and f(0)=0 (continuity), then: $u(b) \approx \bar{\vec{u}} \frac{b}{h}\frac{df}{d\eta}\Big|_{\eta=0}$

Given a free surface flow of h as flow height and u as mean velocity, flowing over a mobilized bed made of the same material as the moving one, the infinitesimal layer of ε as depth situated between the moving layer and the immobile material (interface layer) is submitted to the following forces:

- the friction force exerted by the flow: $\mu\rho ghS\cos\theta$;
- the force resulting from the flow depth gradient: $k\rho gS\varepsilon\cos\theta\vec{\nabla}h$;
- the adhesion and friction forces exerted by the immobile material: $\tau_c S + \mu_{start} S(h+\varepsilon)\rho g\cos\theta.(h+\varepsilon)$;
- and the weight: $\rho gS\varepsilon\sin\theta$;

where:

- μ and μ_{start} are dynamic friction coefficients (Poliquen, 1999);
- g is the gravitational acceleration;
- ε is the depth of the layer;
- S is the surface of the layer;
- τ_c is the internal (adhesion) stress of the layer.

The sum of the external forces is:

$$\rho g S\left[\varepsilon \sin\theta + \mu h\cos\theta - k\varepsilon\cos\theta\vec{\nabla}h - \frac{\tau_c}{\rho g} - \mu_{start}\cos\theta(h+\varepsilon)\right] \tag{46}$$

If this sum is positive, erosion will occur. Before entraining the layer, the flow will first remove the internal forces resulting from friction and adhesion. Afterwards, the velocity of the layer will be progressively brought from zero to the flow velocity. Erosion occurs in two stages: the collapse phase followed by the entrainment phase. During the collapse phase, no movement occurs, and the momentum conservation equation applied to the infinitesimal layer is expressed as:

$$\varepsilon\left(\tan\theta - \mu_{start} - k\vec{\nabla}h\right) - \frac{\tau_c}{\rho g} + (\mu - \mu_{start})h = 0 \tag{47}$$

The depth of the flow that will be disintegrated and entrained is limited by the following value:

$$\varepsilon_c = \frac{\frac{-\tau_c}{\rho} + (\mu(h,u) - \mu_{star})h}{\tan\theta - \mu_{start} - k\vec{\nabla}h} \tag{48}$$

Once the material breaks up, the depth likely to be entrained during the time Δt corresponding to the layer of which the gain in momentum is equal to the sum of the external forces:

$$\frac{d(mu)}{dt} = \rho g\varepsilon\sin\theta + \mu\rho g(h)\cos\theta - \mu\rho g(h+\varepsilon)\cos\theta - \rho g\varepsilon\cos\theta\vec{\nabla}h \tag{49}$$

During the entrainment phase cohesion does not intervene (it was broken up in the disintegration phase) and $\mu_{start} = \mu$. The momentum of the layer increases from zero to $\rho\varepsilon u(\frac{\varepsilon}{2})$. We can then write:

$$\frac{1}{\Delta t}\rho\varepsilon u(\frac{\varepsilon}{2}) = \rho g\varepsilon\sin\theta + \mu\rho gh\cos\theta - \mu\rho gh\cos\theta - \mu\rho g\varepsilon\cos\theta - \rho g\varepsilon\cos\theta\vec{\nabla}h \tag{50}$$

$$\frac{1}{\Delta t}u(\frac{\varepsilon}{2}) = g\cos\theta\left[\tan\theta - \mu - \vec{\nabla}h\right] \tag{51}$$

Thanks to the velocity profile similarity approximation, the entrainment rate can be given by:

$$\frac{\varepsilon}{\Delta t} = \phi_e \approx \frac{2h}{\vec{u}\left.\frac{df}{d\eta}\right|_{\eta=0}} g\cos\theta\left[\tan\theta - \mu - \vec{\nabla}h\right] \tag{52}$$

4.8.2 The deposition model

When the sum of the external forces becomes negative, the flow decelerates. The layer situated at the bottom is the slower layer. The dynamics of this layer is governed by momentum conservation. The depth likely to stop during a lapse of time Δt is fixed by:

$$\frac{d(mu)}{dt} = \rho g \varepsilon \sin\theta + \mu \rho g (h - \varepsilon)\cos\theta - \mu \rho g h \cos\theta - \rho g \varepsilon \cos\theta \vec{\nabla} h \tag{53}$$

If after a lapse of time the layer stops, its momentum will vanish:

$$\frac{-\rho\varepsilon}{\Delta t} u(\frac{\varepsilon}{2}) = \rho g \varepsilon \sin\theta + \mu \rho g (h - \varepsilon)\cos\theta - \mu \rho g h \cos\theta - \rho g \varepsilon \cos\theta \vec{\nabla} h \tag{54}$$

With the velocity profile similarity approximation the deposition rate can be written as:

$$\frac{\varepsilon}{\Delta t} = \phi_d \approx \frac{-2h}{\bar{\vec{u}} \left.\frac{df}{d\eta}\right|_{\eta=0}} g \cos\theta \left[\tan\theta - \mu - \vec{\nabla} h\right] \tag{55}$$

4.9 Erosion deposition processes in the saltation layer (Issler, 1998)

SL-1D (Issler, 1998; Issler et al., 2000) was developed to describe the flow of powder-snow avalanches, taking into account their denser bottom layer consisting of particles ranging in size from snow grains (diameter 0.1–1.0 mm) to snow blocks up to 0.5 m in diameter. This layer is called *saltation layer* by some authors, due to some similarities with the saltation layer well known from blowing snow; the term *resuspension layer* is also used. The saltation layer is characterised by its intermediate density, estimated to range from 10 to 100 kg m^{-3} (Issler, 2003), which implies that particle collisions are not rare, but do not dominate the dynamics either. Saltation-layer deposits are sometimes clearly distinguishable from the deposits of the dense core or the powder-snow cloud (Issler et al., 1996), and they may extend several hundred metres farther than the dense-flow deposits.

In the FMCW radar plot shown in Figure 4, a flow phase with large echo intensity is seen to arrive about 15 s after the front, where the echo intensity and presumably also the density are much smaller. This delay corresponds to a distance of about 500 m from the front. It is also clearly seen that all erosion (approx. 1.5 m in that giant avalanche) occurred underneath the saltation layer. These aspects of powder-snow avalanches are captured in SL-1D by coupling a saltation layer to a suspension layer (the dense flow is disregarded), using depth averaging in both layers. The general structure of the balance equations is like that of other depth-integrated models. However, the key difference from other two-layer models like Eglit's (1983) is the assumption that the dynamics of

the lower layer and the mass exchange with the snow cover is governed by the trajectories of saltating particles. In particular, the depth and the density of the saltation layer are determined by the saltation height of the particles, which is a function of their velocity. Similarly, the bottom friction is determined by the impact rate and concomitant momentum loss of the particles.

In the balance equations for mass and momentum of the snow cover and saltation layer (the suspension layer is not of interest in the present context),

$$\frac{d(\rho_0 h_0)}{dt} = q_{\text{sed}} - q_{\text{erod}}\,, \tag{56}$$

$$\frac{\partial(\rho_1 h_1)}{\partial t} + \frac{\partial(\rho_1 h_1 u_1)}{\partial s} = q_{\text{sett}} + q_{\text{erod}} - q_{\text{dep}} - q_{\text{susp}}\,, \tag{57}$$

$$\begin{aligned}\frac{\partial(\rho_1 h_1 u_1)}{\partial t} + \frac{\partial(\rho_1 h_1 u_1^2)}{\partial s} = \rho_1 h_1 g \sin\theta - \frac{\partial(\Delta\rho_2 h_2 h_1 + \Delta\rho_1 h_1^2/2)}{\partial s} g\cos\theta + \tau_{21}^{(a)} - \tau_{10}^{(a)} \\ + \gamma_a q_{\text{sett}} u_2 + (\beta_a q_{\text{erod}} - \beta_b q_{\text{dep}} - \beta_c q_{\text{susp}}) u_1\,,\end{aligned} \tag{58}$$

the subscripts 0, 1, 2 refer to the snow cover, saltation layer and suspension layer, respectively. ρ is the density, $\Delta\rho$ the density minus the air density, h the layer depth, u the layer-averaged velocity, g the gravitational acceleration, and θ the slope angle. $\tau_{21}^{(a)}$ and $\tau_{10}^{(a)}$ are the aerodynamic shear stresses exerted by the suspension layer on the saltation layer and by the saltation layer on the snow cover; they will not be discussed further here. The first equation keeps track of the erodible snow in the snow cover, with q_{dep} and q_{erod} the mass fluxes of deposited and eroded snow. q_{susp} and q_{sett} are the mass fluxes from the saltation layer to the suspension layer and vice versa. The second equation is not to be understood as a differential equation for h_1, which is determined by the algebraic relation $h_1(s,t) = \beta_d^2 u_1^2/(2g\cos\theta)$, but for the variable density ρ_1.

The fifth term on the right-hand side of the momentum balance equation captures the (vertical) flux of (longitudinal) momentum, carried across the interface between the layers by settling particles; $\gamma_a u_2$ is their mean velocity at the interface. In a similar way, the last three terms describe the momentum fluxes due to the mass fluxes of particles that are, respectively, ejected from the snow cover, impact on it, or are carried into the suspension layer by turbulent eddies. Their mean longitudinal velocities are $\beta_a u_1$ for ejected particles, $\beta_b u_1$ for impacting particles, and $\beta_c u_1$ for suspended particles. From studies of blowing snow, one infers $\beta_a \approx 0.5$, $\beta_b \approx 1$, $\beta_c \geq 1$, and $\beta_d \approx 0.3$–0.5 (with large uncertainties).

Closure of this system of equations is obtained by specifying the mass fluxes, of which only q_{dep} and q_{erod} are relevant to the present topic. The deposition mass flux equals the mass per unit footprint area, $m_1 = \rho_1 h_1$, divided by the mean jump duration:

$$q_{\mathrm{dep}} = \rho_1 \sqrt{\tfrac{1}{8} h_1 g \cos\theta} = \frac{\beta_0}{4} \rho_1 u_1 = \frac{m_1 g \cos\theta}{2\beta_d u_1}. \tag{59}$$

An impacting particle is likely to get stuck in the snow cover if its velocity is low, but the faster it is, the more secondary particles will be ejected from the snow cover. This suggests the ansatz $q_{\mathrm{erod}} = q_{\mathrm{dep}} f(u_1)$ with an ejection efficiency function f, which was chosen as

$$f(u_1) = 1 - \alpha + \alpha \left(\frac{u_1}{u_{\mathrm{thr}}} \right)^2 \tag{60}$$

for the lack of more precise knowledge. u_{thr} is the velocity at which $q_{\mathrm{erod}} = q_{\mathrm{dep}}$ and is mainly a property of the snow cover; its value is in the range 3–10 m s^{-1}. The parameter α is difficult to estimate a priori; back-calculations lead to values in the range 0.01–0.1.

Note that the deposition and erosion rates actually *decrease* as the saltation-layer velocity increases (for $u_1 << u_{\mathrm{thr}} / \sqrt{\alpha}$), in stark contrast to all other models discussed here. This behaviour is a direct consequence of the assumed quasi-ballistic particle trajectories. Another interesting and connected property is the approximate velocity independence of the particle-borne bottom shear stress, $\tau_{10}^{(p)} = (\beta_b - \beta_a f(u_1)) q_{\mathrm{dep}} u_1 = \dfrac{\beta_b - \beta_a f(u_1)}{2\beta_d} m_1 g \cos\theta$ ($\tau_{10}^{(a)}$, the aerodynamic drag, is negligible).

References

Abele, G. and A. J. Gow. 1975. Compressibility characteristics of undisturbed snow. CRREL Report 336. Hanover, New Hampshire, USA, Cold Regions Research and Engineering Laboratory

Ammann, W. J. 1999. A new Swiss test-site for avalanche experiments in the Valleé de la Sionne/Valais. *Cold Region Science and Technology*, **30**, 3–11.

Briukhanov, A. V., S. S. Grigorian, S. M. Miagkov., M. Ya. Plam., I. Ya. Shurova, M. E. Eglit, and Yu. L. Yakimov. 1967. On some new approaches to the dynamics of snow avalanches. *In:* Ôura, H., editor, *Physics of Snow and Ice. Proc. of Intl. Conf. Low Temp. Science, Sapporo, Japan, 1966.* Vol. I, Part 2. Sapporo, Hokkaido, Japan, Institute of Low Temperature Science, Hokkaido University, pages 1223–1241.

Brugnot, G. and R. Pochat. 1981. Numerical simulation study of avalanches. *Journal of Glaciology*, **27**, 77–88.

Dufour, F., U. Gruber, D. Issler,, M. Schaer, N. Dawes, and M. Hiller. 1999. Grobauswertung der Lawinenereignisse 1998/1999 im Grosslawinenversuchsgelände Valleé de la Sionne. Interner Bericht 732. CH-7260 Davos Dorf, Switzerland, Eidg. Institut für Schnee- und Lawinenforschung.

Eglit, M.E.1983. Some mathematical models of snow avalanches. *In* Shahinpoor, M., *ed. Advances in the Mechanics and the Flow of Granular Materials.* Vol. 2. Houston, TX, Gulf Publ. Co., 577–588.

Gauer, P. and D. Issler. Possible erosion mechanisms in snow avalanches. *Annals of Glaciology,* **38**. (in press).

Grigorian, S. S. and A. V Ostroumov. 1977. Matematicheskaya model sklonovih processov lavinnogo tipa (The mathematical model for slope processes of avalanche type*).* Scientific Report 1955. Moscow, Russia, Institute for Mechanics, Moscow State University.

Gubler, H. and M. Hiller. 1984. The use of microwave FMCW radar in snow and avalanche research. *Cold Regions Science and Technology*, **9**, 109–119.

Hungr, O. 1995. A model for the runout analysis of rapid flow slides, debris flow, and avalanches, *Can. Geotech. J.*, **32**, 610–623.

Issler, D. P. Gauer, M. Schaer, and S. Keller. 1996. Staublawinenereignisse im Winter 1995: Seewis (GR), Adelboden (BE) und Col du Pillon (VD). Interner Bericht 694. CH–7260 Davos Dorf, Switzerland. Eidg. Inst. für Schnee- und Lawinenforschung.

Issler, D. 1998. .....

Issler, D., *ed.* 1999. European avalanche test sites. Overview and analysis in view of coordinated experiments. CH-7260 Davos Dorf, Switzerland, Eidg. Inst. Für Schnee- und Lawinenforschung, Mitt. 59.

Issler, D., P. Gauer and M. Barbolini. 2000. Continuum models of particle entrainment and deposition in snow drift and avalanche dynamics, *In* Balean, R., editor. *Models of Continuum Mechanics in Analysis and Engineering. Proceedings of a conference held at the Technische Universität Darmstadt, September 30 to October 2, 1998.* Aachen – Maastricht, Shaker Verlag, pages 58–80.

Issler, D. 2003. Experimental information on the dynamics of dry-snow avalanches. *In* Hutter, K. and N. Kirchner, editors, *Dynamic Response of Granular and Porous Materials under Large and Catastrophic Deformations*, Lecture Notes in Applied and Computational Mechanics, vol. 11. Berlin, Germany, Springer, pages 109–160.

Issler, D., M. Barbolini, M., F. V. De Blasio, F.V., G. Furdada, C. B. Harbitz., K. Kristensen, K., K. Lied, J. N. McElwaine, A. I. Mears, A. Moe, M. Naaim. and R. Sailer. 2003. Simulations of observed dry-snow avalanches in the full-scale test site Ryggfonn, Norway. SATSIE internal report. Postboks 3930 Ullevål Stadion, N–0806 Oslo, Norway, Norges Geotekniske Institutt.

Lied, K., A. Moe, K. Kristensen, and D. Issler. 2002. Ryggfonn. Full scale avalanche test site and the effect of the catching dam. NGI Report 581200–35. Postboks 3930 Ullevål Stadion, N–0806 Oslo, Norway, Norges Geotekniske Institutt.

Naaim, M., T. Faug, T. and F. Naaim-Bouvet. 2003. Dry granular flow: erosion and deposition modelling. *Surveys in Geophyics.*, in press.

Pouliquen, O. 1999. Scaling laws in granular flows down rough inclined planes. *Physics of Fluids,* **11**, No. 3, 542–548.

Rickerby, D. G. and N. H. Macmillan. On the oblique impact of a rigid sphere against a rigid-plastic solid. *Intl. J. Mech. Sci.*, **22**, 491–494.

Sailer, R., L. Rammer L., and P. Sampl. 2002. Recalculation of an artificially released avalanche with SAMOS and validation with measurements from a pulsed Doppler radar. *Natural Hazards and Earth System Sciences*, **2**, 211–216.

Sampl, P. and T. Zwinger. 1999. A simulation model for dry snow avalanches. *Proc. XXVIII IAHR Congress, 22-27 August 1999*, Graz, D. 10, 287.

Savage, S. B. and K. Hutter. 1989. The motion of a finite mass of granular material down a rough incline. *Journal of Fluid Mechanics,* **199**, 177–215.

Sommavilla, F. and B. Sovilla. 1998. The avalanche monitoring system of Mount Pizzac. *In* Hestnes, E., *ed.: 25 Years of Snow Avalanche Research,* Voss 12–16 May 1998. Proceedings. NGI Publication 203. N–0806 Oslo, Norges Geotekniske Institutt, pages 268–273.

Sovilla, B., F. Sommavilla, and A, Tomaselli. 2001. Measurements of mass balance in dense snow avalanche events. *Annals of Glaciology*, **32**, 230–236.

Sovilla, B. and Gruber, U. 2002. Avalanche winter 1999: the importance of the snow entrainment in catastrophic avalanches. *Data of Glaciological Studies*, **93**, 110–116.

Sovilla, B. and P. Bartelt. 2002. Observations and modelling of snow avalanche entrainment, *Natural Hazards and Earth System Sciences*, **2**, 169–179.

Vallet, J., U. Gruber, andF, Dufour. 2001. Photogrammetric avalanche volume measurements at Valléee de la Sionne. *Annals of Glaciology*, **32**, 141–146.

Modelling of snow entrainment in avalanche dynamics

M.E. Eglit, K.S.Demidov

1. Introduction

It is known that a snow avalanche usually entrains a large amount of the snow from the slope during its motion (Sovilla and Bartelt, 2002). Without entrainment an avalanche cannot move for a long distance: it stretches along the slope and its velocity decreases. The entrainment affects the motion in two different ways. From one side, it leads to deceleration of the avalanche due to avalanche kinetic energy expenditure in accelerating the entrained snow masses. From the other side, it makes the avalanche larger, the flow height increases. The bed friction force per unit mass decreases because of that and therefore the avalanche tends to be accelerated. In some situations these two tendencies can be balanced. Then the entrainment may not affect the avalanche runout distance, though it does affect the avalanche dimensions (Eglit, 1982).

The ways of modeling the snow entrainment in avalanche dynamics are not established yet. Besides, the mechanisms of entrainment can be different depending on the avalanche type (whether it is heavy dense avalanche, or light dry one, or a powder one). And in the same avalanche there can be various mechanisms of entrainment (Issler and Gauer, 2003).

The first models for snow entrainment have been proposed in Russian papers (Briukhanov et al., 1967; Grigorian et al., 1967; Eglit, 1968; Grigorian and Ostroumov, 1977; Kulikovskiy and Sveshnikova, 1977; Eglit, 1983). In all mentioned papers exept the paper by Kulikovskiiy and Sveshnikova an approach similar to the shallow water theory had been used to describe the motion. Some models assumed that the entrainment took place at the flow front. The others included gradual entrainment from the bed (from the underlying snow layer).

The entrainment at the front had been proposed in (Briukhanov et al., 1967; Grigorian et al., 1967) for modelling dense avalanches. The first idea was that a dense avalanche operated like a bulldozer pushing the snow ahead of it, breaking its structure and involving it into the motion. Then the front was a kind of "hydraulic" jump with a "phase transition": the media at different sides of the jump were not the same – ahead of the front it was a solid and behind it behaved like a fluid (however, with more complicated properties).

The model for the gradual entrainment from the bed for dense avalanches had been proposed and used by S.S. Grigorian and A.V. Ostroumov (1977), for powder avalanches by A.G. Kulikovskiy and Sveshnikova (1977), and for dry, powder and mixed avalanches by M. E. Eglit (1983). The basic assumptions about the entrainment mechanism for heavy dense avalanches differ from those

for light dry ones. Therefore, the terms responsible for the entrainment in the equations are different in different models. S.S. Grigorian and A.V. Ostroumov (1977) assume that the boundary between the moving avalanche snow and the underlying static snow layer is again a shock wave, in which the snowpack is destructed and involved into the motion. This shock wave is supposed to be inclined to the bed and no jump of the height occurrs in the avalanche front. In the papers (Eglit, 1983; Eglit and Veltischev, 1985) the snow (and air) entrainment is supposed to be caused by a turbulent mixing at the boundaries of the flow. The mechanism is similar to that for mixing in turbulent jets. The main reason for mixing is the instability of the boundaries causing formation and breaking of waves at the boundaries. The disturbances growth rate is known to be proportional to the velocity difference between the flow and the ambient media. So the entrainment rate in the papers (Eglit, 1983; Eglit and Veltischev, 1985) is assumed to be proportional to the avalanche flow velocity and to depend on the flow and the ambient media density ratio.

In the present paper the results of calculations using some formulae for the entrainment rate from the bed are presented. These formulae were found in phenomenological theories for flows of various physical natures. The main conclusion is the following. At any reasonable entrainment law the larger are the velocity and the flow depth – the larger is the entrainment rate. In the transition zone of an avalanche path the maximum velocity and flow depths usually take place near the front. So in motion along steep slopes the snow is entrained mostly by the frontal part of the avalanche. Since this frontal part is usually short in comparison to the length of the whole body of the avalanche, it can be treated from the mathematical point of view as a jump (a discontinuity) and therefore we in fact return to the first model with entrainment at the front, at least for the motion in the transition zone. Of course, in motion along the slope with a varying slope angle the maximum values of the velocity and of the flow depth can be at a distance from the front (Eglit and Sveshnikova, 1979). But it does not always mean that the entrainment rate is maximal there: all available snow could be entrained by the frontal part of the avalanche and in this case there is no entrainment anywhere except the frontal zone.

2. The basic equations

We consider a motion of a dense avalanche in a channel with trapezoidal cross-section. The cross-section averaged equations for mass and momentum conservation are

$$\frac{\partial S}{\partial t}+\frac{\partial Su}{\partial x}=q \ ,$$

$$\frac{\partial Su}{\partial t}+\frac{\partial Su^2}{\partial x}=Sg\sin\psi-\frac{\partial}{\partial x}(\frac{1}{2}g_1\cos\psi\,h^2\,(B+\frac{1}{3}\eta h))-\frac{\tau L_p}{\rho}\operatorname{sgn}u\ , \qquad (1)$$

$$\frac{\partial S_{sc}}{\partial t}=-q\ .$$

Here t is time, x is the coordinate along the path, S is the flow cross-section area, u is the velocity averaged over the cross-section, h is the flow depth, ψ is the flow bottom slope angle, B is the flow bottom width, g is the gravity acceleration and g_1 is the sum of the gravity and the centrifuginal accelerations: $g_1=g+\frac{u^2}{R}$, R is the curvature radius of the path; τ is the friction stress averaged over the wetted perimeter, L_p is the wetted perimeter, ρ is the flow density and η is related to the side wall slope angles φ_1 and φ_2: $\eta=\cot\varphi_1+\cot\varphi_2$. The third equation in the system (1) is the mass conservation equation for the underlying snow layer, δ is its local thickness, and S_{sc} is its local cross section. The following relations between the flow and channel parameters hold:

$$L_p=B+\beta h\ ,\quad \beta=\frac{1}{\sin\varphi_1}+\frac{1}{\sin\varphi_2}\ ,\quad S=(B+\frac{1}{2}\eta h)h\ ,$$

$$S_{sc}=(B_{bed}+\frac{1}{2}\eta\delta)\delta\ ,\quad \psi=\psi_{bed}-\arctan\frac{\partial\delta}{\partial x}\ ,\quad B=B_{bed}+\eta\delta\ .$$

Here B_{bed} and ψ_{bed} are the width of the channel and its slope angle at the ground (under the snow cover) or at the bottom surface of the snow layer, which is supposed to be available for the avalanche.
The following relations determine the friction forces:

$$\frac{\tau L_p}{\rho}=k\,u^2\,L_p+\mu\,g_1\cos\psi\ h(L_p-\frac{1}{2}\beta h)\quad at\ \ h\le h_*\ ,$$

$$\frac{\tau L_p}{\rho}=k\,u^2\,L_p+\frac{\tau_*}{\rho}(L_p-\frac{1}{2}\beta h_*)\quad at\ \ h>h_*\ .$$

Here k and μ are the hydraulic and Coulomb friction coefficients, respectively, τ_* is the minimum value of the shear strength for the flowing snow or the bed material, and h_* is the depth, at which the Coulomb dry friction equals to τ_*:

$$h_* = \frac{\tau_*}{\mu \rho g_1 \cos\psi} \ .$$

To have a closed system of equations we should specify the formula for the snow entrainment rate q. Various possible formulae are presented in the next section.

3. The formulae for the entrainment of the bottom material

3.1. Snow avalanches

3.1.1. Models with entrainment at the front.

Consider first the models, in which the snow from the slope is assumed to be incorporated into an avalanche in its front. The front is a jump: the snow layer depth in front of it is h_0 (the depth of the snow cover in front of the avalanche), and just behind the front it is $\overline{h}$, which is the avalanche flow depth. There are no terms connected with the mass entrainment in the differential equations; the entrainment is taken into account by the boundary conditions only. So we have $q = 0$ in these models.

The boundary conditions at the front $x = x_f$ are the mass and momentum conservation equations. For a flow in a channel with trapezoidal cross-section they are:

$$\rho\ \overline{S}\ (w - \overline{v}) = \rho_0 S_0 w \ ,$$

$$\rho_0 S_0 w \overline{v} = P - \sigma^* S_0 \equiv \Delta P \quad at \quad \Delta P \geq 0 \ , \tag{2}$$

$$P = \frac{1}{2} \rho g_1 \cos\psi\ \overline{h}^2 \left(B + \frac{1}{3}\eta \overline{h}\right) \ .$$

Here w is the speed of the avalanche front, $\overline{h}$ is its height, $\overline{S}$ is the flow cross-section and $\overline{v}$ is the avalanche snow velocity at the front; S_0 is the cross-section area of the snow layer, which is to be involved into motion by the avalanche, σ^* is the strength at the compression for this layer, h_0 is its thickness and ρ and ρ_0 are densities of the snow in the avalanche and in the snow cover, respectively; P is the force (resulting from the pressure), with which the avalanche acts to the snow layer in front of it. If $\Delta P < 0$, i.e., the force P is insufficient to disrupt the snow cover, then, instead of the second relation in (2), it has been proposed to use one of the following conditions (Eglit, 1982):

$$(2.1)\ \ w = \overline{v} = 0; \qquad (2.2)\ \ S_0 = \frac{P}{\sigma^*}; \qquad (2.3)\ \ w = \overline{v},\ \overline{h} = h_0 = 0.$$

These conditions mean: (2.1) - the stop of the front, (2.2) – the entrapment of only a certain part of the available snow cover, and (2.3) - the motion over the snow layer without snow entrapment, respectively. The situation with $\Delta P < 0$ typically occurs in the runout zone where the front velocity and flow height are low. Calculations show (Eglit, 1982) that typically the conditions (2.2) and (2.3) slightly increase the run-out distance comparative to the condition (2.1). For simplicity it is possible always to use the condition (2.1) in calculations. However the form of the front zone of the avalanche and its deposits depends on the choice of the conditions (2.1), or (2.2), or (2.3).

3.1.2. Models with entrainment at the bottom surface of the avalanche flow.

3.1.2.1. Heavy dense avalanches.

Below the approach proposed by Grigorian and Ostroumov (1977) to model the entrainment from the bed by a dense avalanche is described following their paper (1977). A flow in a chute with the rectangular cross-section is considered. The entrainment rate q is supposed to depend on the load p generating by moving snow on an undisturbed snow under it. The boundary between the avalanche and the undisturbed snow is supposed to be a shock wave inclined to the bed. Let h_0 be the thickness of the snow cover, δ be the thickness of the undisturbed snow layer under the avalanche, ω be the velocity of propagation of the shock wave along the normal to it. The jump conditions for the momentum and mass conservation are

$$(\omega - v)\rho_1 = \varpi\rho_0 \,, \qquad \omega v \rho_0 = \begin{cases} p - p_* & at \;\; p > p_* \,, \\ 0 & at \;\; p \le p_* \,. \end{cases} \tag{8}$$

where ρ_0 , ρ_1 are the densities in front of and behind of the shock, ω, v are the normal components of the shock wave velocity and the snow velocity just behind the shock, p_* is the snow cover strength to breaking, p is the full pressure (hydrostatic plus dynamic) on the bed (i.e., on the surface of the snow under the avalanche).

Relations (8) lead to

$$\omega = \sqrt{\frac{p - p_*}{\rho_0 (1 - \rho_0/\rho_1)}} \equiv \sigma \cdot \sqrt{\frac{p - p_*}{\rho_0}}, \qquad \sigma = \sqrt{\frac{\rho_1}{\rho_1 - \rho_0}} \tag{9}$$

The parameter σ characterises the compression of the snow during breaking process and is supposed to be a known constant. The pressure p is given by the relation

$$p = \rho(ah + Cu^2 \cdot \sin\alpha), \qquad \alpha = \operatorname{arctg}\left(\frac{\partial\delta}{\partial S}\right), \qquad (10)$$

where $a = g\cos\psi + \frac{v^2}{R}$, g is the gravity acceleration, R is the curvature radius of the path; h and $\delta(S,t)$ are the local depth of moving snow and the local thickness of the underlying snow cover, respectively, C is an empirical constant. Using (9) one gets the following expression for entrainment rate q

$$q = \omega\frac{\rho_0}{\rho}B = \begin{cases} \frac{\sigma B}{\rho}\sqrt{(p - p_*)\rho_0}, & p > p_* \\ 0, & p \le p_* \end{cases} \qquad (11)$$

Here B is the width of the chute, and the avalanche average density ρ is proposed to be generally different from ρ_1.
If $C = 0$ and the centrifuginal acceleration can be neglected, then the first line in (11) can be rewritten as

$$q = k\sqrt{h - h_*}, \qquad (12)$$

where k is a constant coefficient (in motion along a constant slope).

Remarks. 1) It should be added to (11) that $q = 0$ at $\delta \ge h_0$, or $h_0 = 0$, or $\delta = 0$.
2) It is supposed that the values of ρ_0, h_0, p_* are known. Still additional assumptions on the values of the parameters σ, C, and ρ are needed to make calculations. The authors assumed that $\sigma = 1, C = 1, \rho = \rho_0$ in their later calculations.
3) Calculations by this model show that the entrainment usually takes place in narrow (several meters length) frontal zone only.
4) The dynamical part of the pressure should not enter the jump conditions (8). So C should be set equal to zero.
5) The described approach has sense if the flow velocity normal component v is not equal to zero.

3.1.2.2. Light dry avalanches, powder avalanches and mixed avalanches
For light dry avalanches the entrainment mechanism was supposed to be similar to that for turbulent jets. First this mechanism was proposed for a powder avalanche in (Kulikovskiy and Sveshnikova, 1977). The mixing with the ambient medium is caused by the instability of the boundaries leading to waves formation and breaking on boundaries. It is known that the growth rate of the disturbances on the boundaries between two layers is proportional to the velocity difference of the layers and to the following combination of the fluid densities ρ_1 and ρ_2:

$$\frac{\sqrt{\rho_1 \rho_2}}{\rho_1 + \rho_2}.$$

Besides it depends on the Richardson number. Basing on this approach the following expressions for the mass exchange between the layers are proposed and used (Eglit, 1983; Eglit and Veltischev, 1985; Nazarov, 1992; Eglit, 1998). Three layers are considered. The lowest one is the layer of the snow cover not entrained yet by the avalanche. Above it a dense core moves, and above the core (sometimes in front of it as well) there can be a powder layer. The local thicknesses of the layers are denoted by h_0, h_1, h_2, respectively, and the densities are ρ_0, ρ_1, ρ_2. The formulae for the volume exchange rate V_{ij}, $i = 0,1,2$ between the layers can be found, e.g., in (Eglit, 1998).The volume entrainment rate of the underlying snow cover by a dense core is written as

$$V_{10} = m_{10} | v_2 | \frac{\sqrt{\rho_1 \rho_0}}{\rho_1 + \rho_0} \quad at \quad h_0 > 0; \qquad V_{10} = 0 \quad at \quad h_0 = 0. \quad (13)$$

The rate of the volume income to the dense core from the powder layer is denoted below by V. It consists of two terms: the first one, V_{12} corresponds to the mass, which is entrained by the powder layer (i.e., loss of mass by the core); the second, V_s is connected with sedimentation process in the powder layer:

$$V = -V_{12} + V_s \quad , \qquad V_{12} = m_{12} | v_2 - v_1 | \frac{\sqrt{\rho_1 \rho_2}}{\rho_1 + \rho_2} \, , \; V_s = v_s \cos\psi \quad at \quad h_2 > 0. \quad (14)$$

Here ψ is the slope angle, v_s is the fall velocity of the snow particles in the powder layer, and m_{10}, m_{12} are coefficients, which can depend on the corresponding Richardson numbers, but were taken to be constant in calculations (Nazarov, 1992).

3.2. **Mud flows**

For mud flows the following formula for the entrainment rate from the bed per unit flow width is proposed in the paper (Bozhinskiy and Nazarov, 1999)

$$q = \begin{cases} m_e (U - U_*) & at \; U > U_* \, , \\ 0 & at \; U \le U_* \end{cases} \qquad (15)$$

Here m_e is a coefficient, U is the depth averaged flow velocity, U_* is the threshold velocity. The values $m_e = 0.03$ and $U_* = 2 m/s$ are recommended.
Another formula is proposed by Egizarov (1963):

$$q = kQ\sqrt{i}\left(\frac{\sigma_1}{\sigma_2}\frac{hi}{f_0 d\frac{\rho_p-\rho}{\rho}}-1\right) \qquad (16)$$

Here k is the coefficient, $Q=\rho US$ is the flow flux, $i=\sin\psi$, $\frac{\sigma_1}{\sigma_2}$ is the ratio of the fall velocities of the particles in the mud flow and in the pure water, d is the mean particle diameter, ρ_p and ρ are the particle and flow densities, h is the flow depth.

3.3. Slush flows

The following two models are proposed to describe the entrainment of the bed material by a slush flow. The first one (Bozhinskiy et al., 1996) is

$$q = m_e k(U-U_*)(\sin\psi-\sin\psi_*)B \ . \qquad (17)$$

Here $\psi_* = 1^\circ$, U_* is about $1-2\,m/s$, and the coefficient k depends on the flow density ρ :

$$k = 1-\exp\left(\frac{\rho_s-\rho}{\rho_w-\rho}\right).$$

Here ρ_s ρ_w are the snow and water densities, respectively.

The same authors had proposed a two-layer model (Bozhinskiy and Nazarov, 1998) for a slush flow: the lower layer consists of pure water, and the upper layer is a mixture of water and snow. It is supposed that

$$q = m_e U_\alpha \frac{\rho_\alpha}{\rho_w} \ . \qquad (18)$$

Here the index α corresponds to water or to the snow-water mixture depending on what layer entrains the snow.

3.4. Turbulent jets

3.4.1. Entrainment of the ambient fluid.

The entrainment of the ambient fluid is explained by the turbulent mixing at jet boundaries. For two-dimensional stationary jets over an inclined plane the entrainment rate coefficient E is introduced by the relation

$$E = \frac{1}{U}\frac{d(Uh)}{dx} \ ,$$

with U, h being the height-averaged velocity and the width of the jet, respectively. So we can write

$$q = EU \ . \qquad (19)$$

The coefficient E depends on the Richardson number Ri. There exist many empirical formulae describing this dependence. Some of the authors (Ellison and Turner, 1959; Kato and Phillips, 1969) assume E to be proportional to Ri^{-n} with n varying between 0.5 and 1.5. For $0.8 > Ri > 0$ the following formula had been suggested for a jet with the temperature difference from the ambient one (Koh, 1971)

$$E = E_0 \left(2\left(1 + \frac{Ri}{0.85}\right)^{-1} - 1 \right)^{1.75} ,$$

where $E_0 = 0.075$ is the value of the entrainment rate coefficient in the absence of temperature stratification. Another authors (Stolzenbach and Harleman, 1971) approximated the dependence $E(Ri)$ in similar experiments by a formula :

$$E = E_0 \exp(-5Ri) .$$

For the same range of the Richardson number values the following formula had been suggested for the entrainment of air by water in a spilling breaker in a wave (Longuet-Higgins and Turner, 1974)

$$E = \frac{0.08 - 0.1Ri}{1 + 5Ri} .$$

A.T. Onufriev (1967) had studied the vertical motion of a hot gas vortex ring usually arising as a result of the great explosion. He assumed the following formula

$$E = \alpha \sqrt{\frac{\rho}{\rho_a}} \ , \qquad \alpha = 0.03 - 0.08 .$$

Here ρ, ρ_a are the gas and ambient air densities, respectively; $\rho < \rho_a$. The author refers to the experiments on turbulent jets mixing for the α values.

3.4.1. Entrainment from the bed. Wind – blown sand and dust transport

Many authors assume that the entrainment rate from the bed depends on the shear stress on the bed. The following formula is proposed by Anderson and Haff (1991) for the number of the particles N entrained by the wind per unit bed area and per unit time

$$N = \varsigma(\tau - \tau_c) \ . \qquad (20)$$

Here τ is the mean shear stress at the bed, τ_c is its critical value (no entrainment at $\tau < \tau_c$), and $\varsigma = 10^5 \frac{1}{N \cdot s}$. The bed shear stress is often written as $\tau = \rho u_*^2$, where u_* is the friction velocity and ρ is the flow density. Then the last formula can be rewritten as

$$N = \varsigma \rho (u_*^2 - u_{*c}^2) . \qquad (21)$$

The typical value $u_{*c} = 0.25 m/s$ for the sand particle with the diameter 0.3 mm is recommended. The relation (20) can be rewritten in the form

$$N = k\rho(u^2 - u_{**}^2) \quad , \qquad (22)$$

since it is usually assumed that $\tau = C_D \rho u^2$ where C_D is the drag coefficient.
In study of the dust lifting by air flows the following formula for mass entrainment rate had been proposed in (Korolchenko and Tzarichenko, 1987):

$$\Phi = k\rho_p h\left(\frac{u}{u_c} - 1\right)^{\frac{3}{2}} .$$

Here u, u_c are the air flow velocity and its critical value, respectively, and h is the particle diameter if the separate particles are lifted by the flow, or it is the particle layer depth if the agglomerates of particles can be lifted.

3.5. The erosion of soil by water flows.

The intensity of the soil erosion by flows arising due to a rain fall is proposed to be described by the following formula (Wishmeier and Smith, 1965; Smakhtin , 1993)

$$D_f = \beta k_2 (\tau - \tau_c) \qquad (23)$$

Here D_f is the soil mass flowed out per unit area and per unit time, β equals the fraction of the area where the soil can be entrained by the water flow, and k_2 is the coefficient, which characterises the capability of the soil to be eroded. To determine τ_c the following empirical relation is used (Smerdon and Beasley, 1961):

$$\tau_c = 0.5 \cdot 10^{0.0183r},$$

where r is the concentration of clay in percents; $\tau_c \approx 34 Pa$ at $r = 100\%$ and in the absence of clay it is $0.5 Pa$. In practical calculations the author (Smakhtin , 1993) takes $r = 35\%, k_2 = 10^{-6}$, $\beta = 0.01$ for a grain-growing area and $\beta = 0.06$ for a meadow. In steady flows moving with constant velocity $\tau = \rho g h \sin\psi$. In this case the formula (23) can be rewritten as

$$\tau = k(h - h_*). \qquad (24)$$

3.6. Turbidity currents

C. Teisson et al. (1993) proposed the following formula for the entrainment rate of sediments by turbidity current

$$q = \begin{cases} aB(u^2 - u_*^2)^n & at \;\; u \geq u_* \\ 0 & at \;\; u < u_* \end{cases} \qquad \textbf{(25)}$$

n can be between 1 and 3.5.

Another formula, which determines q for turbidity currents, is used in (Akijama, and Stefan, 1988)

(26)

3.6. Blowing and drifting snow.

Remark. An approach described in (Gauer, 2001) could be included here.

4. Numerical investigation

4.1. The values of the model coefficients, and the initial conditions

Calculations were made for the model described in section 2 with various formulae for the entrainment rate. The goal was to study what is the difference in results at different entrainment laws. The following values of the model coefficients were used.

$\rho = 300 kg/m^3$ - the flow density

$k = 0.05$ - the hydraulic friction coefficient

$\mu = 0.3$ - the Coulomb friction coefficient

$\tau_* = 1530\, Pa$ - the minimum of the shear strengths of the flow and bottom materials

$\varphi_1 = \varphi_2 = 20^\circ$ - the side walls inclination angle

$B_0 = 50m$ - the channel bottom width

Various initial conditions were tried. The results given below the initial conditions were:

$h = 2m, u = 0$ at $50 < x < 100\, m$; $h = 0, u = 0$ out of this interval.

4.2. Formulae for the entrainment rate.

Various formulae for the entrainment rate had been tried in this work. Here the results are presented for the following three simplified versions of those described in the previous section.

Version A

$$q = a B u \ , \qquad (27)$$

where a is a constant coefficient, B is the bottom width of the channel.. This formula can be regarded as a simplified variant of the relation (13): the densities in the snow cover and in the avalanche dense core are supposed to be constant, then the dependence on the density ratio can be included into the coefficient a. A.N. Nazarov (1992) made back calculations of real avalanches and found $a = 0.005$ to be a proper value for mass exchange between the dense core and the snow cover, and $a = 0.015$ for interaction between the powder layer and the snow cover. In fact the formulae (15), (18), (19) have the form (27) as well, if one neglect u_* .

Version B

$$q = a B (h - h_*) \ . \qquad (28)$$

This formula coincides with (24) and is qualitatively similar to (12) in the sense that the entrainment rate depend on the load on the underlying snow cover, i.e., on the flow depth. For the soil erosion by rain flow the values $a \approx 10^{-5} \frac{1}{s}$, $h_* \approx 10^{-2}\, m$ follow from (Smakhtin, 1993).

Version C

$$q = a B (u^2 - u_*^{\,2}) \ . \qquad (29)$$

This formula is a variant of (25) at $n = 1$. The value of $u_* = 3 m/s$ was typically used in our calculations.

4.3. Numerical investigation

Let us describe first the motion in a chute with constant geometry and constant incline to a horizon. The snow cover height under the avalanche body in the moment when the avalanche front is at a distance 920 m from the starting point is shown at Fig.1. The entrainment rate is taken in the form (27) with values of a varying between 0.0001 and 0.05. The initial snow cover height is 0.3 m.

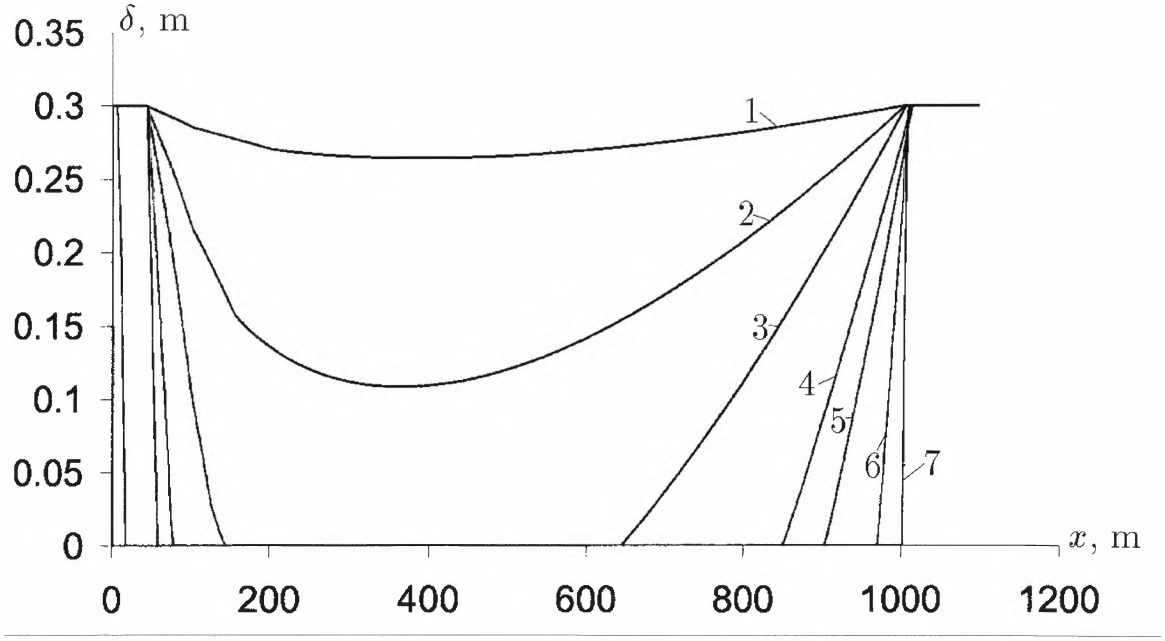

Fig. 1. Distribution of the snow cover depth $\delta(x)$ under an avalanche. Calculations at various values of the coefficient a in (27). The avalanche front coordinate is 1002 m., and the rupture line coordinate is 50 m. (1) $a=0.0001$, (2) $a=0.0005$, (3) $a=0.001$, (4) $a=0.002$, (5) $a=0.003$, (6) $a=0.008$, (7) $a=0.05$.

At low values of the entrainment coefficient a (Fig.1, curves 1 and 2) the avalanche did not entrained all available snow in any point yet. At $a \le 0.008$ the length of the frontal zone where the entrainment of all available snow occurs is less then 3% of the length of the body. There is a short zone in the back part where the snow cover is not entrained yet. It is because the velocity is equal to zero at the initial moment, and it is always lower than the velocity in the frontal part of the avalanche. Still the entrainment by the tail continues during motion, according to (27), and this back zone with the unentrained snow becomes shorter and shorter.

The results obtained by use of formulae (28) and (29) qualitatively coincide with the results described above.

Figures 2 and 3 present the distribution of the flow depth h and that of the velocity u at various values of the entrainment parameter a in the formula (27). The curves at the Fig. 2 are plotted for the moments when the coordinates of the flow cross-section with maximum values of h coincide for different avalanches. Similarly, the curves at the Fig.3 compare the velocity distributions at the moments (different for avalanches with different values of a) when the coordinates of the flow cross-section with maximum value of u are the same (equal to 1002 m.). The location of the point of transition from the parts of the curves with rather steep flow depth and velocities variation to much more

gentle part at curves 4-7 coincide with the back front of the entrainment zone; there is no available snow under the avalanche behind this point.

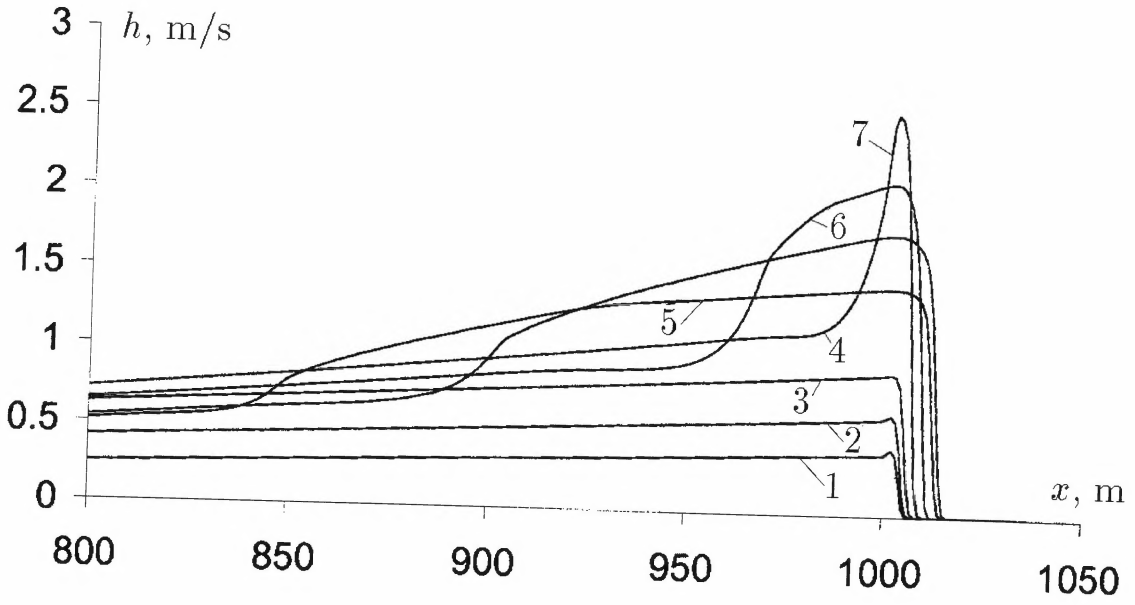

Fig.2. Dependence of the flow depth distribution along the avalanche body on the value of the entrainment coefficient a. Entrainment by the formula (27). The coordinate of the flow cross-section with the maximum value of h is 1002 m. (1) $a=0.0001$, (2) $a=0.0005$, (3) $a=0.001$, (4) $a=0.002$, (5) $a=0.003$, (6) $a=0.008$, (7) $a=0.05$.

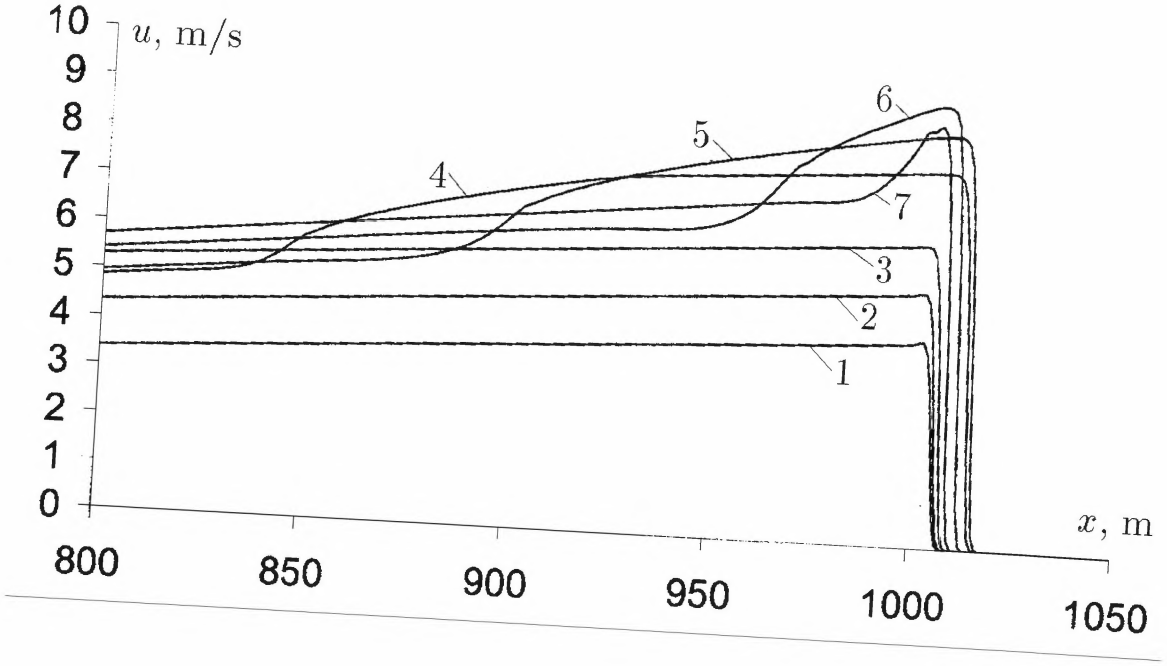

Fig.3. Dependence of the flow velocity distribution on the value of the entrainment coefficient a. Entrainment by the formula (27). The coordinate of the flow cross-section with the maximum value of u is 1002 m. . (1) $a=0.0001$, (2) $a=0.0005$, (3) $a=0.001$, (4) $a=0.002$, (5) $a=0.003$, (6) $a=0.008$, (7) $a=0.05$.

Comparing the curves 1 and 7 at the Fig.2, 3 we see that that if a is 50 times larger then the maximum value of h is only 5 times larger and that of u is 2 times larger. Typically if a is two times larger then the increase in maximum values of h is about 40% and in maximum values of u is about 20%. Analogous behaviour was found using the other formulae for the entrainment rate (see, e.g., Fig. 4, 5).

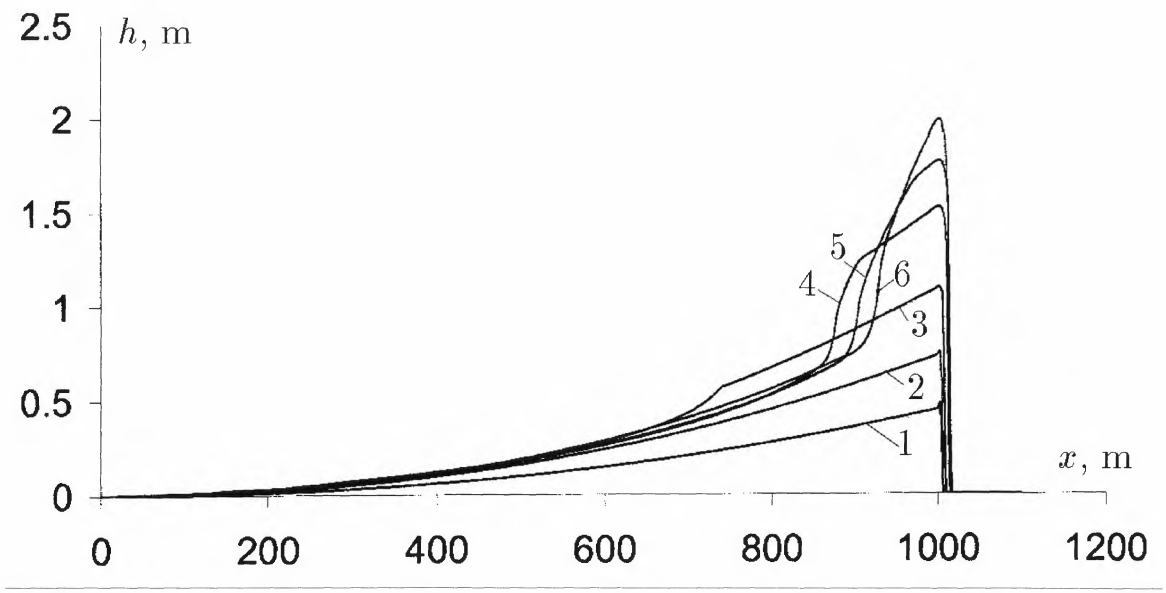

Fig.4. Dependence of the flow depth distribution along the avalanche body on the value of the entrainment coefficient a. Entrainment by the formula (28), $h_* = 0$. The coordinate of the flow cross-section with the maximum value of h is 1002 m. . (1) a=0.002, (2) a=0.006, (3) a=0.01, (4) a=0.014, (5) a=0.018, (6) a=0.02.

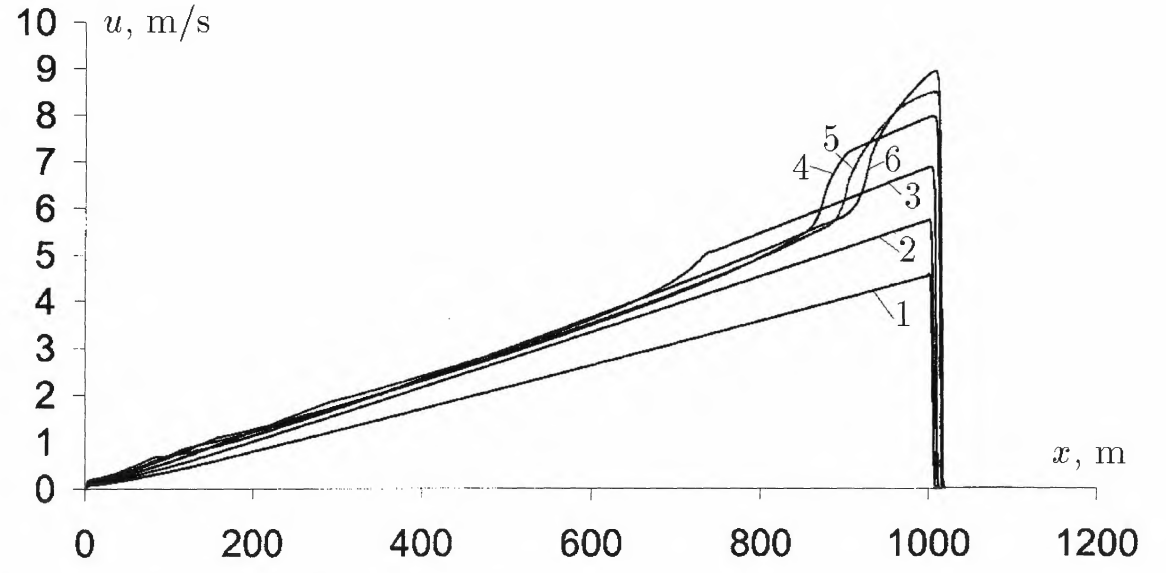

Fig.5. Dependence of the flow velocity distribution on the value of the entrainment coefficient a. Entrainment by the formula (28), $h_* = 0$. The coordinate of the flow cross-section with the maximum value of u is 1002 m. (1) a=0.002, (2) a=0.006, (3) a=0.01, (4) a=0.014, (5) a=0.018, (6) a=0.02.

Figures 6, 7, 8 show the variation of maximum over the avalanche body values of flow depth and flow velocity versus the front coordinate at different values of a. Formula (28) was used in these calculations. During the first moments after start (first 100 hundred meters) there is a strong influence of the initial conditions, but after a rather regular behaviour is observed and at low values of the entrainment coefficient the flow depth and velocity can decrease. If the avalanche starts to entrain all available snow in the frontal zone (values of the entrainment coefficient high enough) then the maximum values of the flow depth and the velocity tend to constant values in motion along the constant slope (see Fig. 8, where larger travel distances are shown).

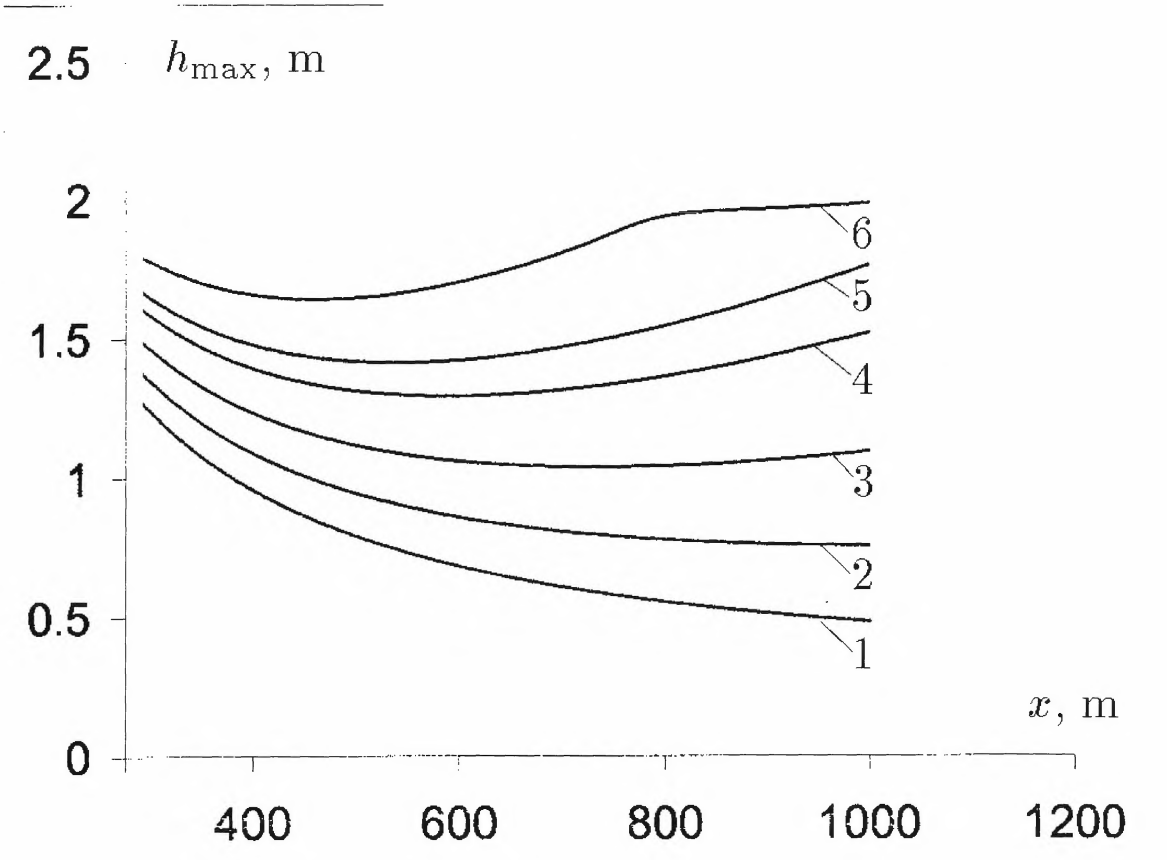

Fig.6. Dependence of the maximum value of the flow depth on the front coordinate at various values of the entrainment coefficient a. Entrainment by the formula (28), $h_* = 0$. (1) a=0.002, (2) a=0.006, (3) a=0.01, (4) a=0.014, (5) a=0.018, (6) a=0.02.

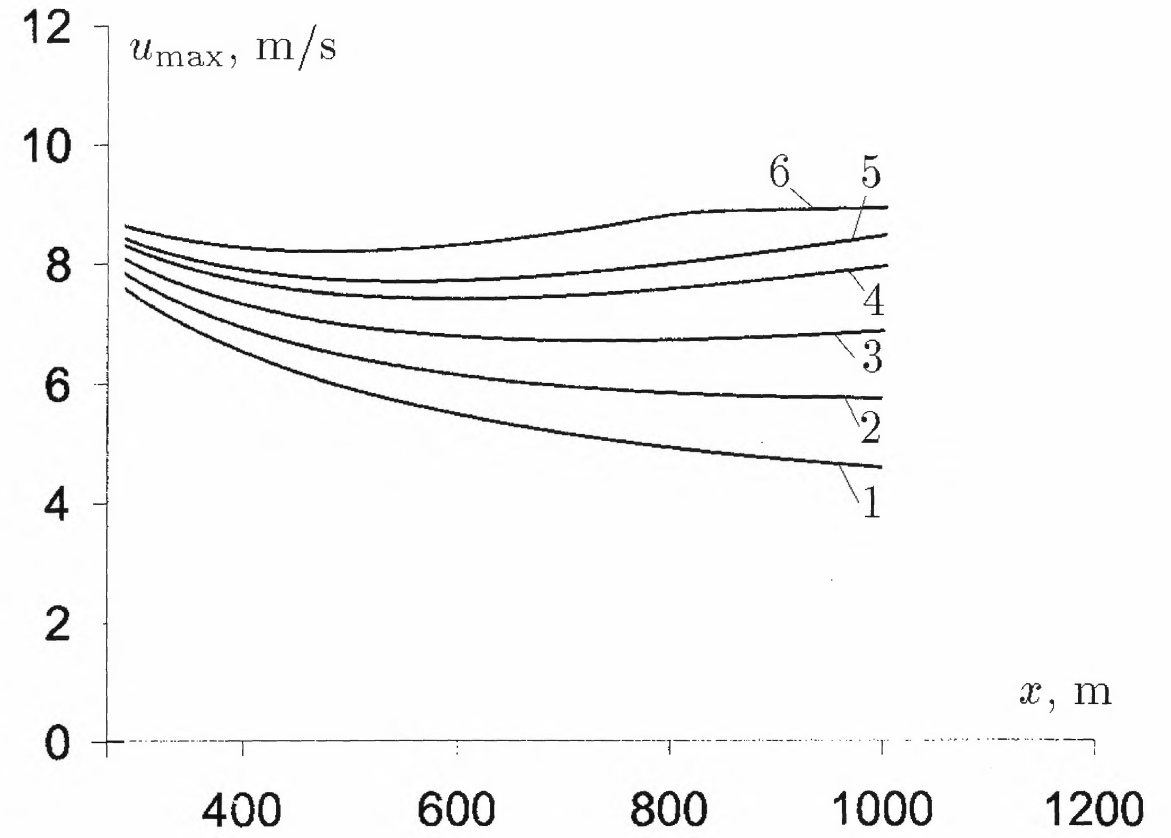

Fig.7. Dependence of the maximum value of the flow velocity on the front coordinate at various values of the entrainment coefficient a. Entrainment by the formula (28), $h_* = 0$. (1) a=0.002, (2) a=0.006, (3) a=0.01, (4) a=0.014, (5) a=0.018, (6) a=0.02.

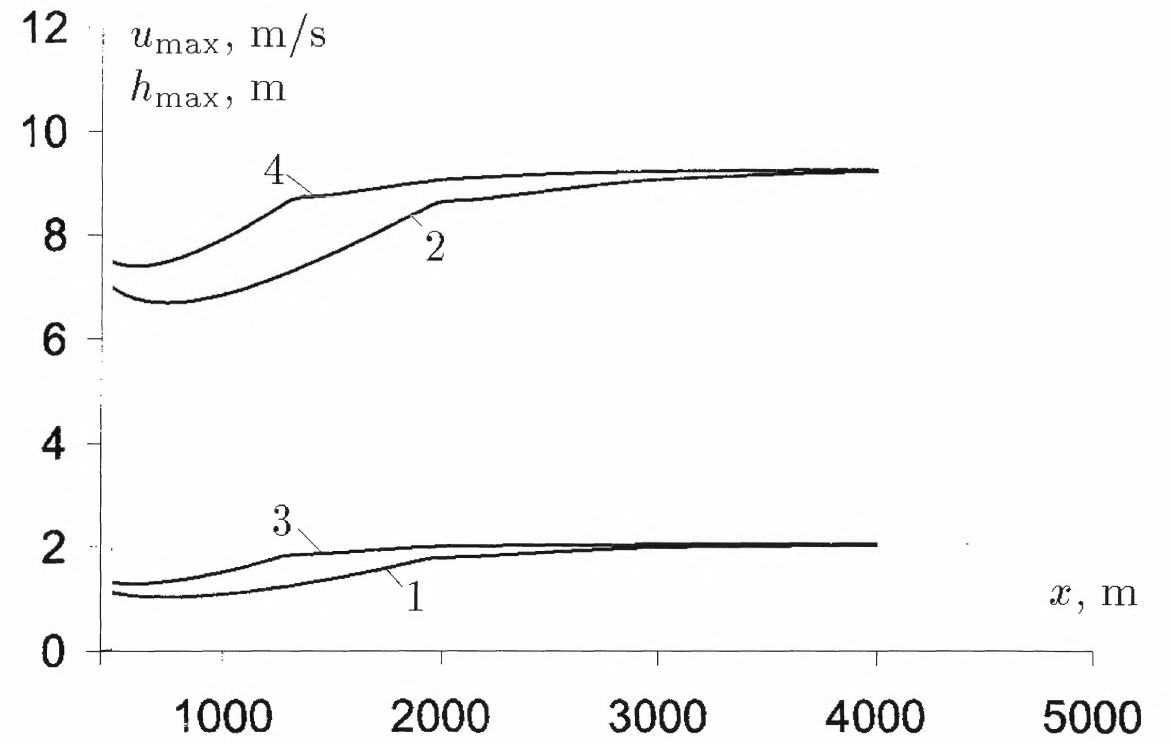

Fig.8. Dependence of the maximum values of the flow depth (curves 1,3) and flow velocity (curves 2, 4) on the front coordinate at various values of the entrainment coefficient a (large travel distance). Entrainment by the formula (28), $h_* = 0$.

Analysis of the calculation results show that if an avalanche entrain all available snow, then the avalanche parameters in motion along a constant slope depend mainly on the depth of the available snow layer and on the length of the entrainment zone, and do not depend on the details of the formula for the entrainment rate. Figures 9, 10, 11 demonstrate the results obtained by use of the formulae (27), (28), (29) with the coefficients, which give the same value of the length of the entrainment zone: $a = 0.0039$ in (27), $a = 0.00055 s/m$, $u_* = 3 m/s$ in (29), and $a = 0.021 \frac{1}{s}$, $h_* = 0$ in (28).

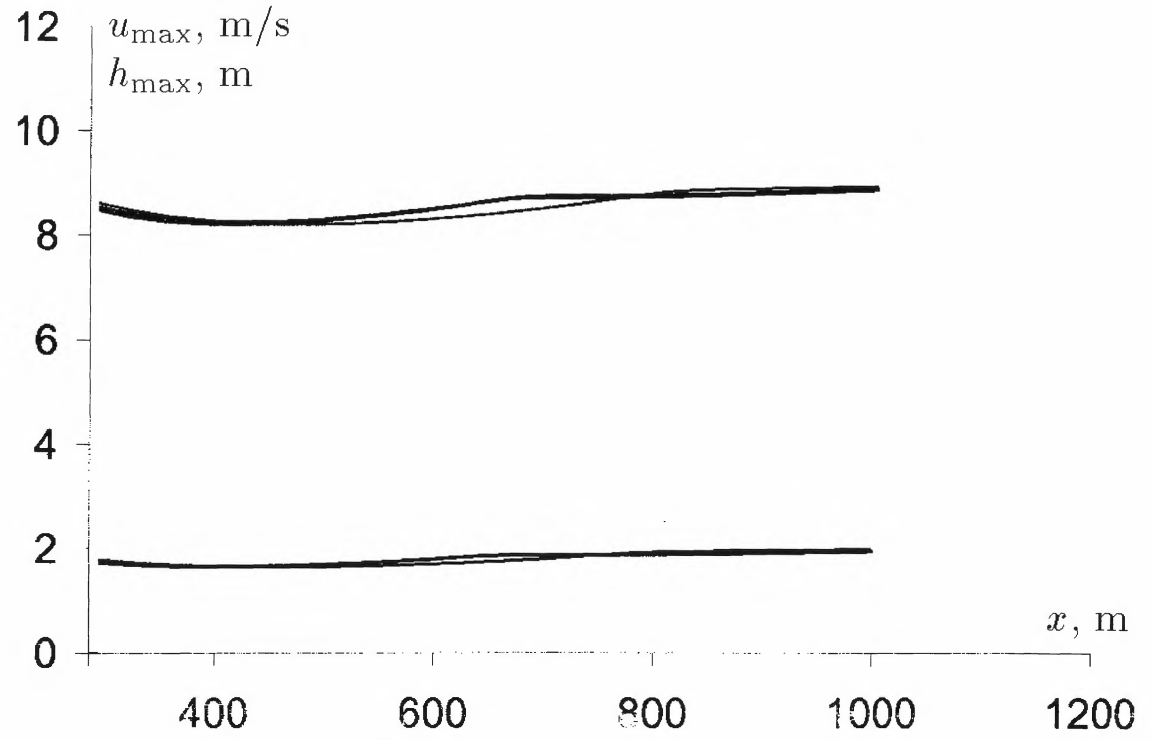

Fig.9. Dependence of the maximum values of the flow depth (lower curves) and flow velocity (upper curves) on the front coordinate at various entrainment laws. The length of the entrainment zone is the same in all variants. For the values of the entrainment coefficient a see the text.

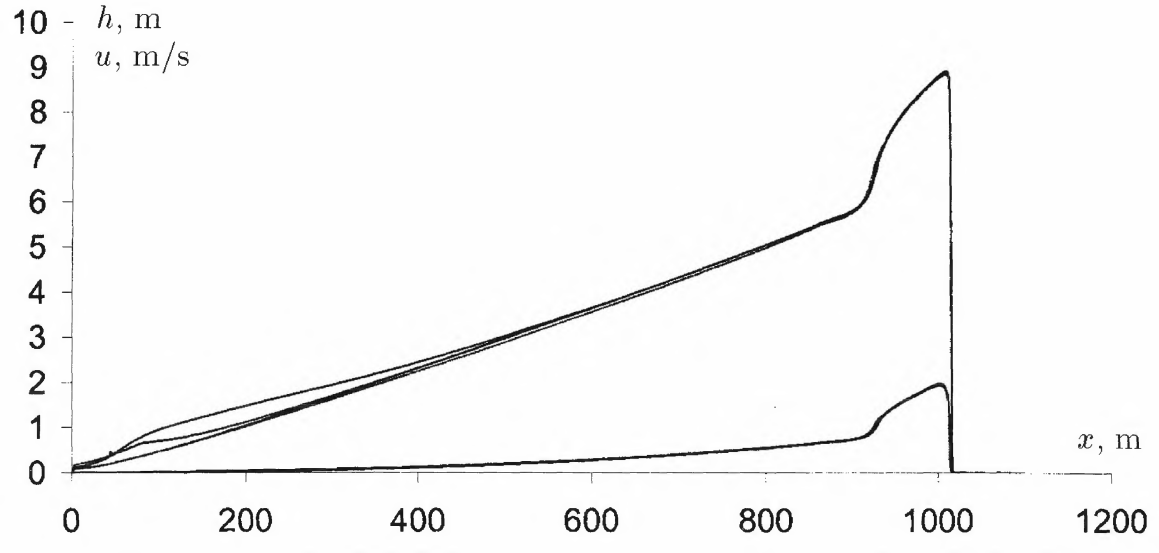

Fig.10. Flow depth (lower curves) and flow velocity (upper curves) distributions along the avalanche body at various entrainment laws. The length of the entrainment zone is the same in all variants.

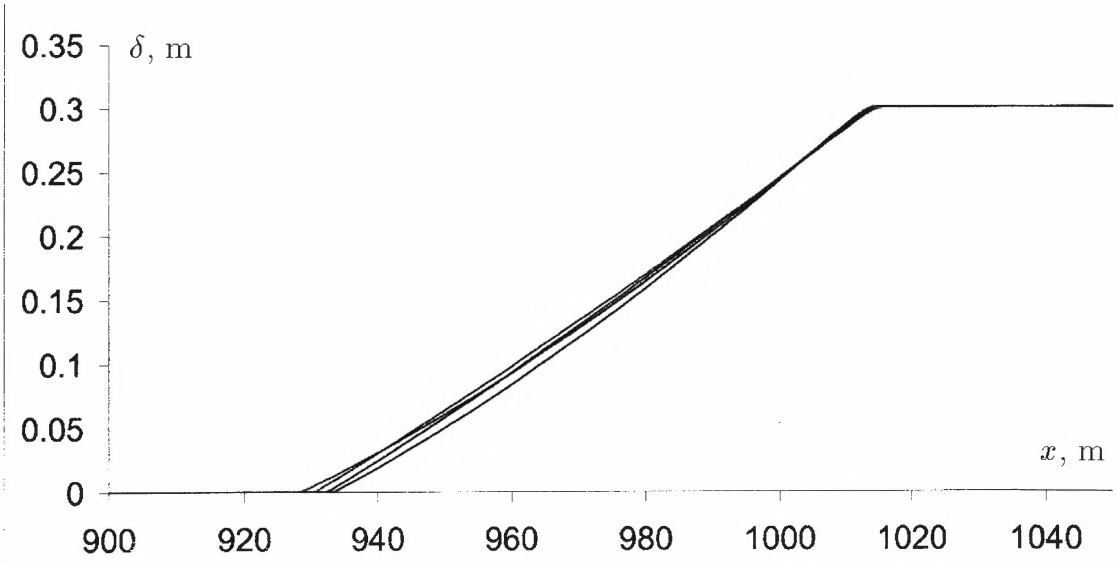

Fig. 11. The shape of the surface separating the snow cover (right) and the avalanche snow (left) at different entrainment laws for the same length of the entrainment zone.

The results presented in the last three Figures allow to hope that the correct values of avalanche dynamical parameters probably can be obtained by any entrainment law which is based on reasonable physical hypotheses.

References

Akijama J., and H.G. Stefan, 1988. Turbidity current simulation in a diverging channel. Water Resourses Res., **24**, No 2, 1988, 579-587.

Anderson R.S. and P.K. Haff. 1991. Wind modification and bed response during saltation of sand in air. Acta Mech., Supplementum 1. Aeolian Grain transport. 1, 21-51

.

Bakhvalov N.S. and M.E. Eglit, 1970. Study of the solutions of equations of motion of snow avalanches. Materialy Glyatsiologicheskikh Issled., 16, 7-14; English transl. in Glaciological Data, Report GD-16 (1984).

Bakhvalov N.S. and M.E. Eglit, 1973. Investigation of the one dimensional motion of a snow avalanche along a flat slope, Izv.Akad. Nauk SSSR Mekh. Zhidk. Gaza, 5, 7-14; English transl.in Fluid Dynamics, 8 (1973).

Bozhinskiy A.N., A.N. Nazarov, SApunov V.N., Chernouss P.A. The mathematical model of slushflow dynamics. Proccedings of the International Conference "Avalanches and related subjects", "Apatit"JSC, Kirovsk, 1996.

Bozhinskiy A.S. and A.N. Nazarov. Dvuhsloinaya model vodosnezhnogo potoka. Vestnik Mosk. Un-ta. Ser.1, Matematika. Mekhanika. No.5, 1998, 22-26

Bozhinskiy A.S. and A.N. Nazarov. Dinamika dvuhfasnogo selevogo potoka (Dynamics of a two-phase mud flow). Vestnik Mosk. Un-ta. Ser.1, Matematika. Mekhanika. No.5, 1999, 15-20.

Briukhanov A.V., Grigorian S.S., Miagkov S.M., Plam M.Ya., Shurova I. Ya., Eglit M.E., Yakimov Yu.L. 1967. On some new approaches to the dynamics of snow avalanches. Physics of Snow and Ice. Proceedings of Int. Conf. on Low Temperat. Sci., Sapporo, Japan, 1967, pp. 1221-1241

Demidov K.S. Mathemaical modelling of snow entrainment in avalanche dynamics. Diploma thesis. Moscow State University, Mech. And Math. Department, 2003.

Egizarov I.V. Dvizhenie neodnorodnih po krupnosti smesi nanosov (Motion of flows, which are inhomogeneous with respect to particles dimensions). Izvestiya AN Arm. SSR, ser. Techn. Nauk., vol 16, No.2-3, 1963, 41-50.

.

Ellison T.H., Turner J.S. 1959. Turbulent entrainment in stratified flows. J. Fluid Mech., 1959, **6,** No 3, 423-448

Eglit M.E., 1968. Theoretical approaches to the calculation of the motion of snow avalanches, in Itogi Nauki, Moscow, VINITI, pp. 60-97. English transl. in Glaciological Data, Report GD-16 (1984).

Eglit M.E., 1982. Calculation of the avalanches parameters in the runout zone, Materialy Glyatsologicheskikh Issled., (Data of Glaciological Studies) 53, 35-39. (Russian).

Margarita Eglit [M.E. Eglit], 1983. Some mathematical models of snow avalanches, in Advances in the Mechanics and the Flow of Granular Materials, M. Shahinpoor, editor, Vol. 2, Trans Tech Publ., Clausthal - Zellerfeld, and Gulf Publ. Co., Houston, Texas, pp. 577-588.

Eglit M.E., N.N. Vel'tishchev, 1985. Investigation of mathematical models of powder-snow avalanches, Materialy Glyatsologicheskikh Issled., (Data of Glaciological Studies) , 53, 116-120, (Russian).

Eglit M.E. 1998. Mathematical and physical modelling of powder snow avalanches in Russia. Annals of Glaciology, 1998, vol. 26 , pp. 281-284

Eglit M.E. 1998. Mathematical modelling of dense avalanches. Norwegian Geotechnical Institute. 1998, Publication No. 203, pp. 15-18.

Kulikovskiy A.G., M.E. Eglit, 1973. A two-dimensional problem on the motion of a snow avalanche along a slope with smoothly changing properties, Prikl. Mat. Mekh. 37 , 837-848; English transl.in J. Appl. Math. Mech. 37 (1973). 65-74 (Russian).

Grigorian S.S., M.E. Eglit, Yu.L. Yakimov, 1967. A new formulation and solution of the problem of the motion of a snow avalanche. Trudy Vycokogornogo Geofizicheskogo Instituta, 12 , 104-113. (Russian)

Grigorian S.S. and A.V Ostroumov. 1977. Matematicheskaya model sklonovih processov lavinnogo tipa (The mathematical model for slope processes of avalanche type). Scientific Report 1955. Moscow, Russia, Institute for Mechanics, Moscow State University.

Nazarov A.N. 1992. Opit primenenija dvuhsloinoi modeli dlja rascheta dvizhenija pilevih lavin (The experience in using the two-layer model for calculations of powder avalanches). Materialy Glyatsologicheskikh Issled., (Data of Glaciological Studies) 73, 73-79. (Russian).

Kulikovskiy A.G. and E.I.Sveshnikova, 1977. Model' dlya dvizheniya pilevoi snezhnoy lavini (A model for calculation of motion of a powder snow avalanche). Materialy Glyatsologicheskikh Issled., (Data of Glaciological Studies), 31, 74-80 (Russian).

Kato H., Phillips O.M., 1969. On the penetration of the turbulent layer into stratified fluid. J. Fluid Mech., 1969, **37**, No 4, 643-655.

Stolzenbach K.D., HarlemanD.R.F., 1971. An analytical experimental investigation of surface discharges of heated water. MIT Ralph M. Parsons Lab. Water Resour. and Hydrodyn. S.1, 1971, Techn. Rep. No 135(02139).

Onufriev A.T., 1967. Teoriya dvizheniya vihrevogo kolca pod deistviem sili tyazhesti (Theory of the vortex ring motion under gravity force). Prikl. Mech. Techn. Fis., 1967, No 2, 3-15.

Korolchenko A.Ya. and S.T. Tzarichenko, 1987. Mekhanism vzvihrenija otlozhenii goryuchih piley (Mechanism of the lifting of burnable dusts). Pozharnaya profilaktika tekhnologicheskih processov v promyshlennosti. M., 1987, 3-11.

Longuet-Higgins M.S., Turner J.S., 1974. . J. Fluid Mech., 1974, **63**, No 1, 1-20.

Wishmeier W.H. and D.D. Smith, 1965. Predicting rain fall erosion losses from cropland last of Rocky Mountains. Agric. Handbook, #282, Washington, 1965.

Smakhtin V.Yu. 1993. Fiziko-matematicheskoe modelirovanie vodno-erosionnih processov na rechnom vodosbore (Physics and mathematics modelling of water-erosion processes) Vodnie Resursi, 1993, v.20, No 6, 677-683.

Smerdon E.T. and R.P. Beasley, 1961. Critical Tractive Forces in Cohesive Soils. Agricultaral eng.,1961, v.12, No 1, 26-29.

Issler Dieter and Peter Gauer. 2003. Possible erosion Mechanisms in Snow Avalanches. Annals of Glaciology, in print

Sovilla, B. and P. Bartelt. 2002. Observations and modelling of snow avalanche entrainment. Natural Hazards Earth Systems Sci., **2**, 169-179.

Possible Erosion Mechanisms in Snow Avalanches

Peter Gauer and Dieter Issler*

Norwegian Geotechnical Institute, Postbox 3930 Ullevaal Stadion, N–0806 Oslo, Norway

ABSTRACT. Snow erosion and entrainment processes in avalanches are classified according to their mechanisms, the flow regimes in which they occur, and their spatial position within the avalanche. Simple, but process-specific models are proposed for erosion by impacts, abrasion, plowing, and blasting. On the basis of order-of-magnitude estimates, the first three mechanisms are clearly expected to be important. The fourth mechanism stipulates that the compaction of the snowcover ahead of the avalanche leads to the flow of escaping air just in front of the avalanche that may disrupt the snowcover and support formation of a saltation layer. The effects of this hypothetical mechanism resemble those of the plowing mechanism. All mechanisms depend strongly on the snow properties, but with plausible parameter values, erosion rates at or above the experimentally found rates are obtained. The entrainment rate of an avalanche is most often limited by the shear stress needed to accelerate the eroded snow to avalanche speed.

1 INTRODUCTION

A few centuries ago, snow avalanches were depicted as ever growing snowballs rolling down the mountain sides. One aspect of this naïve concept of avalanching has been vindicated by recent observations and measurements (Issler and others, 1996; Sovilla and others, 2001): The entrainment of snow has now been recognized as a major factor in the dynamics of avalanches. It must be concluded that perhaps the majority of medium to large avalanches double or even triple their mass from release to runout; in the track, the moving mass may be more than five times the original mass (Sovilla and others, 2001). From measurements with profiling radars (Dufour and others, 1999), erosion rates above $200\,\mathrm{kg\,m^{-2}\,s^{-1}}$ have been inferred (Issler, 2003) during the very rapid removal of up to 1 m of fresh snow at the avalanche front, while they were found in the range of $10\text{–}50\,\mathrm{kg\,m^{-2}\,s^{-1}}$ during episodes of more gradual entrainment in the head of dry-snow avalanches.

It has been clearly recognized for a long time that entrainment has two aspects: One concerns the breaking up of the snowcover into particles (ranging in size from snow grains to large blocks); this process is the main focus of this paper and will be termed *erosion*. The *erosion speed* w_e is the velocity (measured in the direction perpendicular to the ground) at which the surface of the intact snowcover is lowered due to erosion. The other aspect is the *entrainment* of the eroded snow into the flow through acceleration and possibly mixing. The *entrainment rate* $q_e = \rho_s \eta_e w_e$ ($\mathrm{kg\,m^{-2}\,s^{-1}}$) is the snow mass per unit time and unit area that is incorporated into the avalanche, where η_e is the fraction of the eroded snow that is eventually entrained. Entrainment distributes the avalanche momentum over a growing mass; the velocity diminishes unless there is sufficient net momentum gain from the gravitational and resistance forces, mf_G and mf_R (m is the avalanching mass). To see this, the momentum equation for an avalanche entraining mass from a resting snowpack is $m\,du_{av}/dt + u_{av}\,dm/dt = mf_G - mf_R$, or rewritten as equation of motion $du_{av}/dt = f_G - f_R - f_E$. The effect on the avalanche of the entrained mass is that of a pseudo force which causes a deceleration

$$f_E = \frac{u_{av}}{m}\frac{dm}{dt} = \frac{\rho_s}{\rho_{av}}\frac{\eta_e w_e u_{av}}{h_{av}} \,. \qquad (1)$$

Typical values for medium-size dry-snow avalanches on a 30° slope are $f_G = g\sin 30° \approx 5\,\mathrm{m\,s^{-2}}$, $u_{av} \approx 30\,\mathrm{m\,s^{-1}}$, flow depth $h_{av} \approx 1\,\mathrm{m}$, and ratio of avalanche density to snow cover density $\rho_{av}/\rho_s \approx 1\text{–}2$. For $\eta_e w_e$ of $0.05\text{–}0.10\,\mathrm{m\,s^{-1}}$, $f_E \approx (0.15\text{–}0.6) f_G$ is a substantial factor in the dynamics of the avalanche. In traditional avalanche models, these entrainment effects are subsumed in the velocity-dependent resistive forces and may contribute significantly to the wide scatter of back-calculated friction coefficients through the strong dependence of erosion and entrainment on topography, snow and avalanche properties.

This paper focuses on erosion mechanisms, but one should keep in mind that the entrainment rates that can be realized in snow avalanches are often limited, not by the work needed for eroding the snow, but by the large fraction of the available shear stress that is absorbed in the acceleration of the eroded snow.

The majority of dynamical (dense-flow) avalanche models that include snow entrainment do not model a specific entrainment process but add mass to the front of the avalanche at a rate specified by the user (Briukhanov and others, 1967; Brugnot and Pochat, 1981; Hungr, 1995; Sovilla and Bartelt, 2002; Sailer and others, 2002). A heuristic velocity-dependent entrainment function is used by Maeno and Nishimura (1979). Eglit (1983, 1998) assumes the entrainment rate to be proportional

*Mailing address: NaDesCoR, Promenade 129, CH–7260 Davos Dorf, Switzerland

to the velocity, in analogy to the entrainment of ambient fluid in buoyant plumes or jets. Grigorian and Ostroumov (1977) describe the erosion and entrainment process in terms of a compressive shock front propagating through the snow cover underneath the avalanche body, inclined at an angle $\alpha = \arctan(w_e/U)$ to the ground. The hydrostatic and dynamic pressures of the avalanche at the interface to the snowcover determine the compression of the eroded snow and the angle α, thus the entrainment rate. For powder-snow avalanches, an entrainment function derived from flume experiments (Parker and others, 1987) has been used by Fukushima and Parker (1990) and in adapted form by Gauer (1995) to dynamically determine the mass increase of the flow.

The objective of this paper is to infer which erosion mechanisms are most likely to occur in real avalanches and therefore should be studied in more detail, both experimentally and theoretically. We build on concepts sketched in (Issler and others, 2000) and draw on work on wear and fatigue in solid mechanics and on river bed erosion in hydraulics (see Sec. 2). In Sec. 5, we compare our order-of-magnitude estimates of the erosion speeds of the proposed mechanisms with the data from several measured avalanches.

2 EROSION PROCESSES IN OTHER PHENOMENA AND SPECIFIC FEATURES OF EROSION IN SNOW AVALANCHES

Rabinowicz (1995) distinguishes four main types of wear, namely adhesive wear, abrasive wear, corrosive wear, and surface fatigue wear, and a few special mechanisms. Among them, abrasive wear and possibly surface fatigue wear should be most relevant with regard to erosion in avalanches. Impact erosion is generally believed to be the dominant mechanism in blowing and drifting snow, and has also been conjectured (Issler, 1998) to dominate in the saltation layer of powder snow avalanches.

Abrasive wear occurs when hard asperities or particles slide over a softer surface, digging into it and plowing grooves. The snow particles in an avalanche undergo significant compression, by which their strength increases greatly; they are thus capable of indenting the usually much softer snowcover. Figure 7 of (Mears, 1980) gives evidence for abrasive processes at the base of the dense core of avalanches. Surface fatigue wear can be observed during repeated or continuous sliding over a surface. The sliding induces surface or subsurface cracks which eventually result in the breakup of the surface. This mechanism is often observed during spring time, when small avalanches break loose and start to erode the whole snowpack. The photo mentioned above also shows a crack from the sliding surface deep into the snowpack. Impact erosion occurs when particles impinge on the snowcover surface and, while moving along the surface, abrade material or initiate cracking of the surface. In Sec. 3, we present models for the abrasion and impact erosion in avalanches.

Three main erosion mechanisms are discussed in the fluvial hydraulics literature, see e. g. (Partheniades, 1965; Mehta, 1991; Zreik and others, 1998): Gradual erosion of single particles from the surface occurs already at shear stresses an order of magnitude smaller than the mechanical shear strength of the bed. (In non-cohesive granular beds, surface erosion is also observed to set in at shear stresses about one order of magnitude lower than the mechanical shear strength.) Under stresses comparable to the shear strength, entire chunks of material are ripped off the bed following failure along a deeply embedded plane (mass erosion). Finally, waves cause cyclic loading/unloading and shear stress; this may lead to fluidization of the surface layer and subsequent entrainment and mixing (Mehta, 1991).

The mechanisms observed in fluvial systems need not be directly relevant to (dense) snow avalanches because of the low density of air and the overwhelming effect of particle interactions with the snowcover. Nevertheless, there is presently an indication that mass erosion may also occur in snow avalanches (see Sec. 5), and fluidization of the snowpack immediately in front of the avalanche (due to excess pore pressure generated during snow compression) or inside a dilute head (as a consequence of underpressure at the snowcover surface) will be considered in Sec. 4.

In all erosion processes, an important factor is the strength of the eroded material. The snow strength generally grows substantially with depth as the density increases (except for weak layers) and will usually exceed the avalanche stress at some point. It is indeed often observed that erosion proceeds only to the interface between the fresh snow and the old snowpack (Issler and others, 1996; Sovilla and others, 2001). The strength of snow shows a varying strain-rate dependency. Abele and Gow (1975) performed strength tests under rapid uniaxial loading in which the strain rates were close to those expected in the case of an avalanche. The stress-strain curves indicate an initial phase of plastic behavior when the major principal stress exceeds the yield strength, Y. During the plastic collapse, the stress stays approximately constant until the strain reaches the critical plastic strain, ε_m, beyond which rapid strain-hardening occurs. Based on these tests, the following relations between the yield strength under compression, Y (in kPa) and the snowcover density, ρ_s (in $\mathrm{kg\,m^{-3}}$), and between ε_m and ρ_s, are derived to characterize the snowcover properties:

$$Y = 2.1 \cdot 10^{\frac{\rho_s - 100}{150}} \tag{2}$$

$$\varepsilon_m \approx \max(-7.0 \times 10^{-4} \rho_s + 0.268, 0)\,. \tag{3}$$

Some inferences can be drawn immediately from these properties: (i) The exponential dependence of snow strength on snow density leads to a strong variability of erosion speeds, (ii) the yield strength Y can be used in first estimates of erosion rates, but will lead to overestimates, and (iii) strain hardening will limit the densification to similar values in large and fast avalanches as in smaller ones, despite significantly higher stresses.

3 EROSION BY DIRECT PARTICLE-PARTICLE INTERACTION

Measurements with profiling radar (see Fig. 1) show relatively long episodes with gradual erosion at moderate rates, indicating the importance of snow erosion due to

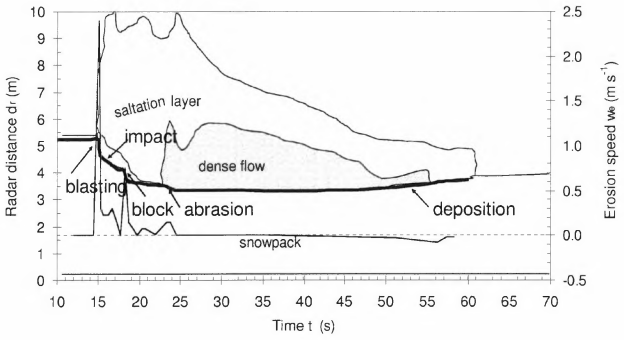

Figure 1: Radar distance of the snow surface from ground vs. time (thick line) and the corresponding erosion speed (thin line). The association to the different flow regimes is based on the radar echo intensity. Vallée de la Sionne test site, radar A2, event of 1999/02/25 (derived from radar plot in (Dufour and others, 1999)).

particles impinging on the snow surface within the saltation layer of avalanches. Each impact partly leads to a densification of the snowpack, partly to loosening of snow and its entrainment by the ambient flow. The impacting particle itself may rebound from the surface or penetrate it and get stuck. The particle sizes range from approximately 0.25 mm to a few decimeters.

At the base of the dense avalanche core, the particles are in continuous contact and slide over one another. Hard particles will plow grooves in the snowpack under their own weight and the overburden load. The snowcover is partly compacted and partly loosened and entrained by the avalanche. This process is commonly known as abrasion. In the following, we present a simple model for impact erosion and its adaptation to the abrasion mechanism.

3.1 Erosion due to particle impact

According to (Johnson, 2001, Chapter 11), the impact of snow particles on the snowpack during an avalanche can cover the whole range from elastic-plastic over fully plastic to extensive plastic flow and the onset of hydrodynamic behavior. For a first estimate of potential impact erosion speeds, we assume fully plastic impacts. We treat the avalanche particle as a rigid sphere with radius $r\,(= d_p/2)$, density ρ_p and mass $m_p = \rho_p V_p$ and the snowpack as a porous, rigid and perfectly plastic material with compressive yield strength Y. During impact the latter decelerates the particle and deflects it upwards (provided the particle is not completely submerged in the snowcover). If the impact angle α (measured from the x-axis and thus negative) is sufficiently small, the particle will not be stopped completely but will leave the snowcover again.

The equations of motion for the impinging particle read (neglecting aerodynamic drag):

$$\ddot{x} = g\sin\phi - \frac{P_L}{m_p}\left(\sin(\alpha+\beta) + \mu\cos(\alpha+\beta)\right)\ , \quad (4)$$

$$\ddot{z} = -g\cos\phi + \frac{P_L}{m_p}\left(\cos(\alpha+\beta) - \mu\sin(\alpha+\beta)\right)\ , \quad (5)$$

where ϕ is the slope angle, $P_L = p_d A_e$ is the force due to the plastic flow pressure acting in the line of motion and μP_L is the contribution of the Coulomb friction tangential to the motion. A_e is the projection of the instantaneous contact area onto the plane defined by $\overline{AB}$ and the y-axis (see Fig. 2).

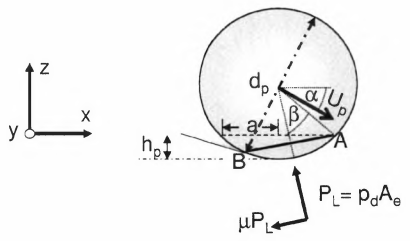

Figure 2: Rigid snow particle impacting onto the plastic snowpack. Adapted from (Rickerby and Macmillan, 1980)).

The plastic flow pressure is approximated as $p_d \approx c_p Y$. For solids, $c_p \approx 3$ in the fully plastic stage. c_p is close to unity in porous media in the fully plastic stage and for small indentations. With increasing indentation, c_p increases to about 3, reflecting strain hardening. Thus, snow as a porous medium might have a c_p similar to that of foams, for which Wilesa and others (1975) give

$$c_p = \left(1 - \frac{\left(\overline{AB}/(4r\varepsilon_m)\right)^3}{\left(1+\left(\overline{AB}/(4r\varepsilon_m)\right)^2\right)^{3/2}}\right)^{-1} \quad (6)$$

for the case of an indenting sphere. The critical strain ε_m is given in Eq. 3. Further hardening of the snowpack due to dynamic flow effects is disregarded. The total volume V_e of the impact crater is

$$V_e = \int_0^{t_i} \mathbf{A}(t)\cdot\mathbf{U}_p(t)dt\ , \quad (7)$$

where $\mathbf{A}(t)$ is the penetrating cross-sectional area perpendicular to the line of motion, $\mathbf{U}_p(t)$ is the instantaneous velocity of the particle, and t_i is the duration of the impact. For a full description of the geometric relations we refer to (Rickerby and Macmillan, 1980). To calculate the total crater volume, (4) and (5) are solved numerically. The impact angle α_i, needed as an initial condition, depends on the ratio between terminal velocity of the particle, W_f, and avalanche velocity and might also be influenced by the turbulence. The number of particle impacts per unit time and unit area, N_i, can be approximated by

$$N_i \approx \frac{cW_f\cos\phi}{2V_p}\ ; \quad (8)$$

here $c/2$ is the volume concentration of particles in downward motion. The erosion speed due to particle impacts can now be written as

$$w_{ei} = N_i V_e \quad (9)$$

Each particle impact causes a momentum transfer $m_p(U_{p1\|} - U_{p0\|})$ from the avalanche to the snowpack even without entrainment, where $U_{p0\|}$ and $U_{p1\|}$ are the mean particle velocities parallel to the surface before

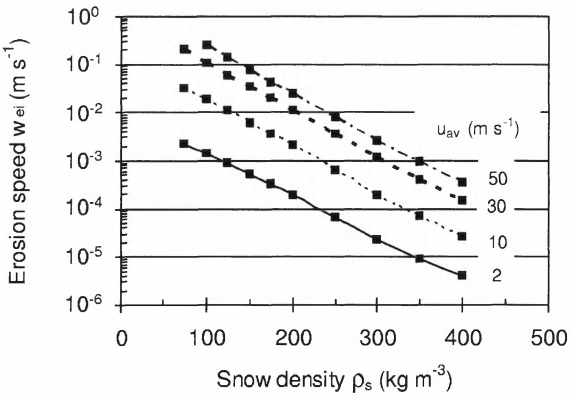

Figure 3: Impact erosion speed vs. snow density, with the avalanche velocity as parameter; $\rho_{av} = 10\,\mathrm{kg\,m^{-3}}$; $d_p = 0.25\,\mathrm{mm}$; $\phi = 0°$.

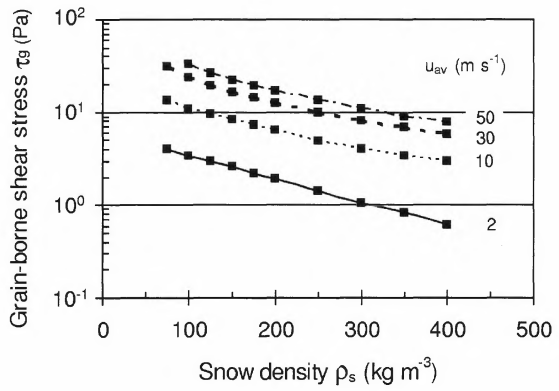

Figure 4: Shear stress due to momentum loss of impacting particles vs. snow density, with the avalanche velocity as parameter; $\rho_{av} = 10\,\mathrm{kg\,m^{-3}}$; $d_p = 0.25\,\mathrm{mm}$; $\phi = 0°$; $U_{pe\|} = 0$.

and after the impact, respectively. Some of this momentum is returned to the flow by the fraction η_{ei} of ejected particles (with mean initial velocity $U_{pe\|}$) that are eventually entrained by the avalanche. The difference of the two contributions is the so-called grain-borne shear stress:

$$\tau_g = N_i m_p (U_{p1\|} - U_{p0\|}) + \eta_{ei} w_{ei} \rho_s U_{pe\|} \,. \qquad (10)$$

Figures 3 and 4 plot the calculated impact erosion speeds and grain-borne shear stresses due to particle impact versus the snow density. The essentially exponential dependence on the snow density is a result of Eq. 2. Another controlling factor is the impact angle. The erosion speed grows with increasing impact angle and thus with particle size because larger particles have a higher fall velocity W_f and thus tend to impact under a steeper angle. The dependence on the impact angle also influences the relationship between avalanche speed and erosion speed because the impact angle decreases with increasing avalanche speed. If the impact angle is artificially kept constant in the simulations, $w_{ie} \propto u_{av}^n$, with $n > 2$, but if it is made to vary according to $\alpha_i = -\arctan(W_f \cos\phi / u_{av})$, one finds $1 < n < 2$ (for $d_p = 25\,\mathrm{mm}$, $n \approx 1.5$). Note that the growth of the erosion speed with increasing impact angle is sharply limited by the maximum angle (depending on the impact velocity) beyond which the particle gets absorbed in the snowpack.

3.2 Abrasion

The methods developed for impact erosion may also be applied to estimate the abrasion speed. Consider a snow particle indenting the snowpack and sliding parallel to the surface ($\alpha = 0$). The particle equations of motion (4) and (5) are supplemented with an overburden load L and the traction exerted by the avalanche:

$$\ddot{x} = \left(g + \frac{L}{m_p}\right)\sin\phi - \frac{P_L}{m_p}(\sin\beta + \mu\cos\beta) + \frac{F_D}{m_p}, \qquad (11)$$

$$\ddot{z} = -\left(g + \frac{L}{m_p}\right)\cos\phi + \frac{P_L}{m_p}(\cos\beta - \mu\sin\beta)\,. \qquad (12)$$

L is determined by the effective pressure transferred through the particle lattice within the avalanche. We assume that each snow block at the interface carries the load $L = \rho_{av} g h_{av}/N_b$, with N_b the number of blocks per unit footprint area. For simplicity, the traction is expressed as a drag: $F_D \approx \frac{C_D}{2}\rho_{av}\pi r^2 |u_{av} - U_p|(u_{av} - U_p)$, with U_p the velocity of the sliding particle. The drag coefficient, C_D, depends on the flow regime.

In the present case of surface-parallel sliding, the left-hand side of (12) vanishes, and the plastic-flow pressure times the z-component of $\mathbf{A}_e$ balance the load due to the particle and its overburden. At the same time the plastic-flow pressure times the x-component of $\mathbf{A}_e$ acts as the retarding force in (11). Summing the retarding forces over all N_b blocks gives the frictional stress, τ_f, acting at the bottom of the avalanche. As long as the slope-parallel component of gravity and the drag force acting on the blocks together equal or exceed the retarding force, the blocks plow through the snowcover and erode it. If the retarding force exceeds the driving forces, the blocks decelerate and the drag force grows accordingly; however, if the maximum drag force is insufficient to overcome the retarding force on the block, deposition begins. The total shear stress at the interface between the plowing blocks and the overriding layer of the avalanche also includes the drag forces on the eroded snow that accelerate it to the avalanche velocity during mixing.

The material eroded by one block per unit time is proportional to the penetrating cross-sectional area, A, perpendicular to the flow direction and the mean velocity of the block, $\overline{U}_p$. Hence, the erosion speed due to abrasion is

$$w_{ea} = N_b A \overline{U}_p \,. \qquad (13)$$

Figures 5 and 6 show the simulated abrasion rates and frictional stresses, τ_f, as functions of the snowcover density. The parameters used are given in Table 1. The avalanche speed, u_{av}, is not treated as a dynamical variable here but as an externally prescribed constant. The determining factors for the abrasion speed are the snow density (via the exponential dependence of strength on density) and the effective overburden of the particles at the base. There is only a weak particle-size dependence. The shear stress between the plowing particles and the snowcover diminishes with increasing snow

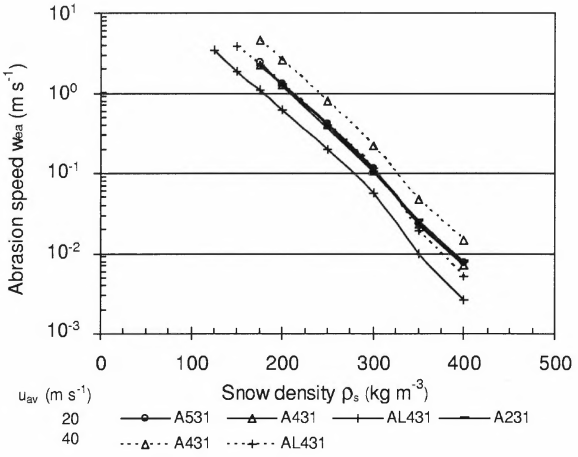

Figure 5: Abrasion speed vs. density of the snowpack for the parameter sets listed in Table 1. Avalanche velocity is treated as an externally prescribed constant; erosion rates in real avalanches would be significantly lower.

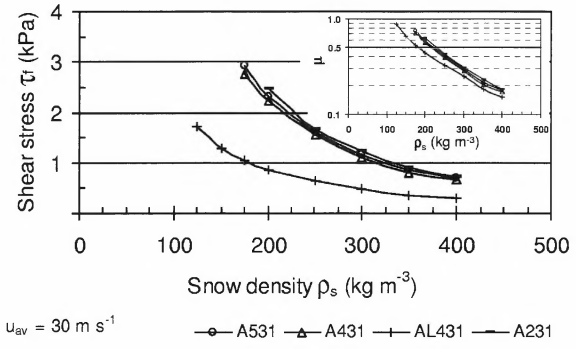

Figure 6: Shear (frictional) stress due to abrasion vs. snow density for the parameter sets listed in Table 1. The inset shows the corresponding friction coefficient μ.

strength because the grooves strongly diminish in depth and the slope-parallel component of the resistance force at the interface becomes rather small while the slope-perpendicular component remains constant.

4 EROSION MECHANISMS AT THE AVALANCHE FRONT

In avalanches, aerodynamic entrainment of the snowcover might play a role just in front of the avalanche where ambient air is rapidly displaced by the approaching avalanche. This phase may last about 1–2 s in a developed powder snow avalanche. Estimates using the widely used excess shear-stress approach for the erosion speed (see e.g. Anderson and Haff, 1991) show that the erosion speeds are in the range of 0–0.003 m s^{-1} under the most favorable assumptions and thus negligible.

4.1 Fluidization of the snowpack by pore air displacement

Excess pore-water pressure can fluidize river beds and thus significantly affect the erosion process (Simon and Collison, 2001). An air pressure gradient can also arise at the front of snow avalanches where (i) the rapid flow of the dilute snow–air mixture causes a pressure drop above the snowcover, or (ii) the snowcover is rapidly compacted by the avalanche and pore air tries to escape through the undisturbed snowcover.

Table 1: Compilation of parameters used in the simulation of abrasion. d_p: particle diameter; ρ_p: particle density; ρ_{av}: avalanche density; h_{av}: avalanche flow depth; μ: apparent dry-friction coefficient of the particle; slope angle $\phi = 0°$.

Simulation	d_p [mm]	ρ_p [kg m^{-3}]	ρ_{av} [kg m^{-3}]	h_{av} [m]	μ [—]
A531	100	450	200	2	0.1
A431	10	500	200	2	0.1
A231	1	750	200	2	0.1
AL431	10	500	200	1	0.1

The first-mentioned situation is expected to occur during the passage of a dilute avalanche front, in which the pressure drop is $\Delta p \sim \frac{1}{2}\rho_{af}u_{af}^2$. ρ_{af} and u_{af} are the density and avalanche speed at the front. This pressure drop has been measured in experiments with ping-pong balls (McElwaine and Nishimura, 2001). Due to this drop, a pressure difference between the interior of the snowpack and the surface builds up during a short but finite time, t_f, of front passage, persists for a while and vanishes gradually. A given volume of snow becomes fluidized when the force due to the flow of escaping air exactly balances the net force due to gravity and strength. Taking for simplicity a hexahedral control volume with length l ($\sim u_{av}t_f$) and width w, and assuming tensile strength Y_t and shear strength Y_s, fluidization should occur to a depth

$$d_e = \frac{\Delta p(d_e, t/t_r) - Y_t}{\rho g \cos\phi + 2\frac{l+w}{lw}Y_s} \,. \tag{14}$$

This is an implicit equation for d_e, showing that simultaneous fluidization of as large an area as the pressure gradient permits is most advantageous. The effectiveness in fluidizing the top of the snowcover moreover depends crucially on the ratio of the build-up time, t_f, to the pressure relaxation time, t_r ($\approx \nu d_e^2/(kRT)$, where k is the intrinsic permeability of the snowpack, ν the kinematic viscosity of air, R the specific gas constant of air and T the temperature). The erosion speed w_{ef} is on the order of d_e/t_f. At present it is unclear whether fluidization due to pressure drop can occur at the front of the saltation layer, as no firm data from snow avalanches is available. Estimates of the pressure drop required for fluidizing snowcovers with density from 75 to 200 kg m^{-3} yield velocities in the range from 20 to 75 m s^{-1} if a (powder-snow) avalanche density of 5 kg m^{-3} is assumed. However, even if complete fluidization is not reached, this mechanism will contribute to the weakening and destruction of the snowpack and is a candidate mechanism for the blast-like erosion seen in Fig. 1.

The second mechanism involves rapid (adiabatic) compression of the snowcover by the weight of the avalanche flowing over it or plowing into it. Snow compaction from a density ρ_{s0} to ρ_{s1} leads to a pore-air

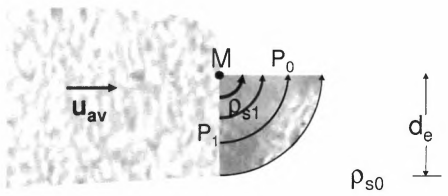

Figure 7: Schematic representation of air flow through the snowpack ahead of the moving avalanche.

pressure rise

$$\Delta p = p_0 \left[\left(\frac{\rho_i - \rho_{s0}}{\rho_i - \rho_{s1}} \right)^{1.4} - 1 \right] , \qquad (15)$$

where p_0 is atmospheric pressure. Some of the pore air is pressed at high speed through the snowcover ahead of the avalanche front in a narrow zone, the length of which is comparable to the erosion depth at the front, i. e., at most a few meters and probably less. The pressure gradient is non-uniform and depends strongly on the geometry of the avalanche head; it should be greatest where the avalanche front intersects the snowcover. Depending on the snow strength and the pressure difference Δp, there is a limiting depth d_e below which the pressure gradient is too weak to fluidize the snowcover.

To illustrate the mechanism, we approximate the streamlines ahead of the (slope-perpendicular) avalanche front by concentric quarter-circles about the intersection of the avalanche front and the snowcover (point M in Fig. 7). From the balance of the moments of the gravity, pressure and shear forces, the erosion depth is estimated as

$$d_e = \frac{3}{2} \frac{\Delta p - \pi Y_s}{\rho_s g (\cos\phi - \sin\phi)} . \qquad (16)$$

The mean erosion speed according to Eq. 16 is equal to u_{av}. However, this estimate implies that the penetration depth of the avalanche front adapts to potential erosion depth. For a more comprehensive approach see discussion in Sec. 6 and the following section.

4.2 Plowing

It has been observed that the front of dense-flow avalanches plows through the snowpack and entrains large quantities of snow thereby, even at moderate velocities. Such plowing implies that the snowpack undergoes strong, rapid shearing and compaction just ahead of the avalanche. We expect the length of this area to be about 1 to 3 m. Part of the snowcover is compacted and overflowed by the avalanche (which may ultimately abrade it). The upper part of the plowed snowcover layer is pushed onto the avalanche front where it may pile up or get advected to the avalanche body, possibly being comminuted and suspended.

In order to describe the compaction and erosion process, consider a prismatic control volume bounded by three surfaces (see Fig. 8). Surface b forms the shear surface, surface c is the boundary towards the avalanche, and surface a forms the boundary to the air flow above.

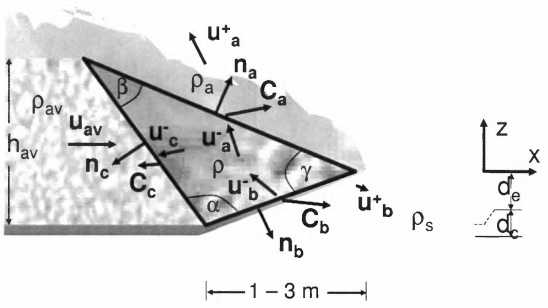

Figure 8: Schematic representation of the head region of a dense-flow avalanche plowing through the snowpack. The triangle represents the control volume for which the jump conditions have to be solved. d_e indicates the erosion depth and d_c the part of the snowpack which will be compacted by the avalanche.

Across each of these surfaces, the jump conditions for mass and momentum must be fulfilled:

$$[\![\rho_r (\mathbf{u_r} - \mathbf{C_r}) \cdot \mathbf{n_r}]\!] = 0 , \qquad (17)$$

$$[\![\rho_r \mathbf{u_r} (\mathbf{u_r} - \mathbf{C_r}) \cdot \mathbf{n_r}]\!] - [\![\mathbf{t_r} \cdot \mathbf{n_r}]\!] = \mathbf{0} , \qquad (18)$$

where r indicates the surfaces a, b and c, respectively. $\mathbf{C}_r$ is the velocity of the (non-material) surfaces, and $\mathbf{t} \cdot \mathbf{n}$ is the normal stress onto the respective surface. The erosion depth d_e is strongly influenced by the normal stresses at the shear plane b. Here, the determining quantities are the compressibility of the snowpack and the overburden load from the avalanche head. Across the interface a, excess pore-air pressure generated by the compaction may play a role in supporting the development of the saltation layer on the upper surface of the dense core. Along the surface c, dispersive pressure may come into play. Further study of this problem is needed in order to obtain approximate solutions that can be compared to measurements.

Two entrainment models have been published that contain elements of the analysis suggested above: Grigorian and Ostroumov (1977) consider only one jump surface underneath the dense core; the entire entrainment is into the dense flow. The model by Sailer and others (2002) distinguishes between entrainment into the dense flow and into the suspension layer, but the jump conditions for the momentum are not evaluated and hence neither the erosion depth nor the ratio between entrainment at the bottom and at the top can be determined dynamically in their model.

5 COMPARISON WITH EXPERIMENTS AND FIELD OBSERVATIONS

Figure 1 shows the time evolution of the snowcover and flow depths as well as the erosion speed for the giant avalanche of 1999/02/25 at the Vallée de la Sionne test site in Switzerland. The plot is derived from data from a profiling radar located in the upper track (Dufour and others, 1999). The association of different areas in the avalanche with different flow regimes is based on the radar echo intensity; the suspension layer is invisible to the FMCW radar. The preliminary analysis of simultaneous Doppler radar measurements indicates velocities

on the order of $50\,\mathrm{m\,s^{-1}}$ at that point. The snow density was in the range 170–300 $\mathrm{kg\,m^{-3}}$. Approximately 0.7 m of snow are eroded virtually instantaneously at the leading front of the saltation layer, corresponding to an erosion speed of about $2.5\,\mathrm{m\,s^{-1}}$. In the following 5 s, erosion is more gradual, with erosion speeds decreasing from $0.25\,\mathrm{m\,s^{-1}}$ to near zero. During this time, an approximately 0.5 m thick layer of higher echo intensity can be seen, indicating a higher density and/or larger block size than in the upper reaches of the saltation layer. The second peak at 18–19 s in the erosion speed curve is tentatively interpreted as a snow block ripped out of a stronger layer. After that, the average erosion speed is about $0.05\,\mathrm{m\,s^{-1}}$ and no denser bottom layer is found until the dense core arrives. During the first second of its passage, the erosion speed jumps back to about $0.15\,\mathrm{m\,s^{-1}}$, but no further erosion is observed afterwards. Snow deposition takes place during the last 10 s of the passage of the dense part. Over the entire avalanche passage (lasting about 45 s), the mean erosion speed is $0.05\,\mathrm{m\,s^{-1}}$.

This recording suggests that both a very rapid plowing or fluidization mechanism at the front and gradual, impact-driven erosion in a relatively dilute avalanche head (tentatively identified as the saltation layer, with an estimated density around $100\,\mathrm{kg\,m^{-3}}$) may occur in large dry-snow avalanches. Additional radar recordings from the same site lend support to this conclusion (Dufour and others, 1999), although the ratio of the masses entrained by the different mechanisms varies considerably. A much more detailed analysis combining data from different sensors and comprising all avalanches measured at the test site is needed for correlating these differences with the dynamics of the avalanches.

For a number of small avalanches, Sovilla and others (2001) carried out a systematic study of the mass balance at the avalanche test site Monte Pizzac at Arabba in the Dolomites, Italy. Additional information on these avalanches is contained in (Sommavilla and Sovilla, 1998; Sovilla and Bartelt, 2002). Perhaps the best described among these events is that of 1997/12/21. The most reliable data for the estimation of the erosion speed are given at the pole no. 1 (position A) at 2024 m a. s. l. For the event of 1999/03/05, the width of the track swept by the avalanche had to be estimated. Both events are classified as dry dense-flow avalanches. Table 2 summarizes the measurements for these two events at pole no. 1 and gives the calculated mean erosion speed and the inferred avalanche density. The avalanche density of the 1997/12/21 event, inferred from the volume and mass estimates, compares quite well with the reported pressures if $p_{\mathrm{impact}} \approx \rho_{av} u_{av}^2$ is assumed for the 10 cm diameter load cells used at Monte Pizzac. The pressure sensor at 1 m above ground was just above the snow surface and thus should reflect the pressure in the flowing part of the avalanche.

Field observations on a small to medium avalanche in Seewis, Grisons (Issler and others, 1996), where the powder-snow part separated from the dense flow at a sharp turn of the gully, allow to estimate the erosion speed within the saltation layer, provided several reasonable but not directly verifiable assumptions are made. The new snow layer had a depth of 0.7–1 m and a density of approximately $120\,\mathrm{kg\,m^{-3}}$. Tracers (mostly fir needles and twigs) in two snow pits excavated at different locations showed that the new snow layer was completely eroded at one location and reduced to 10–20 cm at the other; it remains an open question whether old snow was eroded at the location of the first snow pit.

Table 2: Compilation of measurements at pole no. 1 in the Monte Pizzac path, after (Sommavilla and Sovilla, 1998; Sovilla and others, 2001; Sovilla and Bartelt, 2002), and calculated erosion speeds and avalanche densities at the same point.

Event	1997/12/27	1999/03/05
Measurements		
Velocity	$24\,\mathrm{m\,s^{-1}}$	$19\,\mathrm{m\,s^{-1}}$
Time of passage	9.25 s	12.7 s
Mean flow depth	1 m	1 m
Total mass	365 t	200 t
Entrained mass / area	$150\,\mathrm{kg\,m^{-2}}$	—
Pressure at 1.0 / 1.8 m	80 / 50 kPa	—
Snowcover density	$140–290\,\mathrm{kg\,m^{-3}}$	$160–320\,\mathrm{kg\,m^{-3}}$
Inferred avalanche parameters		
Length	220 m	220 m
Width	13.5 m	≈ 10 m
Erosion rate (mean)	$17.1\,\mathrm{kg\,m^{-2}\,s^{-1}}$	$8.2\,\mathrm{kg\,m^{-2}\,s^{-1}}$
Erosion speed (mean)	$0.075\,\mathrm{m\,s^{-1}}$	$0.034\,\mathrm{m\,s^{-1}}$
Avalanche density	$120\,\mathrm{kg\,m^{-3}}$	$90\,\mathrm{kg\,m^{-3}}$

In the first pit location, the deposit depth measured 30–50 cm and the largest particles had diameters up to 40 cm; in the second, the deposit depth varied between 5 and 10 cm and the largest snow particles had the size of an egg. Depending on the assumed deposit density (measurements are not available), mass deposition from the tail of the powder-snow avalanche was comparable to the erosion in the head at snow pit no. 1, but clearly less at location no. 2 despite the less violent erosion there. This can be explained by the location of the snow pits: Pit no. 2 is close to the side of the path, but in fairly steep terrain, so the velocities were generally lower than in the center of the track, but even the dilute tail is expected not to decelerate. Pit no. 1, in contrast, is in the center of the powder-snow avalanche path, but further downstream in less steep terrain shortly after the cloud had to climb about 20 m along the steep side wall of the gully turn.

From numerical simulations, the front velocity and the length of the powder snow avalanche are estimated as $35\,\mathrm{m\,s^{-1}}$ and 300 m, respectively. If we further assume that erosion occurred only in the front half and deposition only in the tail half, the mean erosion speed was around $0.2\,\mathrm{m\,s^{-1}}$ at pit no. 1 and $0.1\,\mathrm{m\,s^{-1}}$ at pit no. 2. Similar erosion speeds are inferred in the run-up area of the large 1999/02/10 avalanche at Vallée de la Sionne where almost the entire snow pack of 2 m depth was eroded near the shelter (Dufour and others, 1999) and the deposit depth varied from 0.2 to 2 m over distances of 10–20 m.

Table 3 summarizes the predicted contributions to the erosion speeds from fluidization, impact erosion and

Table 3: Simulated erosion speeds in $m\,s^{-1}$ for the four events described in the text. The assumptions for the density of the Vallée de la Sionne avalanche (VdlS) of 1999/02/25 are: leading part of the saltation layer (SL), $90\,kg\,m^{-3}$; dense part (DF), $200\,kg\,m^{-3}$. For the 1995/01/11 avalanche near Seewis, a density of 5–$10\,kg\,m^{-3}$ was assumed for the powder snow part. Values in parentheses indicate the contribution of the respective mechanism to the total erosion depth.

Mechanism	VdlS	Monte Pizzac		Seewis
	99/02/25	97/12/27	99/03/05	95/01/11
Fluidization	13.0	—	—	9.1
	(1.34 m)			(1.0 m)
Impact	0.23 (SL)	0.08	0.02	0.03–0.06
Plowing	?	?	?	—
Abrasion	0.16 (DF)	0.06	0.02	—

abrasion in the four avalanches discussed in Sec. 5. We have not developed a dynamical model for the plowing mechanism yet, so no predictions can be made; it is very likely, however, that the powder-snow part of the Seewis avalanche did not erode by plowing. Considering the uncertainty and incompleteness of the measurements, the agreement between the measured (or inferred) entrainment speeds and the model predictions is encouraging. For the two events at Monte Pizzac, simulated abrasion and impact erosion speeds are similar; it is quite conceivable that the front of those avalanches was more dilute than the main body and that impact erosion dominated in the front, abrasion in the body. For the 1999/02/25 event at Vallée de la Sionne, the maximum impact erosion speed is approximately $1.3\,m\,s^{-1}$ for reasonable assumptions. This is about half the erosion speed inferred from the radar measurement, thus the observed erosion during the front passage cannot be explained by impact erosion alone. The field observations from Seewis also indicate that either our estimates are too low, or an additional mechanism is operating; fluidization is an obvious candidate but more work is needed to make testable predictions.

6 DISCUSSION AND CONCLUSIONS

In this exploratory study, five potential mechanisms for erosion in snow avalanches have been identified. Surface fatigue wear may occasionally occur as localized mobilization of a deeper layer in the snowpack, but may be neglected at present. Impact erosion and abrasion have many common aspects, but the conditions for their occurrence are quite different, especially with regard to the avalanche density. Neither mechanism has been observed directly, but grooves and impact holes have been seen in several cases. Under the mechanical conditions in the saltation layer (relatively low density, large blocks, high velocities), impact erosion appears quite unavoidable. It is conceivable that the saltation layer often erodes the snowcover down to a hard layer of old snow on which the snow blocks in the bottom layer of the dense core are quickly comminuted and abrasion becomes negligible.

The plowing and fluidization mechanisms may be more intimately connected than our crude and incomplete treatment in Sec. 4 suggests; perhaps they should be regarded as two aspects of a single phenomenon. After all, plowing represents the most efficient mechanism for generating a strong pressure gradient in the snowcover immediately in front of the avalanche. Both processes are subjected to feedback mechanisms that require further study and need to be formulated mathematically.

We wish to emphasize two points: First, abrasion, impact erosion, plowing and fluidization all have the potential to contribute strongly to entrainment under certain conditions, and they do so in different locations of the avalanche. Thus they all need to be studied further and eventually incorporated into a comprehensive entrainment/deposition model for avalanche simulation codes. Second, when soft fresh snow is abundant—i. e., under the conditions that favor large, catastrophic mixed avalanches—acceleration of the eroded snow and mixing with the avalanche is the limiting factor. The resistance of the snowcover against erosion becomes important if the snowcover is old and/or relatively warm and humid.

Further progress in the modeling of erosion and entrainment requires not only dedicated theoretical studies of the candidate mechanisms, but also a series of experiments that shed light on the unresolved questions. Some of the experiments are best carried out in the laboratory (or on an outdoor chute), others require a well-equipped full-size test site. In the authors' opinion, the most promising approaches are:

- *High-resolution close-up videos of avalanches in (natural) chutes*, taken from the side, will help distinguish between different erosion mechanisms.
- *Pore pressure measurements.* Such measurements have been carried out at the bottom of debris flows (Iverson, 1997) and should also be feasible in snow avalanches, preferably at several levels on an instrument support structure.
- *Particle-impact experiments* with snowballs of various sizes and hardness, different velocities, and impact angles onto a snow surface of known properties.
- *Direct measurements of the erosion rate.* In real avalanches, the erosion rate is usually limited by the large force needed to accelerate the eroded snow. It might be possible to design laboratory experiments in which the "avalanche" body is pulled across the snowcover at constant speed, irrespective of the entrainment rate and the force needed.
- *Tracer experiments* to determine the degree of mixing of eroded snow into the avalanche. In chutes or small avalanche tracks, various kinds of tracers could be deployed in different locations along the track and at various depths in the snowcover before the avalanche release.
- *Measurement of velocity profiles and density.*

More than one erosion mechanism has to be included in a satisfactory avalanche model: The measurements available so far indicate clearly that entrainment takes place both at the front and along the bottom of the

avalanche body. The flow regime determines which mechanism is dominant; plowing and abrasion require a dense, solid-like avalanche body, perhaps a plug flow, whereas impact erosion seems to be limited to more dilute flows (probably identifiable with the saltation layer). We anticipate a delicate interplay between erosion by fluidization and the avalanche density: The pressure gradient necessary for fluidization is produced only if the avalanching snow is sufficiently hard, dense and impermeable, but the fluidization process itself has the tendency to dilute the avalanche front.

The erosion models presented here were not designed for direct use in any numerical code. Once the mechanisms are better understood, they have to be formulated in terms of the dynamical variables and parameters of the respective model. In view of the flow-regime dependence discussed above, advanced avalanche models explicitly recognizing different flow regimes—e. g., multilayer models or models with dispersive pressure regulating the local density—are to be preferred over simple two-parameter models as platforms for realistic entrainment modules.

ACKNOWLEDGMENTS

This work was funded through NGI's SIP programs "Avalanche research" and "Offshore Geohazards" and through the EU Project SATSIE (Avalanche Studies and Model Validation in Europe), Contract no. EVG1-CT2002-00059. We have received valuable information through enjoyable discussions with E. Adams, M. Barbolini, R. E. Brown, M. E. Eglit, H. Gubler, M. Schaer, J. Schweizer, and B. Sovilla. We also wish to thank our colleagues of the avalanche group at NGI for their interest and discussions.

REFERENCES

Abele, G. and A. J. Gow. 1975. Compressibility characteristics of undisturbed snow. CRREL Report 336. Hanover, New Hampshire, U.S.A., U.S. Army Cold Regions Res. and Engrg. Laboratory.

Anderson, R. S. and P. K. Haff. 1991. Wind modification and bed response during saltation of sand in air. *Acta Mechanica (Suppl.)*, **1**, 21–51.

Briukhanov, A. V., S. S. Grigorian, S. M. Miagkov, M. Ya. Plam, I. Ya. Shurova, M. E. Eglit, and Yu. L. Yakimov. 1967. On some new approaches to the dynamics of snow avalanches. *In* Ôura, H., editor, *Physics of Snow and Ice, Proc. Intl. Conf. Low Temperature Science, Sapporo, Japan, 1966. Vol. I, Part 2.* Sapporo, Hokkaido, Japan, Institute of Low Temperature Science, Hokkaido University, pages 1223–1241.

Brugnot, G. and R. Pochat. 1981. Numerical simulation study of avalanches. *J. Glaciol.*, **27**, 77–88.

Dufour, F., U. Gruber, D. Issler, M. Schaer, N. Dawes, and M. Hiller. 1999. Grobauswertung der Lawinenereignisse 1998/1999 im Grosslawinenversuchsgelände Vallée de la Sionne. Interner Bericht 732. CH–7260 Davos Dorf, Switzerland, Eidg. Institut für Schnee- und Lawinenforschung.

Eglit, E. M. 1983. Some mathematical models of snow avalanches. *In* Shahinpoor, M., editor, *Advances in the Mechanics and the Flow of Granular Materials*, volume II. Clausthal-Zellerfeld, Germany, Trans Tech Publications, 1st edition, pages 577–588.

Eglit, M. E. 1998. Mathematical and physical modelling of powder-snow avalanches in Russia. *Ann. Glaciol.*, **26**, 281–284.

Fukushima, Y. and G. Parker. 1990. Numerical simulation of powder-snow avalanches. *J. Glaciol.*, **36**(123), 229–237.

Gauer, P. 1995. A model of powder snow avalanches. *In* Sivardiére, F., editor, Actes de Colloque Les apports de la recherche scientifique à sécurité neige, glace et avalanche. *Chamonix 30 mai - 3 juin 1995, ANENA*. Editions du CEMAGREF. Antony, France, pages 55–61.

Grigorian, S. S. and A. V. Ostroumov. 1977. Matematicheskaya model sklonovih processov lavinnogo tipa [The mathematical model for slope processes of avalanche type] (in Russian). Scientific Report 1955. Moscow, Russia, Institute for Mechanics, Moscow State University.

Hungr, O. 1995. A model for the runout analysis of rapid flow slides, debris flows, and avalanches. *Can. Geotech. J.*, **32**, 610–623.

Issler, D. 1998. Modelling of snow entrainment and deposition in powder-snow avalanches. *Annals Glaciol.*, **26**, 253–258.

Issler, D. 2003. Experimental information on the dynamics of dry-snow avalanches. *In* Hutter, K. and N. Kirchner, editors, *Dynamic response of granular and porous materials under large and catastrophic deformations*, volume 11 of *Lecture Notes in Applied and Computional Mechanics*. Berlin, Germany, Springer, pages 109–160.

Issler, D., P. Gauer, and M. Barbolini. 2000. Continuum models of particle entrainment and deposition in snow drift and avalanche dynamics. *In* Balean, R., editor, *Models of Continuum Mechanics in Analysis and Engineering. Proc. of a conference held at the Technische Universität Darmstadt, Sept. 30 to Oct. 2, 1998.* Aachen – Maastricht, Shaker Verlag, pages 58–80.

Issler, D., P. Gauer, M. Schaer, and S. Keller. 1996. Staublawinenereignisse im Winter 1995: Seewis (GR), Adelboden (BE) und Col du Pillon (VD). Internal Report 694. CH–7260 Weissfluhjoch/Davos, Switzerland, Eidg. Institut für Schnee- und Lawinenforschung.

Iverson, R. M. 1997. The physics of debris flows. *Rev. Geophys.*, **35**(3), 245–296.

Johnson, K. L. 2001. *Contact Mechanics*. Cambridge, U.K., Cambridge University Press.

Maeno, N. and K. Nishimura. 1979. Numerical computation of snow avalanche motion in a three-dimensional topography (in Japanese). *Low Temp. Sci., Ser. A*, **46**, 99–110.

McElwaine, J. and K. Nishimura. 2001. Ping-pong ball avalanche experiments. *Annals of Glaciology*, **32**, 241–250.

Mears, A. I. 1980. A fragment model of dry-snow avalanches. *J. Glaciol.*, **26**(94), 153–163.

Mehta, A. J. 1991. Review notes on cohesive sediment eerosion. In *Proc. Spec. Conf. on Quantitative Approaches to Coastal Sediment Processes*. New York, U.S.A., ASCE, pages 40–53.

Parker, G., M. Garcia, Y. Fukushima, and W. Yu. 1987. Experiments on turbidity currents over an erodible bed. *J. Hydr. Res.*, **25**(1), 123–147.

Partheniades, E. 1965. Erosion and deposition of cohesive soils. *J. Hydr. Div.*, ASCE, **91**(1), 105–139.

Rabinowicz, E. 1995. *Friction and Wear of Materials*. New York, NY, U.S.A., John Wiley & Sons, Inc., 2nd edition.

Rickerby, D. G. and N. H. Macmillan. 1980. On the oblique impact of a rigid sphere against a rigid-plastic solid. *Intl. J. Mech. Sci.*, **22**, 491–494.

Sailer, R., L. Rammer, and P. Sampl. 2002. Recalculation of an artificially released avalanche with SAMOS and validation with measurements from a pulsed Doppler radar. *Natural Hazards Earth Systems Sci.*, **2**, 211–216.

Simon, A. and A. J. C. Collison. 2001. Pore-water pressure effects on the detachment of cohesive streambeds: seepage forces and matrix suction. *Earth Surf. Proc. Landforms*, **26**, 1421–1442.

Sommavilla, F. and B. Sovilla. 1998. The avalanche monitoring system of Mount Pizzac. *In* Hestnes, E., editor, *25 Years of Snow Avalanche Research, Voss, Norway, 12–16 May 1998*, Publication Nr. 203. N–0806 Oslo, Norway, Norwegian Geotechnical Institute, pages 268–273.

Sovilla, B. and P. Bartelt. 2002. Observations and modelling of snow avalanche entrainment. *Natural Hazards Earth Systems Sci.*, **2**, 169–179.

Sovilla, B., F. Sommavilla, and A. Tomaselli. 2001. Measurements of mass balance in dense snow avalanche events. *Annals Glaciol.*, **32**, 230–236.

Wilesa, M., K. L. Johnson, and M. F. Ashby. 1975. Indentation of foamed plastics. *Intl. J. Mech. Sci.*, **17**, 457–460.

Zreik, D. A., R. G. Krishnappan, J. T. Germaine, O. S. Madsen, and C. C. Ladd. 1998. Erosional and mechanical strengths of deposited cohesive sediments. *J. Hydr. Engrg.*, ASCE, **124** (11), 1076–1085.

Kontroll- og referanseside/
Review and reference page

Oppdragsgiver/*Client* European Commission **Kontraktsreferanse/ *Contract reference*** Contract of 18.10.02	**Dokument nr/*Document No.*** 20021048-3 **Dato/*Date*** 28 November 2003
Dokumenttittel/*Document title* Avalanche Studies and model Validation in Europe, SATSIE **Prosjektleder/*Project Manager*** Karstein Lied **Utarbeidet av/*Prepared by*** Dieter Issler	**Distribusjon/*Distribution*** ☐☒ **Fri/*Unlimited*** **Begrenset/*Limited*** ☐ **Ingen/*None***
Emneord/*Keywords* Snow avalanches, full scale and small scale tests, dynamical models	
Land, fylke/*Country, County* Several **Kommune/*Municipality*** Several **Sted/*Location*** Several **Kartblad/*Map*** **UTM-koordinater/*UTM-coordinates***	**Havområde/*Offshore area*** **Feltnavn/*Field name*** **Sted/*Location*** **Felt, blokknr./*Field, Block No.***

Kvalitetssikring i henhold til/*Quality assurance according to* NS-EN ISO9001

Kontrollert av/ *Reviewed by*	Kontrolltype/ *Type of review*	Dokument/*Document* Kontrollert/*Reviewed* Dato/*Date*	Sign.	Revisjon 1/*Revision 1* Kontrollert/*Reviewed* Dato/*Date*	Sign.	Revisjon 2/*Revision 2* Kontrollert/*Reviewed* Dato/*Date*	Sign.
	Helhetsvurdering/ *General Evaluation* *						
KL		28/11-03	CL				
	Språk/*Style*						
KL	Teknisk/Technical - Skjønn/*Intelligence*	28/11-03	CL				
	- Total/*Extensive*						
	- Tverrfaglig/ *Interdisciplinary*						
KL	Utforming/*Layout*	28/11-03	CL				
KHe	Slutt/*Final*						
JS	Kopiering/*Copy quality*	1/12-03	JS.				

* Gjennomlesning av hele rapporten og skjønnsmessig vurdering av innhold og presentasjonsform/
On the basis of an overall evaluation of the report, its technical content and form of presentation

Dokument godkjent for utsendelse/ *Document approved for release*	**Dato/*Date*** 28/11/2003	**Sign.** Dieter Issler